Surface Properties of Spintronic Materials Probed Using a Spin-Polarised Metastable Helium Beam

Phillip David Bentley

Doctor of Philosophy

University of York

Physics

November 2019

Abstract

Since the isolation of graphene in 2004, there has been an increasing drive to tailor this and other 2D materials for spintronic applications due to their unique electronic properties. Analysis of the surface Fermi-level spin polarisation of 2D materials is crucial in designing spintronic devices, and characterising this property requires extremely surface sensitive techniques. One such approach, metastable de-excitation spectroscopy (MDS), involves the use of helium atoms prepared in the 2^3S state to analyse the surface density of states. This thesis presents the first set of results from an extension to this technique known as spin-polarised metastable emission electron microscopy (SPMEEM), in addition to detailed studies of several materials systems relevant to the development of spintronic devices.

After an introduction and review of how 2D materials are potential candidates for spintronics, a detailed description of MDS is given in Chapter 3 with Chapter 4 outlining other experimental approaches and systems used throughout this project. Chapter 5 reports a detailed study of domain structures at the surface of $Fe_3O_4(001)$ probed using SPMEEM where a significant spin canting effect was found to exist helping to estimate a value for the uniaxial surface anisotropy constant. The use of SPMEEM to observe the spin reorientation transition in $Fe_3O_4(001)$ is outlined with further results showing how the spin asymmetry at the surface of magnetite increases due to exposure to naphthalene. Chapter 6 explores how graphene grown on silicon carbide could be modified for spintronic applications through the adsorption of hydrogen and intercalation of heavy metallic species. Chapter 7 presents results from a study of the organic semiconducting molecule 6T on manganite (LSMO) substrates, a system of interest in organic spintronics. Finally, the thesis concludes with a chapter on conclusions and future work.

Contents

List of Tables

List of Figures

Acknowledgements

First of all I would like to thank the Engineering and Physical Sciences Research Council (EPSRC) for funding this project and the Thomas UKRC Computing Cluster where many of the CASTEP calculations were performed.

Next, a huge thank you to my supervisors, Dr. Andrew Pratt and Dr. Aires Ferreira for providing me with the opportunity of this PhD. Furthermore, thanks to Andy for his enduring patience with my shenanigans, bad English and strange expressions.

During this PhD, I've been very fortunate to work at the National Institute for Materials Science (NIMS) multiple times, where some of the data presented here was collected. In particular, I would like to highlight Yamauchi-san who has been incredibly helpful as well as acknowledge Kurahashi-san, Zhang-san and Suzuki-san.

I would like to highlight a number of names of past project students, postgraduates, postdocs and research staff: Willeke, Alex, Aaron, Sam, Stephen, Barat Kuerbanjiang, Dan Pingstone, Andrew Vick, Adam Stroughair, Phil Hasnip, Matt Probert, Toby Bird, Steve Tear, Chris Walker and Ilaria Bergenti.

I'd like to thank my parents for their constant support during all points of this PhD, the LATEX community, the university choir and the UoY Japanese society.

日本での滞在中、たくさんの素敵な人たちにお会いしました。特に安保さんご一家 、エミコさんやホウセイさん、ホット・スタッフ・バーの方々には大変お世話になりました。日本で出会ったみなさんには本当に感謝でいっぱいで、次に日本を訪ねたときまたお会いできるのがとても楽しみです。

Finally a huge thank you to both housemates Jason Zhang and Kazuki Inoue. Jason for being a constant support, a laugh to be around and putting up with my noisiness. Kazuki for being extremely helpful in the Japanese society and a source of support.

Declaration

I declare that the work presented in this thesis, except contributions acknowledged explicitly in the text or by reference, is based on my own research. No part of this work has previously been submitted for any award or qualification.

The following publications, either in print or soon to be submitted, have arisen from this work:

[1] *Activating buffer layer graphene on SiC through atomic hydrogen exposure* P. D. Bentley, *et al.*, (in preparation)

[2] *Imaging surface magnetic domain structure using a spin-polarized metastable helium beam* P. D. Bentley, R. Evans, X. Sun, M. Kurahashi, A. Pratt, and Y. Yamauchi, (in preparation)

[3] *Aldehyde-mediated protein-to-surface tethering via controlled diazonium electrode functionalization using protected hydroxylamines* N. Yates, M. Dowsett, P. Bentley, J. Dickenson-Fogg, A. Pratt, C. Blanford, M. Fascione, and A. Parkin, Langmuir (accepted for publication)

[4] *Origin of antiferromagnetic exchange coupling at* Fe/Fe_3O_4 *interfaces* J. C. Zhang, P. D. Bentley, X. Sun, M. Kurahashi, Y. Yamauchi, and A. Pratt, (in preparation)

[5] *Observation of conformationally degenerate states in* C_{60} *molecules using a metastable helium beam* J. C. Zhang, S. Mann, P. D. Bentley, I. Bergenti, and A. Pratt, (in preparation)

[6] *Controlling water permeation through* MoS_2 *membranes using phase engineering* R. Nair, P. D. Bentley, A. Pratt, ... *et al.*, Science, (submitted, October 2019)

Chapter 1

Introduction

With Moore's law stalling and the emergence of new technologies and the Internet of Things, there is an increasing need for enhanced computing performance and greater memory storage. To satisfy these demands, the volume of magnetic grains and the length of transistors must be scaled down but both of these metrics are reaching fundamental limits. In hard disk drive media, the signal-to-noise ratio (SNR) of each magnetic grain scales inversely with respect to transition probability (σ_n) where $\sigma_n \propto D^{\frac{3}{2}}$ with D the grain size width [1]. As the volume of the grain decreases to the size limit which is dictated by the thermal stability of the grain, the SNR and write field (associated with the anisotropy of the grain) needed to switch the grain increase. At a certain width known as the limiting medium thickness, incoherent magnetisation reversal dominates. Thus, beyond the limiting medium thickness, the SNR and write field needed to switch the grain are too large to write data and so systems such as PtFe are limited to widths of 4.8 nm [1, 2]. In order to improve computational performance, the number of transistors per unit area must be increased but to do so requires the size of a transistor to be reduced. However, as the length scale decreases, quantum effects start to take place and electrons can tunnel from one end of the gate to the other foregoing the operating principle of a transistor [3, 4]. Sizes as small as 1 nm have been achieved [3], but in recent years, the number of transistors per unit area as a function of time, described by the well-known Moore's law [5], is reaching a limit as the trend starts to plateau. Consequently, conventional electronics cannot be taken that much further and future

devices will need to rely on more than charge in order to communicate information.

One field that could replace conventional electronics is that of spintronics, an abbreviation of spin electronics. Spintronic devices use the spin of an electron and its associated magnetic moment to carry information in addition to, or alternatively without, the associated charge. Spintronics has multiple advantages over conventional electronics such as lower power consumption as well as data transfer via spin current being quicker and non-volatile due to the spin of an electron not being energy dependent [6–8]. Thus in the circumstance of a power outage, information stored in spin currents is retained. Spintronics also has potential applications within quantum computation which would greatly extend the performance of computers beyond their current limits. Ideally spintronic devices need two key properties: (1) large spin relaxation lengths enabling long distance communication; (2) the ability to produce large, robust spin-polarised currents. Unfortunately, the spin injection/detection efficiencies of most devices only increase upon reaching low temperatures and therefore such spin-devices are not applicable outside the laboratory [8]. Hence, new materials and novel device architectures are required for next-generation spin technologies to be realised.

1.1 The 2D Material Revolution

In 2004, researchers Andre Geim and Konstantin Novoselov at the University of Manchester achieved the isolation of monolayer graphene on SiO_2, successfully measuring its unique transport properties [10]. Graphene, a single layer of graphite consisting of carbon atoms arranged in a honeycomb-like lattice (Figure 1.1) has been shown to be extremely strong, to be an excellent conductor of heat, and to have phenomenal electronic properties. Most notably in the context of this project, free-standing graphene has been predicted [11] and shown [10, 12] to have a large spin relaxation length at room temperature making it an attractive candidate for spintronics. Proximity-induced spin-orbit coupling in graphene offers a realistic route towards two-dimensional (2D) topological insulator state engineering. This is particularly relevant for quantum computation, since topological insulators van der Waals coupled to superconductors are predicted to host Majorana fermions, particles which

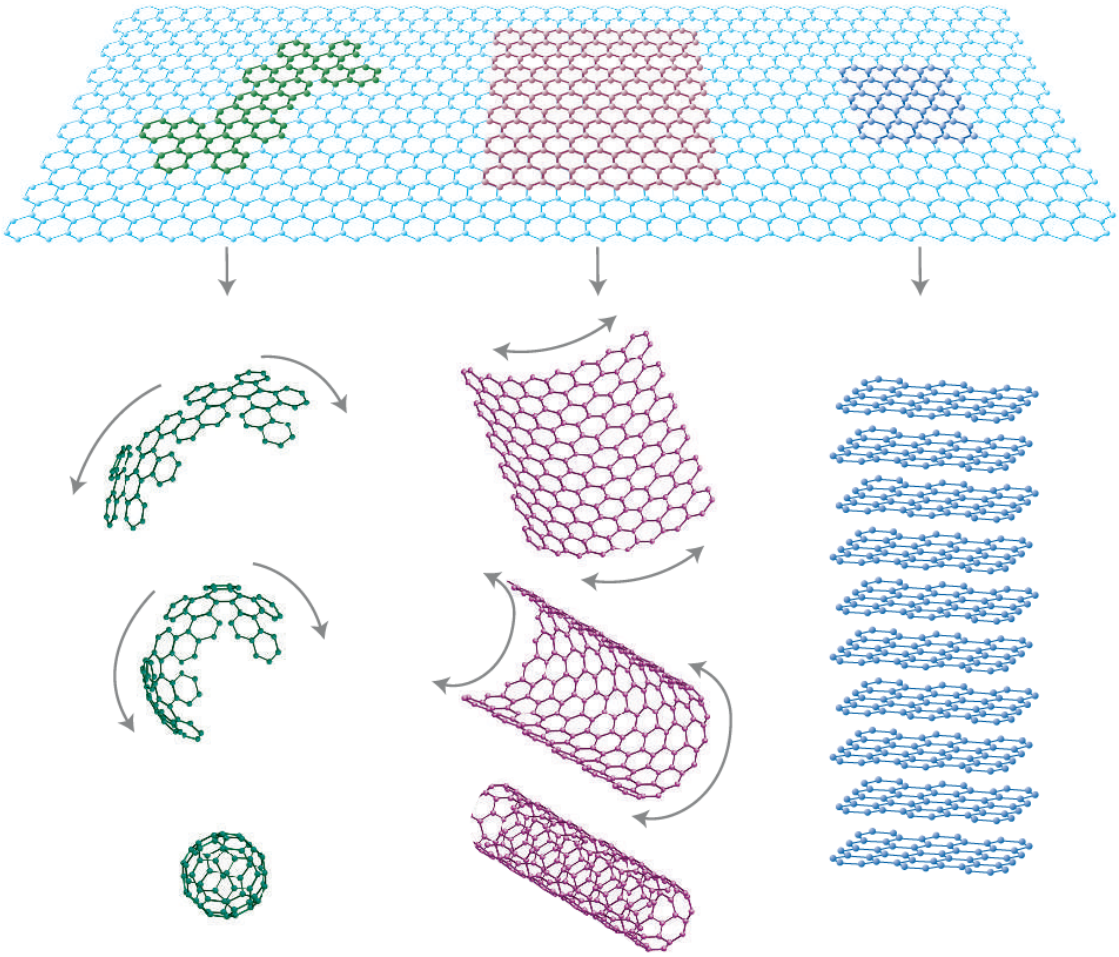

Figure 1.1: Graphene and its various carbon allotropes: C_{60} (left), carbon nanotubes (centre) and graphite (right). Taken from Geim *et al.* [9].

are their own antiparticle [13]. Heterostructures of graphene and other 2D materials such as the transition metal dichalcogenides (TMDs) have shown rich spin textures around the K-point of their respective Brillouin zones [14, 15] offering a viable route for graphene-based spintronic devices. Furthermore, other 2D monolayers such as molybdenum disulphide with its natural breaking of inversion symmetry enable spin and valley-selective light absorption [14] making these materials not only applicable in spintronics but also in an emerging area called valleytronics. Graphene, TMDs and black phosphorous have in recent years garnered a huge amount of interest in photonics, particularly in single photon emitters and detectors, with a large amount of focus on single layers of WSe_2 as well as heterostructures assembled from multiple 2D materials [16–18]. Finally, in terms of utilising its electronic properties, graphene has seen some use in organic light emitting diodes [19], a multi-billion dollar industry

that is still continuing to grow.

Despite graphene's unique properties at room temperature, the reason that graphene spintronic devices have not yet been fully realised is a result of two key issues. The first is graphene's weak intrinsic spin-orbit coupling (SOC) [20] which is too small to result in the spin-Hall effect [12]. Thus a pristine monolayer of graphene alone cannot act as a spintronic device and it is only through the decoration/intercalation of atomic species that the SOC can be enhanced locally [21] or globally [22]. The second issue is controlling the growth/production of graphene monolayers. Graphene produced from the exfoliation of highly-oriented pyrolytic graphite (HOPG) has the highest transport properties reported of any other form of graphene [23, 24], but, with this method, it is difficult to control the number of layers. Devices which incorporate exfoliated graphene report primarily monolayer graphene growth, but also some existence of bilayer graphene [25]. Unfortunately, this is problematic for device applications since multilayer graphene as well as wrinkles and defects warp the bandstructure of a single layer of graphene and drastically reduce the electron mobility in-plane [26]. Controlling the growth of other 2D materials such as TMDs is equally challenging, with factors such as temperature having a significant influence on the domain size [27].

Understanding, observing and characterising monolayers of graphene and how it is influenced by the intercalation/decoration of heavy metallic species, requires a range of complementary techniques which probe a variety of properties of the surface. One way to approach analysis of graphene is by using photoemission electron spectroscopy, which enables observation of valence band states with ultraviolet (UV) photons and core states with X-ray photons. By tuning the photon source to around 40 eV, photoemission can be extremely surface sensitive, with minimal contribution from subsurface and bulk states [28]. Angle-resolved photoemission spectroscopy (ARPES) can be used to characterise the unique dispersion relation of graphene as well as the influence of adatom decoration and intercalation on the spin-split density of states [29]. Yet, despite the benefits of photoemission electron spectroscopy, there is still some emission of bulk/subsurface state electrons which is not ideal when trying to analyse a monolayer of graphene or any other 2D material. Ideally, there is a need for techniques which only probe surface states whilst ignoring bulk states

and one promising candidate is metastable de-excitation spectroscopy (MDS). This technique uses metastable helium atoms prepared in the 2^3S state, which de-excite when in close proximity to a surface resulting in the emission of an Auger electron which carries information of the surface density of states of a material. Due to the large de-excitation cross section of metastable helium, all de-excitation events occur a couple of Ångstrom above a surface and consequently only the outermost surface states are probed. The energy of the He 2^3S state is 19.8 eV which is very similar to that of He I α UV photons of 21.2 eV, and so both techniques produce spectra that in many cases are directly comparable.

Furthermore, the spin-polarised equivalent of MDS can be performed by preparing the atoms in the $m_j = \pm 1$ magnetic sublevels and applying a quantization axis, thereby allowing the spin-split density of states of a material to be probed. The technique is then known as spin-polarised metastable de-excitation spectroscopy (SPMDS) [30, 31]. This has revealed unique phenomena relating to surface magnetic properties such as a small positive spin polarisation at the (111) face of magnetite [32] and the spin asymmetry of chemical vapour deposition graphene grown on Ni(111) [33]. The surface sensitivity of MDS and the ability to spin-polarise the source, coupled with complementary techniques such as photoemission, will allow systematic studies of global spin-orbit coupling effects in graphene and 2D material spintronic devices. Additionally, a He 2^3S source combined with an emission electron microscope has been used to image the surfaces of various materials [34] and in principle could be used as a spin-polarised microscopy technique. The work presented in this thesis shows the first results of such a technique and offers an attractive route to studying surface magnetic properties in 2D materials.

1.2 Thesis Overview

Following this Introduction, Chapter 2 explores 2D materials and their potential use in spintronic applications in more detail, with a particular focus on graphene. This chapter starts by outlining the structure and properties of graphene before moving on to its role in spintronics and how spin-orbit coupling can be enhanced within the material. Methods with which to fabricate graphene and related 2D materials are

then introduced.

As a large part of this project has involved the use of a beam of He 2^3S atoms in the form of MDS and its associated microscopy, Chapter 3 is dedicated to exploring how these atoms de-excite when in contact with another gas or a surface. Additionally, the application of optical pumping and a sextupole magnet in order to electron spin-polarise the He 2^3S atoms is discussed.

Since multiple laboratories and experimental systems were used to exploit a variety of techniques in this project, Chapter 4 explores both the systems used in York, as well as that used at the National Institute for Materials Science (NIMS) in Tsukuba, Japan. The principles and practicalities of surface analysis methods including X-ray and ultraviolet photoemission spectroscopy and low-energy electron diffraction are described, in addition to spin-polarised photoemission and sample growth procedures. The chapter finishes by briefly describing CASTEP, a density functional theory (DFT) code used to produce theoretical calculations that support experimental measurements.

Chapter 5 explores the work performed at NIMS, in particular, the development of spin-polarised metastable emission electron microscopy (SPMEEM), the microscopic extension of SPMDS that is demonstrated here for the first time. Results from a study of magnetic domain structure on the clean $Fe_3O_4(001)$ surface are presented in addition to the hydrogen-passivated and napthalene adsorbed $Fe_3O_4(001)$ surfaces.

The majority of experiments performed in York revolved around analysing graphene grown on six-hexagonal silicon carbide (6H-SiC) and how this could be tailored for spintronic applications. In Chapter 6, the first carbon layer grown on the silicon-rich face (buffer layer) is explored through photoemission and MDS as well as simulations using CASTEP for a clean crystal and after growth of the buffer layer. This chapter then explores how this can be activated using atomic hydrogen and potentially erbium.

Organic monolayers grown on top of magnetic materials have also been of interest within spintronics due to the observation of unique electronic phenomena such as interfacial magnetoresistance. To further understand the interaction between organic molecules grown on ferromagnetic substrates, Chapter 7 explores growth of

α-sexithiophene (6T) monolayers on $La_{0.7}Sr_{0.3}MnO_3$ thin films. The clean surface of LSMO thin films were analysed using different electron spectroscopy techniques. Different coverages of α-sexithiophene were then deposited on top of these thin films and characterised using electron spectroscopy and atomic force microscopy.

Finally, some suggestions for the future direction of the SPMEEM system as well as how to develop on the results obtained for SiC are suggested.

Chapter 2

2D Materials for Spintronic Applications

Throughout the 20th century and into the early 21st century, experimental reports on graphene (as well as other 2D materials) considered it to be part of a 3D structure rather than something which could exist on its own, for example monolayer graphite on nickel [35]. It was not until the isolation of free-standing graphene by a group in Manchester using the well-known Scotch tape method [10], that the 2D materials revolution began. Interest in materials such as graphene [9], molybdenum disulphide [36] and silicene [37] in spintronic applications stems primarily from their extraordinary electrical properties at room temperature. This chapter introduces 2D materials and how their properties can be exploited for spintronic applications.

2.1 Graphene

As can be seen in Figure 2.1, a pristine monolayer of graphene is a 2D-material spanning 'infinitely' in x and y, consisting of sp^2 hybridised carbon atoms arranged in a honeycomb-like lattice [11]. The bond length between each carbon atom is 1.42 Å and all bond angles are 120° [11]. It is a single layer of graphite from which other carbon allotropes can be made including Buckminsterfullerene (C_{60}) [38] and carbon nanotubes. Graphene at room temperature has extremely beneficial electronic properties such as a high charge carrier mobility of 200,000 $cm^2V^{-1}s^{-1}$, an

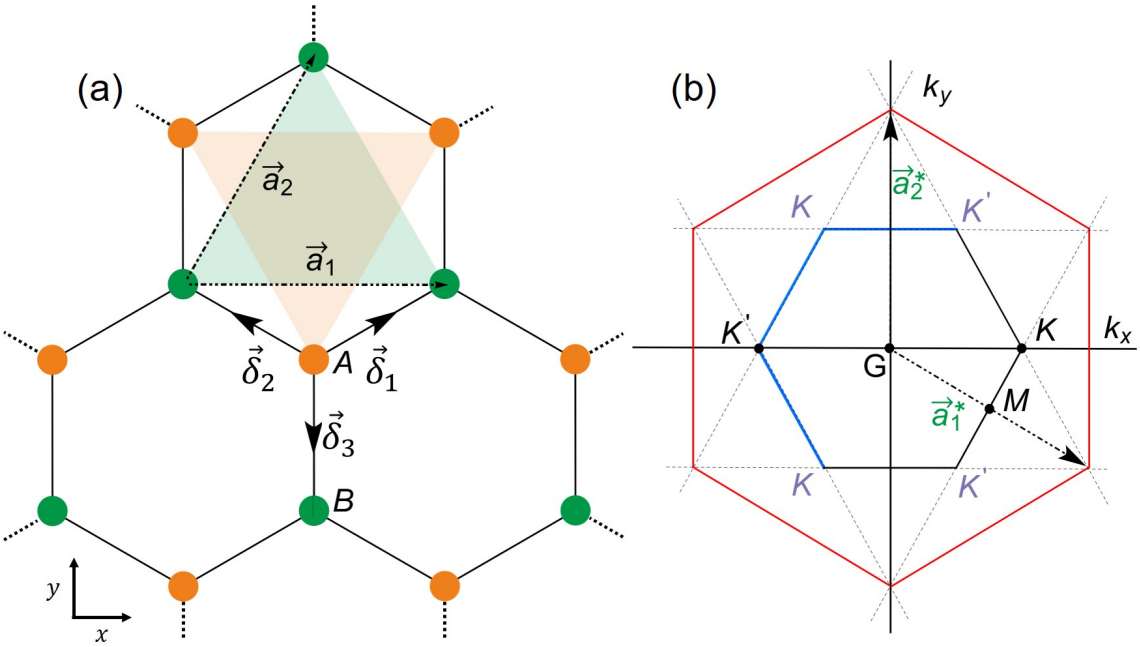

Figure 2.1: (a) Graphene can be split into two inequivalent sublattices A and B. For an atom in the A sublattice, its nearest neighbours located at $\vec{\delta}_1 = \frac{a}{2}(\sqrt{3}, 1)$, $\vec{\delta}_2 = \frac{a}{2}(-\sqrt{3}, 1)$, and $\vec{\delta}_3 = a(0, -1)$, where a is the lattice constant, can be used to determine the reciprocal lattice vectors and consequently the K-point in reciprocal space which is the intersection between the two Bravais lattices, as shown in (b).

electrical conductivity of 10^6 Scm^{-1} and a thermal conductivity of 5000 Wm^{-1}K^{-1}, thus making it an attractive material in both electronics and spintronics [39].

These transport properties originate from the bonding structure of graphene which gives rise to a unique dispersion relation that is a feature of certain 2D electron gasses and materials [37]. Graphene consists of two inequivalent sublattices, A and B, as seen in Figure 2.1, where the hexagonal Bravais lattices consist of parallelogram unit cells. The associated reciprocal lattice vectors are given by:

$$\mathbf{a}_1^* = \frac{2\pi}{\sqrt{3}a}\left(\hat{\mathbf{i}} - \frac{1}{\sqrt{3}}\hat{\mathbf{j}}\right) \quad \text{and} \tag{2.1}$$

$$\mathbf{a}_2^* = \frac{4\pi}{3a}\hat{\mathbf{j}} \tag{2.2}$$

where a is the lattice constant (≈ 1.42 Å). The K-point can be determined from these vectors to be $K = \frac{4\pi}{3\sqrt{3}a}\hat{\mathbf{i}}$. To determine the electronic structure of graphene, a 2$^{\text{nd}}$

order quantisation approach of tight binding theory for π electrons is used, restricting electron interactions to nearest neighbours. The following unitary transformations are used:

$$a_i = \frac{1}{\sqrt{N_A}} \sum_{\mathbf{k}} e^{-i\mathbf{k}\cdot r_i} a_{\mathbf{k}} \tag{2.3}$$

$$b_i = \frac{1}{\sqrt{N_B}} \sum_{\mathbf{k}} e^{-i\mathbf{k}\cdot r_i} b_{\mathbf{k}} \tag{2.4}$$

where N is the number of atoms on sublattice sites A and B, $\mathbf{k}$ is the wave vector and r_i is the atomic site in a periodic lattice. By solving the Hamiltonian using tight binding theory, the dispersion relationship can be found to be:

$$E(\mathbf{k}) = st\sqrt{3 + \sum_{a \neq b} \cos(\mathbf{k}\cdot\boldsymbol{\delta}_a - \mathbf{k}\cdot\boldsymbol{\delta}_b)} \tag{2.5}$$

where the Fermi velocity around the K-point is $v_f = \frac{3at}{2\hbar}$, t is the nearest-neighbour hopping integral energy (≈ 3 eV), $\hbar$ the reduced Planck constant, and $s = \pm 1$ is a band index denoting the positive (negative) energy branches of the spectrum [40]. At the K and K' points, at the edges of the Brillouin zone the valence and conduction bands meet, as seen in Figure 2.2, with $E(\pm K) = 0$. The meeting of these bands is known as the Dirac point and graphene is therefore sometimes known as a zero-overlap semimetal or a zero-gap semiconductor [9]. The Fermi edge is situated at the intersection between the bands when graphene is charge neutral and it is only with graphene grown on substrates such as SiC that the doping will shift the position of the Fermi level into either the valence or conduction bands [41].

The result of linear dispersion in graphene is the formation of quasiparticles known as massless Dirac fermions which can be seen as electrons that have lost their rest mass [9, 40]. Theoretically, the speed of these fermions at the K-point is approximately 300 times slower than the speed of light on substrates such as hexagonal boron nitride (H-BN) or SiO_2 [40, 42]. Yet, measurements for exfoliated graphene on H-BN have measured the drift velocity to be 29.4% [43] of the theoretically predicted value [44]. This reduction in electron mobility in graphene is a consequence of factors such as carrier scattering from surface optical phonons [43].

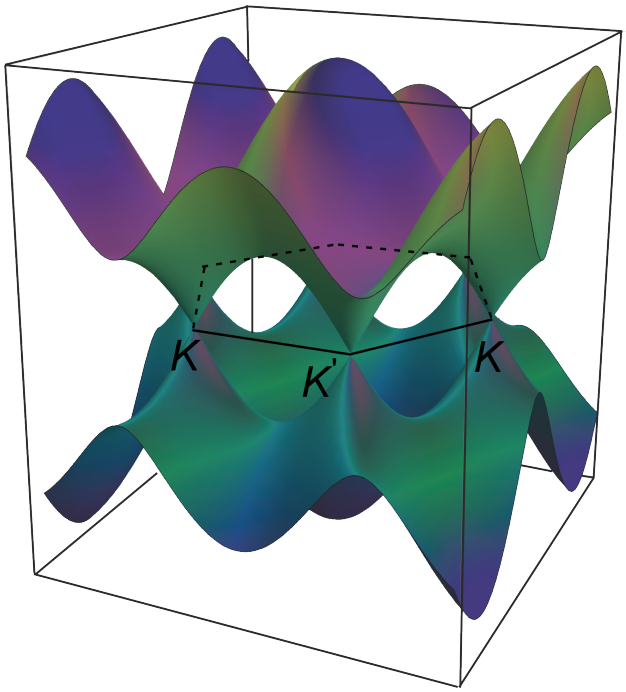

Figure 2.2: The hybridisation of graphene results in the formation of linear dispersion in reciprocal space, where the valence and conduction bands meet at the K-point, known as the Dirac point.

Graphene layers stacked on top of each other are van der Waals bound with the stacks tending to align primarily in one of two ways: Bernal or rhombohedral [40]. Bernal stacking (ABABAB) is the most favourable stacking formation with approximately 80% of naturally occurring graphite having this crystal structure [45]. The second most favourable stacking structure is rhombohedral (ABCABC) [46–48] and other stacking formations such as hexagonal can also occur in graphite. The average separation between each of these stacks is around 3.4 Å but this varies slightly depending on the specific formation [40].

The first predictions of the bandstructure of graphene were made by Wallace in 1947 [49] who observed a linear-like dispersion around the K-point, labelling graphite as a zero-activation-energy semiconductor. As discussed above, for a pristine layer of free standing graphene, the bandstructure is linear around the K-point. Yet, as the number of layers of graphene increase, tending towards graphite, the bandstructure changes quite drastically as a consequence of interlayer interactions between each carbon layer. For example, a bandgap was observed in multiple layers of graphene due to disorder in the c-axis [50]. Furthermore, in Bernal-stacked graphene, the

bandstructure around the K-point is modified heavily when multilayer graphene is grown on silicon carbide [45]. In graphite, the linear dispersion broadens at the K-point [11].

Similar to multilayer growth, the introduction of wrinkles/defects [26] also modifies the bandstructure resulting in huge losses in electrical conductivity and mobility. Therefore, progress in using graphene as a material for electronic devices has stalled since a bandgap would be required for any conventional transistor. More recently, graphene has received increasing interest for applications in spintronics due to its large spin relaxation length at room temperature [9], with the aim of enhancing its intrinsically small spin-orbit coupling (SOC) as defined below [20].

2.2 Spin-Orbit Coupling in Graphene

When an electron moves in the finite electric field of its nucleus, it experiences a magnetic field in its rest frame. This magnetic field couples with the electron's associated magnetic moment (spin) and introduces a term $V_{SOC} = -\mu_s \cdot B$ in the scattering potential [51]. The coupling between the electron's spin and its orbital motion around the nucleus is known as spin-orbit coupling (SOC) which results in a shift in the electron's atomic energy levels [52]. The strength of SOC scales with atomic number (Z) [52] and consequently, since graphene consists entirely of carbon, its SOC is small. Around the K-point of graphene, there is a predicted spectral bandgap of around 24 μeV at 0.28 K due to a weak SOC splitting [12, 20]. The Hamiltonian of an electron affected by the SOC interaction is represented by the following equation [12]:

$$\hat{H}_{SO} = \frac{\hbar}{4m_e^2c^2}\left(\nabla V \times \hat{p}\right) \cdot \hat{s} \tag{2.6}$$

where V is the effective crystal field potential, m_e is the rest mass of the electron, c the speed of light, $\hat{p}$ the momentum operator, and $\hat{s}$ represents the array of Pauli matrices acting on spin degrees of freedom [12]. Since SOC in graphene is small, the only way to enhance it is either by changing the hybridisation [21] or introducing large atomic number species whose bands overlap with those of graphene. Many

different heavy metallic species such as ruthenium [53], cobalt [29] and gold [54] have been used, enhancing the SOC through interactions described below.

Two approaches to enhancing SOC in graphene have been attempted so far: either through adatom-decoration (extrinsic-like) [21, 55] or by placing graphene on a substrate (typically a transition metal) and intercalating heavy metallic species underneath (intrinsic-like) [13, 22]. Adatom decoration, for example using hydrogen [21], has resulted in a sizeable local extrinsic (scattering) SOC of around 10 meV as a consequence of the diamond-like hybridisation at the point where the atoms are bonded. Whilst this method results in a significant enhancement to SOC there are several issues with this approach. The first is that, although adatom-decoration changes the hybridisation to enhance SOC, this is accompanied by a loss in linear dispersion at the $K(K')$-point. Secondly, adatom decoration further results in inter-valley scattering (at the $K(K')$-point), which is detrimental to spintronic applications since it results in reduced performance of the device [13, 56].

Interest has also developed in growing graphene on metallic as well as semiconducting and insulating substrates [29, 57] and then intercalating with heavy metallic species such as gold [54] or lead [22]. This results in the so-called "proximity effect", an intrinsic (topological) and uniform global SOC which alters symmetries within the graphene whilst maintaining the sp^2 hybridisation [13, 58]. Proximity-induced SOC avoids the issues introduced through adatom decoration whilst enhancing the SOC and creating rich spin textures around the $K(K')$-point [59]. Some of the main difficulties faced with this approach include the choice of substrate on which to grow graphene as well as controlling the growth such that there exists only a monolayer (to avoid interlayer interactions caused by bilayer/multilayer formation). For example, graphene grown on single crystal Ni(111) has a very low lattice mismatch enabling growth of large regions of epitaxial graphene, but this is much more closely bound to the substrate resulting in back-bonds [60]. This alters the hybridisation of graphene and it is only through the intercalation of atomic species that this back-bond can be broken [54, 61]. A substantial amount of work has been performed to determine the best systems for inducing SOC through the proximity effect, some of which are discussed in Section 2.3.

The consequence of enhancing SOC in graphene is a breaking of chiral symmetry (described by the so-called Berry curvature in momentum space [62]) leading to a transition in phase to one of various different quantum effects such as the quantum anomalous Hall effect, quantum spin-Hall effect (QSHE) and Rashba–Edelstein effect (current-induced spin-to-charge conversion) [6]. The quantum anomalous Hall effect originates from the coupling of spontaneous magnetic moments and SOC. This coupling gives rise to a topologically nontrivial structure, which results in the quantised Hall effect in the absence of an external magnetic field [63]. The intrinsic QSHE is defined as when a charge current is influenced by SOC such that under an applied electric field, a spin current is generated which travels perpendicularly to that applied field [62]. The importance of SOC in graphene is that it may result in a transition to one of these phases which then may be used to tailor graphene for spintronic applications. There has been a drive since the isolation of free-standing graphene [10] to enhance SOC and generate a spin-current.

2.2.1 Symmetry in Graphene and Intrinsic SOC

A pristine monolayer of graphene belongs to the D_{6h} point group symmetry, also known as a dihexagonal-dipyramidal crystal structure [12, 64]. Graphene is sixfold rotation and mirror inversion symmetric about its plane [62, 64] as can be seen in Figure 2.3. As a consequence of graphene's symmetry, a pristine layer allows only one type of SOC known as intrinsic SOC, characterised by a hopping length of λ_I [12]. This SOC comes about primarily due to coupling between p_z and d orbitals at T = 0.28 K [12, 20, 65] for which λ_I is heavily dependent on the $3d_{xz} \pm i3d_{yz}$ orbital configuration [12, 65]. This splitting term is too weak experimentally for a detectable transition into the quantum spin-Hall phase [12, 20] and it is only by further manipulating symmetry that SOC in graphene can be enhanced.

2.2.2 Bychkov-Rashba Splitting

Bychkov-Rashba (mostly referred to as Rashba) splitting was first proposed in 1959 by Emmanuel Rashba in two separate papers studying the spin-orbit interaction in würzite structures [66–68]. This type of spin-splitting results as a consequence of

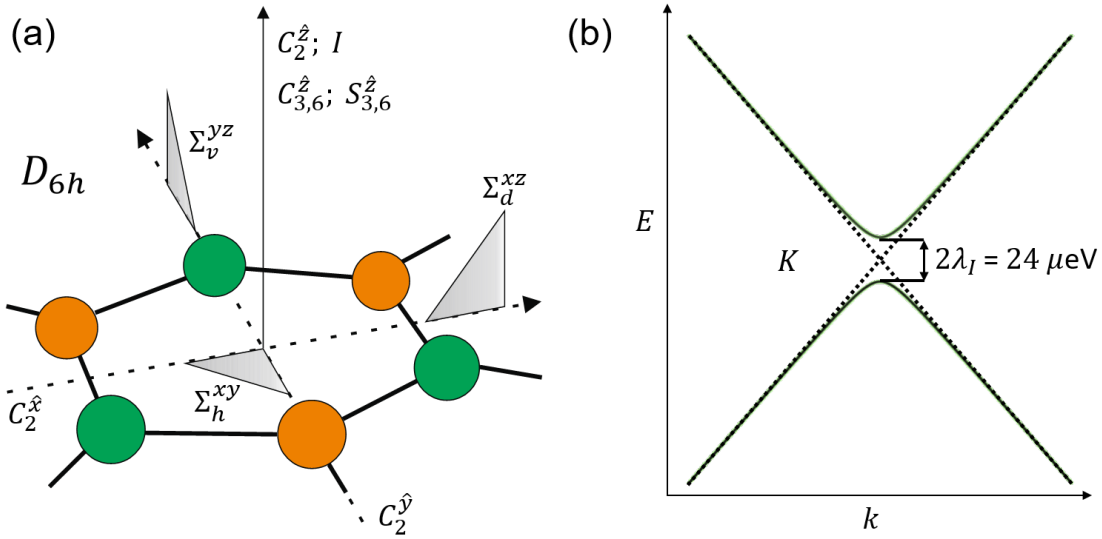

Figure 2.3: (a) A pristine monolayer of graphene, represented here by carbon atoms belonging to the two nonequivalent lattice sites (green and orange), is sixfold-rotation and mirror-inversion symmetric about its plane and is therefore of the point group dihexagonal-dipyramidal (D_{6h}). (b) As a consequence of coupling between p_z and d orbitals, a small bandgap of 24 µeV opens up, known as intrinsic SOC.

graphene transitioning from the D_{6h} point group symmetry to C_{6v} (dihexagonal-pyramidal) and an associated breaking of inversion symmetry through interaction with the substrate resulting in a perpendicular electric field [62, 68, 69]; an example of this symmetry change can be seen in Figure 2.4. The Hamiltonian used to describe electrons at the K-point subject to a uniform Rashba interaction is:

$$H = \int d\mathbf{x}\ \Psi^{\dagger}(\mathbf{x})\left[v\ \boldsymbol{\sigma}\cdot\mathbf{p} + \lambda_{BR}(\boldsymbol{\sigma}\times\mathbf{s})\cdot\hat{z} + V(\mathbf{x})\right]\Psi(\mathbf{x}) \tag{2.7}$$

where v is the bare velocity of massless Dirac fermions, $\mathbf{p}$ is the 2D kinematic momentum operator, $\mathbf{k}$ is the 2D quasi-momentum, λ_{BR} is the Bychkov-Rashba SOC hopping length, $V(x)$ is a disorder potential describing elastic scattering from non-magnetic short-range impurities and $\sigma_i, s_i (i = x, y, z)$ are Pauli matrices associated with sublattice (pseudospin) and spin degrees of freedom respectively [69]. In the equation above, intervalley scattering processes have been ignored for simplicity [69]. The dispersion relation of the free Hamiltonian ($H_0 = H - V$) for the subbands μ, ν (majority and minority spin states) therefore becomes:

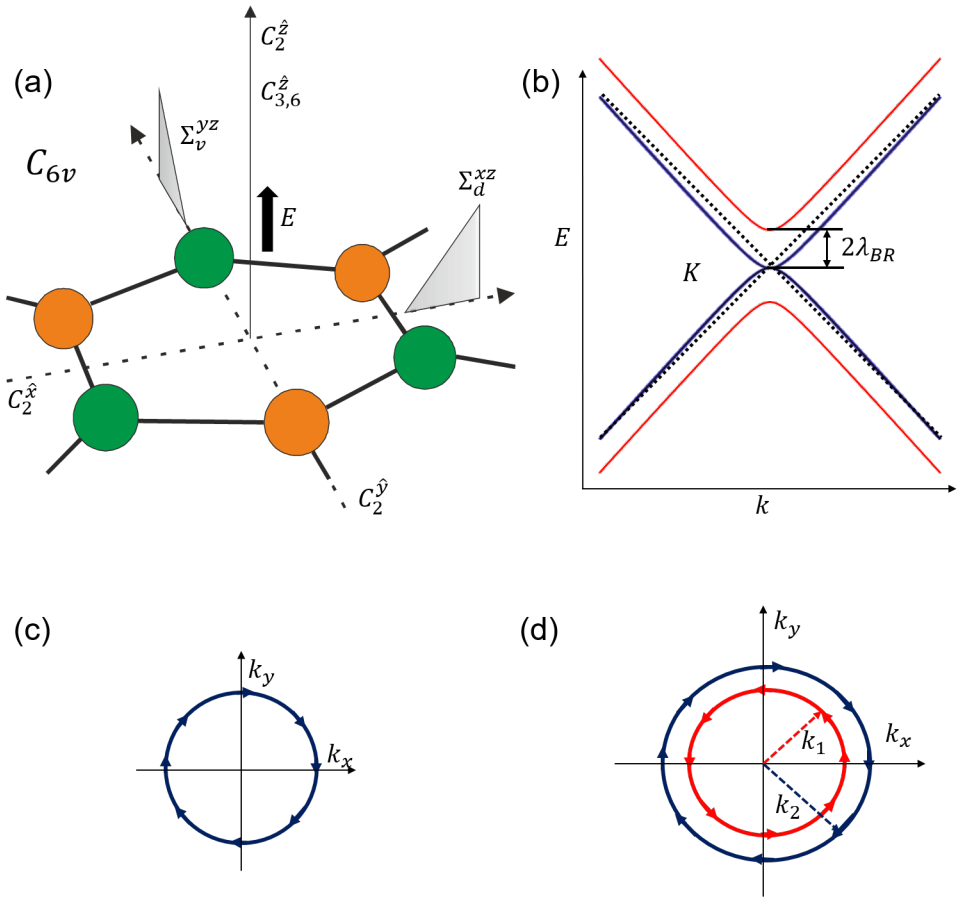

Figure 2.4: (a) Rashba-type SOC is a result of breaking of inversion symmetry, transforming the graphene into the point group dihexagonal-pyramidal (C_{6v}). This results in the formation (b) of a pseudogap ($2\lambda_{BR}$) between the majority and minority spin-states and (c) a Fermi level that intercepts a single subband when $|\varepsilon_f| < 2|\lambda_{BR}|$. (d) Counter-rotating spin textures result when $|\varepsilon_f| > 2|\lambda_{BR}|$.

$$E_{\mu\nu}(\mathbf{k}) = \mu\lambda_{BR} + \nu\sqrt{\lambda_{BR}^2 + v^2|\mathbf{k}|^2} \tag{2.8}$$

The Rashba interaction results in the formation of a pseudogap (spin gap) between the majority and minority spin states equal to 2λ and aligns the electron spin at right angles to the wavevector, an effect known as spin momentum locking [69–71]. Depending on the Fermi level (ε_f), there exists one of two different regimes. The first of these is when $|\varepsilon_f| < 2|\lambda|$ such that the Fermi energy intersects a single subband with electronic states having well-defined spin helicity and there is a topological-insulator-like phase [69]. For a 2D electron gas (2DEG), this only occurs at a single point where the two parabolic bands intercept [69, 72]. The other regime is when

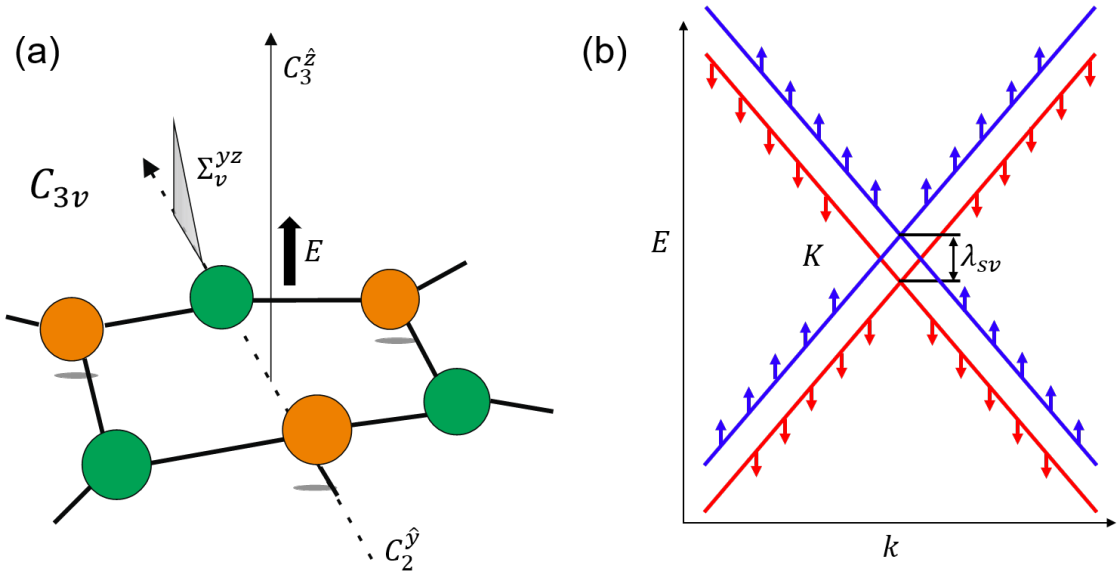

Figure 2.5: (a) Sublattice symmetry breaking leads to an energetic splitting in spin states and transformation to point group ditrigonal-pyramidal (C_{3v}) with (b) subbands split by an amount characterised by the spin-valley SOC hopping length λ_{sv}.

$|\varepsilon_f| > 2|\lambda|$ where the split Fermi surface displays counter-rotating spin textures similar to that of nonchiral 2DEGs with the Rashba interaction [69, 73]. Rashba SOC is a momentum splitting and therefore is only observable through techniques which probe k-space such as ARPES. Importantly, large Rashba splitting has been observed in a variety of systems including gold intercalation under graphene on nickel [54] and graphene/Au/Co(0001) [29].

2.2.3 Spin-Valley Splitting

Further manipulation of SOC in graphene can be achieved through breaking of sublattice symmetry [14, 59, 69, 74]. This changes the point group symmetry of graphene to ditrigonal-pyramidal (C_{3v}), making it only threefold rotationally symmetric as can be seen in Figure 2.5. This change of symmetry results in a splitting of the two subbands, but not the formation of a bandgap and so this type of splitting is known as spin-valley SOC (magnetic exchange coupling and valley-Zeeman are also used), an out-of-plane spin-orbit interaction. This is a spin conserving interaction, for which the Hamiltonian is expressed as [69]:

$$H_{sv} = \lambda_{sv}\tau_z\sigma_0 s_z \tag{2.9}$$

where λ_{sv} is the spin-valley hopping term, τ_z is the spin relaxation time, s_z is the z spin degree of freedom and σ_0 is the Pauli identity matrix [69]. Whilst no bandgap is opened from this proximity effect interaction alone, systems which experience multiple SOC interactions (Rashba and spin-valley), such as graphene on various dichalcogenides including MoS_2, have been shown to have a small bandgap around the K-point [14].

2.2.4 Kane-Mele Splitting

Kane-Mele SOC was first proposed in 2005 following analysis of the QSHE in graphene [62]. This type of SOC shows that in an experimentally accessible low temperature regime (near the temperature of liquid helium), the symmetry-allowed spin-orbit potential converts graphene from a zero-overlap semimetallic state at the $K(K')$-point to a quantum spin-Hall insulator. In this state of matter, it is 'gapped' in the bulk supporting transport of spin and charge in gapless nonchiral edge states that are insensitive to disorder and propagate at the sample boundaries [62]. The Hamiltonian of this state as presented in the original paper is:

$$\mathcal{H}_{SO} = \Delta_{SO}\psi^\dagger\sigma_z\tau_z s_z\psi \tag{2.10}$$

where $2\Delta_{SO}$ is the energy gap when the Bychkov-Rashba hopping length λ_{BR} is equal to zero. This gapped phase occurs when $\lambda_{BR} < \Delta_{SO}$ [62]. It is important to note that such splitting is weak and difficult to detect but has been observed in graphene decorated with Ir clusters at temperatures lower than 20 K [75].

2.3 Graphene in Spintronics

Early work in tailoring graphene for spintronics focused around adatom decoration to enhance its intrinsically weak SOC [21]. However, as discussed earlier, this approach results in inter-valley scattering, which is not ideal for spintronic applications

due to potential loss of information [13, 56]. Thus, there has recently been a greater interest in the so-called proximity effect and finding systems in which it exists such that there is a transition to the spin-Hall phase. One such system is graphene grown on the Ni(111) surface due to its low lattice mismatch of 1.2% and its well-ordered (1×1) atomic structure [76]. Spin-asymmetry has been observed in graphene on Ni(111) due to splitting between π and π^* orbitals which strongly overlap with nickel d states [33, 76, 77]. However, graphene on Ni has also been found to back-bond to the substrate, resulting in a loss of linear dispersion at the K-point [60]. Through the intercalation of atomic species such as gold [54] and bismuth [78], this back-bonding can be broken leading to the observation of large SOC. The difficulty though is controlling the intercalation [79] and therefore other ferromagnetic/metallic substrates have been investigated. Alternative substrates such as copper [13, 57] and iridium have been used [22] and have reported proximity-effect SOC enhancement within the graphene.

One system that has garnered a lot of interest in recent years is graphene on group-VI dichalcogenides (also referred to as TMDs) such as MoS_2 [14]. The general formula for TMDs is MX_2 where M refers to a transition metal, typically tungsten or molybdenum, and X is one of the group VI elements such as sulphur or selenium [14]. What makes systems such as MoS_2 interesting is the lack of inversion symmetry in a monolayer [14, 80], which enables spin and valley selective light absorption [80], meaning these heterostructures have applications in both spin and valley electronics [81, 82]. In fact, optical injection of spin has been observed in TMD-graphene spin valves [25, 83] as has large proximity-effect SOC in graphene/WS_2 heterostructures [84, 85] and high mobility in H-BN/MoS_2/graphene monolayers [86]. Rich spin textures have been predicted theoretically at the K-point, consisting of a combination of Rashba and spin-valley SOC, enabling a transition into the quantum spin-Hall and anomalous-Hall phase [14, 59]. This has led to the realisation of graphene/TMD spin valves [25] and observation of the QSHE at room temperature in graphene/MoS_2 heterostructures [87]. However, fabrication of such devices has typically involved using exfoliated graphene, where it can be quite difficult to control the thickness/number of layers of graphene [25].

One other promising route for graphene as a system for spintronic applications is

through growth on silicon carbide. This system is of interest due to silicon carbide's large bandgap of 3.02 eV [88], the ability to change the face polarity of the substrate [89] and the cutoff angle. By controlling the preparation conditions, it is also possible to grow large regions of epitaxial graphene, making it a much more controlled form of fabrication compared to the exfoliation technique. Various high-Z species have been intercalated including Eu [90], Re [91], Ir [92] and Au [93, 94]. In certain cases, for example Au, large Rashba SOC has been predicted [95] and experimentally observed [93]; similarly Eu has been shown to intercalate and not oxidise after months of exposure to atmospheric pressure [90], but no measurements have yet been made to measure possible SOC effects of rare-earth metal intercalation on SiC. The quantum Hall effect and nonlocal transport have been observed in graphene Hall bars formed on 4H-SiC [96] and, furthermore, there has been a keen focus on activating the buffer layer [41], with interesting phenomena such as observation of the Dirac point in unpinned regions of the buffer layer, but with a bandgap of 0.4 eV due to nanoscale superperiodicity [97].

2.4 Fabrication of Graphene

2.4.1 Exfoliated Graphene

Multiple techniques exist in order to produce graphene. One of these methods is through the exfoliation of graphene from highly-oriented pyrolytic graphite (HOPG) using the well-known scotch tape method, the same technique used to first isolate graphene in 2004 [10]. By using adhesive tape, multilayer graphene is removed from HOPG over multiple cycles, gradually reducing the number of layers. Eventually, when the layers have been minimised, ideally to a monolayer, the tape is dissolved leaving large regions of free-standing graphene. This is then placed onto substrates such as SiO_2 or H-BN, which isolate the graphene such that resistivity measurements can be made. Theoretically, exfoliated graphene on substrates such as H-BN and SiO_2 has been predicted to have mobilities of 170,000 and 200,000 $cm^2V^{-1}s^{-1}$ respectively [44]. However, due to factors such as scattering from surface optical phonons or impurity scattering in the substrate, the measured mobility for exfoli-

ated graphene varies drastically with values ranging from 120,000 $cm^2V^{-1}s^{-1}$ [23, 98] to 50,000 $cm^2V^{-1}s^{-1}$ [43]. Yet, as it stands, exfoliated graphene still presents the highest electron mobility compared to other methods of growth of graphene such as thermal decomposition of silicon carbide which has been measured to yield values varying between 3,000 $cm^2V^{-1}s^{-1}$ at room temperature and 11,000 $cm^2V^{-1}s^{-1}$ at 0.3 K [24].

The higher electron mobility in exfoliated graphene has made it one of the most attractive candidates for device fabrication. Yet, one major difficulty faced with such an approach is isolating a single layer of graphene. As mentioned in Section 2.3, typical devices which use exfoliated graphene do not always consist of a monolayer [25]. The consequence of this is interlayer interactions between regions of multilayer graphene which will influence the electronic properties of the device and consequently affect its performance. Furthermore, exfoliated graphene is more often subject to wrinkles/defects which will further influence its electronic properties [26].

2.4.2 Chemical Vapour Deposition Growth

Chemical vapour deposition (CVD) involves the cracking of precursor organic gasses on a hot metallic surface to form graphene [99]. Typically, a thin film [29, 54] is grown using molecular beam epitaxy (MBE) or a single crystal (for example Cu(110) [100]) of the metallic substrate is prepared through cycles of annealing and argon sputtering. The sample is then flashed at temperatures greater than 1373 K for a single crystal, or a lower temperature of around 873 K for thin films, after which it is exposed to an organic gas [101–103]. Upon cooling, the carbon aggregates to form large regions of graphene [57, 60].

The kinematics of growth for CVD are influenced by a number of parameters which affect graphene formation. Previous studies have suggested the growth to be dependent on the carbon solubility [104], however, whilst this model applies to nickel (2.03 atom%) [60], it is not applicable for copper due to its much lower carbon solubility of 0.04 atom% [105]. Instead a Gompertzian sigmoidal growth has been suggested, where the size of the graphene flakes is dependent on the flow rate of the organic gas [105]. Recent experimental work of graphene on copper foil supports this

idea, where µm grain boundaries were achieved by varying the gas flow rate [106].

Aside from gas flow and carbon solubility, temperature is also known to influence the formation of graphene grains. High enough temperatures are needed in order for hydrocarbon dissociation to occur, which is problematic for substrates such as copper where the melting temperature of the surface is close to the dissociation temperature of ethylene [57, 103]. Consequently, grain sizes of graphene on copper using ethylene are much smaller than those for nickel because of the maximum temperature which the substrate can be annealed to [99]. Yet, it has also been theoretically predicted that as the temperature transitions from 973 K to 1273 K, the rate of graphene formation slows and there is a small change to the size of the grains [107]. Therefore, it may be possible that lower temperatures could be used to form large graphene grains provided the hydrocarbon used has a lower dissociation temperature. Annealing flakes of graphene on copper foil has also been shown to influence the electronic properties around the K-point, where the graphene became n-doped and a bandgap was opened, occurring as a consequence of diffusion of oxygen at around 573 K [108].

One final parameter which influences CVD growth is the choice of organic gas. A variety of different sources have been used including ethylene [57, 101, 105], 1,3,5-benzenetribenzoic acid [102], naphthalene [109] and petroleum asphalt [99]. Ethylene has been one of the most popular choices, but could be expensive for mass production and it has been suggested that petroleum asphalt could be used instead to grow relatively defect-free graphene [99].

2.5 Beyond Graphene and Alternative 2D Materials

It is not just graphene that has been of interest for device applications. Graphene oxide has attracted a huge amount of attention in a variety of different applications including water filtration devices [110, 111], as an anode in lithium ion batteries [112, 113], and in self-assembling monolayers for hydrogels [114]. Whilst these areas are not the main focus of this project, they certainly highlight alternative applications

for graphene aside from spintronics.

As discussed earlier, MoS_2 monolayers have been of interest due to their inherent lack of inversion symmetry [80, 115] enabling valley-dependent optical selection rules for interband transitions at the K-point [80]. Furthermore, MoS_2 monolayers give rise to the valley Hall effect where carriers in different valleys flow to opposite transverse edges when an in-plane electric field is applied [80, 81], thus highlighting this material's role not only in spintronics but also valleytronics.

As has been briefly mentioned, other 2D materials have been of interest such as silicene [37] and germanene [116] due to their sizeable electron mobilities at room temperature. The mobility of silicene, for example, has been measured to be 3900 $cm^2V^{-1}s^{-1}$ [37]. As for graphene, these materials display a linear dispersion at the K-point. Consequently, their transport properties are very much akin to graphene with some suggestions that silicene could compete with graphene for device applications [37]. However, silicene and germanene are difficult to fabricate and, additionally, germanium is not as inexpensive to produce compared to graphene.

Chapter 3

Metastable De-excitation Spectroscopy and Microscopy

When studying the interaction of graphene (and other 2D materials) with a supporting substrate and/or intercalated atomic species, it is desirable to isolate interface and surface effects from bulk properties. The challenge is that the majority of techniques typically applied to this task, both in spectroscopy and microscopy, probe not only the top surface but also sub-surface and bulk interactions. One technique that is not commonly used but that is extremely surface sensitive is metastable de-excitation spectroscopy (MDS). MDS involves directing helium atoms in the excited metastable 2^3S state to within close proximity of a surface of a sample where various de-excitation processes may occur usually resulting in the emission of an Auger-type electron [117]. In addition to MDS, several other names have been used to describe this method including metastable atom electron spectroscopy and metastable impact electron spectroscopy. The reader, however, should be careful not to confuse this with the related technique of ion neutralisation spectroscopy which instead uses higher energy helium ions to induce electron emission. This chapter will detail the main He 2^3S de-excitation processes, how a He 2^3S beam can be spin-polarised for magnetic studies and the benefits of using MDS and metastable emission electron microscopy (MEEM).

3.1 A Metastable Helium 2^3S Beam

In 1924, the first observation of electron emission from a surface due to the impact of atoms in an excited state was made by Webb when exposing a nickel plate to a beam of metastable Hg atoms [118]. Further observation of this phenomena was performed by Penning who noticed electron emission from a gas due to metastable atoms, leading to this electron emission process taking the name Penning ionisation [119]. Electron emission due to metastable de-excitation is a consequence of overlap of orbitals of the topmost surface atoms (or target atoms or molecules in the case of Penning ionisation) with the $2s$ metastable state or $1s$ ground state of helium. Due to the overlap, which occurs within several Ångstrom above a surface, the metastable atoms de-excite causing an electron to be emitted from either the surface or the atom. The electron emitted is an Auger-type electron, although other de-excitation channels can occur for He 2^3S as discussed in Section 3.2.

Since helium (as well as other noble gas atoms) has a large de-excitation cross-section (for example the He 2^3S - N_2 cross-section is approximately 1×10^{-19} m^2 [120]), only states at the topmost surface will overlap with the 2^3S state or the ground state of helium. Therefore, the resulting electron emission spectrum contains information only on the surface density of states (SDOS). Hence MDS is extremely surface sensitive when compared to other spectroscopic or microscopic techniques which use electrons or photons to probe the surface where emitted electrons carry information from both the top-most surface and sub-surface [121]; examples include low energy electron microscopy (LEEM) and ultraviolet photoemission spectroscopy (UPS). Surface sensitivity is particularly relevant when studying 2D materials such as graphene [122] as well as magnetic structures on the surface of magnetic materials such as magnetite [123] for which it is also desirable to only probe surface states whilst ignoring subsurface and bulk contributions. For example, understanding the Fermi-level spin polarisation at the surface of magnetic materials is key to designing devices for spintronic applications.

Whilst there are several noble gas atoms that possess a metastable state, the helium 2^3S state is the most beneficial in terms of surface analysis. This is due to its energy of 19.8196 eV [124] compared to Ne (3^3P_2; 16.62 eV) and Ar (4^3P_2; 11.55 eV) [125],

making it the highest available energy of any metastable noble gas atom and giving access to the broadest range of electronic states in the valence band. An additional benefit of He 2^3S is its long lifetime of 8000-9000 s, which is much longer than for any other metastable noble gas atom [125]. This long lifetime is a consequence of a doubly forbidden transition back to the true ground state. Selection rules state that the change in the spin quantum number for a transition must be $\Delta S = 0$. Yet, due to Pauli's exclusion principle, the transition from 2^3S_1 to 1^1S_0 (ground state) would require $\Delta S = 1$. Secondly, the change in orbital angular momentum (l) is equal to zero, since both the excited and ground state have l=0 (for the s state). The relevant selection rule for orbital angular momentum states that $\Delta l = \pm 1$, hence making the transition from 2^3S_1 to 1^1S_0 doubly forbidden. For the He 2^3S atom to decay back to the ground state, a two-photon process is required; however this itself needs emission of radiation from a source such as an oscillating magnetic dipole. A schematic of relevant electron transition processes in helium can be seen in Figure 3.1.

MDS is generally a non-destructive technique due to its small associated kinetic energy. The average thermal velocity of helium atoms produced from a cold cathode discharge source is typically around 1000 ms^{-1} which corresponds to a kinetic energy of 21 meV [121]. Consequently, MDS can be used for a variety of systems whilst avoiding damage to the structure or changes to the stoichiometry of a surface. In fact, of particular relevance to the scope of this project, various studies on graphite [126] and graphene [76, 122] have shown no damage to the surface as a consequence of exposure to a beam of metastable helium atoms. Furthermore, MDS can be used to study the orientation of molecules [127] which, as seen later, becomes relevant when considering the effect of naphthalene on the surface of magnetite and the formation of organic/magnetic interfaces [128].

Since MDS uses orthohelium, a spin-triplet system, it is possible to access the magnetic sublevels $m_j = +1$ and $m_j = -1$ of the 2^3S metastable state enabling spin-polarised equivalents of MDS and metastable emission electron microscopy (MEEM) to be performed. The He 2^3S source will produce atoms that occupy all three states, $m_j = +1, 0, -1$, and a specific sublevel can be accessed either through optical pumping [129] or using a sextupole magnet [130]. As can be seen in Figure 3.1, another

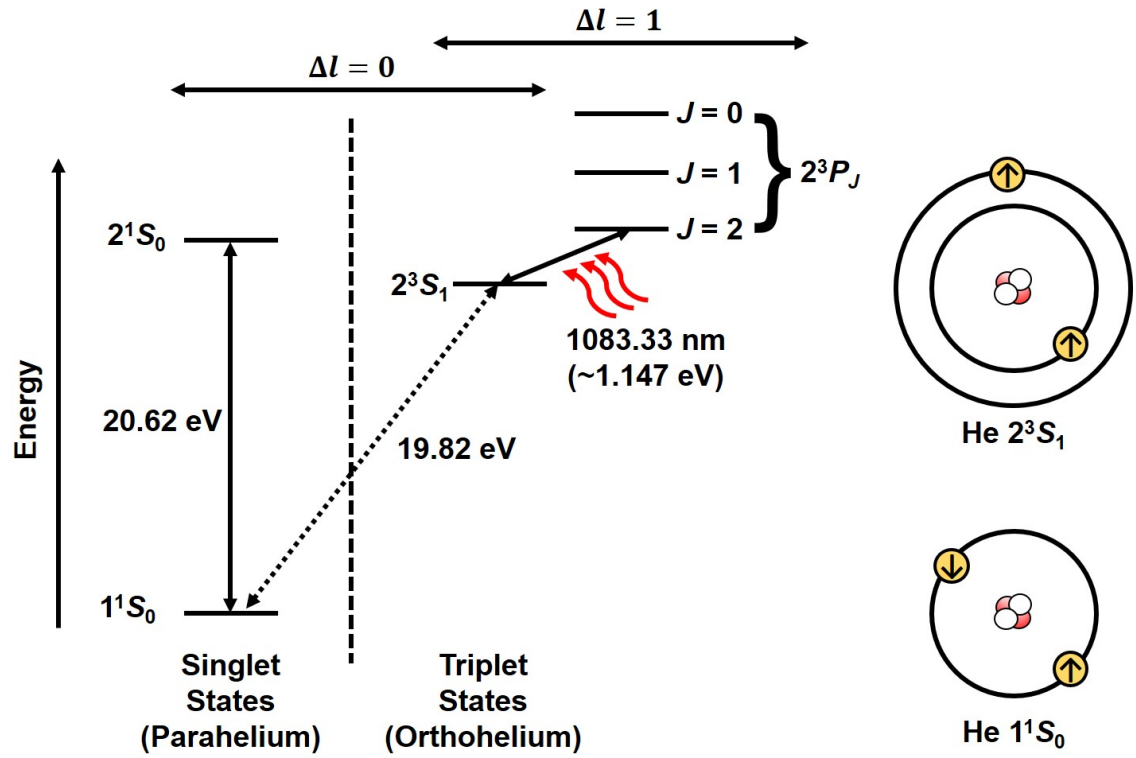

Figure 3.1: Energy level diagram of helium (left) and schematic of the ground state and 2^3S_1 metastable state of helium (right). The $2^3S_1 \rightarrow 1^1S_0$ transition is doubly forbidden and therefore requires a two-step electron transition process. The 2^3S_1 - 2^3P_2 transition at 1083.331 nm is used to spin polarise He 2^3S atoms using optical pumping.

possible excited state which helium can occupy is the 2^1S singlet state in para-helium. The He 2^1S state has a higher energy of 20.62 eV as a consequence of Hund's 1st rule, has a lifetime of 20 ms and cannot be spin polarised [131]. Helium atoms excited in the source have a 2^1S:2^3S ratio of 1:10 and, if not removed, singlet states will contribute to MDS spectra and can make it more difficult to interpret the data [117].

3.2 He 2^3S De-excitation Mechanisms

In MDS, there are two dominant de-excitation mechanisms which can occur when a helium atom in the 2^3S state is incident on a surface, both resulting in the emission of an Auger-type electron. The de-excitation mechanism that occurs is dependent

on the workfunction (ϕ) of the material and the position of the Fermi level and energy distribution of surface orbitals with respect to the excited state. For metallic and semiconducting surfaces, the dominant de-excitation mechanism is a two-step process of resonance ionisation (RI) followed by Auger neutralisation (AN). In the majority of cases for an insulating surface, de-excitation occurs via the one-step process of Auger de-excitation (AD). The yield of electrons varies as a consequence of these two different transitions, with more electrons emitted through AD. As explained below, this is a consequence of the emission of an electron from Auger neutralisation being dependent on the electron which neutralises the helium ion. Some surfaces may undergo both electron transition processes which can make it more difficult to interpret the resulting spectrum. Additionally, Auger neutralisation is a two-step de-excitation process which leads to a convolution of the SDOS. The contributions of RI followed by AN (RIAN) and AD in a spectrum can be determined through methods such as single value decomposition [122] and the spectra resulting from AN can be deconvoluted through a Fourier transform of the self-folded integral of the transition probability [132].

3.2.1 Penning Ionisation

In 1927 [117, 119], it was first demonstrated that when a metastable atom (A^*) comes from infinity to within close proximity of another atom or molecule (T), the interaction switches from predominantly van der Waals forces to Pauli repulsion (as described by the well-known Lennard-Jones potential). As a consequence of this, the following ionisation process occurs:

$$T + A^* \rightarrow T^+ + A + e^-. \tag{3.1}$$

The ionisation is a result of an overlapping of orbitals of the metastable atom and the target atom/molecule. Following this, an electron from the atom/molecule will tunnel into a lower energy state of the metastable atom to neutralise it, whilst causing the simultaneous emission of the electron from the metastable state leaving the target atom or molecule positively charged. This phenomena is known as Penning ionisation and can be observed by exposing a gas to a He 2^3S beam and obtaining

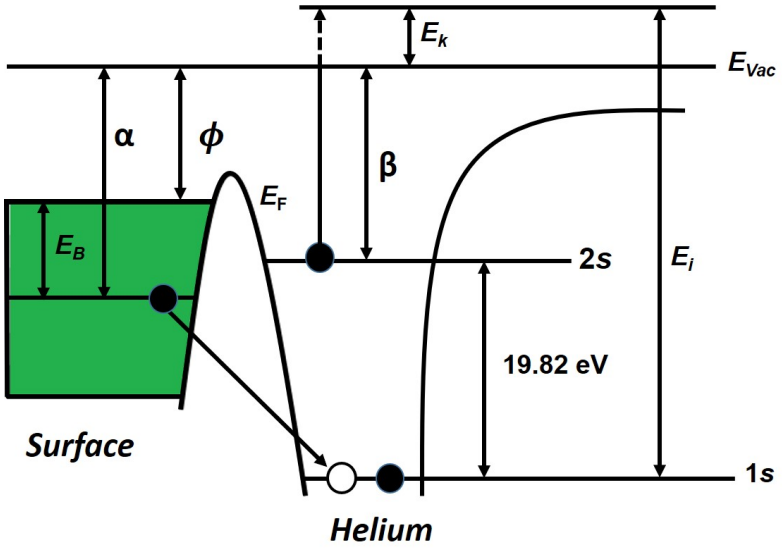

Figure 3.2: The Auger de-excitation process for a metastable He 2^3S atom. Since there is no possible way for the $2s$ electron to tunnel into the surface, an electron from the surface tunnels into the ground state of the He atom causing the release of the excited $2s$ electron in an Auger-type process. α, β, E_i and E_k are defined in the text.

the electron emission spectrum. As such, this spectroscopy technique can be used to infer information regarding molecular orbitals and states within the gas.

3.2.2 Auger De-excitation

Similar to Penning ionisation, Auger de-excitation (AD) is a single step process which involves the emission of the $2s$ electron from a helium atom instead of an electron from the surface. The emission of an electron from helium occurs as a result of an electron from the surface tunnelling into the $1s$ ground state as shown schematically in Figure 3.2. The difference between AD and PI is that in AD a solid surface or liquid is involved contrary to a single atom/molecule. This process will only take place when there are no empty states in the surface for the 2^3S electron to tunnel into, for example when the Fermi level of the surface is at a higher energy than the excitation energy of the helium atom.

The AD process is most commonly seen in materials with a large band gap or that have a small workfunction [121, 133], which generally occurs in insulators and or-

ganic molecules. The atomic radius of the metastable helium atom is approximately 2.9 Å [134, 135], so for the bands to overlap and AD to occur, the helium atom must be in close proximity to the surface. Similarly to PI, the highest probability of AD occurring is in the range of 3 to 5 Å from the surface [117]. The features due to AD are sharp and energy broadening is limited [136] contrary to the two-step electron process of RIAN. Thus the results from AD are comparable to those observed in UPS.

The kinetic energy of the electron emitted in AD can be described by the following equation, where E_k is the kinetic energy, E_i is the effective ionisation potential of the ground state He atom, α is the energy difference between the surface state and the vacuum level and β is the energy difference between the $2s$ metastable state and the vacuum level:

$$E_k = E_i - \alpha - \beta. \tag{3.2}$$

Since this is a quasi one-electron process [132] the initial energy of the emitted electron is constant. Therefore, the only variable in AD is the energy released by the surface electron that tunnels into the $1s$ state. Consequently, the ionisation energy can be approximated to be equal to the following:

$$E_i - \beta \approx 19.82 \text{ eV}. \tag{3.3}$$

Expressing this in terms of kinetic energy, the AD process can be approximated to the following equation, where ϕ is the work-function of the surface and E_B is the binding energy of the electron from the solid:

$$E_k \approx 19.82 - \phi - E_B. \tag{3.4}$$

3.2.3 Resonance Ionisation and Auger Neutralisation

If Auger de-excitation is the dominant de-excitation mechanism for insulators, then the two-step electron process of resonance ionisation (RI) and Auger neutralisation

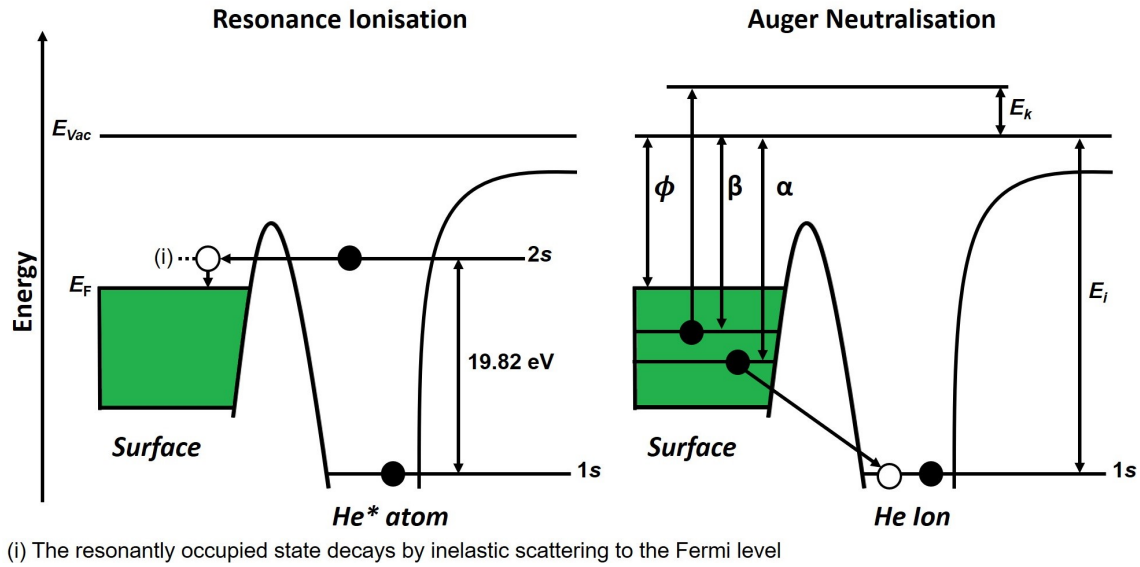

Figure 3.3: Schematic diagrams of the resonance ionisation (RI) and Auger neutralisation (AN) electron transition processes. For this two-stage de-excitation mechanism, α is the initial energy of the neutralising electron and β is the initial energy of the emitted Auger-type electron.

(AN) will generally be the dominant de-excitation process for metallic and semiconducting surfaces. Contrary to AD, the Fermi level (E_{F}) now lies below the energy of the 2^3S state, meaning that there are unoccupied states above E_{F} for the electron to tunnel into. Figure 3.3 shows schematic diagrams of both RI and AN.

As the metastable atom approaches the surface of the material, at about 9 Å [137], the $2s$ electron will tunnel into an empty state resulting in the ionisation of the helium atom; this process is known as resonance ionisation (RI). The created He^+ ion will then continue to travel towards the surface until, at a distance of around 5-3 Å [138, 139], an electron from the surface will tunnel into the $1s$ hole to neutralise the ion. The energy of this transition, equivalent to $E_i - \alpha$ (see Figure 3.3) is transferred to another electron in the surface such that no energy is lost as radiation [132]. If the energy of the transition is sufficiently large [117], an Auger electron will be emitted with kinetic energy as described by Equation 3.2. This de-excitation mechanism is known as Auger neutralisation (AN). The maximum possible kinetic energy of the liberated electron is when both electrons involved in AN are initially at the Fermi edge. If this is the case, it can therefore be deduced from Figure 3.3 that $\alpha = \beta = \phi$ meaning that the maximum kinetic energy can be derived as:

$$E_{kmax} = E_i - 2\phi. \tag{3.5}$$

Contrary to UPS, or MDS where the He 2^3S has de-excited though AD, the electron emission spectrum obtained from RIAN is convoluted as a consequence of two different factors. Firstly, the effective ionisation energy will vary due to the image potential (as described in Section 3.2.5) resulting in the kinetic energy of the electron emitted to vary slightly. Secondly, the neutralising electron and the emitted electron will not always originate from the same level (excluding the Fermi level), i.e. $\alpha \neq \beta$. This arises from the fact that the location of the emitted electron will vary as a consequence of the distance from the surface where de-excitation of the He 2^3S atom occurs [138] as well as the termination of the surface [139]. Since neither the neutralising or emitted electrons originate from a set energy, the binding energy of the electron cannot be directly calculated from its kinetic energy [132]. Therefore the spectrum is a self-convoluted SDOS described by a self-folded integral, where $F(\varepsilon)$ is the transition probability (which relates to the intensity of the spectrum at a given energy ε), H_{fi} is the Auger matrix element and $N(\varepsilon)$ is the local density of states:

$$F(\varepsilon) \propto \int_{-\varepsilon}^{\varepsilon} |H_{fi}|^2 N(\varepsilon - \Delta\varepsilon) N(\varepsilon + \Delta\varepsilon) d(\Delta\varepsilon). \tag{3.6}$$

Furthermore, for any given surface, there is a probability of both AD and RIAN occurring. According to Dunning *et al.*, this happens when the helium atom is approximately 3-4 Å from the surface, where AD may compete effectively with RI [140]. The RIAN de-excitation mechanism will still remain the dominant process for metallic and semiconducting surfaces, but this additional factor further complicates interpretation of the obtained spectra.

3.2.4 Resonance Neutralisation

Similar to Auger de-excitation, resonance neutralisation (RN) of He^+ ions can occur when the work function of the surface is sufficiently low that the Fermi level is at a higher energy than that of the empty He^+ $2s$ state [117]. Subsequently, an

electron from the surface tunnels into the excited level in order to neutralise the atom which leaves a metastable helium atom which may then undergo AD. The transition probability for this process becomes more appreciable with larger atoms [117], but is low in most cases since the state lifetime is approximately 10^6 times longer than that of Auger neutralisation. Therefore, for the majority of systems which have been looked at in this project, the contribution due to RN is small enough to ignore. However, it is worth noting that due to the band effect in highly-oriented pyrolytic graphite (HOPG), the transition probability of RN is increased [141] by one order of magnitude and has been predicted to be similar with graphene [142].

3.2.5 Image Potential

The effective ionisation potential of a helium ion undergoing Auger neutralisation, E_i, is dependent on the image charge potential experienced by the ion as it approaches the surface. The image potential is a function of separation from the surface due to the image force, which itself is a consequence of the Coulomb interaction between the helium ion and the surface [143]. Since the maximum kinetic energy of the emitted Auger electron in RIAN is dependent on E_i, in order to interpret the obtained spectrum, the image potential of the surface needs to be considered. The effective ionisation potential of helium has a gas phase value of 24.6 eV. This value is then reduced according to the relationship described by Equation 3.7, when a He^+ interacts with a solid surface. Here ΔE_i is the change in ionisation potential (eV), R is the distance from the centre of the ion to the surface (Å) and d is a corrective distance to account for the image force (which is generally about 0.6 Å) [144, 145].

$$\Delta E_i = -\frac{3.6}{(R-d)/\text{Å}} \text{ eV} \tag{3.7}$$

Consequently, when Auger neutralisation occurs at a greater distance, ΔE_i will be smaller and therefore the kinetic energy of the emitted electron will be larger. For distances smaller than 1 a.u., this approximation breaks down as the potential no longer scales with Q^2 (where Q is the charge on the point charge) and energy no longer changes as a function of distance [144].

3.3 Spin-Polarised Measurements

In certain materials, the spin resolved density of states is asymmetric and the number of electrons in each spin state is not equal leading to majority and minority spin states at different energies [132]. This occurs in ferromagnetic and ferrimagnetic materials, whose electron spins and magnetic moments are arranged in a regular order [146]. Spin polarisation is expressed as a ratio of the difference in the density of majority and minority spin states. The spin polarisation at the Fermi level can be defined by the following expression:

$$P(E_{\mathrm{F}}) = \frac{n_{\uparrow} - n_{\downarrow}}{n_{\uparrow} + n_{\downarrow}} \tag{3.8}$$

where $n_{\uparrow,\downarrow}$ are the densities of state at the Fermi level for majority ($\uparrow$) and minority ($\downarrow$) spin states. As discussed in Section 3.6, spin polarised metastable helium atoms can be used to determine this property. However, it is worth first highlighting how the response from spin polarised helium atoms differs depending on the de-excitation mechanism which takes place.

In Chapter 5, the surface spin polarisation of magnetite is explored using SPMEEM. Since magnetite is a semimetal, the dominant de-excitation mechanism for such a surface will be the two-step de-excitation process of RIAN (Section 3.2.3). Following ionisation of the helium atom as a consequence of the metastable $2s$ electron tunnelling into an empty state above the Fermi level (RI), an electron from the surface tunnels to the $1s$ state to neutralise the ion (AN). Due to Pauli's exclusion principle, the neutralising electron must be of opposite spin state to the helium $1s$ electron already present in the ground state (Figure 3.4). RI+AN is therefore dependent on the spin state which exists at the surface [132].

The electron generated through AN may arise from either spin state, however it has been observed that both electrons involved in Auger neutralisation tend to have anti-parallel spins [140]. Two mechanisms have been proposed for why this occurs: (1) despite RIAN being the dominant de-excitation mechanism for a given surface, AD still plays a role in the observed SPMDS spectrum [132] or alternatively, (2) a two-hole singlet state in the surface is preferred. The latter is consistent with Pauli's

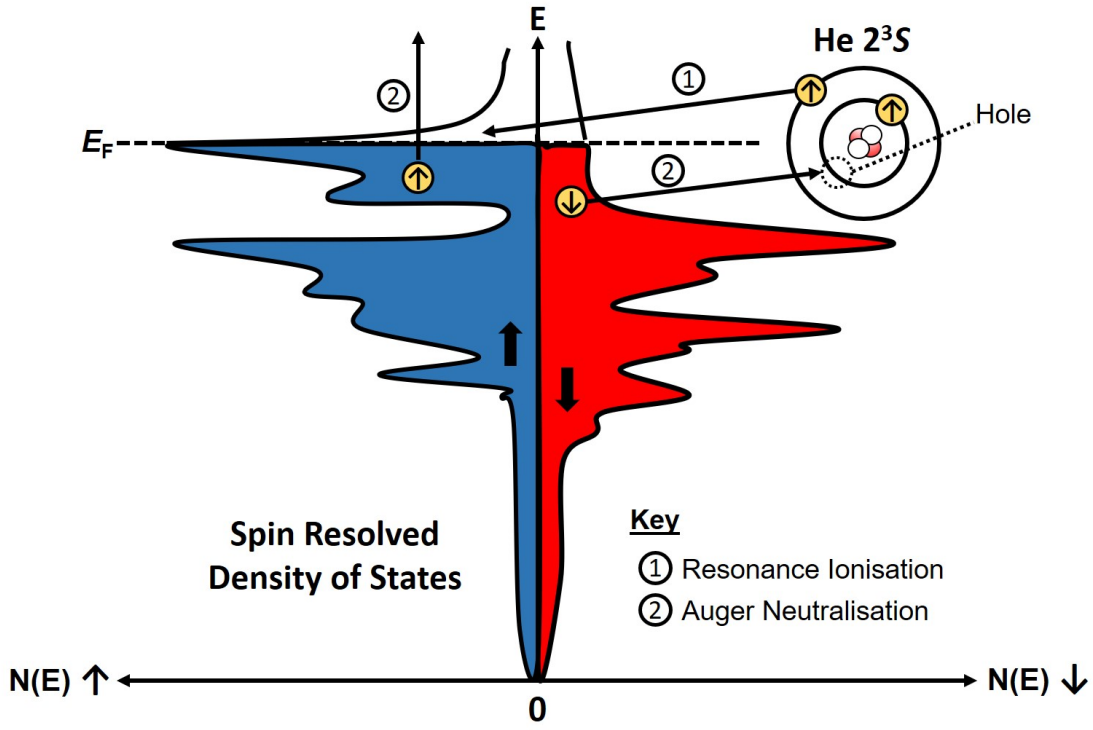

Figure 3.4: The resonance ionisation (RI) and Auger neutralisation (AN) de-excitation mechanism for a magnetic surface. The neutralising electron in the AN step must have the opposite spin state to the ground state electron of the helium ion in order to obey Pauli's exclusion principle.

exclusion principle and the couplet effect is more pronounced when both electrons originate close to the Fermi edge [147, 148]. Since the spin of the electrons involved in AN can have both parallel and anti-parallel configurations, then subjecting a surface where RIAN is the dominant de-excitation mechanism to a particular metastable magnetic sublevel, does not only probe one spin state of the SDOS as a certain contribution of electrons will be generated from the other spin state [132].

The consequence of both the neutralising electron and the emitted electron having anti-parallel spins is that it further complicates the spectrum making it more difficult to interpret the data. As was discussed in Section 3.2.3, the RIAN de-excitation mechanism results in a convoluted spectrum due to the fact that neither electron necessarily originates from the same energy. In the circumstance of both electrons originating from the same spin state but not the same energy, then the spectrum is only convoluted as a consequence of energy. However, if both the energy and

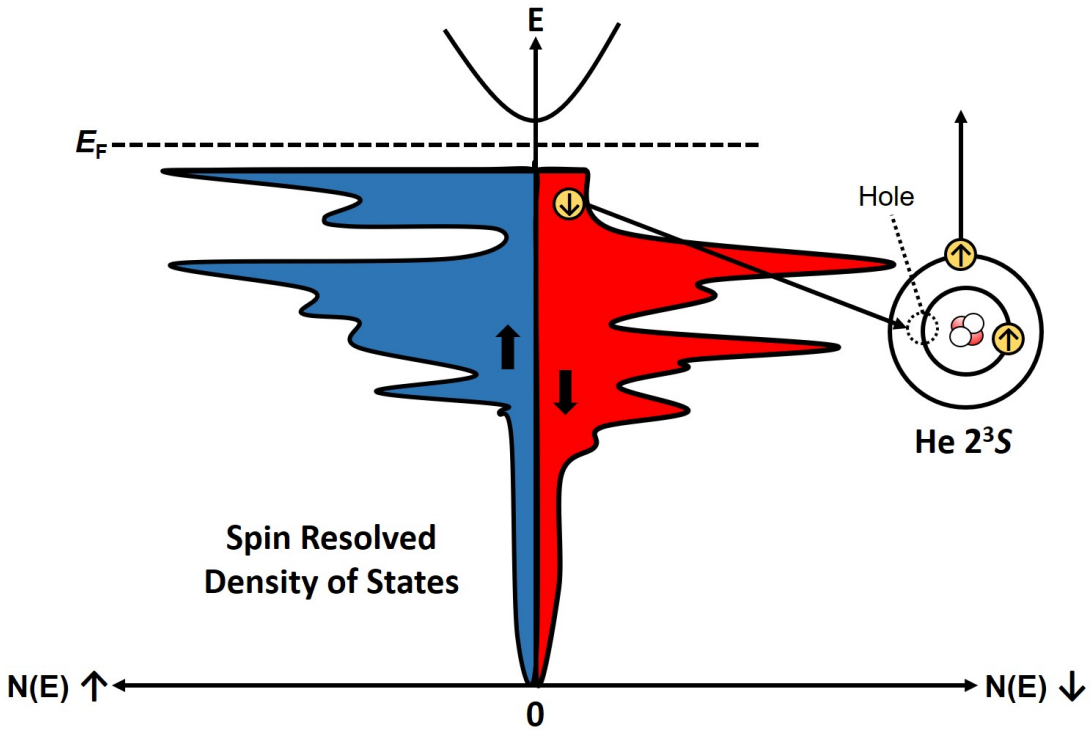

Figure 3.5: The Auger de-excitation (AD) process for a magnetic surface. The electron that tunnels from the surface into the $1s$ state of the helium atom must have opposite spin state to the $2s$ electron.

spin state of the neutralising electron and the emitted electron are different, then the spectrum is doubly convoluted. In reality, both the antiparallel and parallel cases exist, and yet despite the prior being favoured, some information regarding the spin-split SDOS is retained within the RIAN process. The actual value of spin asymmetry measured by SPMDS will be less than the corresponding value for the spin polarisation of the material.

When analysing insulating magnetic surfaces, metastable helium atoms will most likely de-excite by the one-electron process of Auger de-excitation, as shown schematically in Figure 3.5. Here the surface electron that tunnels into the $1s$ hole of He will have the opposite spin state to that already present. If the majority spin state of the surface is antiparallel to that of the metastable state, there will be a more substantial yield of electrons emitted, contrary to if the spins were parallel. If the polarisation of the helium beam is aligned to the magnetisation direction of the sample, then only the opposite spin state will be probed and the emitted electrons will

have the same spin polarisation as that of the initial metastable helium beam. Consequently, the spin-split SDOS for a surface which undergoes AD is not convoluted compared to a surface which undergoes RIAN, and the measured spin asymmetry is much closer to the actual value. The only problem with surfaces which undergo AD is that the production of secondary electrons from the surface will lead to a slight deviation between the measured spin asymmetry and the actual spin asymmetry in the spin-split SDOS [147].

3.4 A Metastable Helium Source

The various methods that have been employed to produce a metastable helium beam include colliding helium gas with a coaxial electron beam [149, 150], using a pulsed discharge [151], and using a liquid-nitrogen-cooled direct-current (DC) discharge (similar to that used in UPS) [152, 153]. The approaches used during this project at NIMS and York involve the later two due to their high yield of metastable helium atoms of up to 10^{14} atoms s^{-1} sr^{-1} [152]. For more information on the use of a coaxial electron beam, the reader is referred to Rundel *et al.* [149] and Johnson *et al.* [150].

3.4.1 Electron Spectroscopy System (York)

The source on the electron spectroscopy system at York uses a liquid-nitrogen-cooled DC discharge to produce a high flux of metastable helium atoms. This consists of a hollow oxygen-free copper cylinder measuring 60 mm in length and 20 mm in diameter which acts as a cathode as shown in Figure 3.6. Regulated helium gas of 99.999% purity is fed through a leak valve into the cathode which is cooled using a liquid nitrogen (LN_2) cold finger. At the end of the cathode is a boron nitride disk with a central 0.3 mm aperture used to generate conditions for supersonic expansion of the emitted helium gas. Boron nitride is used due to its high durability and good thermal conductivity. Using this ceramic is ideal since the velocity distribution of the source is dependent on the temperature of the final point of contact between the exiting helium atoms and the source [121, 129]. A threaded polyimide cap is placed

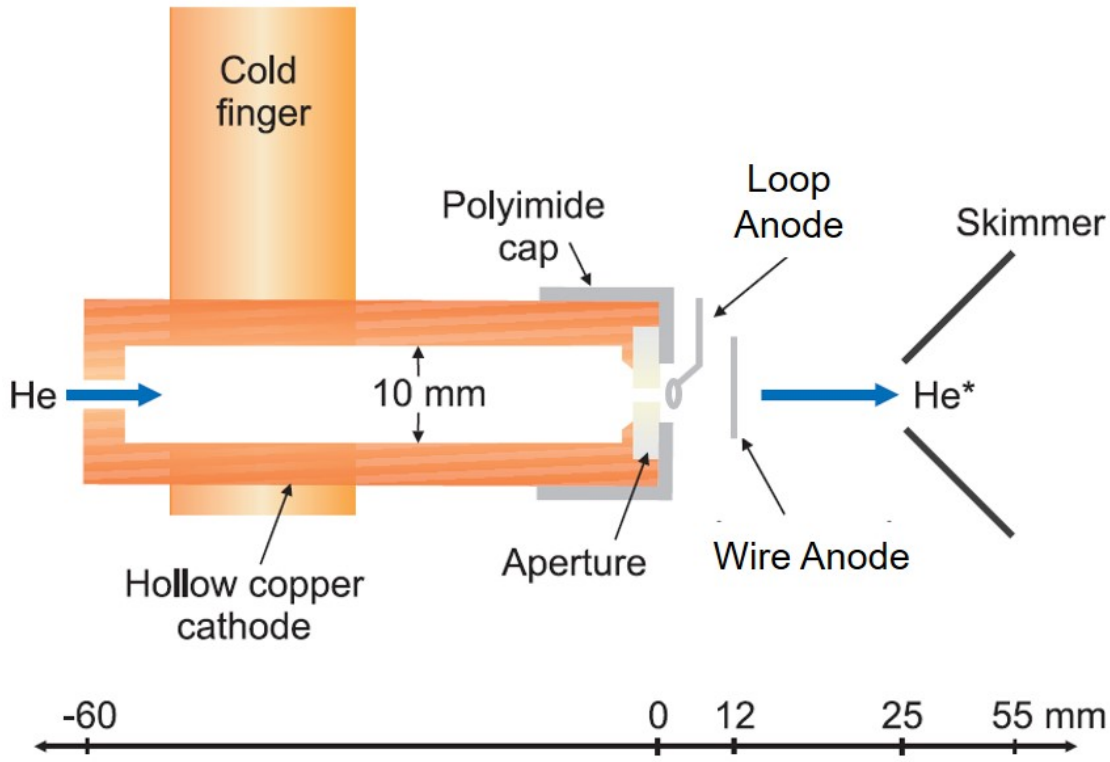

Figure 3.6: Schematic of the liquid nitrogen cooled hollow-cathode metastable helium (He*) source used in York. Reproduced from Ref. [121].

at the end of the copper cathode to insulate it from the anodes.

To strike the discharge, attached to the end of the polyimide cap are two anodes made of tungsten wire. The wire anode is held at 5.0 kV to strike a discharge at which point the voltage drops to $\approx$ 600 V (current limited to 3 mA). To help start the discharge but more importantly to stabilise it, nearer to the boron nitride aperture is a ring shaped anode (loop) held at 1.2 kV. Following this, at the end of the chamber sits the skimmer (a frustrum) held at -500 V, which constrains the electric field of the discharge, helping to reduce the profile of the beam whilst simultaneously increasing the charge density around the source exit so that more metastable atoms are generated [121]. To initially strike the source, a high inlet pressure of helium (around 60 mbar) is used and, once struck, the pressure is then rapidly reduced to 10 - 12 mbar.

The flux of the source against driving pressure follows a log-normal distribution, with a maximum at 11 mbar based on previous measurements made in our group [129]. The source cannot sustain a discharge at low pressures and is likely to therefore

extinguish. However, at higher pressures, collisions between the atoms result in de-excitation before reaching the sample. Therefore, the helium inlet pressure of the source during operation is kept at 11 mbar to produce the highest flux of He 2^3S atoms which has been reported to be 5×10^{13} atoms s^{-1} sr^{-1} [121].

Additionally, temperature will affect the velocity distribution of the He 2^3S atoms and it is therefore important to make sure the source is constantly cooled. Atoms which have a lower temperature will have a lower velocity. The velocity distribution of this metastable helium source peaks at ≈ 950 ms^{-1} with a speed ratio, $v/\Delta v$, of $\approx$1.5 indicating the beam is weakly supersonic [121]. The combination of temperature and inlet pressure will not only influence the intensity of the source but also its lifetime before needing to be serviced, so maintaining a constant pressure and temperature is desirable.

During the initial stage of igniting the discharge, the pressure inside the chamber is quite high and consequently a large proportion of UV photons are produced in the source [132]. To counteract this, the source is allowed to run for about 10 minutes to ensure a pressure equilibrium has been achieved and ensure stability of the source. Furthermore, to help reduce the number of UV photons arriving at the sample (creating background noise and peaks in the spectrum), a beam blocker is used. As shown schematically in Figure 3.7, this consists of a 5 mm stainless-steel foil disk supported on a 60 mm copper gasket mounted on a rotatable and translational feedthrough. The size of the aperture is the same as the one prior to the analysis chamber and is used to limit the profile of the beam since any particles in line with the foil disk will be blocked. An alternative approach to limiting the number of UV photons reaching the sample is through a velocity selective chopper wheel [121].

To measure the flux of the source, a Faraday cup is used. A Faraday cup consists of a stainless-steel plate (the cup) grounded through a picoammeter with an additional stainless-steel cylinder surrounding the cup. When metastable atoms de-excite at the plate, electrons are liberated from the surface and the compensation current is measured through the picoammeter. To ensure that a true value is measured on the picoammeter and low kinetic energy electrons are not attracted back to the plate, the stainless-steel cylinder surrounding the cup is held at +50 V to attract

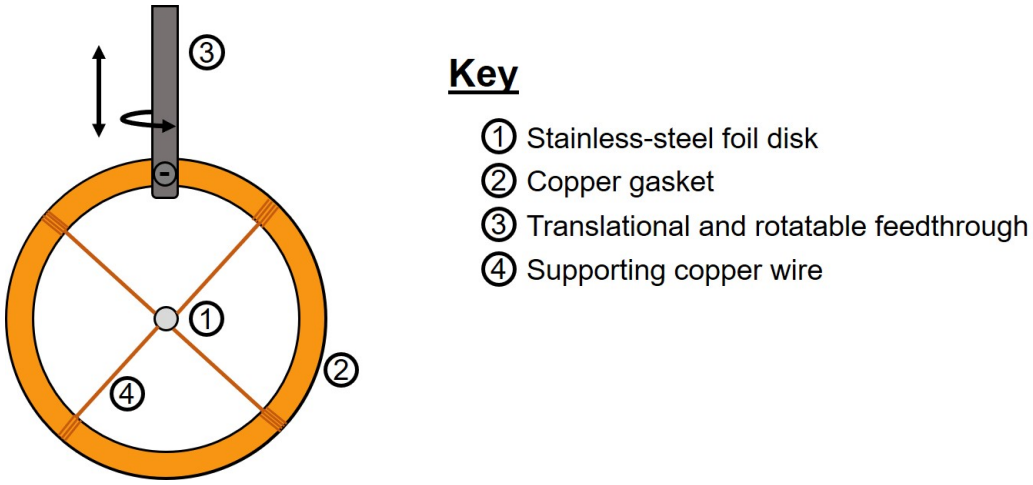

Figure 3.7: The beam blocker is rotated in-line with respect to the metastable helium beamline in order to block a proportion of particles exiting the source and therefore restrict the number of UV photons reaching the sample.

the emitted electrons.

He 2^3S Source Vacuum Setup

The metastable helium source at York is positioned in a chamber that has a base pressure of around 1×10^{-7} mbar. To manage the pressure at the source and pump away excess helium which may collide with metastable helium atoms thus causing them to de-excite, as shown schematically in Figure 3.8, a Varian NRC diffusion pump with a nominal pumping capacity of 4000 ls^{-1} is used, backed by a single stage Edwards M40 rotary pump. During operation, this provides a pressure of approximately 10^{-5} mbar in the source chamber. After the skimmer and towards the analysis chamber where the sample is located, various chambers are pumped by two turbomolecular pumps, an Edwards EXT250 and a modified Leybold Turbovac 360CSV with respective pumping rates of 240 ls^{-1} and 345 ls^{-1}. Both of these pumps are backed by a two-stage Edwards M40 rotary pump. These chambers enable laser cooling to be applied to the He 2^3S beam, greatly enhancing its intensity; for more information, the reader is referred to Ref. [121]. The beamline chambers are all suspended by a frame in order to isolate the beamline from the optical table which is used to enable techniques of laser cooling to be applied to collimate and focus the He 2^3S beam and greatly increase its intensity. See Ref. [121] for a detailed

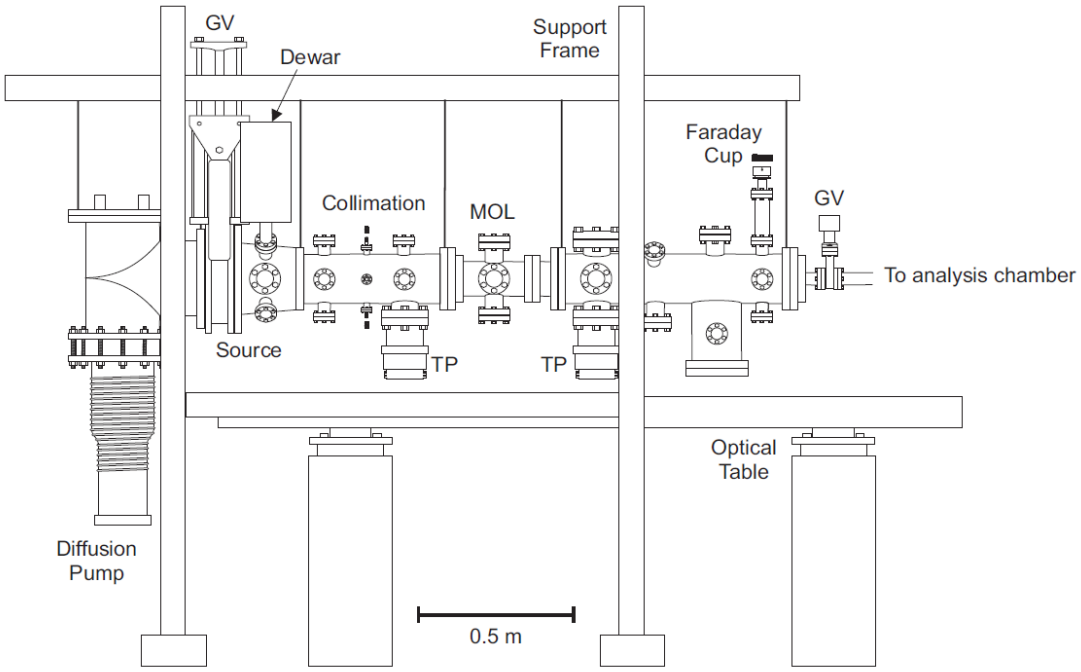

Figure 3.8: Schematic of the metastable helium beamline used in York. MOL = magneto-optical lens. TP = turbomolecular pump. Figure reproduced from Ref. [121].

description of this set up. Since vibrations from the pumps may interfere with the various optical elements used, suspending the beamline is necessary.

3.4.2 MEEM System (NIMS)

The metastable helium source at NIMS, shown schematically in Figure 3.9, uses a pulsed discharge to generate a He 2^3S beam. The helium gas is LN_2 cooled through a copper pipe which then feeds into a pyrex tube (diameter of 9 mm) with a concentric orifice of 0.3 mm acting as the nozzle. Placed behind the nozzle and central with it is a tantalum wire needle 1 mm in diameter spot-welded to a stainless steel cylinder 6.4 mm in outer diameter. Between a skimmer and the pyrex tube is a trigger electrode held at ground potential through a 200 kΩ resistor. To strike a discharge and maintain it, the needle and cylinder are supplied with a fixed pulse of up to 900 V superimposed upon a variable DC voltage of up to 600 V [151]. The pulsed discharge is stabilised in two domains. First of all, a series resistor coarsely regulates the discharge current, but fast enough for a pulse duration of 10 - 100 µs. Secondly,

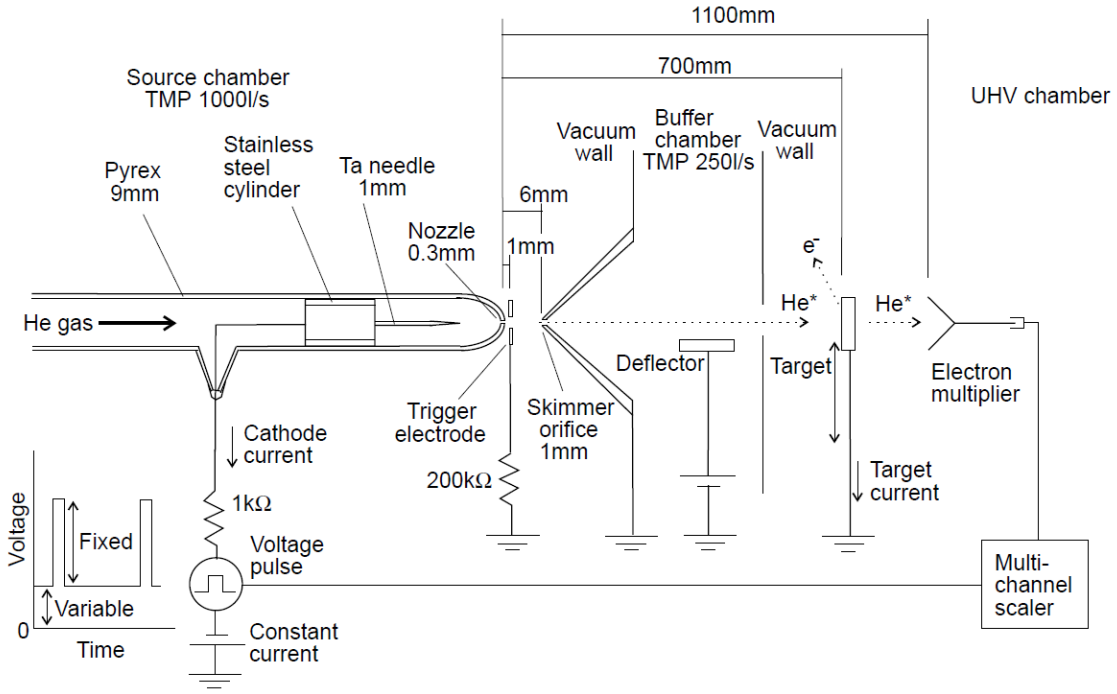

Figure 3.9: Schematic of the source used at NIMS in order to perform metastable emission electron microscopy. Reproduced from Ref. [151].

the average discharge current is simultaneously controlled slowly and precisely by a DC power supply in constant current mode [151]. Similar to the source in York, the He 2^3S beam then passes through a skimmer but with a 1 mm orifice and this is held at ground potential.

The pulsed discharge time-of-flight set-up is reported to be equivalent to an intense metastable helium beam with mechanical chopping [151]. Therefore, due to the extremely low flux of UV photons being generated at the source, no additional procedures are applied to further limit UV photons from reaching the sample. Additionally a 1000 ls^{-1} turbomolecular pump is used to provide the correct pressure profile through the system to generate a stable beam. For more information on this source, the reader is encouraged to read Ref. [151].

3.5 Spin Polarisation of the He 2^3S Beam

In order to perform spin-polarised measurements in SPMDS and SPMEEM, the He 2^3S beam needs to be spin polarised so that all of the atoms are in either the m_j=+1

or m_j=−1 magnetic sublevel. To spin polarise the metastable helium beam, optical pumping or a sextupole magnet can be used as described below.

3.5.1 Spin Polarisation Using Optical Pumping

In addition to providing optical forces needed to intensify the He 2^3S beam through laser cooling, laser light tuned to the $2^3S_1 \rightarrow 2^3P_2$ transition at 1083.331 nm can also be used to selectively place the metastable helium atoms into the $m_j = \pm 1$ sublevels using optical pumping. Since photons are massless, excitation events due to an incident photon are bound by the selection rule of $\Delta m_j = \pm 1$. Due to the coupling between the aligned spin of the photon ($s = 1$) and the electron $\left(s = \frac{1}{2}\right)$, using right-hand circularly polarised light (σ^+) will result in the He 2^3S atoms being placed into the $m_j = +1$ magnetic sublevel with left-hand circularly polarised light (σ^-) resulting in atoms in the $m_j = -1$ state.

By applying a weak magnetic field across the metastable helium beam, the degeneracy of the 2^3P_2 state is lifted and separated into five different magnetic sublevels from m_j=-2 to m_j=+2 as shown schematically in Figure 3.10. The 2^3P (J=2) sublevel is chosen since 2^3S_1 (m_j=-1,0,+1) magnetic sublevels can all be excited to the next highest magnetic sublevel based on the selection rule discussed above. Whilst the J=1 sublevel could be used, this transition would see a reduced efficiency in optical pumping since excitation to the m_j=+2 magnetic sublevel (from the m_j=+1 sublevel of 2^3S_1) would not be possible. All de-excitations from the 2^3P_2 level follow the rule $\Delta m_j = 0, \pm 1$ and therefore atoms in the 2^3P_2 (m_j=+2) can only de-excite back to the 2^3S_1 (m_j=+1) magnetic sublevel forming a closed transition cycle, since no other de-excitation routes are available [132]. Over several cycles, the result is that the majority of He 2^3S atoms will occupy the m_j=+1 magnetic sublevel. Similarly, if σ^- light is used, then the majority of helium atoms will occupy the m_j=-1 magnetic sublevel. A quantisation axis is defined in optical pumping by applying a weak transverse magnetic field in the direction of the laser [121].

Circularly polarised light is generated by passing the linearly polarised light produced from a diode laser locked to the 2^3S_1-2^3P_2 transition through a quarter-wave ($\lambda/4$) plate. A $\lambda/4$-waveplate consists of a birefringent material where the refractive

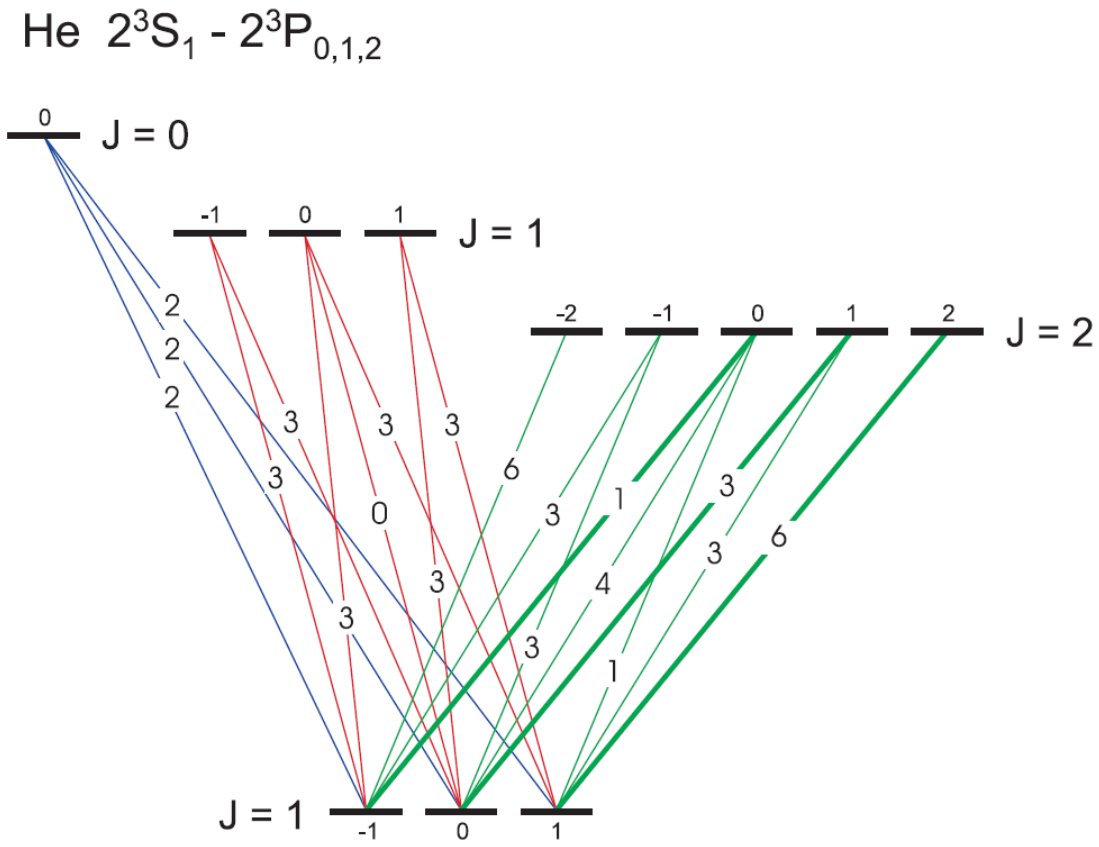

Figure 3.10: The helium $2^3S_1 \rightarrow 2^3P_2$ transition used for optical pumping showing the magnetic sublevel structure and transition strengths normalised to the weakest transition. Excitation with resonant σ^+ circularly polarised light optically pumps atoms into the 2^3P_2 (m_j=2) magnetic sublevel where it forms a closed transition with the 2^3S_1 (m_j=1) magnetic sublevel. Figure reproduced from Ref. [121].

index varies depending on the linear polarisation of the light, and consequently the linearly polarised light with the larger refractive index will be retarded by $\pi/4$ in phase with the linear polarisation with the smaller refractive index.

3.5.2 Spin Polarisation Using Permanent Magnets

An alternative method of placing the majority of He 2^3S beam into the $m_j = \pm 1$ magnetic sublevels is through the application of a series of permanent magnets. Here, an arrangement of hard and soft magnetic materials (composing of Nd, Fe and B) are arranged in a cylinder-like shape around the beamline [154], as shown in Figure 3.11. When metastable helium atoms travel through the pole gap, they

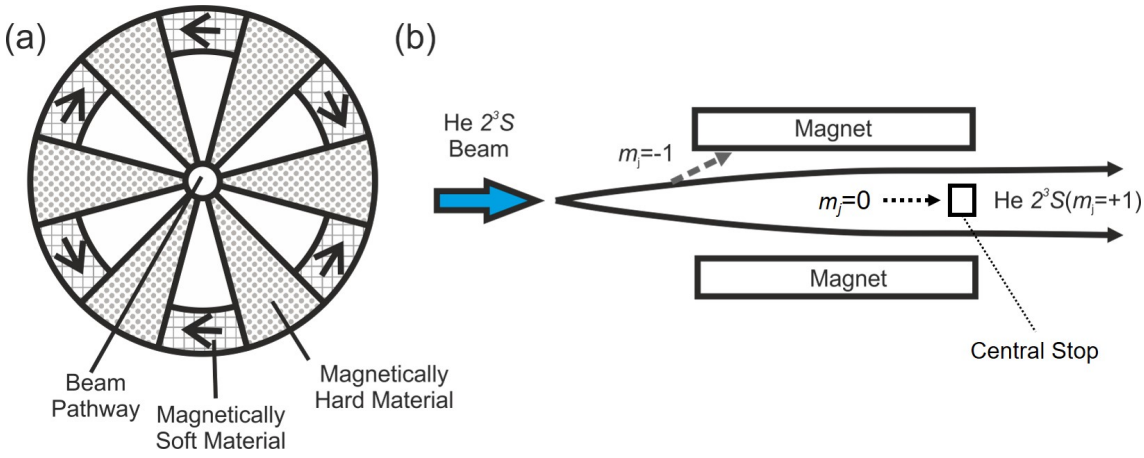

Figure 3.11: (a) The sextupole magnet consists of a series of soft and hard magnets arranged in a cylinder like shape around the beamline. (b) As a consequence of this magnet, metastable helium atoms $m_j = +1$ state will experience a force towards the beamline axis whilst atoms in the $m_j = -1$ state will feel a force away from the axis and the magnet therefore behaves like a positive lens. The design of this magnet is based on work by Baum *et al.* [155].

experience an inhomogeneous magnetic field [155] the force of which is proportional to their radial distance from the axis (the beam axis which is in the direction towards the sample) [155]. Atoms in the $m_j = +1$ state experience a force towards this axis, whilst atoms in the $m_j = -1$ state will feel a force away from the axis and those of $m_j = 0$ experience no force at all. The result is that the sextupole magnet behaves like a positive lens which only directs metastable helium atoms in the $m_j = +1$ state towards the sample and the focus of the beam is limited by the velocity spread of the helium atoms [155]. To restrict $m_j = 0$ metastable helium atoms and parahelium from reaching the sample, a central stop is placed at the exit point of the sextupole magnet. This is a 1.5 mm diameter disk held by a thin needle with the position adjusted using a linear drive [155].

Since around 95% of the metastable helium atoms are placed in the $m_j = +1$ state by this method (adiabatic case), to also produce $m_j = -1$ He 2^3S atoms, a zero-field spin-flipper is used, as described by Kurahashi *et al.* [130, 155]. If the magnetic field seen by the metastable helium atom changes more quickly with respect to its Larmor precession frequency (diabatic case), then the spin state will flip to $m_j = -1$. Since the Larmor frequency is proportional to the magnetic field, a weak B-field is

applied within the flipping region [130]. Furthermore, to eliminate leakage fields, primarily due to the Earth's magnetic field (measured to be around 50 µT [130]), the flipping region is contained within a series of permalloy shields. The extent of spin polarisation of the metastable helium beam can be seen in Figure 3.13 where 250 mG is the strength of the transverse magnetic field applied in the zero-field spin-flipper.

3.6 Spin Asymmetry Measurements

Spin asymmetry is the ratio of the difference over the sum of electrons generated and measured from He 2^3S atoms whose spin magnetic moments are aligned parallel (antiparallel) to an applied magnetic field [32]. This is expressed as:

$$A(\%) = \frac{1}{|P_z|}\frac{I_\uparrow - I_\downarrow}{I_\uparrow + I_\downarrow} \times 100 \tag{3.9}$$

where P_z is the polarisation of the He 2^3S beam and $I_\uparrow$ and $I_\downarrow$ are the intensities of electrons collected by the analyser when the metastable helium atoms are in the $m_j = +1$ ($\uparrow$) and $m_j = -1$ ($\downarrow$) states respectively. The polarisation of the metastable helium beam is expressed as:

$$P_{z\pm} = \frac{n_\uparrow \mp n_\downarrow}{n_\uparrow + n_0 + n_\downarrow} \tag{3.10}$$

where $n_\uparrow$, $n_\downarrow$ and n_0 are the number of helium atoms in the m_j +1, -1 and 0 magnetic sublevels [147]. The beam polarisation is measured using a Stern-Gerlach analyser (see below) and the polarity of the spin-polarisation is changed by using either the spin-flipper and sextupole magnet setup or alternatively by changing the helicity of circularly polarised light [147].

3.7 Stern-Gerlach Analyser

Before attempting spin polarised measurements, it is first important to check the extent of spin polarisation of the He 2^3S beam since it needs to be ideally >95%.

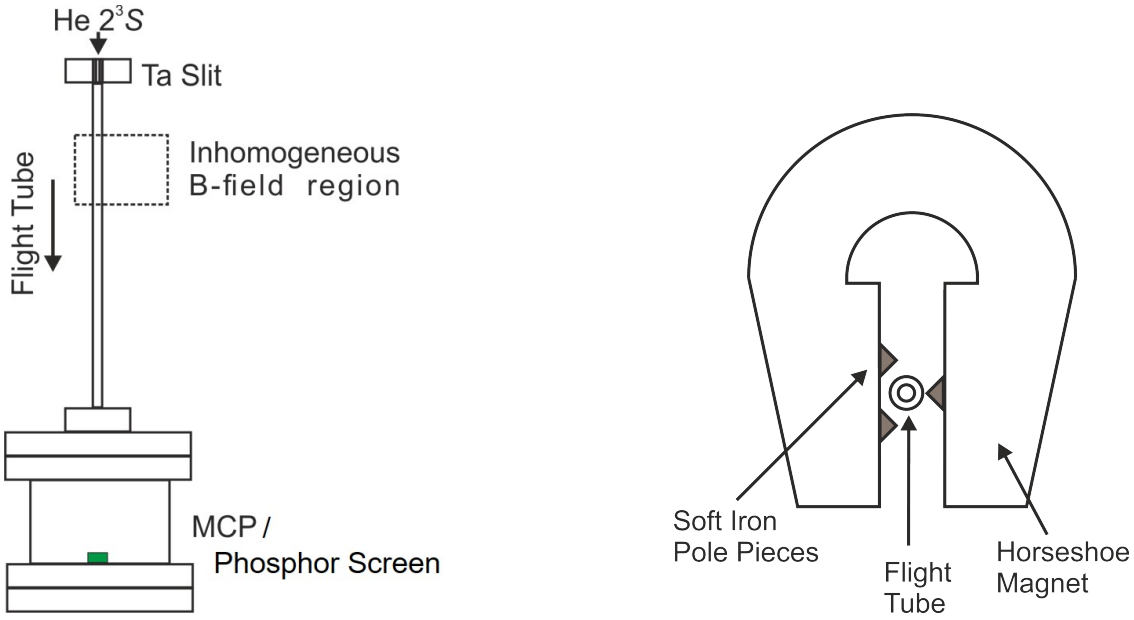

(a) (b)

Figure 3.12: In order to determine the extent of spin polarisation of the metastable helium beam, a Stern-Gerlach analyser is used. (a) Plan view of the Stern-Gerlach analyser setup used in the electron spectroscopy laboratory at York. (b) Cross-section of the horseshoe magnet used to produce an inhomogeneous magnetic field across the beamline.

This spin polarisation can be checked using the same principles as those of the 1922 landmark Stern-Gerlach experiment [156]. By passing a beam of silver atoms through an inhomogeneous magnetic field, Stern and Gerlach were able to demonstrate quantisation of angular momentum of the electron. After passing through the magnetic field, these silver atoms were observed on a photographic plate and it was found that the quantisation of the electron spin had two orientations, later to be defined as spin up and spin down.

Both at York and NIMS, a similar setup to that of the original experiment is used. After the analysis chamber where MDS/MEEM takes place, an extra vacuum system is located in which the helium atoms first pass through a narrow vertical rectangular slit of width around 50 µm. This is used to provide a well-defined beam profile that results in clearly resolvable magnetic sublevels. Immediately after the slit is an inhomogeneous magnetic field; at York, this is produced using a horseshoe magnet with three extra soft Fe pole pieces in the arrangement shown in Figure 3.12. This

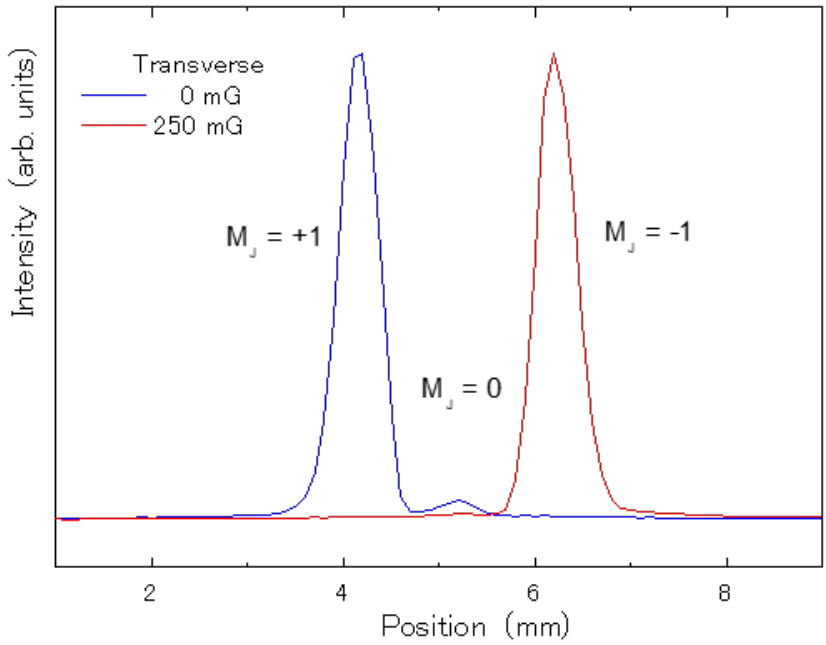

Figure 3.13: The measured response on a channel electron multiplier (CEM) from a spin polarised He 2^3S source in the MEEM system before (blue) and after (red) the spin flipper is used. Position is the vertical height of the CEM relative to the beamline axis.

non-uniform magnetic field causes a splitting along the direction of the field gradient, resulting in three vertical spots on the detector corresponding to $m_j = -1, 0, +1$. If the source is 100% spin-polarised, then only one spot will be observed at the detector.

The detector is either a scanning channel electron multiplier mounted on an automatic adjustable height platform (NIMS) or a microchannel plate/phosphor screen assembly (York); see Chapter 4 for more information on this.

The extent of spin polarisation obtained using a sextupole magnet and a zero-field spin-flipper can be seen in Figure 3.13. In the adiabatic case, not all of the helium atoms are in the $m_j = +1$ state and there is a small population of atoms in the $m_j = 0$ magnetic sublevel (less than 10%). After applying the spin-flipper, 99% of the He 2^3S atoms now occupy the $m_j = -1$ magnetic sublevel.

3.8 Quantisation Axis

One further challenge faced with spin polarised measurements is the influence of the Earth's magnetic field which causes the spin of the He 2^3S to precess to align with this field [130]. This will influence spectroscopic/microscopic measurements when attempting to measure the surface spin polarisation of a material in a particular magnetisation direction. To account for the Earth's magnetic field, a series of coils are placed around the sample region. By applying a small current within the coils, the Earth's magnetic field is cancelled out (as checked using a Hall probe). A small field ($\approx$ 0.1 Gauss) is applied in a particular magnetisation direction to define a quantisation direction at the sample surface. A quantisation axis is applied to align the spins of the He 2^3S atoms parallel with that of the magnetisation axis of the sample or to enable in-plane and out-of-plane magnetisation to be probed.

At York, six sets of coils, in pairs of two, connected in series with an equal number of turns and separation of approximately 140 cm (Helmholtz coils), are placed around the spectroscopy system such that each pair of coils acts in a particular direction (x, y, z) [157].

At NIMS, the photoemission electron microscopy (PEEM)/MEEM system has two different coils wound around the chamber of the main system with each defining a quantisation axis either in-plane or out-of-plane relative to the sample. One coil applies an in-plane quantisation axis in the plane of the surface of the sample, with a field strength of 50 mG across the plane (I=4.5 A). The other axis is out-of-plane, with a field strength of 630 mG (I=2.8 A) out of the plane of the sample.

Chapter 4

Experimental Techniques

This chapter aims to detail the main experimental systems used in this project and the techniques (aside from MDS) used to characterise graphene, Fe_3O_4 and other systems studied. Starting with a description of ultra-high vacuum systems, this is then followed by an explanation of the setups used both in York and at NIMS. The chapter then covers the various surface analysis techniques used in this project with a focus on photoemission spectroscopy and emission electron microscopy. Finally, a brief overview of CASTEP, a DFT code used here to provide *ab intio* calculations to support experimental results is also covered.

4.1 Ultrahigh Vacuum Systems

In order to characterise organic/ferromagnetic interfaces and the proximity effect in 2D materials, it is desirable to produce these systems in a clean environment, where contaminant gasses do not modify the material's properties or make the surface "dirty". To prepare samples in such a manner and perform certain experimental techniques, for the majority of experiments performed in this project an ultra-high vacuum (UHV) was used. UHV conditions exist in systems where the pressure is between 8×10^{-9} to 10^{-10} mbar [158]. Anything lower than 1×10^{-10} mbar is classed as extreme high vacuum [159] and pressures at 10^{-8} mbar and above are classed as high vacuum. At pressures of 1×10^{-10} mbar, in theory, it takes approximately three days for a monolayer of residual gas to form on a surface therefore enabling growth

and preservation of clean surfaces. In practice, contamination of the sample is limited to no more than one day but this is dependent on the sticking coefficient of the surface [158]. A further benefit of UHV is the ability to perform certain techniques which cannot be carried out at atmosphere such as the electron spectroscopy and microscopy methods used here [160].

During this project, three main systems were developed and used, as detailed in the following sections: the electron spectroscopy laboratory, the low energy electron diffraction (LEED) I/V system (both in York) and the SPMEEM system at NIMS. All of these are described in more detail below.

4.1.1 Electron Spectroscopy System

The electron spectroscopy system, shown schematically in Figure 4.1, is where the majority of the work performed in this project took place. The system consists of three chambers: a fast entry lock (FEL), a preparation chamber for growth and preparation, and an analysis chamber which hosts the various different spectroscopy techniques.

The FEL is equipped with an Omicron-style storage rack with three slots enabling up to four samples to be used in the system at any given time. The sample storage rack is connected to a six way cross (CF40 flanges for each face) which acts as the FEL chamber. A transfer arm 160 cm long connects all three chambers together and a gate valve separates the FEL from the preparation chamber. Between the transfer arm and the FEL chamber is an adjustable CF40 bellows section for fine tuning of the transfer arm position.

An Edwards EXT75DX 61 ls^{-1} turbomolecular pump backed by an Edwards RV5 rotary vane pump is used to pump the FEL chamber. An ion gauge (sensitivity set to N_2) measures the pressure and when a value of 5×10^{-7} mbar or lower is reached, samples are transferred to the analysis or preparation chamber. Nitrogen gas is used to vent the chamber during sample exchange to help maintain clean conditions.

The FEL is separated from the preparation chamber by a CF40 gate valve and a large CF160 gate valve connects the other side of the preparation chamber to

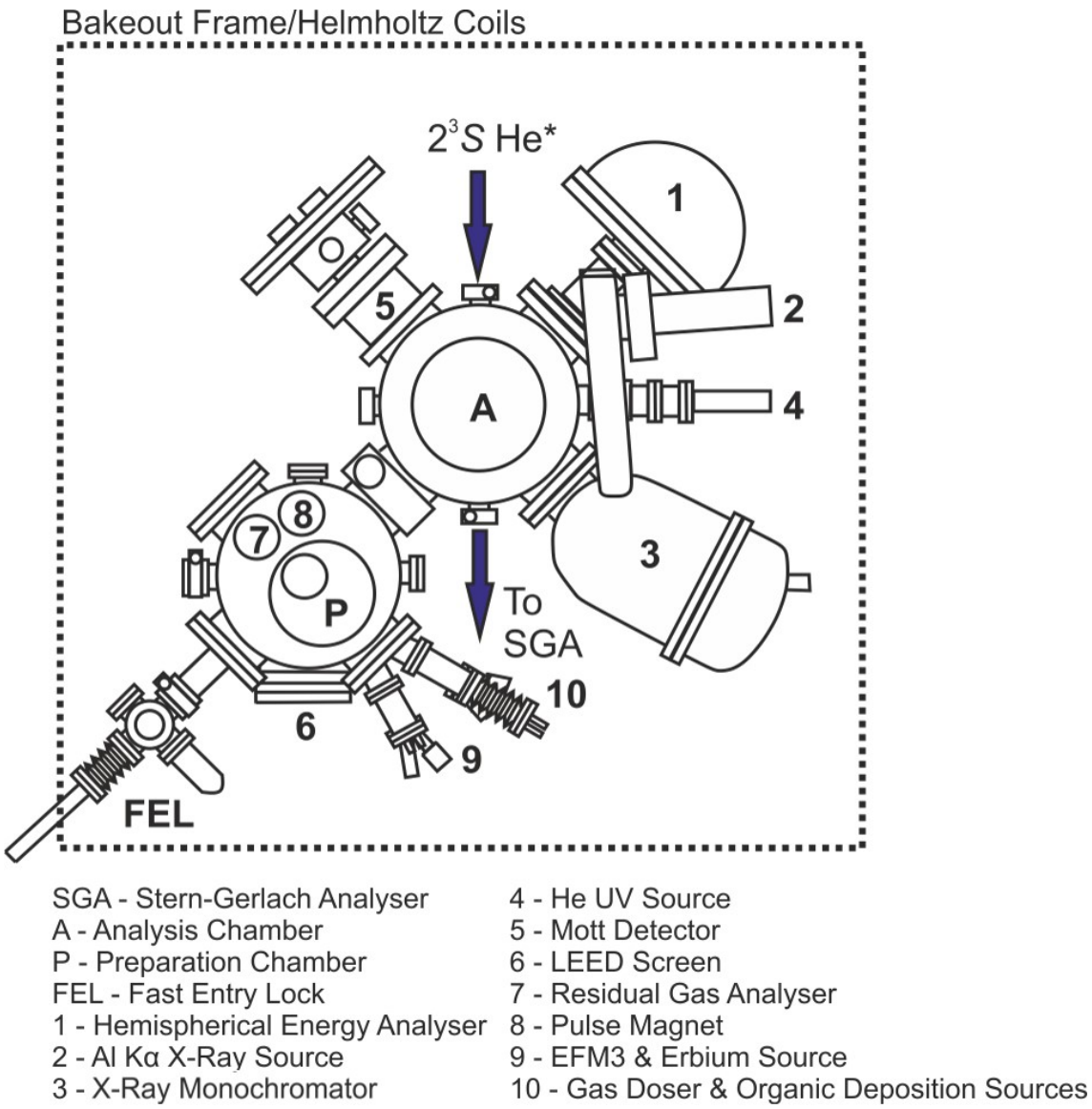

Figure 4.1: Plan view schematic of the electron spectroscopy system at York developed and used throughout this project. See text for details.

the analysis chamber. The preparation chamber holds samples using an Omicron sample stage equipped with both a Th/W filament for e-beam heating and a Mo comb for DC heating. This sample stage is mounted on a modified transfer arm and port aligner which provide the necessary range of positions for different purposes. The sample stage is also equipped with a quartz crystal microbalance (QCM) for monitoring the deposition rate of the metallic and organic deposition sources in the preparation chamber.

The preparation chamber is pumped beneath its supporting table using a 420 ls^{-1} Seiko Seiki STP-400 turbomolecular pump, backed by an Edwards RV3 rotary pump.

Combined with a titanium sublimation pump, this results in a base pressure of $< 5 \times 10^{-10}$ mbar (as measured using an ion gauge). For more information on the layout see Ref. [157].

Mounted on a CF160 flange of the main chamber is a cluster flange with four CF40 flanges. In the final arrangement used in this work, the cluster flange supported an erbium source, an Omicron EFM3 Fe source and an MBE-Komponenten NTEZ low temperature effusion cell for deposition of organic molecules. The final flange is for a gas doser with two Swagelok 6 mm gas delivery lines. Externally, these gas lines are connected to two needle valves followed by two stop valves. One of these is used generally for the inlet of oxygen and the other for hydrogen. The hydrogen gas line is connected to a 50 W tungsten filament DC bulb with 2 mm holes drilled either side. The purpose of this is to act as a hot tungsten filament to crack molecular hydrogen to atomic hydrogen (as discussed in Chapter 6), and this requires a temperature of 1873 K or greater [161]. For most cases, approximately 30 W was used to successfully crack molecular hydrogen into its atomic form. This gas doser is mounted on a linear drive allowing it to be brought in close proximity to the sample. Additionally, there is a SmartLAB residual gas analyser for monitoring partial pressures of remnant gases in the chamber.

A pulse magnet on a rotational drive to position it around a sample in the preparation chamber can be used to magnetise thin films. This provides a field strength up to 100 mT, in a 30.1 µs period using a 127 V pulse delivered from a 100 µF capacitor. Testing of this as well as calculations and its design are explored in much more detail in Ref. [157]. There is also an ISE10 ion gun for Ar^+ sputtering and cleaning of samples. Finally, the preparation chamber is equipped with an Omicron SPECTALEED low energy electron diffraction (LEED) apparatus equipped with a W/Th filament to probe the surface reconstruction of samples.

The analysis chamber is equipped with a five-axis Omicron manipulator enabling motion in the x, y and z directions as well as rotation around the vertical axis and the sample normal axis (azimuthal). This range of motion is important when considering sample position with respect to the various probe sources as well as the entrance aperture of the hemispherical energy analyser (Section 4.4). The manipulator can

be cooled to liquid nitrogen temperatures through a copper labyrinth and braid. The analysis manipulator is equipped with the same Omicron DC setup as the preparation chamber but instead of a Th/W filament for e-beam heating, there is instead a pyrolytic boron nitride heater for more gentle heating of samples up to 1073 K. A thermocouple is attached to the end of the stage to measure the sample stage temperature.

The analysis chamber is pumped beneath the table using a 400 ls^{-1} Edwards nEXT 400 turbomolecular pump backed by an Edwards RV3 rotary pump, with a mesh above to prevent samples from falling into the turbomolecular pump. Attached to the chamber is a titanium sublimation pump to help reach lower pressures. The base pressure in the chamber reaches values $\leq 1 \times 10^{-10}$ mbar (ion gauge sensitivity tuned to N_2) and has a general backing pressure of 5×10^{-3} mbar (pirani guage). For more information on the pumping arrangement, the reader is encouraged to look at Ref. [157].

The UPS source, an Omicron VUV HIS 13, is connected to the analysis chamber through a CF40 flange and sits at a 45° angle to the analyser and monochromator, as can be seen in Figure 4.1. Using a cold cathode discharge, He I α photons (hf=21.22 eV) are produced when helium is introduced through a needle valve which is connected to a 99.999% pure He cylinder. The helium is let into the chamber through a thin glass capillary which requires additional pumping to control the pressure at both ends of the source. This is achieved using a 33 ls^{-1} Leybold Turbovac 50 turbomolecular pump backed by an Edwards RV5 (the same one that backs the FEL). To pump excess helium, an additional pumping line is used during source operation, backed temporarily by an RV12 rotary pump. This source requires cooling during operation and this is achieved through a shroud surrounding the source supplied with cold mains water.

The monochromated X-ray source (Oxford Instruments XM1000 MKII Mono X-ray) is connected to a bespoke CF160 to CF100 adaptor with a 5° offset to ensure correct alignment relative to the sample position. The source is mounted at 90° to the analyser. X-ray Al $K\alpha$ photons (1486.7±0.1 eV) are produced from one of two filaments, either short or long enabling control of the emission current and consequently the in-

tensity of X-rays being generated. The power used in standard operating conditions ranges from 300-450 W depending on the filament, and to maintain a constant temperature, this source is cooled with a recirculating temperature-controlled cooling system driven by an ATC KT1 chiller pumping deionised water at 18 °C. The emitted X-rays are aligned via a port aligner to the quartz crystal in the monochromator which focuses and monochromates the X-rays onto the sample stage. An additional CF40 pumping line is connected to one of the ports on the main chamber to provide additional pumping of the source.

To analyse electrons produced from the three forms of spectroscopy available in this system (UPS, XPS or MDS), an Omicron EA 125 hemispherical energy analyser is used. The analyser consists of seven channel multipliers with a reported energy resolution of 10 meV over a range of up to 2000 eV and a maximum count rate of 10^7 s^{-1}. This is mounted at 90° to the transfer position and the entrance optics are set at the same height as the transfer mechanism, UV source and Mott detector. For more information on how this functions, see Section 4.4.

4.1.2 Low Energy Electron Diffraction I/V System

To perform LEED I/V measurements, an additional system was used that is primarily for room temperature scanning tunnelling microscopy (STM). This system has an Omicron SPECTALEED instrument but instead of an Th/W filament, the electron gun here is equipped with a LaB_6 filament for a more stable source of electrons. LEED I/V measurements are performed on two pieces of software, Neptune and kSA 400 and images are taken using a kSA K-30FW camera. The system has a five-axis Omicron manipulator, and, as for the electron spectroscopy system, uses an Omicron sample stage, with both a Th/W filament for e-beam heating and a Mo comb for DC heating. There are multiple metallic sources available including for rare-earth metals and iron as well as an argon sputter gun for cleaning samples. In an adjacent chamber there is a hydrogen cracking source, similar to the one used in the electron spectroscopy system [162]. The capabilities of both of these system allow samples to be prepared under the same conditions so that, nominally, the same surfaces are studied.

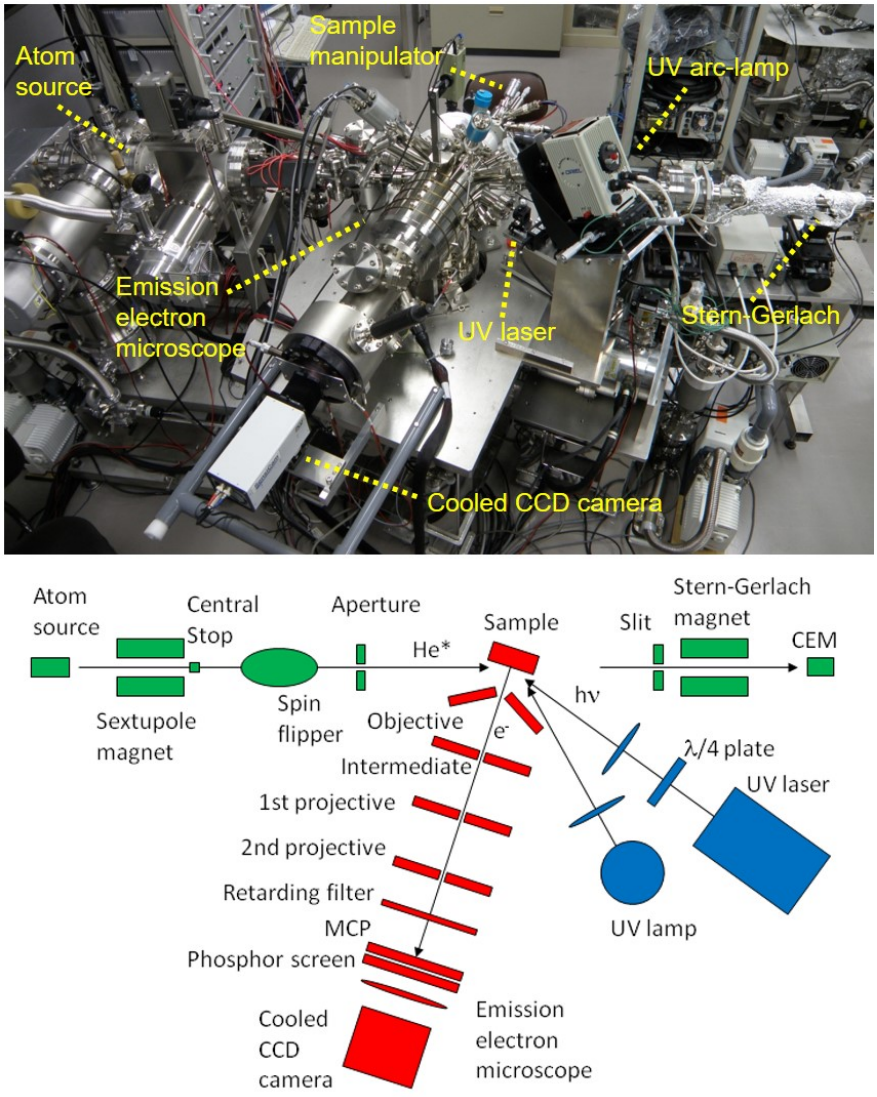

Figure 4.2: A photograph (above) and plan view schematic (below) of the MEEM/PEEM system at NIMS in Tsukuba, Japan, used during this project.

4.1.3 Emission Electron Microscopy System

All SPMEEM data in Chapter 5 were collected in an emission electron microscopy system at the National Institute for Materials Science (NIMS) in Tsukuba, Japan. This consists of four chambers: a FEL for transferring in samples from atmosphere, the He 2^3S source, the main chamber which contains the PEEM/MEEM optics, and a final chamber used for checking the spin-polarisation of the He 2^3S source (Stern-Gerlach analyser). A photograph and schematic view of this system can be seen in Figure 4.2.

The main chamber is pumped by two turbomolecular pumps, an 800 ls^{-1} Shimazu

TMP-803L and a 50 ls^{-1} Mitsubishi PT-50; these are connected in tandem to obtain a high compression ratio for hydrogen and helium and ensure efficient differential pumping between the He 2^3S source and the sample. These turbos are backed by an Adixen rotary pump with a pumping rate of 324 ls^{-1}. Additionally, below the support table is a titanium sublimation pump for helping maintain low pressures within the system. Typical base pressures are, for the main chamber, 1.3×10^{-10} mbar, for the FEL, 1×10^{-9} mbar and for the beamline, 5×10^{-9} mbar.

The main chamber is equipped with an Elmitec XYZ-manipulator to enable full range of motion, with an internal reservoir enabling temperatures as low as 126 K to be reached using liquid nitrogen. Different positions along the z axis enable transfer, imaging, cleaning or deposition on the sample. The main chamber consists of a Ni molecular beam epitaxy (MBE) source, an argon sputter gun (PHI 04-191; N.B this was originally a flood-type ion gun but was modified to enable differential pumping capability at the source), and a leak valve which was used as a source of both oxygen and naphthalene. The electron optical system used is a STAIB-PEEM-350 instrument and a PHOTONIS APD 2 PS 40/12/10/8 I 60:1 6"FM P20 microchannel plate was used for imaging. Samples are mounted in Elmitec sample plates made of non-magnetic metals equipped with a W/Th filament enabling e-beam heating of the sample.

Three different excitation sources are present on the system (He 2^3S, Hg/Xe UV arc-lamp, and a UV laser), all mounted at an angle of 72° with respect to the sample. A Hg/Xe ORIEL UV arc-lamp is used for photoemission electron microscopy (PEEM) imaging and a UV laser with a wavelength of 266 nm is used for spin-polarised PEEM; a detailed schematic of this setup can be seen in Figure 4.3. Finally, a He 2^3S beamline using the source described in Section 3.4.2 provides the capability for (spin-polarised) MEEM.

The UV laser is generated using a series of different optics. Firstly, a diode-pumped Nd^{3+}:YVO_4 vanadate laser is used to generate 1064 nm laser light. This is then passed through the first frequency doubler made of potassium titanyl phosphate (KTP) which is a crystal material lacking inversion symmetry and exhibiting non-linearity [163]. Consequently, when an input wave passes through this material, it

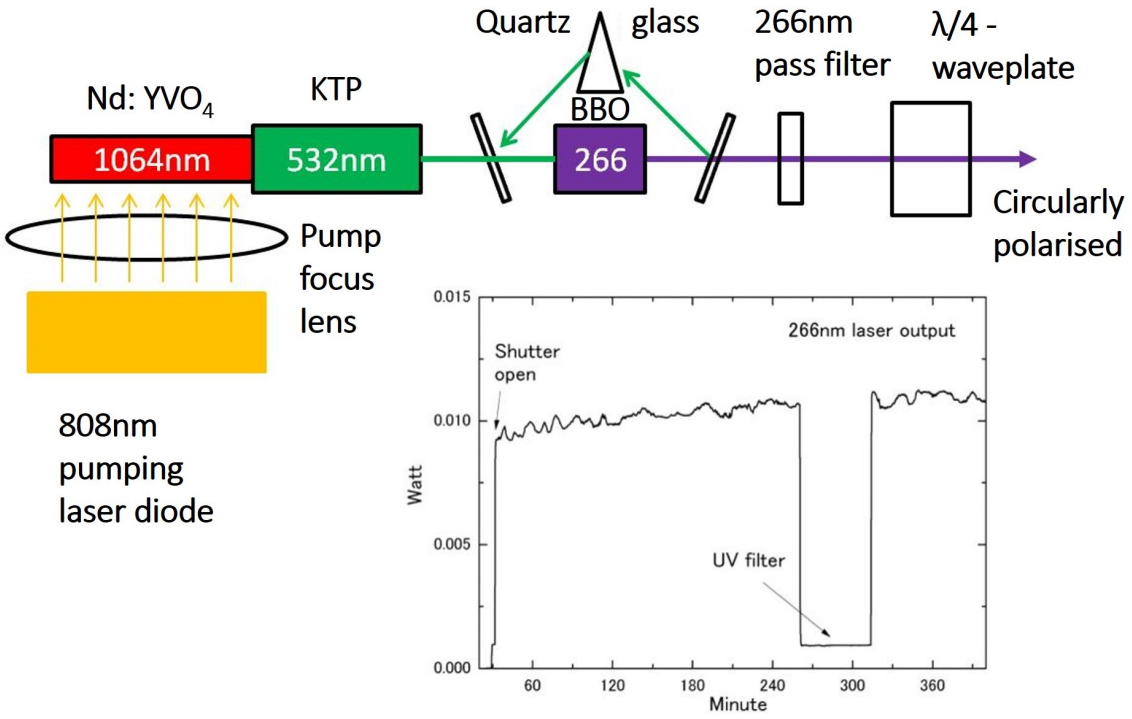

Figure 4.3: Demonstration of how a 266 nm UV laser is used in the PEEM/MEEM system and input through a series of lenses and filters. 1064 nm laser light is generated using a diode-pumped Nd^{3+}:YVO_4 vanadate laser and then passed through two frequency doublers of potassium titanyl phosphate (KTP) and β-barium borate (BBO) to reduce the wavelength to 266 nm. This light is cycled using mirrors and quartz glass to ensure an intense UV beam before being passed through a 266 nm pass filter to remove any other wavelengths of light. Finally, before reaching the sample, the light is circularly polarised through a $\lambda/4$-waveplate. The graph below the laser setup is the power output of the 266 nm UV laser.

generates a wave with double the frequency of the input wave and in this case a 532 nm wavelength. This is then passed through a mirror and into a second frequency doubler of β-barium borate (BBO, β-BaB_2O_4) which converts the 532 nm laser light to 266 nm light. Excess 532 nm light is reflected back through the BBO using a glass prism to improve the intensity of the UV laser. A 266 nm pass filter then removes any additional wavelengths of light before the laser is circularly polarised using a $\lambda/4$-waveplate.

To check the spin polarisation of the He 2^3S beam, in-line with the source, a Stern-Gerlach analyser is mounted consisting of a slit to provide a defined beam, an

inhomogeneous magnetic field created using NdFeB magnets and a channel electron multiplier (CEM) mounted on an electronically adjustable stage.

For the experiments described in Chapter 5, the FEL was temporarily setup to act as a chamber in which samples could be exposed to atomic hydrogen. The design of the hydrogen cracker is the same as that used in the electron spectroscopy system at York, but the tungsten bulb has a tolerance of 20 W instead of 50 W. It was found that around 10.3 W was needed to successfully turn molecular hydrogen into atomic hydrogen. Additionally, a needle valve was used to allow the introduction of oxygen.

4.1.4 Bakeout

Ultra-high vacuum is generally regarded as a region where the pressure is below 10^{-9} mbar [158, 164]. UHV systems are generally made of steel with low rates of outgassing of absorbed and desorbed gases, and by using a series of pumps in tandem, UHV conditions can eventually be reached over time [164]. A challenge faced with UHV systems is that the chamber pressure is increased by desorption of absorbed gases within chamber walls, where residual gas has absorbed into these walls whilst the system is exposed to atmospheric pressure. Since water and other gases from air have slow desorption rates, it is difficult to achieve UHV conditions in a short period of time. To reduce the time needed to achieve UHV, the system is "baked" which is a process of bringing the entire system to temperatures above 373 K. This causes gases which have adsorbed in the chamber walls to more rapidly desorb and then be pumped away reducing the time needed to achieve UHV to no more than a couple of days.

The electron spectroscopy and LEED I/V system both use bake-out panels combined with fan heaters to uniformly raise the temperature of each system. Heating tape is also sometimes used during bake-out with the current regulated using variable AC power supplies. The temperature of the electron spectroscopy system is set to 403 K due to the quartz crystal housing in the monochromator which can be damaged by heating the system above this temperature. These systems are typically baked between 24 - 48 hours, with the bake only starting when pressures reach

the mid-10^{-7} mbar range and then stopped when the pressure does not reduce significantly. For the electron spectroscopy system, this is typically around 2×10^{-7} mbar. Immediately afterwards, whilst the system is still hot, the titanium sublimation pumps are outgassed and then fired every 10 minutes for the first hour to help remove residual gas as the system cools.

4.2 Low Energy Electron Diffraction

To prepare certain materials such as Si(111) or 6H-SiC(0001) for studies relevant to electronic and spintronic applications, a clean, well-ordered surface is required. A surface reconstruction is a stable configuration of atoms at the surface of a material with a low free energy and a minimum number of dangling bonds [165]. To check the surface reconstruction of a material, one technique which can be used is low energy electron diffraction (LEED) which involves diffraction of low energy electrons by a material which constructively and destructively interfere. The resulting diffraction pattern can then be used to determine the surface reconstruction based on the same principle as Bragg scattering [164, 166].

The basis of LEED was first demonstrated by Davisson and Germer in 1927 who were studying the diffraction of electrons through nickel in order to probe the wave nature of the electron [167]. Since then, this has been developed into a commonplace UHV technique which is used to provide information on the surface structure. An example of a LEED setup as well as an example diffraction pattern can be seen in Figure 4.4. By flashing a surface at high temperatures followed by a slow cool, certain surface reconstructions such as the 6H-SiC(0001)-$((\sqrt{3} \times \sqrt{3})R30^{\circ})$ can be achieved as seen in Figure 4.4 (b).

The de Broglie wavelength of an electron with respect to its kinetic energy is expressed by the following equation:

$$\lambda = \frac{h}{\sqrt{2m_e E_k}} \tag{4.1}$$

where λ is the de Broglie wavelength, h is Planck's constant, m_e is the mass of an electron and E_k is the kinetic energy. From this equation, it can be seen that elec-

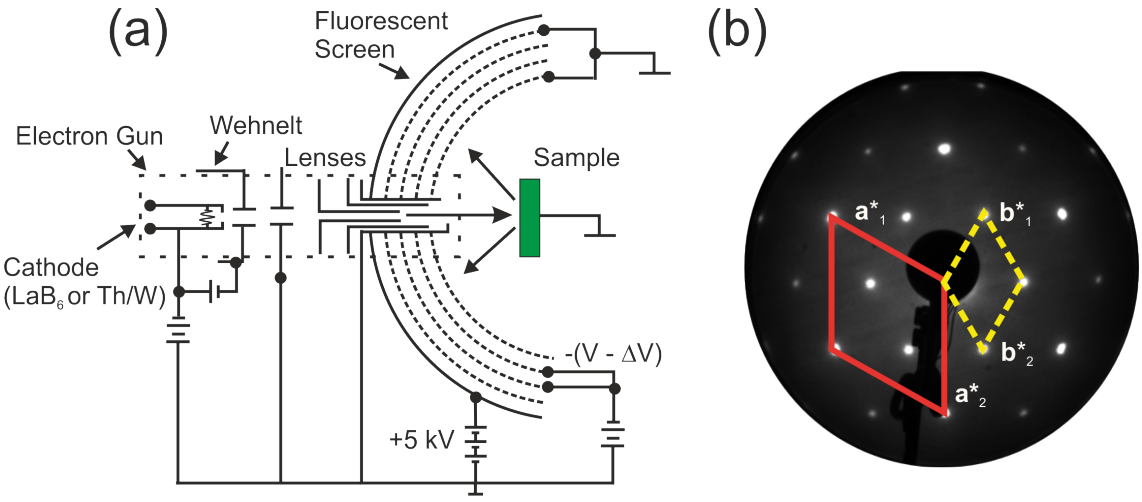

Figure 4.4: (a) A diagram of a typical setup for performing LEED where the sample surface sits orthogonal to and within close proximity of the electron gun. (b) LEED pattern of the 6H-SiC(0001) $(\sqrt{3} \times \sqrt{3})R30°$ reconstruction where $\mathbf{a}^*$ and $\mathbf{b}^*$ are the reciprocal lattice vectors. Image taken at 80 eV.

trons with a kinetic energy in the range of 20 - 200 eV have a de Broglie wavelength effectively equivalent to the atomic spacing of a well-ordered crystal. Electrons within this energy range will therefore diffract constructively and destructively (as described by the Laue equations), resulting in a diffraction pattern which can be observed using a phosphor screen or other detector. The energy of the escaping electron relates to the information depth of the technique. In LEED, the electrons are of low energy and so the information depth according to the universal curve (Figure 4.5 [28]) is within the range of a few atomic layers thus making it a surface sensitive technique.

The Omicron SPECTALEED generates a cathode ray through thermionic emission from a Th/W or a LaB_6 filament, with the latter being a more stable source of electron emission and also having a longer lifetime and greater current density [168]. These electrons are then focused and accelerated to a point on the surface of the sample using a series of electrostatic lenses. A negative potential, the Wehnelt potential, is used to focus the beam by retarding the electrons being emitted from the cathode. After hitting the sample, the diffracted electrons then pass through a series of fine mesh retarding grids which remove inelastically scattered electrons which may reduce the sharpness and contrast of the diffraction pattern. Beyond

these grids, the electrons are accelerated by a large positive potential (5 - 6 kV) applied to the screen to visualise the pattern.

To interpret LEED patterns, Wood's notation is used [164]. This notation is valid when the overlayer structure and the bulk planar structure have the same symmetry; i.e. the angles between the lattice vectors of the surface unit cell in the bulk, $\mathbf{a}_1$ and $\mathbf{a}_2$, are equal to the angle between lattice vectors of the overlayer $\mathbf{b}_1$ and $\mathbf{b}_2$. Take for example the $(\sqrt{3} \times \sqrt{3})R30°$ of the 6H-SiC(0001) reconstruction in which the notation is split into two parts. The first part specifies the length of the overlayer with respect to the bulk where in this case, $|\mathbf{b}_1|=\sqrt{3}|\mathbf{a}_1|$ and $|\mathbf{b}_2|=\sqrt{3}|\mathbf{a}_2|$. The second part of the notation indicates rotation of the overlaying cell with respect to the bulk, so the $(\sqrt{3} \times \sqrt{3})R30°$ reconstruction has a 30° rotation. The LEED pattern of the $(\sqrt{3} \times \sqrt{3})R30°$ surface reconstruction is shown in Figure 4.4 with the reciprocal lattice vectors highlighted.

4.2.1 LEED I/V

LEED can be further developed in a technique known as LEED I/V which measures the intensity (I) of particular spots as a function of electron voltage (V) or energy. This can be used to characterise the extent of growth in certain systems, and is particularly useful when looking at graphene growth on SiC. As discussed in Chapter 6, the $(6\sqrt{3} \times 6\sqrt{3})R30°$ surface reconstruction indicates the formation of a buffer layer [169, 170] but may also indicate the existence of additional layers of graphene (monolayer, bilayer, etc.). Depending on the number of layers present, the intensity of the diffraction spots associated with graphene will change at particular electron energies. Therefore, LEED I/V can be used to characterise the number of layers of graphene on SiC [41, 171].

The software used to track the spots and measure their intensity as a function of beam current is kSA 400. This tracks a spot's intensity by predicting its position using the following equation:

$$t = \left[\frac{L\hbar}{nd_{\parallel}\sqrt{2m_e}}\right]\frac{1}{\sqrt{E}} = \frac{A}{\sqrt{E}} \tag{4.2}$$

where t is the distance between specular and nth-order diffraction spots, L is the distance from the centre of the sample to the centre of the phosphor screen, $d_{\|}$ is the atomic spacing between rows of atoms in the plane of the surface and E the beam energy. Such a technique has been used to solve a variety of different structures such as SiC [41] and to theoretically predict structural effects due to oxidisation of ferromagnetic surfaces [172].

4.3 Photoemission Spectroscopy

One of the earliest examples of photoemission was in 1887 when Hertz experimented with UV light on a spark gap and observed passage of the spark [173]. However, it was not until 1905 that Einstein was able to describe the phenomenon of emission of electrons from a surface due to incident light, a process given the name "the photoelectric effect" [174]. Previously, light had been treated as a wave, but the observation of the photoelectric effect led to light being considered instead as quanta, with an electron only emitted if the energy of the incident photon is greater than or equal to the workfunction of the surface. Explanation of this process would result in Einstein being awarded the physics Nobel prize in 1921 [174].

The kinetic energy, E_k, of the electron emitted due to the photoelectric effect is given by the following equation:

$$E_k = hf - \phi_s - E_B \tag{4.3}$$

where ϕ_s is the work function of the surface, hf is the energy of the photon with f the frequency of incident light, and E_B is the binding energy of the state from which the electron originates. By measuring the intensity of the emitted electrons as a function of their energy, a spectrum is obtained which will contain peaks that correspond to the discrete energy states from which they are emitted. Inspection of Equation 4.3 shows that the maximum kinetic energy of a photoelectron is a function of the energy of the incident photon and the work function of the surface.

Similar to LEED and other techniques involving electrons, the energy of the emitted photoelectron also corresponds to the information depth. The surface sensitivity of

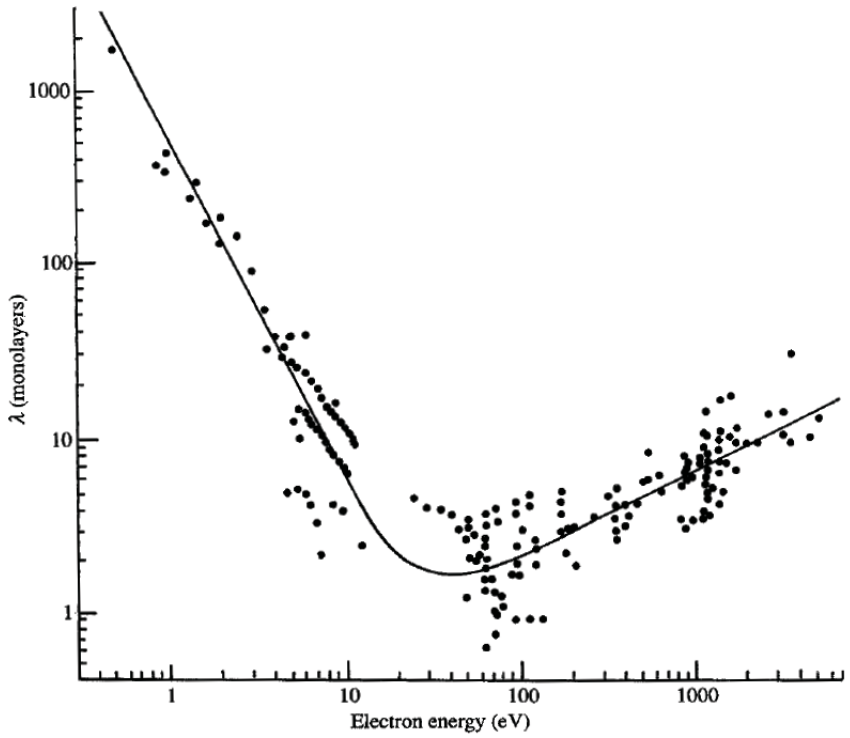

Figure 4.5: A plot, known as the universal curve, showing the relationship between attenuation length (λ, in atomic monolayers) and kinetic energy of the emerging electron for a wide range of materials. It is photons in the range of 50 - 200 eV that are most surface sensitive, with $\approx$ 40 eV being an ideal energy for the escaping electron. Graph taken from Briggs *et al.* [28].

photoemission does not depend on the penetration depth of the photon but instead the probability of the photoelectron, once generated, being able to escape to the surface without further energy losses [164]. Plasmons, electron-electron interactions and single or double-particle excitations can all result in the escaping electron losing energy. For the greatest surface sensitivity (smallest information depth), the wavelength of light needs to be in principle closest to the minimum of the universal curve seen in Figure 4.5 which appears at around 40 eV; therefore an ideal energy range for photons is between 50-200 eV [164]. Aside from synchrotron facilities, some progress has been made towards developing UV sources with variable energy, for example, "harmonium", a laser-assisted source for time-resolved UV photoemission spectroscopy [175].

It is also worth noting that the emission of electrons from the surface is affected

by the response of the atom to the creation of the hole/photoelectron which can result in additional features in the spectrum intrinsic to the photoemission process. Extrinsic losses such as plasmon excitation can also influence the spectrum [176].

4.3.1 Ultraviolet Photoemission Spectroscopy

Due to the low energy of ultraviolet photons, the corresponding photoelectrons will originate from loosely bound occupied states from the Fermi level to within >10 eV of the valence band. Ultraviolet photoemission spectroscopy (UPS) in this project used He I α photons with an energy of 21.22 eV. From inspection of Equation 4.3, it can be seen that each electron will have a measured kinetic energy that corresponds to a particular binding energy. Measuring the intensity of electrons over a range of different kinetic energies will result in an electron emission spectrum that directly relates to the density of states of the valence band for the surface and first few sublayers of the sample. A representation of this electron emission process is shown in Figure 4.6.

The penetration depth of UPS is around 1 - 2 nm, however, the information depth is dependent on the energy of the incident UV photon. Based on the universal curve (Figure 4.5), photoelectrons generated from He I α UV photons which have escaped to the surface without undergoing inelastic collisions will originate from around one to three atomic monolayers of the material. Consequently, probing valence band states using He I α UV photons is fairly surface sensitive. Since some photoelectrons generated will originate from bulk states, the electron emission spectrum obtained will be a mixture of both subsurface and surface states.

One feature of using this particular transition is that the excitation energy of the He I α UV photons, 21.22 eV, is very similar to that of the 2^3S metastable state of helium, 19.82 eV. Consequently, the spectra collected from both of these techniques are relatively comparable, depending on the de-excitation mechanism of He 2^3S atoms. In particular, in the case of the one-electron process (Auger de-excitation), the spectra obtained through MDS and UPS are similar, as seen, for example, for many organic molecules on various surfaces such as C_{60} on Si(111) [177]. An example of this is shown in Figure 4.7, where the molecular orbitals are clearly observed with

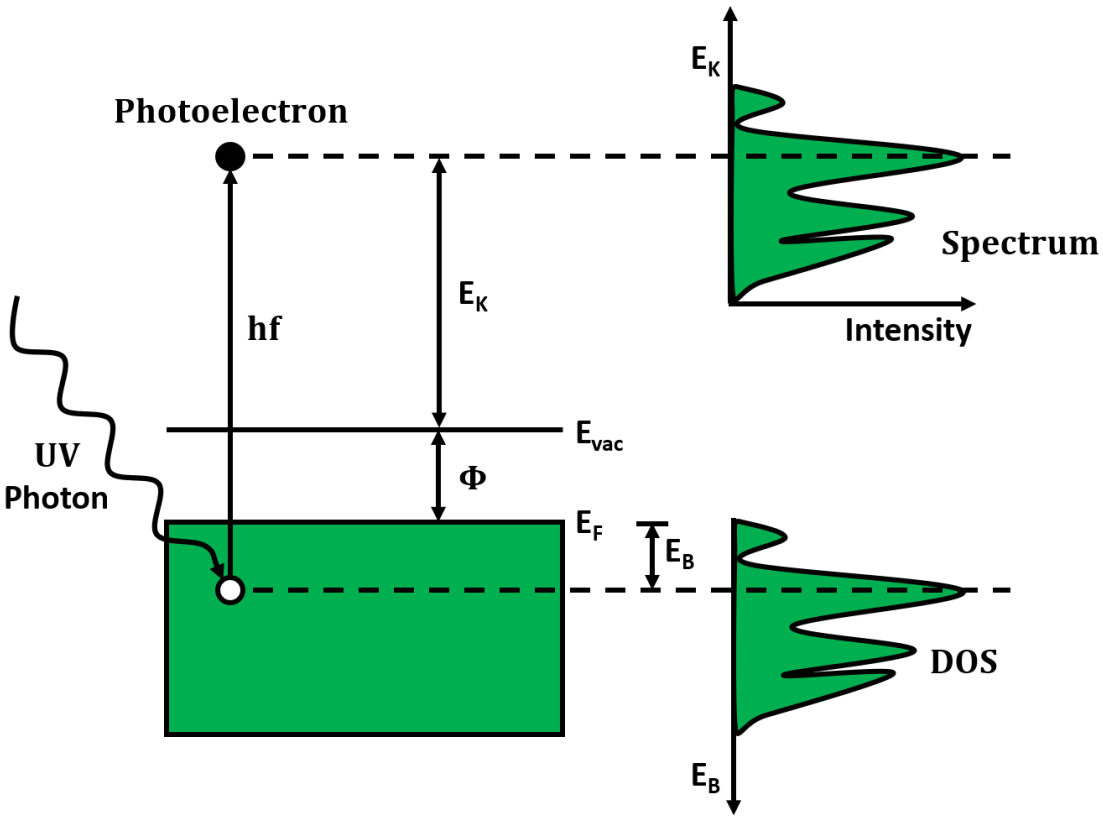

Figure 4.6: When a UV photon is incident on the surface of a material, an electron from an occupied state in the valence band is emitted. The resulting emission electron spectrum (top right) represents the density of states of the valence band (bottom right).

both techniques.

One further benefit of UPS is that it can be used to measure the surface work function of a material. The work function is defined as the minimum energy required to remove an electron from a solid to a distance where it no longer experiences a Coulomb interaction with its corresponding image charge, created as a result of its removal [121]. Measuring this parameter is particularly important when designing multilayer electronic devices which ideally require matching of the valence and conduction bands of different layers. Additionally, changes in the workfunction can be used to indicate structural changes at the surface, for example, the number of layers of graphene present on 6H-SiC [178]. Measuring the workfunction using UPS is achieved by applying a negative bias to the sample, typically -15 V. This offsets the measured spectrum, separating the workfunction of the surface from that of the

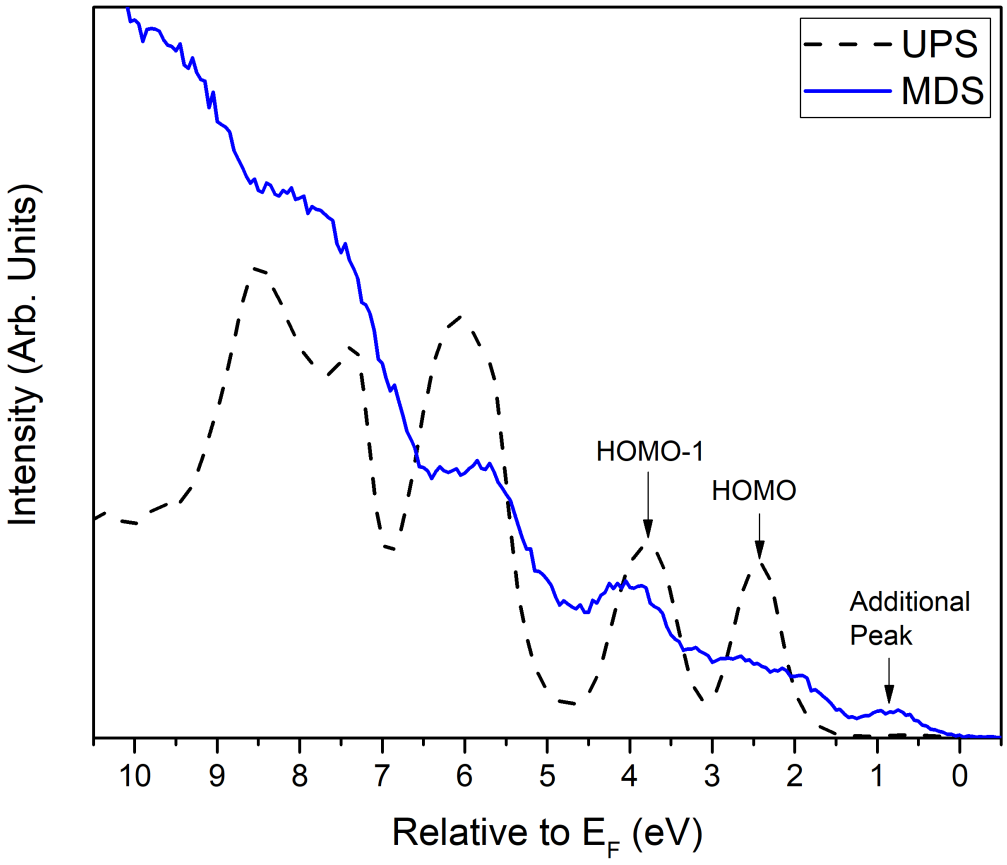

Figure 4.7: Multilayer C_{60} results in the observation of highest occupied molecular orbitals (HOMOs) both in UPS and MDS. The spectra, in particular peak positions, are directly comparable since the main de-excitation mechanism with C_{60} is Auger de-excitation. For more information on these states, the reader is encouraged to read Ref. [157].

hemispherical energy analyser, such that both the Fermi edge and low kinetic energy cut off of the spectrum can be measured. The difference between these values (the spectral width) is then subtracted from 21.22 eV to give the surface workfunction.

To produce He I α UV photons, a cold cathode discharge source is used. Helium gas of 99.999% purity is passed through a glass capillary surrounded by a water-cooled shroud. Helium is let into the source until the analysis chamber pressure reaches $\approx 1 \times 10^{-8}$ mbar and a positive 1 kV bias is then applied to an anode at the end of the capillary to cause breakdown of the gas. Typical operating conditions for the discharge are an emission current of 100 mA and a voltage of $\approx$ 480 V. UPS measurements were performed with the sample at 45° to both the source and the analyser. To ensure that the majority of electrons originate from the sample, a 1 mm

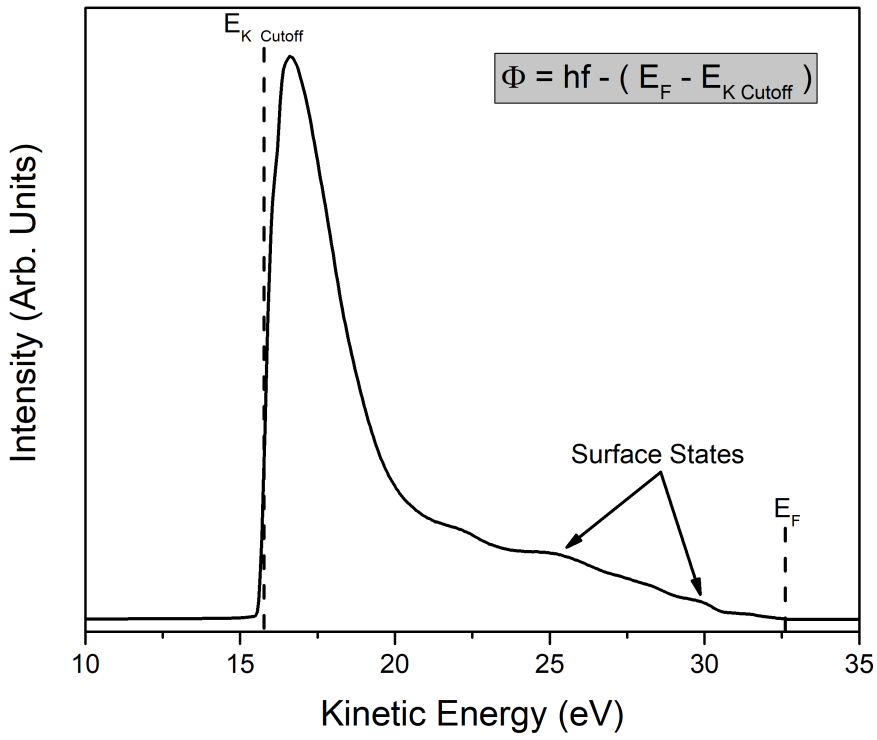

Figure 4.8: When a negative bias is applied to a sample when taking UPS measurements, the work function of the surface can be determined by subtracting the spectral width from the photon energy, in this case 21.22 eV.

entrance aperture of the hemispherical energy analyser is typically used which still yields count rates of ≥50,000 per second. For reference, the typical SiC sample size was 13×4 mm^2.

4.3.2 X-ray Photoemission Spectroscopy

X-ray photoemission spectroscopy (XPS) in a standard laboratory setup involves photons of a much higher energy than used for UPS. These are soft X-rays with an energy between 1000 - 1500 eV so that the photoelectrons generated originate from much more tightly bound states, known as core electronic states. These electronic states do not overlap with their neighbours contrary to electrons within the valence band. Consequently, they form distinct states with unique energies corresponding to each element as shown schematically in Figure 4.9. Therefore, by comparing spectra

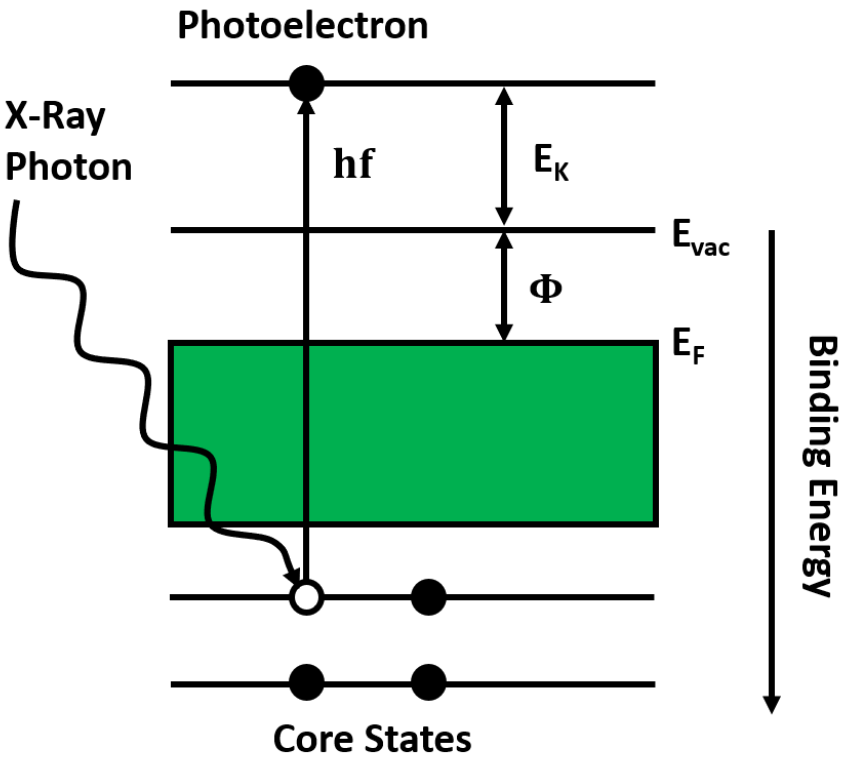

Figure 4.9: Photons with an energy between 1000 - 1500 eV liberate more tightly bound electrons in core states which do not overlap with one another. XPS therefore allows elemental identification of a sample.

taken using XPS to known peak positions of a particular element, the composition of a surface can be determined.

Not only can XPS be used to determine the elements present in the sample but it can also determine the abundance of a particular element through quantitative analysis; this aspect of XPS is of particular interest when checking the extent of deposition when attempting submonolayer growth of iron [179] or erbium. To determine the abundance of a given element on a sample, the following expression is used:

$$I_i \propto N_i \sigma_i \lambda_i \tag{4.4}$$

where I_i is the intensity of peak i, N_i is the average concentration of the peak, σ_i the photoionisation cross-section of the state and λ_i the inelastic mean free path of the emitted electron. Whilst other factors such as angle of emission, analyser transmission function and vacuum chamber pressure may affect the relative intensity

of the peak, these are generally kept constant and are therefore ignored as the sample is typically exposed to the same experimental conditions.

The sampling depth of XPS is related to the inelastic mean free path of the electron which can be described by the Beer-Lambert law:

$$I = I_0 e^{-\frac{d}{\lambda}} \tag{4.5}$$

where I is the intensity of the transmitted radiation at a particular kinetic energy, I_0 is the intensity of radiation falling on the sample, d is the depth inside the surface and λ the inelastic mean free path. Around 95% of electrons escaping from the surface are emitted within 3λ of the surface, which is considered the sampling depth. Since for most materials λ falls within 1 - 3.5 nm [28], the sampling depth for this technique is around 3 - 10 nm. Whilst more electrons originate from bulk-like states, this technique is still considered to be fairly surface sensitive. To further improve surface sensitivity, the sample can be placed at more of a grazing angle with respect to the source, lowering the effective penetration depth of the X-ray photons. This however does also reduce the number of photoelectrons generated which consequently lowers the count rate measured by the hemispherical energy analyser.

Monochromated XPS source

The main application of using XPS is to infer different chemical environments in a sample due to different bonding states. All electrons within a material contribute to the electrostatic shielding of the nuclear charge. Different chemical environments from different bonding states change this shielding consequently resulting in a shift in the effective binding energy of certain core states to higher or lower energies. If multiple chemical environments exist within a material then the linewidth of a measured peak corresponding to a certain core state, for example C $1s$, will increase due to a convolution of peaks at different binding energies; this peak can then be deconvoluted into a series of Lorentzian/Gaussian peaks. An example of where this can be used is in analysing the extent of graphene growth on 6H-SiC where the carbon-carbon chemical environment increases with further graphitisation of the

material [179, 180].

Different chemical environments can be observed by illuminating the surface of a material with non-monochromated X-rays. However, due to multiple frequencies impinging on the surface of the sample, the linewidth of the observed peaks will be broadened, and thus it is more difficult to deconvolute or even distinguish the difference between different chemical environments which may exist. As an example, light produced from a non-monochromated aluminium X-ray source will contain both Al $K\alpha$ and $K\beta$ radiation. Furthermore, such sources also produce Bremsstrahlung radiation, which is not ideal as it can damage the surface of a material over extended periods of time. To improve the energy resolution of XPS and remove harmful radiation from impinging on the sample, a monochromated X-ray source can be used. At York, this monochromated X-ray corresponds to the Al $K\alpha_1$ (1486.7 ± 0.1 eV) spectral line. To produce monochromated X-rays, an aluminium anode is used to first generate various different X-rays which are then directed through a quartz crystal back-plane. As the lattice spacing of the quartz crystal planes matches the wavelength of the Al $K\alpha_1$ spectral line, X-rays incident on the crystal undergo constructive interference according to Bragg's law:

$$n\lambda = 2d\sin(\theta) \tag{4.6}$$

where λ is the wavelength of the X-ray, d is the lattice spacing and θ is the Bragg angle. The Al $K\alpha_1$ X-ray has a line width of 0.25 eV and the quartz crystal is curved to focus the diffracted X-rays onto a roughly 2×5 mm^2 spot reducing the chance of photoelectrons being generated outside the sample region.

The Oxford Instruments XM1000 MKII Mono X-ray source consists of two different filaments (long and short) which can be controlled using the filament current (0-4.8 A), emission current (0-20 mA) and anode voltage (0-15 kV). Typical operating conditions for this source are an emission current of 18 mA and an anode voltage of 12 kV corresponding to a power of 216 W. Due to the relatively low intensity of counts produced by this source, a 6 mm circular entrance aperture to the hemispherical energy analyser is typically used.

4.4 Hemispherical Energy Analyser

An Omicron EA 125 hemispherical energy analyser is used to analyse the electrons generated in MDS, UPS and XPS. As can be seen in Figure 4.10, the electrons emitted from a sample pass through a series of cylindrical electrodes before then being deflected around two concentric hemispheres. Between each electrode exist lines of equipotential which refract the electrons. By employing a three electrode arrangement and changing the bias applied to each electrode, the passing electrons can be accelerated/retarded by varying amounts whilst keeping the focusing properties constant; therefore these electrodes behave like a series of electrostatic lenses. The first set of electrodes act as an Einzel lens which selects the analysis area (spot size) and angular acceptance. This does not change the electron energy and operates in three different magnification modes: high, medium and low. High magnification mode (most regularly used) results in the focal plane being near to the sample and accepts a wide angle of electrons from a small region. A second lens then accelerates or retards the electrons to match the pass energy of the analyser and uses a zoom lens function to ensure that the focal point remains on the analyser entrance aperture. The pass energy is a bias applied just before the electrons enter the hemisphere acting as a bandpass filter only admitting electrons within a certain bandwidth of this potential. The entrance aperture consists of a set of built in slits and apertures. These are matched with an exit plate slit which lies just before the detector.

The electrons are then deflected in a semicircular path around two concentric hemispheres, with the inner hemisphere (V_1) held at a negative potential and the outer one held at a positive potential (V_2) with respect to the pass energy of the analyser. On the other side of the hemisphere, these electrons then pass through an exit aperture into the detector which consists of seven channel electron multipliers (CEMs) placed at different positions in the exit plane. Each CEM is made of a material with a high surface resistance. A high voltage is applied between the funnel-shaped input and cylinder-shaped output resulting in the formation of a continuous dynode, where secondary electrons are produced by an incident electron impinging on the surface of the walls of the CEM [181]. Generation of these secondary electrons causes an avalanche-like effect where secondary electrons generate further electrons resulting

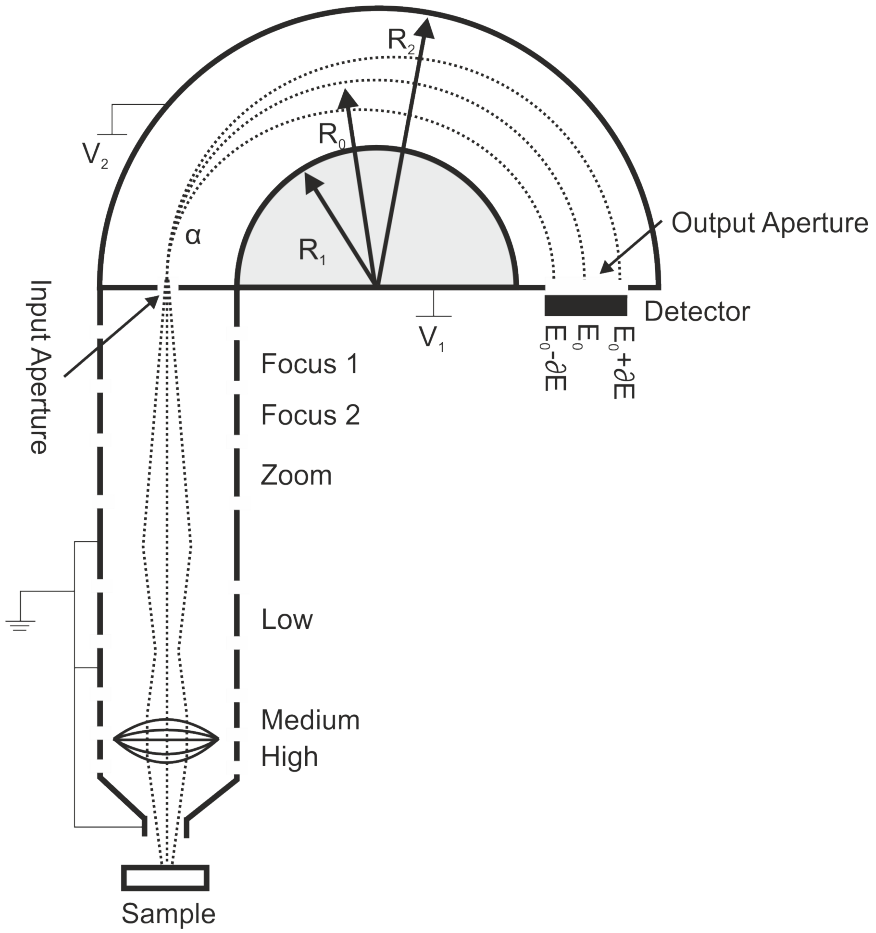

Figure 4.10: The Omicron EA 125 hemispherical energy analyser is equipped with a series of lenses, used to focus and then decelerate the electrons towards the two concentric hemispheres. Lines of equipotential between the lenses refract the electrons. Upon reaching the input aperture, they are then deflected in a semicircular path around the inner hemisphere towards an array of seven channeltrons. This figure is based on schematics presented in the EA 125 Energy Analyser User's Guide.

in 10^7 to 10^8 electrons at the output. The duration of each pulse of electrons tends to be around 8 ns [181]. Therefore, the maximum count rate can be exceeded if the bias voltage or incident electron intensity is too high.

The measured kinetic energy of electrons collected by the analyser is expressed as the following equation:

$$E_{Km} = E_R + E_p + \phi_a = hf - E_B \tag{4.7}$$

where E_{Km} is the measured kinetic energy of the electron, E_R is the retarding energy,

E_p is the pass energy and ϕ_a is the analyser workfunction. The true kinetic energy of the electron requires the surface workfunction ϕ_s to be known and is expressed as $E_K = E_{Km} - \phi_s$. The energy resolution of the hemispherical energy analyser is represented by the following equation:

$$\Delta E = E_p \left(\frac{d}{2R_0} + \alpha^2 \right) \tag{4.8}$$

where ΔE is the energy resolution, R_0 is the mean radius of the hemispheres, d is the slit width and α is the half angle of electrons entering the analyser. The angular term tends to be very small and therefore is generally ignored. The Omicron EA 125 used has a mean radius of 125 mm and a chosen exit aperture width of 2 mm. Therefore, calculated values of ΔE are 0.08 eV using a pass energy of 10 eV (typically used in UPS) and 0.4 eV for a pass energy of 50 eV (typically used in XPS). All spectra obtained for this project were obtained in constant analyser energy mode which keeps the pass energy constant whilst scanning through various kinetic energies. Since the pass energy is constant, the resolution remains constant as well. To improve the energy resolution, the pass energy needs to be lowered or the radius of the semi-circular path increased.

4.5 Photoemission Electron Microscopy

Data presented in Chapter 5 involved the use of an emission electron microscope to image surface structure from both photoelectons and electrons generated from He 2^3S atoms. Similar to the hemispherical energy analyser used in electron spectroscopy, the instrument involves focusing and manipulating electrons using a series of electrostatic lenses. One difference between this technique and electron spectroscopy is that when performing photoemission/metastable emission electron microscopy (PEEM/MEEM), the sample is situated at a much closer proximity to the entrance aperture at around 5-10 mm. Therefore, electrons emitted from either photoemission or from a metastable helium beam are accelerated from the surface towards the first electrode as a result of the electric field generated by the transfer voltage. The transfer voltage is the potential applied between the first electrode and

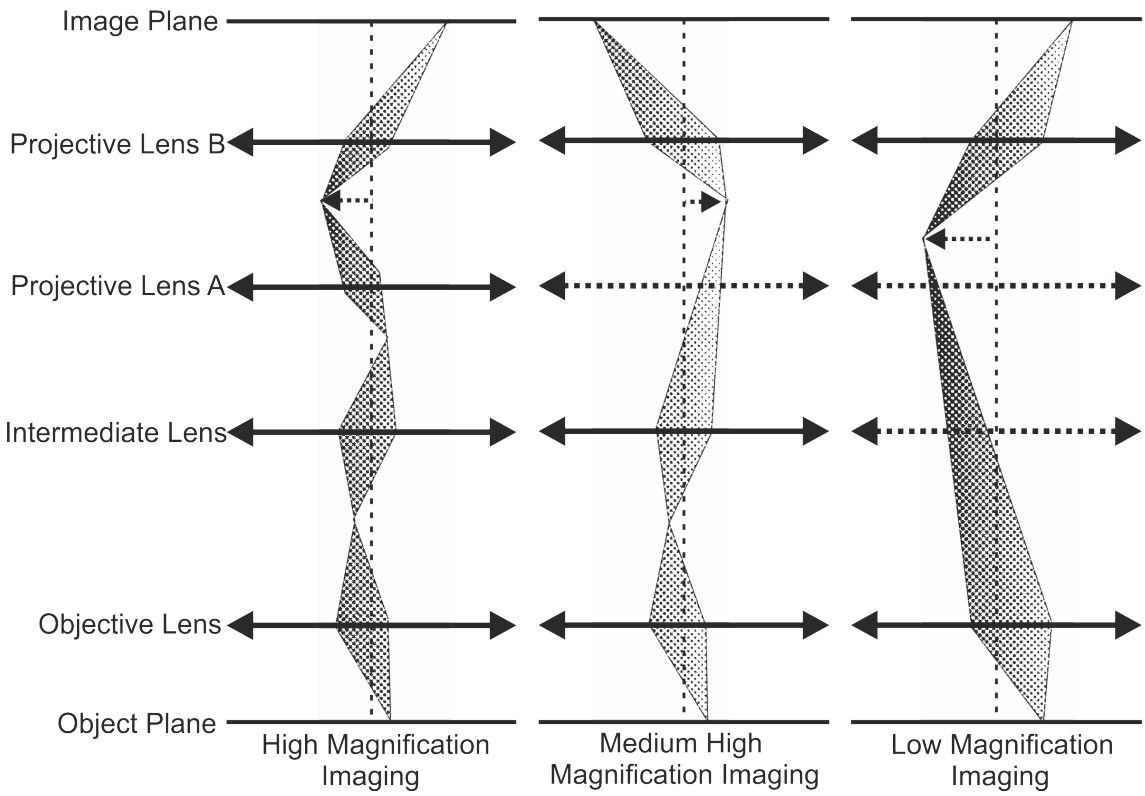

Figure 4.11: The STAIB PEEM-350 is equipped with a series of electrostatic lenses to which different high voltages are applied. Depending on the lenses used, a variety of different imaging modes are available. The high magnification mode has a spacial resolution of up to 100 nm. Redrawn from the STAIB PEEM - 350 V 1.0 manual.

outside of the column, and is typically 10 keV.

As can be seen in Figure 4.11, different imaging modes are available when performing PEEM depending on the spatial resolution required. Each of the lenses used in PEEM are formed of three radially symmetric electrodes. These lenses operate in the so-called "DECEL-ACCEL" mode where the middle electrode is negative relative to the entrance and exit electrodes. Consequently, electrons are decelerated between the first and middle electrodes and accelerated again between the middle and end electrodes.

High magnification mode works when the intermediate lens and projective lens A are near ground potential which results in these two lenses forming a real intermediate image. If the voltage at the middle electrode of the intermediate lens is near ground potential and the voltage at the middle electrode of projective lens A is similar to that of the transfer voltage, then the optics operate in medium high magnification

mode. In this mode, the intermediate lens (but not the projective lens) forms a real intermediate image. Low magnification mode is achieved by setting the voltage of the middle electrode of the intermediate lens and projective lens A near to that of the transfer voltage which results in a virtual intermediate image being formed by the two lenses. During this project only high magnification mode was used which has a reported spatial resolution of up to around 100 nm [182].

Following the projective lenses, electrons are then accelerated again by the transfer voltage towards a microchannel plate (MCP) which forms the image. A MCP is an array of 10^4 - 10^7 miniature electron multipliers aligned parallel to one another [183]. The typical diameter of each channel is around 12 µm with 15 µm centre-to-centre spacing and length to diameter ratios between 40 and 100 [183]. The channel array is typically made of lead glass, treated in such a way so as to optimise the secondary electron emission from each individual channel [183]. The channel array is also made from a semiconducting material such that an external bias can be applied to replenish electrons within each multiplier. The contrast of the image can be improved by applying a higher voltage to the output of the MCP, but this will affect its lifetime.

Electrons with a higher energy will result in a decrease in the detection efficiency of the MCP. For electrons with an energy in the range of 0.2 - 2 keV, the detection efficiency is anywhere between 50 - 85%. Beyond this energy range, the detection efficiency decreases drastically as observed for electrons [183] but also high-energy photons [184]. To improve detector sensitivity, a lens known as Decel is used to decelerate the electrons to an energy level within the high sensitivity range of the MCP. The Decel lens voltage is the potential applied to the front of the MCP with respect to ground, and the difference corresponds to the energy of the electrons impinging on the MCP.

During operation, since a large potential is active in close proximity to the sample, field emission can occur if dust is present on the sample or sample plate. Field emission from dust will result in bursts of pressure which can damage the electron optics and the detector. It is therefore important that before introducing a sample to the chamber, the sample plate is cleaned thoroughly. Then, once introduced to

the chamber, the transfer voltage is increased slowly past 5 kV to ensure that there is no burst in pressure. During sample preparation, the PEEM optics are shielded to avoid exposure to contamination.

4.6 Spin-Polarised Photoemission and Magnetic Circular Dichroism

4.6.1 Introduction

Since UPS is in many ways comparable to MDS and, furthermore, since MDS can be spin polarised to probe the spin-split SDOS, it is desirable to also use UV photons to probe the spin polarisation of a material so that surface and bulk states can be compared. This becomes even more relevant when testing SPMEEM for the first time and confirming whether the spin asymmetry observed is real. For this reason, two different setups, one at York and the other at NIMS have been developed to measure spin polarisation from photoemission. At York, a Mott polarimeter has been added to the analysis chamber and at NIMS, the SPMEEM system is equipped with a UV laser to perform magnetic circular dichroism. Below is a very brief overview of these techniques and for more information on spin-polarised photoemission and Mott detectors the reader is encouraged to look at References [51] and [185–187].

4.6.2 Retarding Potential Mott Polarimeter

In 1929, Nevill Francis Mott proposed the idea that the associated magnetic moment of an electron could be determined through a double scattering experiment [51]. In 1942, Schull *et al.* demonstrated a scattering asymmetry based on Mott's proposal, and with some corrections for instrumental effects, found a value which was in close agreement with initial predictions made by Mott [51, 188]. The principle of Mott scattering starts with the fact that when an electron comes within close proximity of a nucleus, the motion of the electron in the electric field of the nucleus results in a magnetic field in the rest frame of the electron [51]. The interaction of the magnetic moment of the electron with this magnetic field introduces a spin-orbit

term to the scattering potential which results in a spin dependence in the scattering cross-section [51]. Depending on the associated magnetic moment, from the double scattering experiment, spin-up electrons will scatter to the left (L) and spin-down electrons to the right (R) [51]. Therefore, a spin-asymmetry term for an unpolarised source of electrons can be derived, where N is the number of electrons collected at one detector:

$$A(\theta) = \frac{N_L - N_R}{N_L + N_R} \tag{4.9}$$

The spin polarisation $P(\theta)$ of the source of electrons can then be described as a function of the asymmetry:

$$A(\theta) = S_{eff}(\theta)P(\theta) \tag{4.10}$$

S_{eff} is the effective Sherman function which takes into account the effect of multiple scattering events which occur in the target (a metal foil) which reduce the value of the scattering function. The Mott polarimeter used at York is a retarding potential type allowing energy-dependent spin asymmetry to be measured due to fine copper grids at the entrance optics which behave as a bandpass filter [51]. The detector uses a gold target held at 20 kV and four channeltrons placed symmetrically around the vertical axis, two for N_L and two for N_R. The Mott polarimeter can not only be used to measure the spin asymmetry of a magnetised sample from electrons produced through UPS, but also can be used to verify the spin polarisation of the He 2^3S beam.

4.6.3 Ultraviolet Magnetic Circular Dichroism

The origin of magnetic circular dichroism (MCD) arises due to the interplay between the alignment of electron $\left(s = \frac{1}{2}\right)$ and photon ($s = 1$) spins [185]. Consequently, light of each helicity (right-or left-hand circular polarisation) will elicit a different response from electrons in a particular spin-state [185, 187, 189]. Similar to how right- (σ^+) and left-hand (σ^-) polarised light is used to optically pump 2^3S He atoms into magnetic sublevels, σ^+ light will probe spin-up electrons and σ^- light

will probe spin-down electrons. Thus, a spin asymmetry can be measured using ultraviolet or X-ray circularly polarised light. Furthermore, through the application of angle-resolved MCD, the interplay between spin-orbit and exchange interactions can be observed [186]. Particularly in single crystals, the photoelectron wavevector and crystalline axis lead to magneto-dichroic effects in the angular distribution and the magnetisation axis of domains in magnetic materials can therefore be determined [187]. In the SPMEEM system, a UV laser is used to perform MCD on the sample and the observed spin asymmetry reflects both in-plane and out-of-plane components of magnetisation. It should be noted that dichroic effects can also be observed using linearly-polarised light [190].

4.7 Density Functional Theory

Both MDS and UPS are used to probe the density of states (DOS) of a material experimentally. To complement these techniques, it is desirable to model the dispersion relation and DOS of the same material in order to help provide a greater understanding as to the origin of certain states observed experimentally. To analyse the properties of a given system theoretically, the Schrödinger equation must first be solved, however, solving this for any system aside from the hydrogen atom becomes increasingly more difficult with an increasing number of electrons due to the strong Coulomb interaction between each electron pair [191]. Therefore, an alternative approach to solving the Schrödinger equation whilst foregoing solving the wavefunction directly is to instead treat the total energy of a system of electrons and nuclei as a unique functional of the electron density [191]. This approach assumes the variational minimum of the energy to be exactly equivalent to the true ground-state energy and thus band-structure and DOS calculations can be performed for any given system. Multiple different computational codes have been developed for this approach, broadly known as density functional theory (DFT), but the one used in this project is the Cambridge serial total energy package (CASTEP) [192]. For more details on the working of this code the reader is directed to References [191] and [192]. Below is a brief description of the functionals used in this project as well as alternatives to DFT which can be performed using CASTEP.

4.7.1 CASTEP

DFT is based on Bloch's theorem and the Kohn-Sham equations, which treat a system as a periodic array of atoms with a quasi-periodic wavefunction and the ground state energy and charge density are exactly the same as those of non-interacting particles. When analysing a particular system, two properties determine the accuracy of the measured ground state energy: the k-point sampling and the cutoff energy (E_{cut}). The k-point sampling is the number of points with which the system is analysed over reciprocal space. Cutoff energy is a single parameter used to determine the quality of the basis set of plane waves. Increasing either parameter will improve the accuracy of the ground state energy measured [191], however, this also increases the time it takes for a simulation to complete. Furthermore, past a certain E_{cut} or number of k-points, the ground state energy will only vary by a small amount ($< 1 \times 10^{-5}$ eV) potentially decreasing or increasing in value. If the energy does not change significantly as a result of increasing either parameter, then it is not necessary to further increase either the k-point sampling or E_{cut}. To find the ideal values to use, a convergence test should first be performed where a series of single point calculations are run, and at each step, the variation in energy is measured. When the difference in energy is sufficiently small, then that particular k-point sampling or E_{cut} should be used.

In DFT, different exchange correlation functionals can be used to minimise the ground state energy of the system. The local density approximation (LDA) assumes that the exchange correlation energy at some point $\mathbf{r}$ is the same as if every point has the same density. It is a local approximation suitable for many simple systems, for example silicon, but tends to over-bind atoms resulting in shorter, stronger bonds within the lattice. Alternatively, the generalised gradient approximation (GGA) can be used which is a semi-local approach that under-binds atoms and makes bonds longer but which is suitable for modelling surface structures.

An alternative to DFT which can also be performed using the CASTEP code is the Hartree-Fock approach which instead solves the wavefunction using Fermi statistics and treats the effective potential as a non-local average of the Coulomb potential between an electron and all other electrons in the system [191]. Contrary to

DFT, calculations using this approach will over-predict the bandgap of semiconductors/insulators and are more computationally expensive.

A final alternative approach to solving the wavefunction utilises a mixing of DFT and Hartree-Fock to create what is known as a hybrid functional. This has the advantage of predicting correctly the properties of a particular system, such as the bandgap. Yet, a problem faced with this approach is that the hybrid functional is not applicable to any other system except the one it is designed for. Determining the correct mixing is also difficult and simulations are computationally expensive.

Chapter 5

Spin-Polarised Metastable Emission Electron Microscopy

Techniques which are extremely surface sensitive are ideal for observing possible proximity-effect SOC in graphene and other 2D materials. To map the surface spin polarisation of magnetic materials, various different techniques have been developed such as SPLEEM and spin-polarised STM. However, techniques such as SPLEEM, although considered surface sensitive, still probe bulk and subsurface states in addition to top-most surface states. As discussed earlier, an alternative approach is to use spin-polarised metastable helium atoms to probe the spin-split SDOS. Furthermore, in 1994, Harada *et al.* demonstrated that, by combining an emission electron microscope with an intense He 2^3S beam, micrometer scale images of the surface could be observed which show similar image contrast to those generated through photoemission [34]. The name commonly adopted for this technique since this first demonstration is metastable emission electron microscopy (MEEM). Whilst spin-polarised metastable helium atoms have been used as a spectroscopic technique, to date, there has been no attempts to perform the spin-polarised microscopic equivalent (SPMEEM). Challenges faced with SPMEEM include incorporation of an emission electron optical system, spin-polarising the He 2^3S beam and comparing results *in situ* from SPMEEM to a complementary technique, for example, spin-polarised PEEM. The work presented in this chapter shows the first successful measurements using SPMEEM to characterise the domain structure at the surface of a single crystal

of magnetite at room temperature and comparison of these results to those obtained using ultraviolet magnetic circular dichroism (UVMCD). The clean and hydrogen-passivated $Fe_3O_4(001)$ surface are explored, as well as changes in the domain structure as temperatures approach the Verwey transition. Naphthalene monolayers were also grown on magnetite to explore the effect this has on the spin asymmetry at the surface.

5.1 MEEM

There are two significant differences between the images obtained using PEEM when compared to MEEM: (1) the difference between bright and dark regions and (2) the information depth of the signal used to generate the image. Provided that the UV source used in PEEM is of a fixed wavelength, then the observed image contrast from different regions of the surface is primarily dependent on the local workfunction of those regions [189]. In other words, regions with a lower workfunction will yield a greater number of electrons and therefore will appear brighter in the corresponding image whilst regions with a higher workfunction will be, *vice versa*, less intense. A demonstration of the influence of workfunction on the image contrast of the image can be seen in Figure 5.1, where the iron dots are brighter than the SiO_2 substrate in the PEEM image. Comparing the workfunction, ϕ, of these two materials, for iron ϕ ranges from 4.65 - 4.88 eV (depending on the face termination) [193] whilst for SiO_2 ϕ is higher at around 5 eV [194]. Therefore, it can be determined that the bright spots observed in the image are a result of photoemission from these iron dots. At NIMS, a Hg/Xe UV arc-lamp is used which emits a number of different wavelengths of light, with a maximum energy of 5.53 eV or 225 nm [195].

With MEEM, the contrast of the image is dependent instead on the de-excitation mechanism which occurs, with brighter regions being a consequence of AD [34]. Whilst the workfunction of a surface may influence the de-excitation mechanism which takes place, as discussed in Chapter 3, the de-excitation mechanism which occurs is dependent on whether there is an empty state for the 2^3S electron to tunnel into. Since emission of an electron from Auger neutralisation is dependent on the transition of the electron which neutralises the helium ion, the number of

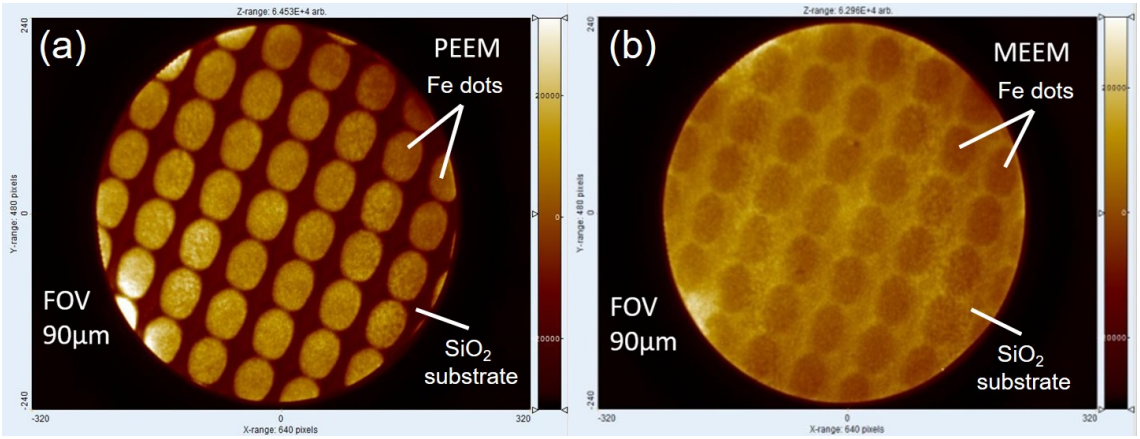

Figure 5.1: (a) PEEM and (b) MEEM images of iron dots (dimensions $\approx 9 \times 12\ \mu m^2$) grown on a SiO_2-capped Si substrate. Contrast in PEEM is mainly dependent on the difference in local surface workfunction whilst with MEEM, contrast is primarily dependent on the different de-excitation mechanisms which occur at the surface. Field-of-view (FOV). Images taken by Dr. Yasushi Yamauchi of the Spin Characterization Group at NIMS.

emitted electrons from RIAN is lower than it is for AD. Therefore, regions of the sample where AD occurs will be brighter than those where RIAN is the dominant de-excitation mechanism. Insulating surfaces tend to more likely to undergo AD, and thus, as expected, the SiO_2/Si substrate in Figure 5.1 is brighter than the iron dots.

One other difference between PEEM and MEEM is the information depth of the signal used to generate the image. The information depth of PEEM is dependent on the kinetic energy of the escaping electron (see Chapter 4). Therefore, whilst the majority of electrons originate from the surface, a small amount of information will be from bulk states as well. On the contrary, He 2^3S atoms always de-excite within a couple of Ångstrom of the surface, meaning that only the top-most surface states are probed. Consequently, any features observed in PEEM but not in MEEM will be a result of underlying surface features, demonstrating the complementary nature of the results obtained from both techniques.

Finally, it is worth noting that topography can also contribute to the image contrast observed via PEEM. Depending on the angle of the photoexcitation source with respect to the plane of the surface (angles less than 20°), the side of a topographical

feature exposed to the photon source will appear brighter contrary to the opposite side which will appear darker and can even give rise to shadow regions on the surface [189]. Surface topography can also lead to interference effects which further provide contrast in PEEM images [189]. Both photoexcitation sources used at NIMS are mounted at an angle of 72° to the surface normal and therefore surface topography is expected to contribute slightly to the observed image contrast. However, when comparing PEEM and MEEM images, as stressed by Harada *et al.* in their first demonstration of MEEM [34], differences and similarities in image contrast in both techniques should be primarily expressed in terms of local surface workfunction (PEEM) and de-excitation mechanism (MEEM) before discussing with respect to surface topography. This is particularly relevant when discussing the differences between image contrast observed in Figure 5.1 (a) and (b) where the iron dots are brighter in PEEM but not in MEEM.

5.2 SPMEEM

To spin polarise the metastable helium beam for SPMEEM, a combination of a sextupole magnet and spin flipper was used, with the degree of spin polarisation confirmed using a Stern-Gerlach analyser (Figure 3.13). Greyscale images were obtained using a cooled CCD PCO.Sensicam combined with the Cam Ware V3.08 software which measured the intensity of each pixel of the microchannel plate over a set period of time and then generated a TIFF image with pixel values (β) ranging from 0 - 255 (max value $= 2^8 - 1$). For a given region, the same acquisition time was used for measuring $I_\uparrow$ ($m_j = +1$ or σ^+ for UVMCD) and $I_\downarrow$ ($m_j = -1$ or σ^-), where I is the intensity of the image. Spin-polarised measurements were performed by changing between $I_\uparrow$ and $I_\downarrow$ typically up to twelve times and the acquisition time was set in order to maximise the intensity but avoid over-saturation of each pixel of the CCD.

The spin asymmetry images presented in this chapter were generated using a bespoke MATLAB code, which converted the greyscale value (pixel value) of each pixel of the TIFF image into a numerical value ranging from 0 - 65535 (class of image, Uint16 ($\beta \times 2^8$, max value $= 2^{16} - 1$))). Spin asymmetry was calculated based on

the definition discussed in Chapter 3 and each measurement (unless specified) was averaged over six pairs of images ($N = 6$):

$$A(\%) = \frac{1}{N} \sum_{N} \left(\frac{I_{\uparrow} - I_{\downarrow}}{I_{\uparrow} + I_{\downarrow}} \times 100 \right) \tag{5.1}$$

A greyscale value of 65535 (white) is a result of 100% $I_{\uparrow}$ with 0 (black) a consequence of 100% $I_{\downarrow}$ emission relative to the quantisation axis of the He 2^3S atoms at the surface. This quantisation axis is defined by applying a weak magnetic field of ≈100 mG at the sample, generated from two different coils wrapped around the chamber, one for in-plane ([100] direction of $Fe_3O_4(001)$ in the plane of the image) and the other for out-of-plane ([001] direction) measurements (see Section 3.8).

5.3 Magnetite (Fe_3O_4)

Fe_3O_4, or magnetite, is a naturally occurring ferrimagnet that is the oldest magnetic material known to mankind. Magnetite is an attractive candidate for spintronic applications due to its large Curie temperature of 858 K and predicted half-metallicity arising due to 100% spin-polarisation of the minority band at the Fermi level [196]. Its half-metallicity makes it an ideal source for the production of spin-polarised currents, yet current devices which incorporate Fe_3O_4 have performed with limited success. This decreased performance is largely a consequence of surface effects [196], resulting in "magnetic deadlayers" [197] and an increased number of antiphase boundaries with decreasing Fe_3O_4 film thickness [198]. Antiphase boundaries are problematic as they are structural defects which act as scattering centres, hindering electron transport across the film and therefore significantly increase the resistivity of a magnetite thin film [198]. Such defects are not ideal in the development of Fe_3O_4 spintronic devices and therefore, techniques such as SPMEEM, which exclusively probe the top-most states at the surface are needed to gain a greater understanding of surface properties such that improvements can be made to magnetite-based spintronic devices. High-quality Fe_3O_4 single crystal surfaces are also relatively easy to prepare meaning that this material is a good candidate for the development of SPMEEM.

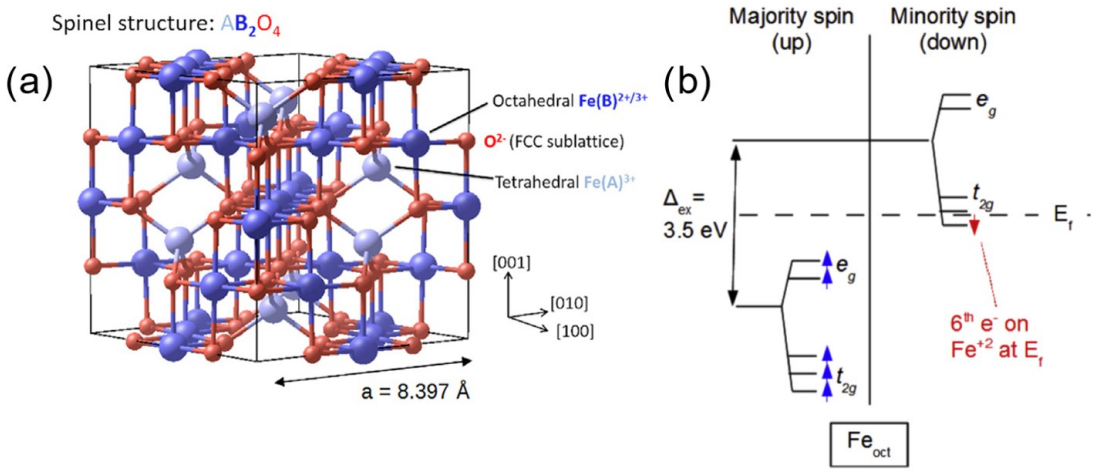

Figure 5.2: (a) Fe_3O_4 has an inverse spinel structure where the Fe^{2+} cations take up 1/2 of the octahedral interstitial sites and the Fe^{3+} cations displaced by these occupy the tetrahedral interstitial sites. (b) The energy level diagram for Fe^{2+} cations. Between the minority and majority spin states there is an exchange splitting of ≈ 3.5 eV whilst the crystal field in magnetite leads to additional splitting in each band. Both figures reproduced from [196].

5.3.1 Background to Fe_3O_4

Magnetite crystallises into an "inverse spinel" structure. A spinel structure is based on a face-centred cubic (FCC) lattice of O^{2-} anions with the chemical formula AB_2O_4. In a spinel structure, A^{2+} cations occupy 1/8 of the tetrahedral interstices and the B^{3+} cations occupy 1/2 of the octahedral interstices. Due to magnetite's large crystal field stabilisation energy, the Fe^{2+} cations take up 1/2 of the octahedral interstitial sites and the Fe^{3+} cations displaced by these occupy the tetrahedral interstitial sites. Hence Fe_3O_4 is described as having an "inverse spinel" structure [196]. A schematic of magnetite's structure can be seen in Figure 5.2 (a). A number of magnetite's unique properties such as its half-metallicity are a result of the coexistence of Fe^{2+} and Fe^{3+} cations in the octahedral sublattice [196].

The clean $Fe_3O_4(001)$ surface has a $\left(\sqrt{2} \times \sqrt{2}\right) R45°$ reconstruction and the current model used to account for this is the subsurface cation vacancy (SCV) model [199, 200]. The $\left(\sqrt{2} \times \sqrt{2}\right) R45°$ periodicity arises from a rearrangement of atoms in the first few sublayers, with two octahedral Fe atoms in the third sublayer being replaced by an interstitial Fe atom with tetrahedral coordination in the second layer [199].

This interstitial Fe atom in the second sublayer blocks the adsorption of metal atoms on the tetragonal bulk continuation sites, and therefore is consistent with STM measurements analysing the absorption of atoms such as Co and Au on the clean surface [200]. Furthermore, the predicted LEED I/V curve theoretically predicted from the SCV model more closely matches the experimentally measured curve when compared to previous models such as the distorted bulk truncation (DBT) model, showing an improvement in the Pendry R-factor [196, 199].

The half-metallicity of bulk magnetite, as first predicted by Néel in his landmark 1948 paper [201, 202], is suggested to originate from the Fe^{2+} cations since the tetrahedral and octahedral Fe^{3+} cations antiferromagnetically couple, therefore cancelling each other out. For the Fe^{2+} cations, there is an exchange splitting of ≈ 3.5 eV between the majority and minority spin-states. These energy levels are further split by the crystal field ($\approx$ 2 eV), leading to three degenerate t_{2g} states and two degenerate e_g states as seen in Figure 5.2 (b) [196, 203]. The octahedral Fe^{2+} cation has six d electrons, five of which occupy the majority band with one electron occupying the minority band at the Fermi level [196]. This results in a predicted net magnetic moment of 4 μ_B (low spin state) which is similar to experimentally measured values [202]. X-ray magnetic circular dichroism (XMCD) measurements have however shown a reduced net magnetic moment of 3.4 μ_B which has been explained to originate from Fe^{3+} cations in the first four sublayers and is consistent with the SCV model instead of the DBT model for the $\left(\sqrt{2} \times \sqrt{2}\right) R45°$ surface reconstruction [199, 204].

Whilst magnetite is predicted to be an ideal half-metallic ferrimagnetic, current devices which have tried to utilise it have seen a reduction in performance [197]. Previous XMCD measurements associate this reduced performance to be due to strain in multiple subsurface layers in the bulk caused by distortions in the surface reconstruction of $Fe_3O_4(001)$ as well as antiphase boundaries [205]. Work by Pratt and Yamauchi *et al.* further confirmed the influence of the surface reconstruction and chemical composition on the Fermi level spin-polarisation by using SPMDS [32]. They observed, contrary to bulk magnetite, a weakly negative Fermi-level spin asymmetry at the (111) face implying a weakly positive spin-polarisation, whilst for the (001) face, a weak positive spin asymmetry was observed [32]. Fur-

thermore, by exposing the different magnetite surfaces to atomic hydrogen, they observed an increase in the Fermi-level spin asymmetry from 5% to 50% on the (001) face. Absorption of other molecular species such as nitric oxide have also been proposed to significantly enhance the spin polarisation at the Fermi level of magnetite and recover its half-metallicity at the surface [206]. Therefore, by exploring the absorption of molecules on the surface of magnetite using SPMEEM, it may be possible to observe an enhancement in the Fermi-level spin polarisation.

Domains at the surface of $Fe_3O_4(001)$ have been reported to be magnetised along the <110> directions [123]. This in-plane magnetisation stems from the balance between magnetocrystalline anisotropy which favours <111> magnetisation directions in the bulk, and surface dipolar forces (or shape anisotropy) which favour in-plane magnetisation directions. This rearrangement in the easy axis at the surface of $Fe_3O_4(001)$ due to the dominance of shape anisotropy has been confirmed by simulations and measurements made using SPLEEM [123].

As magnetite approaches low temperatures, it undergoes a unique phase change known as the Verwey transition, which generally occurs around T_v=125 K [207]. The Verwey transition results in a drop in conductivity of two orders of magnitude, changing magnetite from a semimetal to an insulator [196]. Near this phase change (about 10 K above), the crystal symmetry is distorted transforming from cubic to monoclinic which results in a change to the magnetic bulk easy axis from the <111> directions to the <100> directions [208, 209]. This phase change was first postulated by Verwey to originate from charge at the octahedral iron sublattice sites where electrons are unable to exchange between the Fe^{2+} and Fe^{3+} cations [210]. Current models for electronic transport in magnetite are based on this exchange of electrons between the two iron cations on the octrahedral sites so that prevention of charge hopping between these sites results in a significant increase in the resistivity [211]. Stoichiometry and stress have also been shown to influence the temperature at which the Verwey transition occurs. Natural inclusions of other iron oxides such as hematite within the crystal result in the Verwey transition temperature being reduced by a small amount away from 125 K, and therefore for natural single crystals, the measured T_v is typically lower than it is for synthetic crystals [211]. For a more detailed study of this transition, the reader is encouraged to read the review

by Walz [207].

5.4 Spin Polarisation at the Surface of $Fe_3O_4(001)$

5.4.1 Cleaning the Surface

A natural single crystal of magnetite purchased from Surfacenet GmbH was mounted on an Elmitec sample plate and placed into the FEL of the SPMEEM system. To clean the surface, the $Fe_3O_4(001)$ single crystal was first sputtered with 1 keV Ar^+ ions for 15 minutes (sample current of -0.64 nA) at an argon pressure of 1.3×10^{-7} mbar (the base pressure of the SPMEEM analysis chamber is $<1.3\times10^{-10}$ mbar). The sample was then exposed to oxygen at a pressure of 2.6×10^{-7} mbar whilst e-beam heating the crystal at 623 - 643 K with the temperature measured using an infrared pyrometer and an emissivity of $\varepsilon = 0.65$. After introducing the sample to the main chamber, this cleaning process was performed three times before taking any measurements and also after several days in the vacuum system. This established cleaning procedure is similar to that performed by Parkinson *et al.* who looked at the ratio of Fe(A) to Fe(B) atoms at the surface of the $\left(\sqrt{2} \times \sqrt{2}\right) R45°$ reconstruction [212]. It was not possible to check the surface chemical composition in the emission electron microscopy system (for example using XPS or Auger electron spectroscopy), however, following a single cleaning cycle, the observed contrast (spin asymmetry) was much clearer. This was particularly noticeable after exposing the surface to naphthalene where the contrast was improved significantly following a single cleaning cycle.

5.4.2 The Clean Surface

Following several cycles of argon sputtering and oxygen roasting, the 'clean' surface was examined using SPMEEM with images obtained across a field-of-view (FOV) of 100 µm and 50 µm, examples of which are shown in Figure 5.3 (a) and (d). These were both obtained for a single spin-state ($I_\uparrow$) with the acquisition time increasing from 30 s to 90 s for the smaller FOV images. The outside ring of the image has

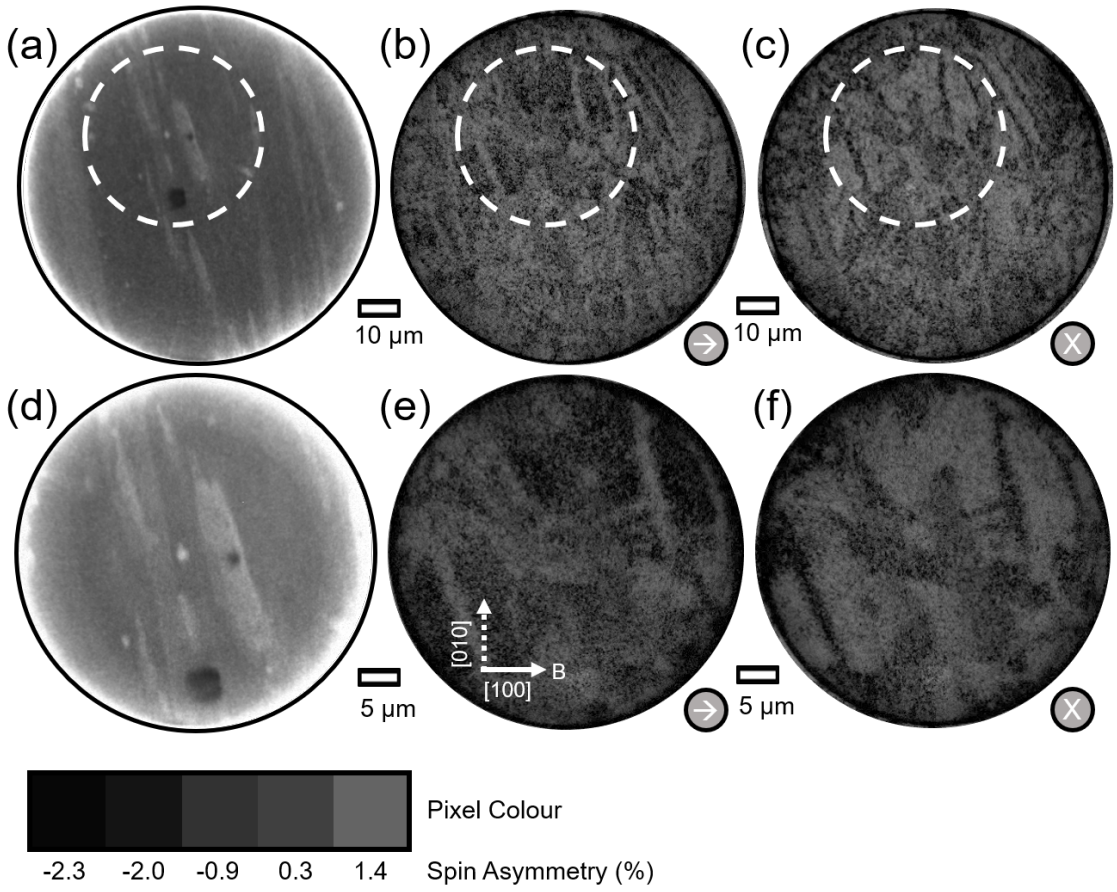

Figure 5.3: (a) A 100 µm diameter raw image ($m_j = +1$, in-plane (IP)) of the surface following three cleaning cycles. (b) In-plane and (c) out-of-plane (OP) spin asymmetry of the 100 µm region. (d) A 50 µm raw image ($m_j = +1$, IP) from the region in (a) highlighted by the white circle. Images (e) and (f) show the IP and OP spin asymmetry for this region, respectively. Below these images is a colour bar which matches pixel colours to corresponding spin asymmetry values (%).

oversaturated as a result of longer acquisition times used to maximise the pixel value of the majority of the image and is a common observance in PEEM and MEEM [189]. This is believed to originate from secondary electrons which accumulate more at the edges of the image maximising the pixel value for this region [189]. Within the 100 and 50 µm diameter images, a series of brighter stripes and dark spots can be seen. Comparing these images to that of PEEM (not presented here) as well as previous LEEM/PEEM images of natural crystals of magnetite, it is probable that these features are a result of scratches and defects [213, 214]. Defects here refer to other iron oxides such as hematite and maghemite which are more prevalent

in natural crystals of Fe_3O_4 [196]. The workfunction of other iron oxides such as hematite, maghemite and $Fe_{1-x}O_x$ vary significantly depending on stoichiometry and face termination, with lower (2.61 eV) [215] and higher (5.7 eV) [216] workfunctions than that of the surface of Fe_3O_4 (5.15 eV) [217]. Therefore, the contrast observed in PEEM will vary as a result of these different workfunctions leading to brighter and darker regions in the image. With MEEM, contrast is mainly dependent on the de-excitation mechanism which takes place. Iron oxides aside from Fe_3O_4 are insulating and therefore the dominant de-excitation channel for metastable helium atoms is most likely AD rather than RIAN. Therefore, other iron oxides present at the surface are more likely to appear brighter in the corresponding image. These features may also be evidence of regions of different surface topography where the brighter features examined in the MEEM image (and PEEM) are a result of raised areas of the surface, whilst the dark spot at the bottom of the 50 µm image (Figure 5.3 (d)), is most likely a consequence of a well. These defects did not change in shape or size when switching between $I_\uparrow$ and $I_\downarrow$ nor when changing the quantisation axis between in-plane (IP) and out-of-plane (OP).

By using Equation 5.1 for six pairs of images, the spin asymmetry was calculated both IP and OP for this 100 µm diameter region. Six pairs of images were found to improve the SNR of the measured spin asymmetry whilst balancing the time needed to acquire the data. As can be seen in Figure 5.3 (b) and (c), a series of domains are observable both IP and OP which span several micrometers, similar to that observed by de la Figuera *et al.* [123]. To further understand a particular set of domains, the FOV was reduced from 100 to 50 µm and the spin asymmetry calculated for the region highlighted by the white circle in Figure 5.3. The domains observed in Figure 5.3 (e) and (f) repeat those evident in the 100 µm images. The majority of the domains observed IP and OP are similar but, significantly, they have opposite image contrast. The alternating image contrast between the 'H'-like domain at the top of the IP and OP images in Figure 5.3 (e) and (f) is consistent with the magnetisation direction rotating out-of-plane and therefore is most likely a domain separated by a Bloch domain wall [189]. Bloch domain walls are where the spins rotate out-of-plane between neighbouring domains. Domains separated by Bloch domain walls dominate the majority of the surface shown in these images except

for the top left-hand section of the IP image where the magnetisation direction appears to change IP but not OP which is consistent with domains separated by Néel domain walls [123]. Néel domain walls are where spins rotate within the plane from one domain to another.

The IP quantisation axis aligns the spins of the metastable helium atom parallel and antiparallel along the [100] direction as shown in the inset of Figure 5.3 (e). By inspecting the domains observed IP with respect to this axis, it can be seen that when moving down the image from top to bottom, the majority of these features appear to move either diagonally from the left of the image to the right or *vice versa* right to left. Therefore, the domains appear to not be oriented along either the <100> or the <010> crystallographic directions but are at angles of 45 - 70° away from either axis. If the angle is 45° away from the <100>/<010> directions, then it can be said that the domains are magnetised along the <110> directions. This is in good agreement with previous work by de la Figuera *et al.* [123] who observed the same magnetisation direction in-plane using SPLEEM. Since the quantisation axis was only applied across the in-plane [100] direction, from the images presented here, it is not possible to derive the exact magnetisation direction along which each domain is orientated. Therefore, a further development to the SPMEEM system would be to add an additional in-plane quantisation axis in the y-transverse direction.

What was also observed via SPMEEM was a significant out-of-plane spin asymmetry as can be seen in Figure 5.3 (c) and (f). Previous measurements using SPLEEM observed an out-of-plane component, but it was found to be only 6% of that observed in-plane [123]. As discussed earlier, the magnetisation direction of the (001) face of Fe_3O_4 arises from the interplay between the magnetocrystalline anisotropy and dipolar forces (shape anisotropy). The latter has been predicted [213] and observed to dominate over the former resulting in the magnetisation direction realigning away from the bulk <111> easy axis, and more into the plane of the surface with a small out-of-plane component, or of "magnetization canting" [123]. By comparing the images shown in Figure 5.3, it is clear that the IP and OP spin asymmetries are of similar magnitude indicating that spin canting at the surface is significantly greater than 6%. Such an observation is a significant finding as it reveals intriguing details of the magnetisation behaviour of a ferrimagnet oxide surface. It is also an early

indication of the benefits afforded by the surface sensitivity of SPMEEM.

A much stronger spin canting than previously observed could possibly be explained by the Dzyaloshinskii-Moriya interaction (DMI) or antisymmetric exchange coupling. DMI is an asymmetric magnetic exchange between magnetic moments which is an effect of spin–orbit coupling combined with broken inversion symmetry [218]. The DMI competes with the Heisenberg exchange interaction that tends to align the moments parallel to each other, resulting in a spin-canting effect which drags the spins back out-of-plane [218]. The DMI in magnetic materials such as Fe_3O_4 originates from the uniaxial surface or Néel-type anisotropy which is a result of reduced symmetry in the atomic environment of surface atoms [219]. If the relative intensity of the out-of-plane and in-plane components can be compared, then this can be used to determine the magnitude of the surface anisotropy constant. The only previous estimation for this value for $Fe_3O_4(001)$ is by Coey *et al.* in 1993, who, using spin-polarised STM, estimated the value to be in the range of $\approx 10^{-3}\mathrm{Jm}^{-2}$. A direct measure of this value would not only help validate the accuracy of various micromagnetic models of the magnetite surface, but it would also help in the design of spintronic devices that incorporate Fe_3O_4. Further details on how SPMEEM results presented in this thesis can be used to yield an estimate for the surface anisotropy constant are given in Section 5.5.

It has been reported that a "lack of good order" of surface atoms will influence the observed spin asymmetry and structure of the domains observed [209]. It was therefore of interest to use SPMEEM to explore whether cleaning the surface via argon sputtering and oxygen roasting would influence the observable spin asymmetry. As can be seen in Figure 5.4 (c) and (d), the IP and OP spin asymmetry and domains observed after a further single cleaning cycle are similar to those observed after the first cleaning cycle (Figure 5.4 (a) and (b)). There are small changes to the domains near the 'H' domain in the top half of the image, but the majority of the observed features have remained relatively unchanged. This observation demonstrates the reproducibility of domain structures at the surface of Fe_3O_4, which, as discussed in more detail in Section 5.7, are likely a result of hematite inclusions [213]. Additionally, as seen particularly in the OP images (Figure 5.4 (b) and (d)), the pixel intensity of the 'H'-like domain and surrounding domains appears brighter follow-

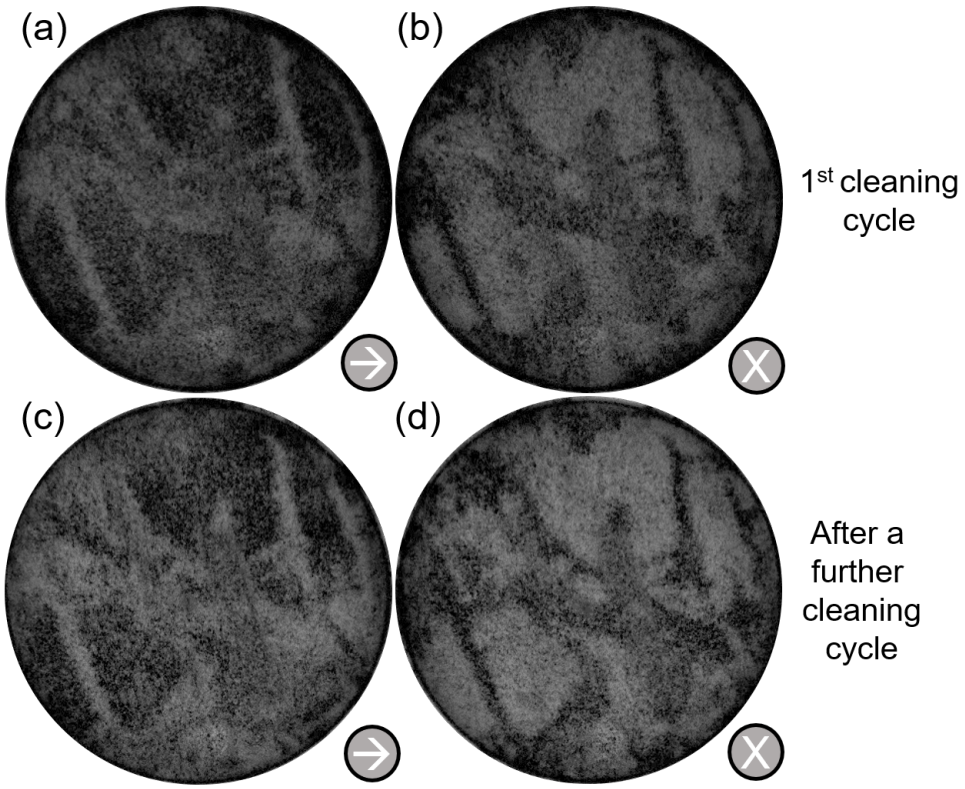

Figure 5.4: The spin asymmetry (a) IP and (b) OP of the same 50 µm region shown in Figure 5.3 (e) and (f). (c) IP and (d) OP of the same region following a further single cleaning cycle.

ing a cleaning cycle. This is an indication of a slight increase in spin asymmetry which is believed to originate from an improved order of atomic environments at the surface [209].

5.4.3 The Hydrogen-Passivated Surface

To passivate the surface with hydrogen, a self-made atomic hydrogen cracker, described in Ref. [32], was used. Hydrogen gas was passed through a 20 W bulb, with 10.3 W used to successfully crack hydrogen based on previous measurements by the Spin Characterization Group in NIMS. To ensure that the majority of the surface was passivated, the $Fe_3O_4(001)$ single crystal was exposed to atomic hydrogen at a pressure of 6.6×10^{-7} mbar for 30 minutes (1201 Langmuir). Following hydrogen passivation, the sample current (compensation current) from exposure to the UV arc-lamp was measured to be -16.2 nA, a large increase from -3 nA mea-

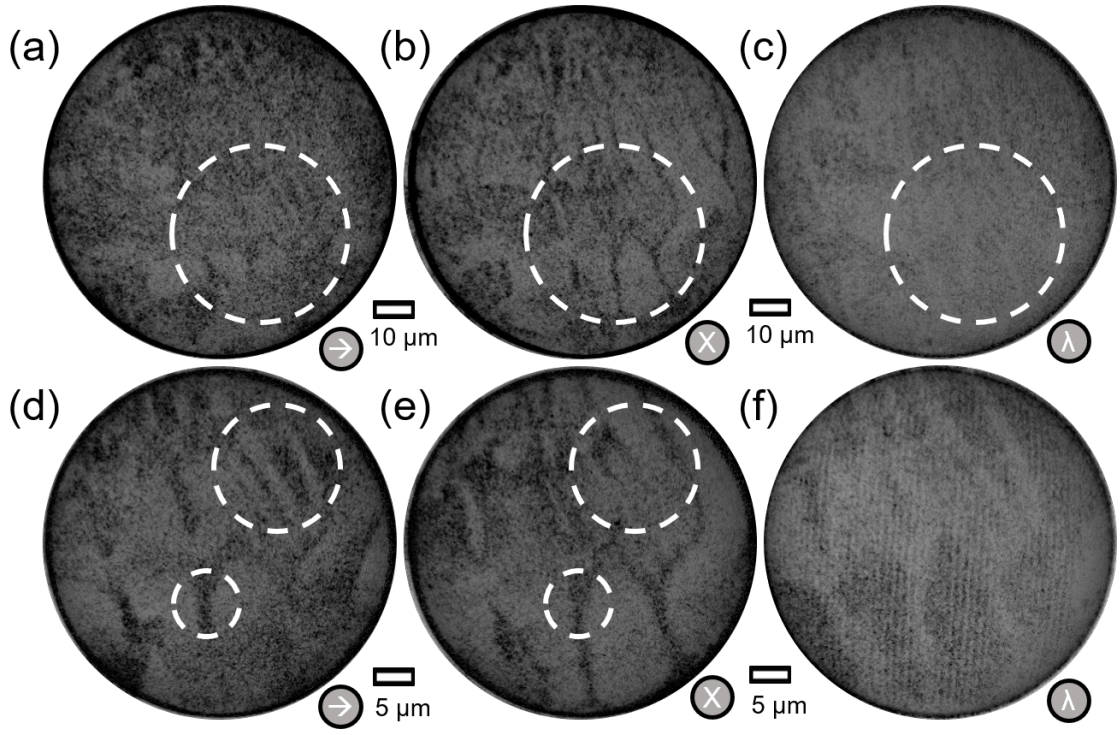

Figure 5.5: Spin asymmetry of a 100 µm diameter region of a hydrogen-passivated $Fe_3O_4(001)$ surface as measured using SPMEEM (a) in-plane and (b) out-of-plane, as well as the UVMCD response (c). The spin asymmetry of the 50 µm section highlighted in (a) - (c) was then observed (d) in-plane and (e) out-of-plane using SPMEEM and compared to the UVMCD response (f).

sured for the clean Fe_3O_4 surface. Furthermore, the sample current from the UV laser following exposure to atomic hydrogen was measured to be -0.8 nA, whilst for the clean surface, the sample current was observed to be 0 nA and no image was seen on the MCP. The workfunction of the clean $Fe_3O_4(001)$ is approximately 5.15 eV [217] which is too large for the UV laser used here ($E = 4.67$ eV) to induce photoemission. Hence, observation of an increase in sample current for both UV excitation sources after the surface is exposed to atomic hydrogen indicates significant passivation as this is known to reduce the workfunction [217]. Therefore, one of the benefits of passivating the surface with atomic hydrogen is that it enables spin asymmetry measurements to be performed using the UV laser. The results measured using UVMCD can then be compared to measurements performed using SPMEEM, enabling the study of the spin polarisation of top-most surface states as well as bulk states. Furthermore, as discussed earlier, absorption of atomic hydrogen

has been measured [32] and predicted [217] to partially recover the half-metallicity of the (001) face of magnetite. It is therefore possible that recovery of half-metallicity at the surface might be accompanied by an increase in the observed image contrast measured by SPMEEM.

As can be seen in Figure 5.5, the spin asymmetry of a 100 µm diameter region of the surface was measured both IP and OP using SPMEEM as well as using UVMCD. A 50 µm section of the same region of the sample was chosen and further spin-polarised measurements performed. From the SPMEEM measurements presented for the clean surface in Figure 5.3 (e) and (f), it appears that large regions of the IP image have a spin asymmetry that is opposite in sign to the corresponding OP image. In other words, a more intense signal from metastable helium atoms in the $m_j = +1$ state was observed when spins were aligned IP for a given region, but when spins were aligned OP, then a greater signal was observed for $m_j = -1$ in the same area. This was not always the case, and the observed spin asymmetry varied significantly across the sample, with regions IP and OP displaying the same contrast in some areas of the sample and opposite contrast in other places, as is seen in Figure 5.5. This is a very interesting observation and will be discussed further below.

The measured IP spin asymmetry (Figure 5.5 (a) and (d)) still revealed the magnetisation direction to be predominantly in the <110> directions. The top-right section of Figure 5.5 (d) (highlighted by a large white circle) shows a series of alternating stripes similar to those due to domains separated by 90° walls (domain walls where spins have rotated by 90° between one domain and another) previously observed using SPLEEM [123]. Since these features are observed only in-plane, this is consistent with the magnetisation direction having rotated IP therefore implying that these domains are most likely separated by Néel domain walls. Comparing the lower section of both the IP and OP images, Figure 5.5 (d) and (e), there is a negative, highlighted by small circle, spin asymmetry (darker) domain around 1-2 µm in width in both quantisation axes. This suggests evidence of a domain separated by a Bloch domain wall, since either side of this dark strip are domains with the opposite magnetisation direction both IP and OP and therefore the magnetisation direction must be rotating out-of-plane between these domains.

Comparing the results obtained from SPMEEM to UVMCD, a similar set of domains can be seen both in the 100 µm and 50 µm images (Figure 5.5 (c) and (f)). The spin asymmetry observed via UVMCD has features comparable to both the IP and OP SPMEEM measurements, but also differs from both in the lower section where the opposite spin asymmetry is observed for the larger domains. The observation of IP and OP features in the UVMCD measurement can be explained by the angle at which the UV laser is aligned with respect to the sample. Since the laser is not aligned parallel/orthogonal to the sample and is instead at an angle of 72°, both IP and OP spin states are probed. With respect to the difference in the spin asymmetry between the SPMEEM and the UVMCD measurements in the lower section of Figure 5.5 (f), this can be explained to be a consequence of Pauli's exclusion principle. The dominant de-excitation mechanism at the surface of magnetite is RIAN and therefore, as discussed in Chapter 3, the measured spin asymmetry is anticorrelated with the Fermi-level spin polarisation. However, for UVMCD, the helicity of circularly polarised light directly corresponds to majority/minority spin states and therefore the measured spin asymmetry will not have this anticorrelation. The origin of the striped features which run diagonally across the entirety of Figure 5.5 (f) are unknown but are believed to be a possible result of noise. These features did not occur in the majority of UVMCD measurements (for example Figure 5.6 (f)) and in this case, are believed to not detract from the overall spin asymmetry of the image.

To further test the reproducibility of domain structures observed using SPMEEM, the clean surface was compared to the hydrogen-passivated surface, shown in Figure 5.6. Comparing the clean surface to the hydrogen-passivated surface it can be seen that, overall, exposing the sample to atomic hydrogen has not resulted in any significant changes to the overall observed contrast both IP and OP as measured by SPMEEM. There are some small changes to certain regions of the surface which are consistent with small defects/changes in atomic order at the surface [209]. The spin asymmetry measured by UVMCD of this region for the H-Fe_3O_4(001) surface shows some significant differences from that measured both IP and OP using SPMEEM. The difference between UVMCD and SPMEEM is most likely a consequence of bulk states that are only being probed by the UV laser.

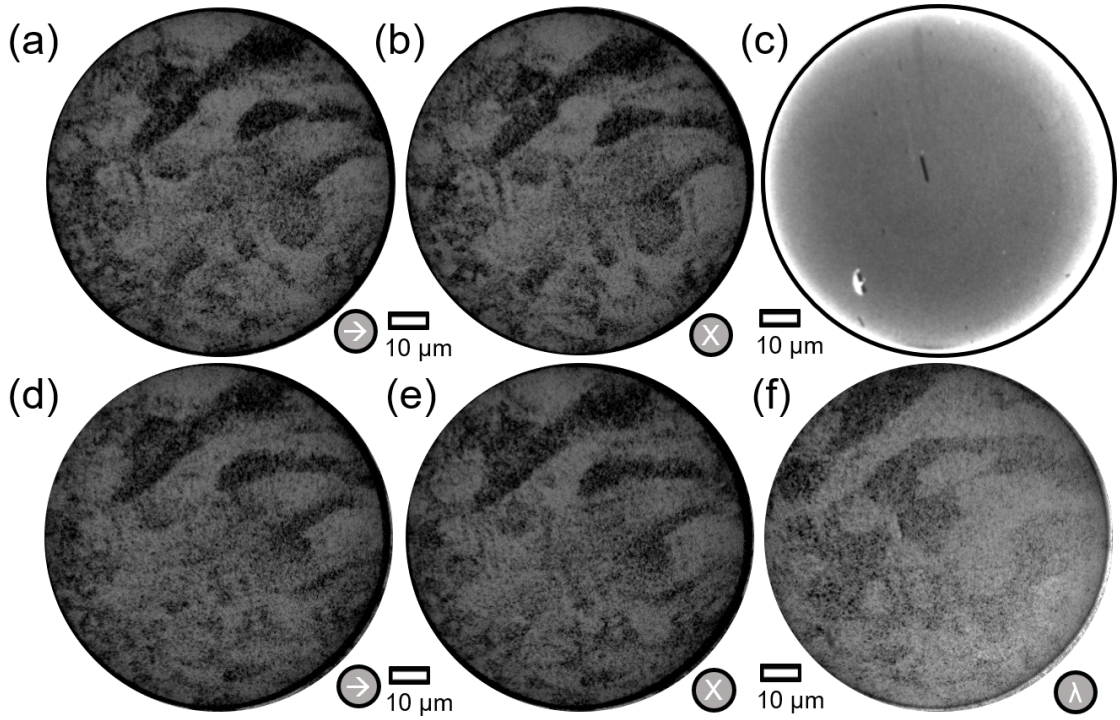

Figure 5.6: SPMEEM spin asymmetry (a) in-plane and (b) out-of-plane for the clean surface. (c) Hg/Xe arc-lamp PEEM image of the same region following exposure to atomic hydrogen. (d) SPMEEM spin asymmetry in-plane and (e) out-of-plane and (f) UVMCD of the hydrogen-passivated surface. All images have a field-of-view of 100 µm.

5.5 Surface Anisotropy Constant

To determine the extent of spin canting observed using SPMEEM, one approach is to compare the pixel intensities of regions observed both in-plane and out-of-plane. By looking at the lower half of the 50 µm images of Figure 5.5 (d) and (e), both IP and OP measurements show a series of alternating magnetisation direction domains where the pixel values for both appear to be very similar. This suggests that spins are most likely oriented so that their direction vector has a similar magnitude along both quantisation axes. By measuring pixel intensities from the same region IP and OP, the ratio of these values can then be used to determine the extent of spin canting at the surface of magnetite. A crude way of representing the resulting values is in a histogram, as shown in Figure 5.7. A number of different ratios are observed but the vast majority of pixels were found to have a ratio ranging between 3:2 to 1:1

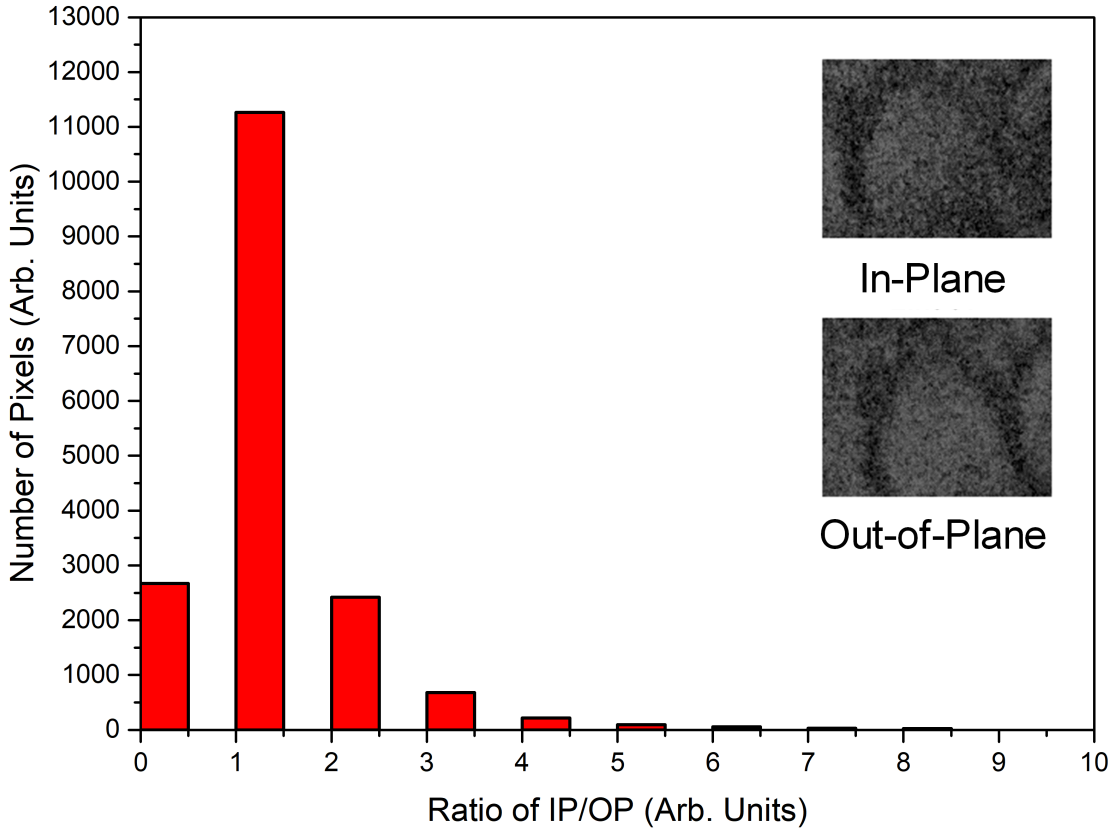

Figure 5.7: Histogram of the number of pixels plotted against the ratio of pixel value IP/OP of the region shown by the inset images, which have dimensions of 150 pixels by 117 pixels.

which implies that the out-of-plane component is anywhere between 66% to 100% of that in-plane, or, in other words, spins are canted between 22.5 - 45° (up to 50%) relative to the surface plane. This is significantly larger than previously measured by de la Figuera *et al.*, who quote a value of only 6% OP spin asymmetry compared to that observed IP [123]. If the spin canting angle can be modelled as a function of the uniaxial surface anisotropy, then a value for this constant can be estimated using SPMEEM.

In order to investigate spin canting at the Fe_3O_4 surface further, micromagnetic simulations were performed by Dr. Richard Evans of the Spin Dynamics research group at the University of York. These calculations were performed using the VAMPIRE code which is a software package for atomistic simulations of magnetic materials [220]. Using an approach similar to that described by de la Figuera *et al.* to model the magnetite surface [213], a $10 \times 10 \times 100$ nm^3 stack of $Fe_3O_4(001)$ was used

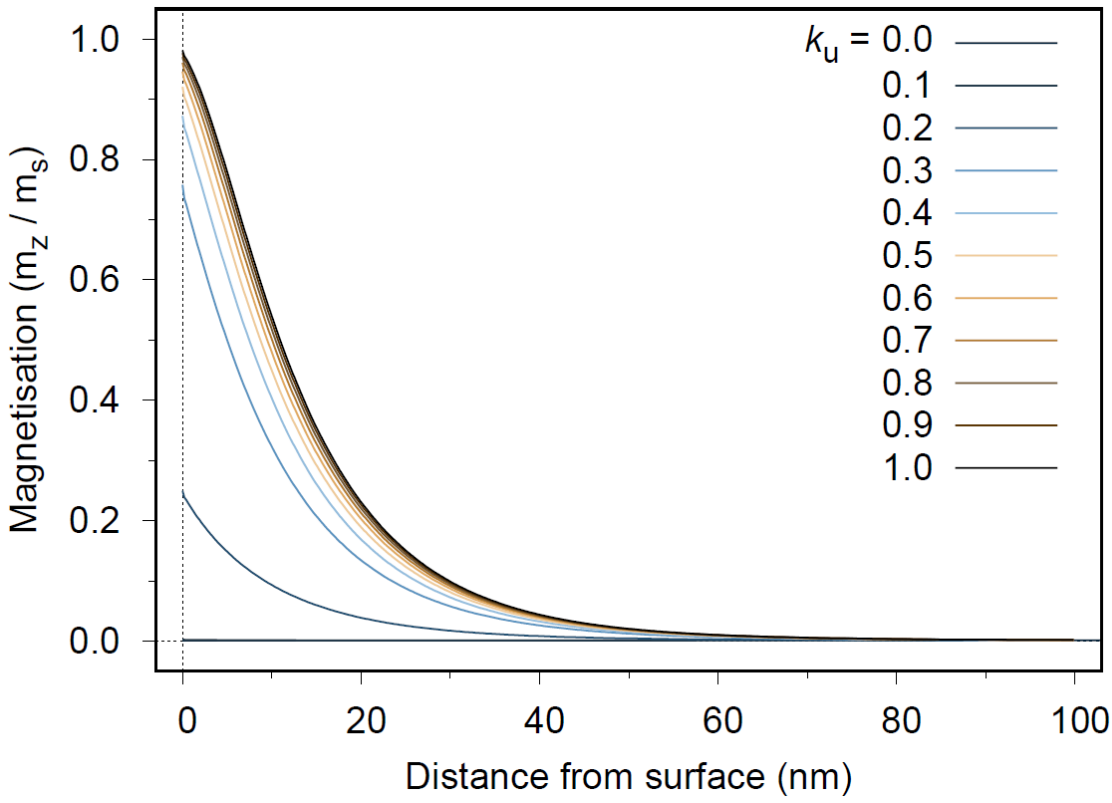

Figure 5.8: Ratio of out-of-plane magnetisation (m_z) and saturation magnetisation (m_s) as a function of distance from an $Fe_3O_4(001)$ surface as a result of different uniaxial surface anisotropy constants (k_u) in units of 10×10^{-3} Jm^{-2}. Calculations performed by Dr. Richard Evans.

to calculate the ratio of out-of-plane magnetisation (m_z) and saturation magnetisation (m_s) as a function of distance from the surface. Using different uniaxial surface anisotropy constants resulted in the ratio varying significantly between 0% to 100% out-of-plane spin polarisation. The degree of spin canting when the uniaxial surface anisotropy constant (k_u) is equal to 0 is nearly 0% whilst for $k_u \geq 3 \times 10^{-3}$ Jm^{-2}, the spin canting ranges between 84 - 100%.

Since the spin canting is predicted to be $\approx 50\%$ from the SPMEEM measurements presented above, based on the results shown in Figure 5.8, the uniaxial surface anisotropy constant can be predicted to be between 1 - $2{\times}10^{-3}$ Jm^{-2}. As the level of spin canting varies significantly within this range further simulations are required to improve the precision of the value for the uniaxial surface anisotropy constant of magnetite. However, this work provides a more accurate value than that reported by Coey *et al.* who suggest this value to be within the larger range of $\approx \times 10^{-3}$ Jm^{-2}.

Importantly, the results presented here demonstrate the surface sensitivity of SPMEEM and the significant influence properties such as the uniaxial surface anisotropy have on the orientation of spins at the surface of magnetic materials. SPMEEM shows spin canting at the surface to be stronger than that which has been previously reported and, by supporting this data with micromagnetic simulations, has been used to predict a value for k_u. In fact, prediction of k_u is crucial when discussing Fe_3O_4 nanoparticles, where for small nanoparticles, the surface anisotropy is comparable to that of the bulk magnetocrystalline anisotropy [221]. By estimating the surface anisotropy constant, SPMEEM could be used to provide further insight into the spin dynamics of magnetic nanoparticles, an area of physics where a huge amount of time and research has been invested to utilise materials such as Fe_3O_4 for a variety of different applications including healthcare and the environment [221].

5.6 Naphthalene on $Fe_3O_4(001)$

Naphthalene is a polycyclic aromatic hydrocarbon consisting of two carbon rings with the chemical formula $C_{10}H_8$. A schematic of this molecule can be seen in Figure 5.9. Naphthalene is commonly used to protect clothing from moths in 'mothballs'. Recently, the molecule has attracted interest as a precursor in the CVD growth of graphene with a flat lying down geometry preferred for both the Ni(111) and Pt(111) surfaces [109]. Additionally, naphthalene has been used on nickel to reduce the surface workfunction [109], and, like other organic molecules, is of interest for its interaction with magnetic materials for applications in spinterface engineering [8]. Since naphthalene is reported to reduce the surface workfunction of nickel, it was similarly believed that it may reduce the workfunction of magnetite, and so to further compare results obtained from SPMEEM to UVMCD, the same single crystal of $Fe_3O_4(001)$ was exposed to different coverages of naphthalene. Furthermore, since proximity-effect SOC has been observed in graphene on magnetite [58], it is possible that naphthalene could be used to grow graphene on magnetite such that SOC effects are observed using SPMEEM. Currently, it appears that this is the only work exploring the absorption of naphthalene on a natural single crystal of magnetite. Some work involving catalysis of organic molecules including naphthalene

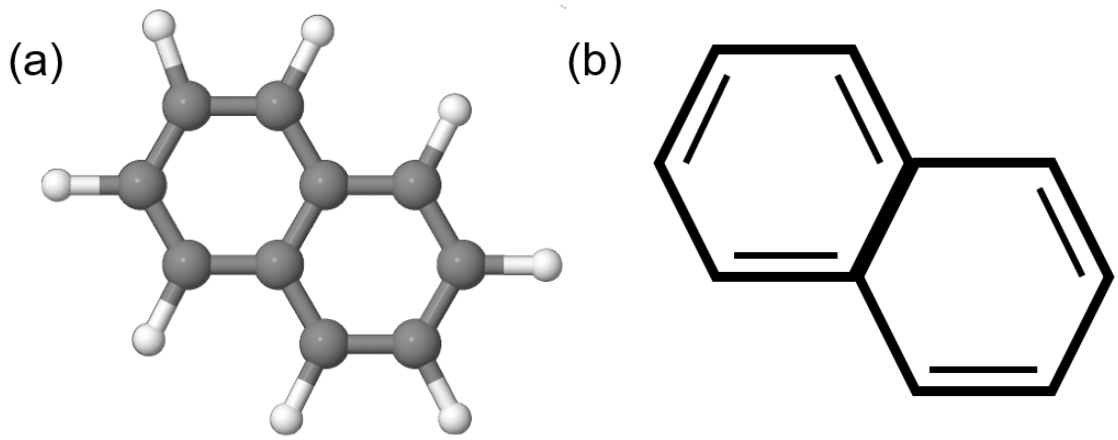

Figure 5.9: (a) Naphthalene consists of ten carbon atoms and eight hydrogen atoms with a resonance structure between the two carbon rings, as shown in (b).

using Fe_3O_4 nanoparticles has been performed for which the reader is encouraged to look at References [222–224].

Crystals of naphthalene (98% purity) were purchased from Junsei Chemical Co. Ltd. These were placed into a blanked-off conflat T-section (flange size CF25) connected to a needle valve. Due to the high vapour pressure of naphthalene at room temperature [225], the T-section was cooled using an ice bath. This T-section was then pumped out using a rotary pump, flushed with argon gas and pumped again in order to reduce the overall residual gas present therefore ensuring a high purity of naphthalene. Originally, the naphthalene source was placed on the FEL of the SPMEEM system, the same chamber as used for hydrogen exposure. However, this did not seem to influence the response from SPMEEM and it was believed that the sample was too far away for successful adsorption of naphthalene on the surface. All subsequent exposures to naphthalene were therefore performed using a needle valve attached to the main chamber. Furthermore, based on multiple measurements, it was found that naphthalene did not adsorb onto the surface at any temperature above 173 K. This was particularly evident after exposing the single crystal of magnetite to 25 L, where, following a series of measurements and then allowing the sample to warm towards room temperature, the pressure was observed to rise rapidly to 1.3×10^{-7} mbar from 1.3×10^{-10} mbar at approximately 173 K. All subsequent exposures to naphthalene took place at temperatures of 153 K or lower. The sample stage was cooled by pumping LN_2 into the internal reservoir of

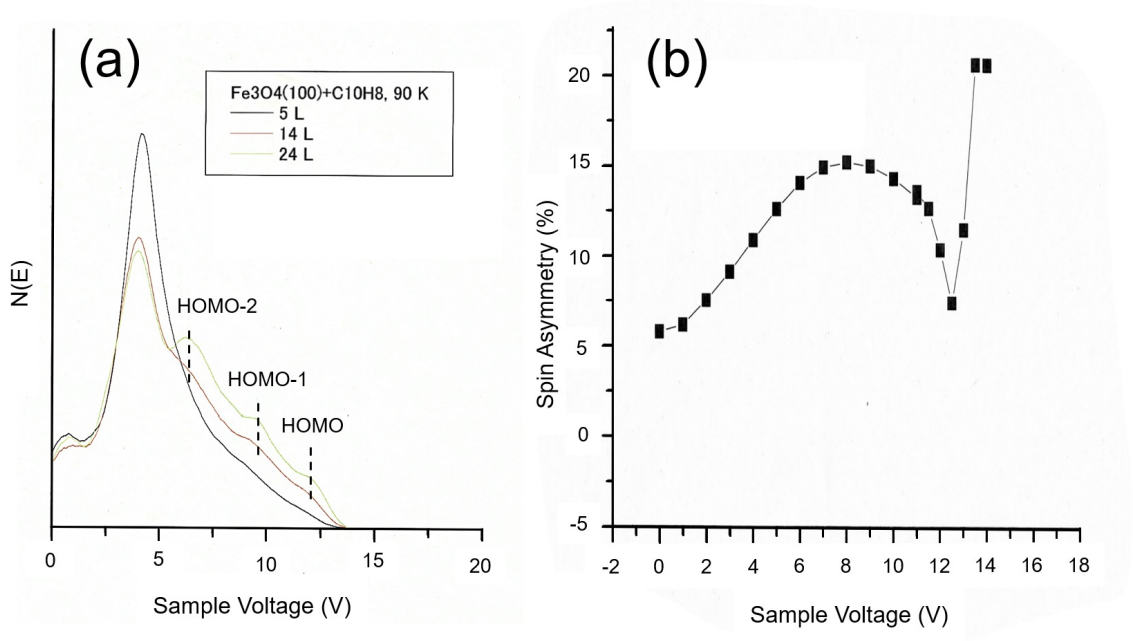

Figure 5.10: (a) SPMDS spectra from an $Fe_3O_4(001)$ single crystal exposed to increasing amounts of naphthalene. By 24 L, a multilayer of naphthalene has formed indicated by the strong presence of molecular orbitals near the cutoff point. (b) At around 5 L exposure to naphthalene, spin asymmetry at the Fermi level (14.5 V) is enhanced by nearly 25% compared to the clean surface.

the SPMEEM manipulator with temperature measured using a chromel and alumel K-type thermocouple. Measurements for SPMDS were performed in a different system where the naphthalene source was further away from the sample which consequently resulted in a slight difference between these results and those obtained using SPMEEM in terms of the quoted exposures.

SPMDS measurements presented in Figure 5.10 were performed by Dr. Mitsunori Kurahashi at NIMS in the high-field spectroscopy system (for more information see Ref. [130]). As seen in Figure 5.10 (a), exposing magnetite to increasing amounts of naphthalene resulted in the observation of molecular orbitals at the following peak positions relative to the Fermi level: 2 eV (highest occupied molecular orbital (HOMO)), 4.4 eV (HOMO-1) and 7.6 eV (HOMO-2). These peak positions are consistent with previous photoemission spectra of naphthalene [226, 227] and have been predicted to correspond to the following molecular states of the polycyclic rings: a_u-π_5 (HOMO), b_{2g}-π_3 (HOMO-1) and b_{3u}-π_{3u} (HOMO-2) [228]. The observed states

are similar to those of naphthacene suggesting that the measured spectrum is of multilayer naphthalene or a similar aromatic molecule [117]. At 5 L, these molecular states are present but weak possibly indicating sub-monolayer coverage [157].

Exposing the $Fe_3O_4(001)$ single crystal to 5 L of naphthalene was accompanied by an increase in the Fermi-level spin asymmetry up to nearly 25% (Figure 5.10 (b)) from a value of 5% for the clean surface based on previous measurements by the Spin Characterization Group [32]. Long exposures to naphthalene were found to result in a decrease in the spin asymmetry implying that by 24 L, multilayer coverage had been achieved. The observation of an increase in the spin asymmetry at 5 L is believed to be an indication of spin-polarised charge transfer between the magnetite surface and the naphthalene, as discussed in further detail below.

With SPMDS showing a clear increase in spin asymmetry upon naphthalene adsorption, it was expected that a similar change would be visible using SPMEEM. To investigate this, following a cleaning cycle, the $Fe_3O_4(001)$ single crystal was exposed to different amounts of naphthalene. The sample cleaning procedure followed the same approach as before, with argon sputtering at 1 keV in a pressure of 1.3×10^{-7} mbar for 15 minutes, and then annealing in oxygen for 40 minutes at 623 K with a pressure of 2.6×10^{-7} mbar. It was found that exposing the single crystal of magnetite to 1 L of naphthalene resulted in a large increase in the measured spin asymmetry to the extent that image contrast was visible in a single raw image as seen in Figure 5.11 (a). The features highlighted by the white circles are a result of defects at the surface. However, the areas labelled (i) and (ii) appear to be domains which were found to not be observable in single images for the clean surface. This indicates that the spin asymmetry at the surface has been enhanced by exposing the Fe_3O_4 to naphthalene. By measuring the spin asymmetry over six pairs of images, as shown in Figure 5.11 (b), these domains become much more apparent.

The origin of this increased spin asymmetry is believed to be a result of a combination of charge transfer between the Fe_3O_4 surface and the naphthalene and increased Auger de-excitation (AD) occurring at the surface, similar to copper phthalocyanine on magnetite [229]. Organic layers are more likely to undergo the one step de-excitation mechanism of AD, which results in a greater number of electrons

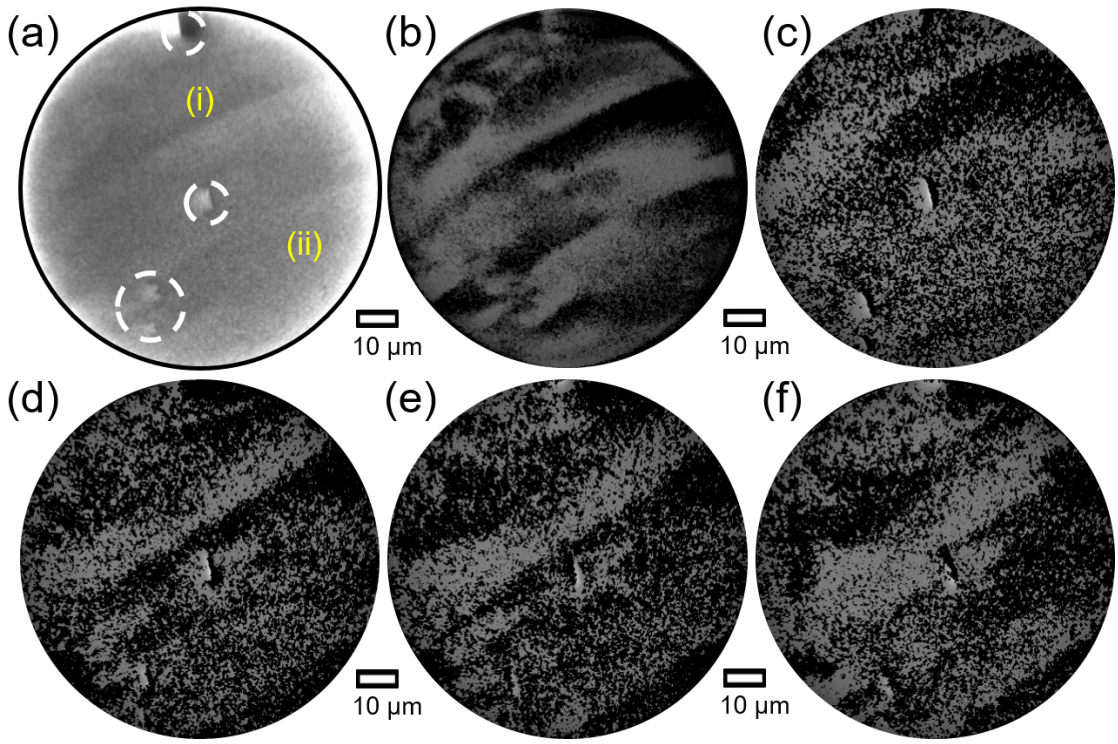

Figure 5.11: Spin asymmetry out-of-plane 100 µm FOV of $Fe_3O_4(001)$ post cleaning and following a 1 Langmuir exposure of naphthalene. (a) A single raw image with $m_j = -1$. (b) Spin asymmetry averaged over six pairs of images. (c) - (f) Spin asymmetry at temperatures of 138 K, 143 K, 145 K, and 148 K respectively showing a noticeable change in the size and shape of the domain structures observed. Due to the rate of temperature change, the spin-asymmetry plots are produced from a single pair of images.

being emitted from the surface of the sample compared to RIAN [34]. AD occurs at the surface of organic films as a consequence of the fact that since molecular crystals are held together by van der Waals forces, the electronic structure of the individual molecules in the solid phase is essentially no different from that of molecules in the vapour phase and therefore metastable atoms de-excite at the surface through Penning ionisation [117]. Since an increase in the sample current from ≈ -2 to ≈ -3 nA was measured from the metastable beam being incident on the surface, this is consistent with AD being the dominant de-excitation mechanism instead of RIAN. Additionally, as discussed in Chapter 3, if the surface undergoes AD, then the measured spin asymmetry will be non-convoluted compared to Auger neutralisation and therefore the measured value will be larger than that for a surface where

the dominant de-excitation mechanism is RIAN. Comparing the spin asymmetry measurement to the SPMDS spectra, the HOMO peak from the a_u-π_5 orbital in naphthalene overlaps with the point where the spin asymmetry starts to increase ($\approx$13 V) towards the Fermi level (14.5 V). Similar to copper phthalocyanine on magnetite [229], it is believed that charge transfer between the Fe_3O_4(001) surface and the naphthalene molecules is resulting in an induced negative spin polarisation in the HOMOs leading to an enhancement of the measured spin asymmetry. It would be of interest to further study this system using UVMCD as well as model the interaction between naphthalene and the surface. However, it was observed that whilst the sample current due to the Hg/Xe arc-lamp had increased by 4 nA from a 1 L exposure of naphthalene, for the UV laser, the sample current still remained at 0 nA, the same as that observed for the clean surface. This would suggest that the surface workfunction had decreased slightly, but not less than 4.67 eV since no photoemission was observed via UVMCD. Therefore to measure a response via UVMCD for this surface, the energy of the laser light used would need to be increased.

Exposure to smaller or greater coverages of naphthalene (less than or more than 1 L) resulted in either a weaker spin asymmetry being observed or no contrast at all. As seen in Figure 5.12, 0.5 L and 2 L both show a weaker spin asymmetry compared to Figure 5.11 (b). At 0.5 L, it is believed that only a submonolayer of naphthalene has formed so that the spin asymmetry has only slightly increased compared to the clean surface. At 2 L, it is possible that multilayer naphthalene has started to form on the surface and therefore, similarly, the spin asymmetry observed using SPMEEM is less than it is for 1 L exposure. By 5 L, the measured spin asymmetry is significantly weaker which is consistent with multilayer formation. According to Yazdi *et al.*, it takes around 3.5 L of naphthalene to form a "saturated monolayer" at room temperature on the Ni(111) surface [109]. Therefore, 5 L exposure is consistent with multilayer formation occurring and hence is most likely the reason for observation of a weaker spin asymmetry. However, since contrast is still observable, it would imply that the coverage is still not multilayer across the entire sample. At 25 L, no spin asymmetry is observable which is consistent with a multilayer coverage of naphthalene across the entire surface. This is also seen for similar coverages in the corresponding MDS spectrum, with clearly defined molecular orbitals and no

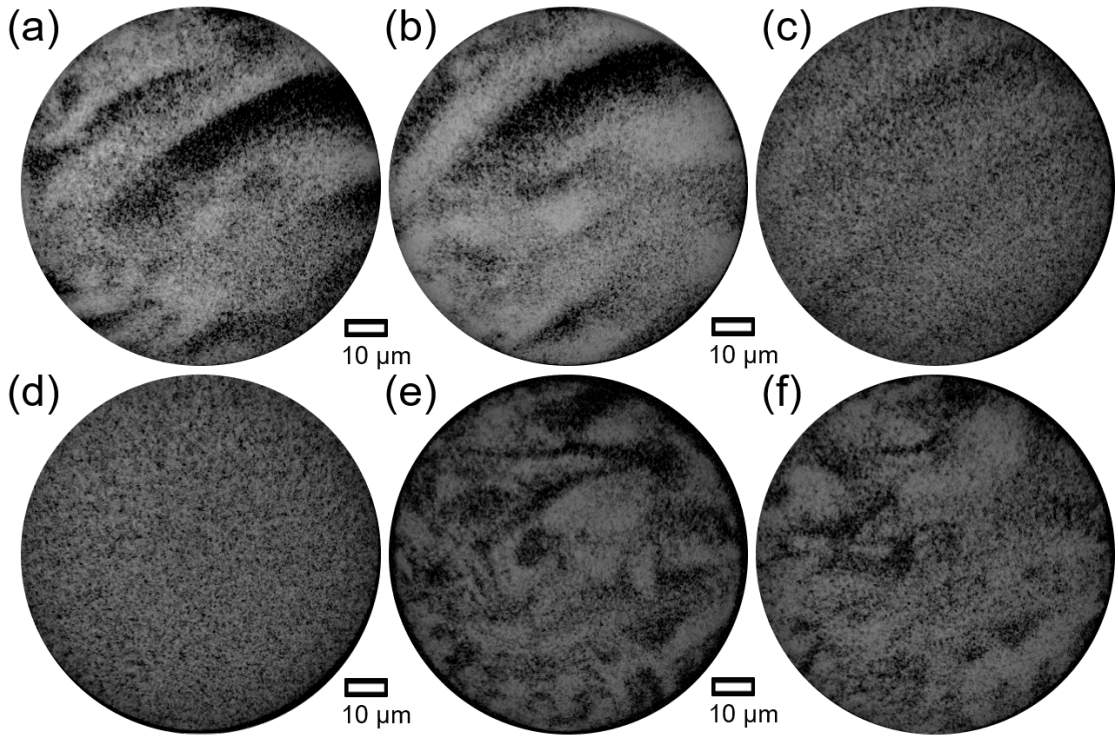

Figure 5.12: The influence of different coverages of naphthalene on the spin asymmetry at the surface of $Fe_3O_4(001)$. (a) - (d) Out-of-plane spin asymmetry of a 100 µm diameter region at approximately 138 K following (a) 0.5 L, (b) 2 L, (c) 5 L and (d) 25 L exposure to naphthalene. (e) Room temperature spin asymmetry of the clean $Fe_3O_4(001)$ surface and (f) following a 25 L exposure to naphthalene at 143 K and subsequent warming to room temperature.

observation of states intrinsic to the clean $Fe_3O_4(001)$ surface after 24 L. Furthermore, the sample current due to the He 2^3S beam increased from -2 nA for the clean surface to -6 nA following an exposure of 25 L of naphthalene consistent with multilayer formation and AD being the dominant de-excitation mechanism. After 25 L exposure, the surface was allowed to return to room temperature after which contrast at the surface was again observable (Figure 5.12 (f)), providing further evidence that the majority of naphthalene desorbs from the surface at temperatures above 173 K. The sharpness of the contrast and the appearance of the domains have significantly changed compared to the clean surface (Figure 5.12 (e)). This is likely due to residual carbon changing the chemical composition at the surface of the $Fe_3O_4(001)$ sample [209].

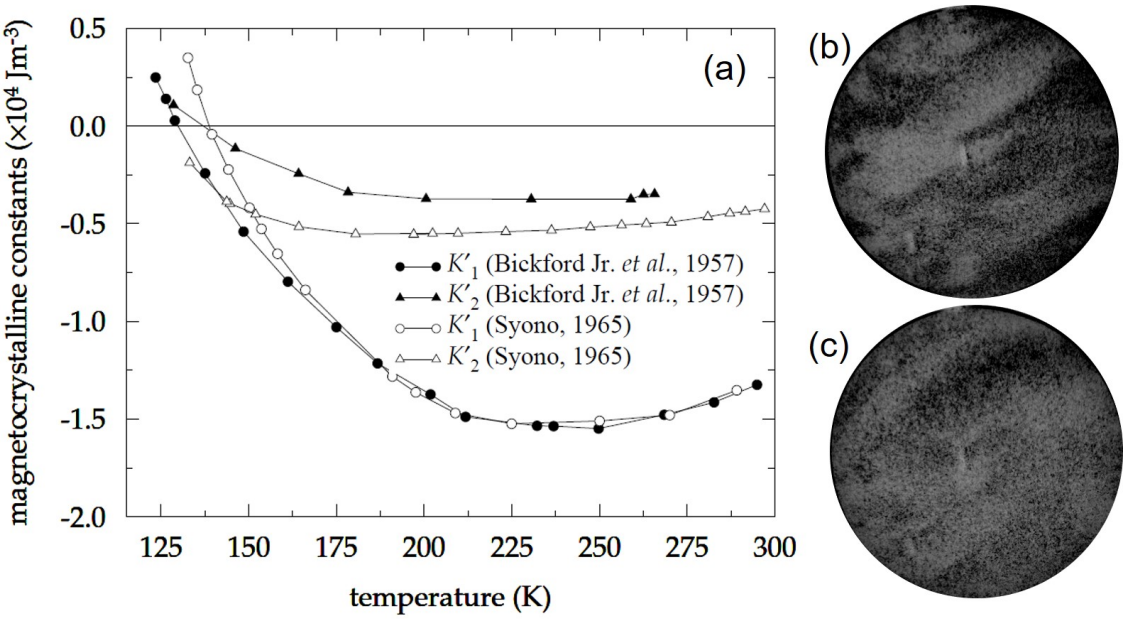

Figure 5.13: The first-and second-order magnetocrystalline anisotropy constants as a function of temperature measured by two different research groups. (b) OP spin asymmetry (FOV = 100 µm) of the hydrogen-passivated $Fe_3O_4(001)$ surface at 148 K and (c) 133 K. Figure (a) reproduced from [211].

One other observation made during experiments involving naphthalene was observation of spin reorientation as the sample transitioned from 138 K to 151 K. As will be discussed below, as the sample approaches the Verwey transition temperature, there is a change in crystal structure reflected by a change in magnetisation direction. This was seen clearly after 1 L exposure to naphthalene (Figure 5.11), where a reorientation of spins was observed both IP and OP.

5.7 Spin Reorientation Near the Verwey Transition

Figure 5.13 (a) shows that as the sample approaches to within 10 K of the Verwey transition, the first-order magnetocrystalline anisotropy constant changes sign [211]. The cubic magnetocrystalline anisotropy energy according to Kittel is expressed as "$E_k^c = K_1(\alpha_1^2\alpha_2^2 + \alpha_2^2\alpha_3^2 + \alpha_3^2\alpha_1^2) + K_2\alpha_1^2\alpha_2^2\alpha_3^2 + ...$", where α_i are the direction cosines associated with the different magnetic easy axes and K_1 and K_2 are the first-

and second-order magnetocrystalline anisotropy constants [146, 211]. Additionally, the cubic first-order magnetocrystalline anisotropy constant according to Aragon *et al.*, is expressed as "$K_1 = 4(F[110] - F[100]))$", where $F[110]$ and $F[100]$ are the Helmholtz potentials associated with certain crystallographic directions [230]. Since the crystal symmetry in Fe_3O_4 changes from cubic to monoclinic near the Verwey transition temperature, this results in a change in the direction cosines and Helmholtz potentials associated with the magnetocrystalline anisotropy energy and first-and second-order constants. Therefore, this leads to a change in sign of the first-and second-order magnetocrystalline anisotropy constants and a reorientation of spins at the surface and a change in magnetisation direction from <110> to <100>. The reorientation of spins is a smooth transition with temperature rather than a sudden change and occurs as a two-stage process of: (1) nucleation of <100> domains and (2) reorientation of other spins towards this axis [209]. This reorientation of spins has been observed using SPLEEM [209] as well as using unpolarised UV He I α photons [214]. With the surface sensitivity of SPMEEM and the discovery using this technique of significant spin canting at the clean $Fe_3O_4(001)$ surface, it is interesting as to what happens to the top-most surface spins through this transition.

Comparing the domain structures observed for the hydrogen-passivated $Fe_3O_4(001)$ surface at room temperature (Figure 5.5) to those at 148 K and 133 K (Figure 5.13 (b) and (c)), it can be seen that there is a clear change in the shape and size of the domains observed OP. At room temperature, the domains observed are small, and when moving down the image from top to bottom, appear to move diagonally from the left of the image to the right. However, at 148 K and 133 K, these small domains have been replaced by much larger µm features which span across almost the entire 100 µm diameter image. When moving down the image from top to bottom for the OP image at 133 K (Figure 5.13 (c)), the domains appear to span more horizontally across the image contrary to that observed at room temperature. Furthermore, Figure 5.13 (b) and (c) show that between 148 K and 133 K, there is a clear change in the shape and structure of the domains observed. This evolution in the shape is more clearly reflected in the measured spin asymmetry for a set of single pair images following 1 L exposure to naphthalene (Figure 5.11), where as the sample is cooled, smaller domains observed at the right-hand side of the image are

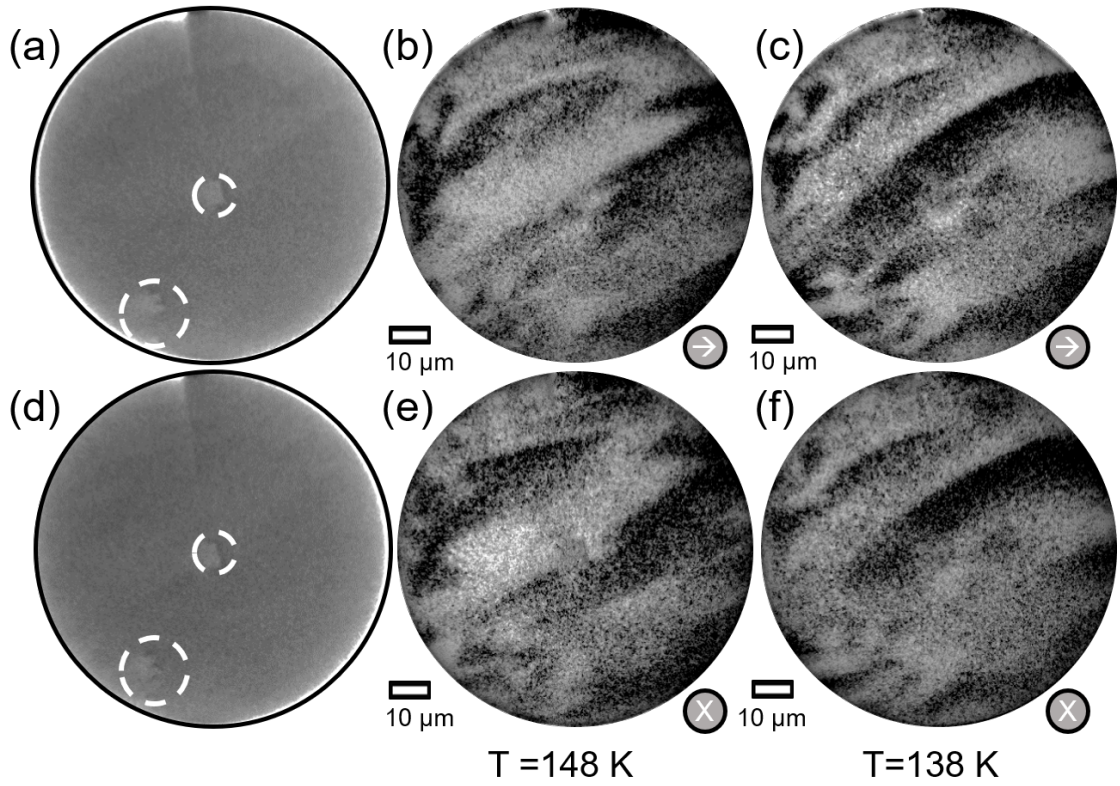

Figure 5.14: (a) Single raw images of $I_{\uparrow}$ IP and (d) OP from a 100 µm diameter region after exposure to 1 L of naphthalene (image contrast highlighted by the white circles is due to defects at the surface). (b) and (c) show the IP spin asymmetry at 148 K and 133 K and (e) and (f) show the corresponding OP images.

replaced by much broader domain structures. Notably, at temperatures lower than 143 K (Figure 5.11 (d)), there is a significant change in the shape and size of the observed domains suggesting a transition temperature around this value.

This change in domain structure was not only observed OP but also IP as shown in Figure 5.14. The measured spin asymmetry was observed for the same 100 µm diameter region where a similar set of domains are seen for both quantisation axes at 148 K and 138 K. However, comparing this to room temperature measurements (Figure 5.3 and Figure 5.5), the domains observed IP and OP vary quite significantly in shape and size. Therefore, SPMEEM shows that as temperature is decreased, the shape and size of the domains change both IP as well as OP, where a similar spin asymmetry is observed in both quantisation axes at low temperatures. The broadness of the domains at 138 K and the transition in shape and size at temperatures particularly around 143 K is consistent with that previously reported by de

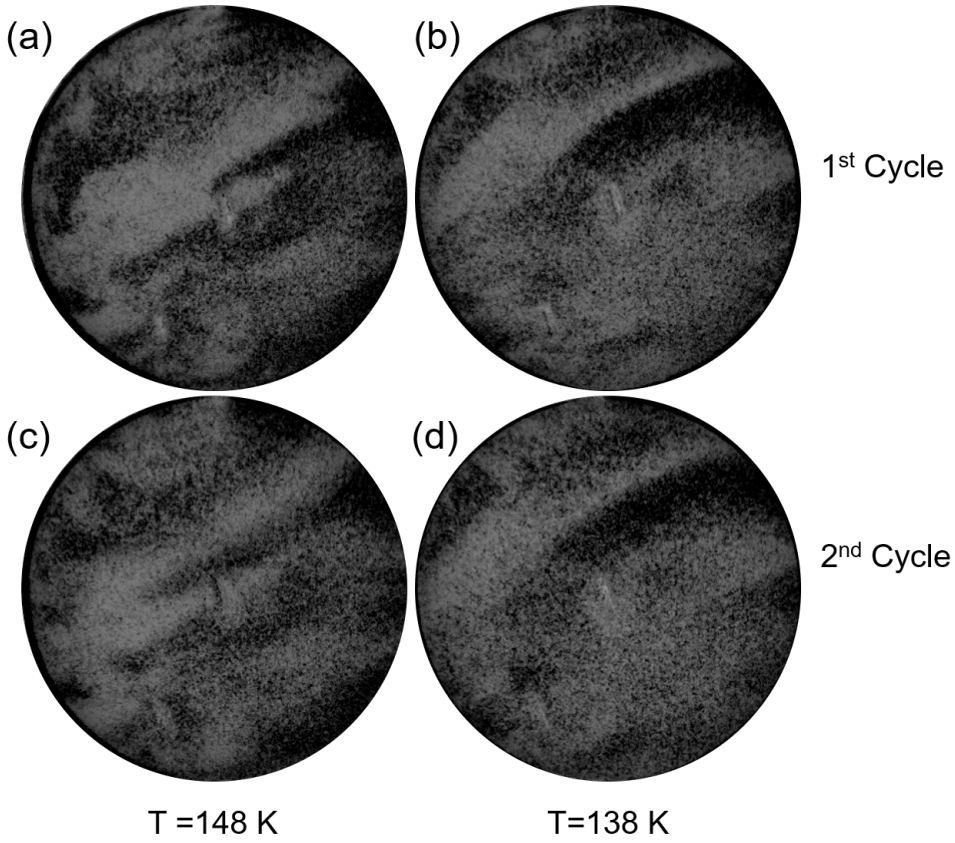

Figure 5.15: 100 µm FOV OP images of 1 L of naphthalene on the $Fe_4O_4(001)$ surface following several cooling and heating cycles.

la Figuera *et al.* for the spin reorientation phase of magnetite using SPLEEM [209]. Therefore, SPMEEM shows evidence of a spin reorientation transition at the surface of $Fe_3O_4(001)$ supporting previous measurements made using SPLEEM.

Since OP spin asymmetry was observed at low temperatures, this is a strong indication that surface anisotropy still has a significant influence within this temperature range. Due to the manipulator setup used for SPMEEM measurements, it was not possible to reach the Verwey transition for this system, however, at temperatures as low as 133 K, broad OP spin asymmetry was still observed as seen in Figure 5.13 (c). Furthermore, whilst the reorientation of spins was observed for the $Fe_4O_4(001)$ surface following exposure to 1 L of naphthalene, as discussed above, a similar change in the domain structure was observed for the hydrogen-passivated surface as seen in Figure 5.13 (b) and (c).

It was found that this spin reorientation was repeatable and similar over multiple

cooling and warming cycles as can be seen in Figure 5.15. Reducing to temperatures below the Verwey temperature, T_v, has been reported to affect multidomain remanence and the stability of closure domains [211]. Previous studies of cooling $Fe_3O_4(001)$ to below the Verwey transition temperature or heating to above the Curie temperature, T_c, observed similar domain structures to that prior to lowering or raising the temperature [213]. The same group led by de la Figuera *et al.* suggest hematite inclusions (which are particularly prevalent in naturally occurring magnetite) cause a "memory effect", which results in repeatable domain structures despite going above T_c or below T_v [213]. The reversibility of the observed spin asymmetry in SPMEEM, as seen in Figure 5.15, is consistent with the idea of this "memory effect" from hematite inclusions.

5.8 Summary

The work presented here shows the first results from the development of a spin-polarised metastable emission electron microscope. In order to observe spin asymmetry using SPMEEM, a single crystal of $Fe_3O_4(001)$ was used where domains at the surface were successfully characterised. In-plane and out-of-plane measurements were performed revealing a significant spin canting effect. The OP spin asymmetry was measured to be almost the same as that observed IP suggesting a spin canting of 50% at the surface of $Fe_3O_4(001)$, much larger than had been previously reported. This strong spin canting effect is believed to be a consequence of the Dzyaloshinskii-Moriya interaction which originates from the uniaxial surface anisotropy. Comparing SPMEEM results to micromagnetic simulations performed using VAMPIRE, a value of 1-2$\times10^{-3}$ Jm^{-2} has been estimated for the uniaxial surface anisotropy constant of magnetite, providing a more accurate value than has been previously estimated by Coey *et al.* [231]. SPMEEM results were compared to those obtained using ultraviolet magnetic circular dichroism, with similar domain structures observed in both techniques. The measured spin asymmetry using UVMCD enabled comparison between top-most surface states to subsurface and bulk states. Further measurements made using SPMEEM showed domains to be magnetised along the <110> directions.

Exposing $Fe_3O_4(001)$ to 1 L of naphthalene at temperatures lower than 153 K was found to significantly increase the spin asymmetry. It was found that shorter or longer exposures to naphthalene did not further increase the observed spin asymmetry. Exposures greater than 2 L resulted in a weaker spin asymmetry being observed and by 25 L no spin asymmetry was observed at all which is consistent with the idea that a multilayer has formed. The increase in the spin asymmetry following a 1 L exposure is believed to be a result of He 2^3S atoms undergoing Auger de-excitation (instead of RIAN) at the surface and is an indication of charge transfer between the naphthalene monolayer and the $Fe_3O_4(001)$ surface.

It was found that as the $Fe_3O_4(001)$ surface approached the Verwey transition temperature, the domains observed using SPMEEM changed gradually from being small and distinct to broad, large features spanning tens of µm across. This change in domain structure is a consequence of spin reorientation at the surface of $Fe_3O_4(001)$ which occurs as a result of a strong temperature dependence of the first-order magnetocrystalline anisotropy term. This was found to occur at similar temperatures to what has been previously reported with a significant change in domain structure observed at around ≈ 143 K.

The work in this chapter presents a new and powerful technique for measuring the surface magnetic properties of materials. The significant influence of uniaxial surface anisotropy and spin canting at the surface of magnetite is highlighted using SPMEEM complementing previous measurements made using SPLEEM. SPMEEM presents itself as a technique to possibly analyse the properties of magnetic nanoparticles and other magnetic materials which will hopefully provide a greater understanding of spin dynamics at the surface of such systems.

Chapter 6

Activating Graphene on 6H-SiC(0001) Using Atomic Hydrogen

Since the isolation of free-standing graphene in 2004 [10], there has been an increasing drive for research into this material due to its unique electrical and mechanical properties [9, 39]. As discussed earlier, many different methods have been developed to fabricate graphene including the well-known scotch-tape method [10] and chemical vapour deposition [13]. Substrates of silicon carbide, a semiconducting material composed of sp^3 hybridised silicon and carbon atoms, also present a route to production of high-quality graphene through thermal decomposition of the six and four hexagonal polymorphs. What makes silicon carbide attractive is its large bandgap of 3.02 eV (6H-SiC polytype) [88] as well as the ability to change the face polarity of the substrate and the cutoff angle [89]. By controlling the preparation conditions, it is possible to grow large regions of epitaxial graphene on the (0001) Si polar face. As a material, there has been a wide amount of interest in utilising SiC for a variety of electronic applications such as Schottky barriers [232] and in superconductivity [233]. In spintronics, graphene on SiC has been used as part of various 3D stacked devices such as spin valves [234] and in combination with organic molecules such as vanadyl phthalocyanine to generate molecular spin qubits [235]. Silicon carbide has also been of interest recently due to predictions of ferromagnetic behaviour

as a result of induced vacancies within the lattice [236]. Yet various questions still remain with respect to graphene grown on SiC such as whether the formation of the $(6\sqrt{3} \times 6\sqrt{3})R30°$ is a Moiré pattern of graphite and the SiC substrate both in a (1×1) cell [41, 237, 238] or if it is due a (6×6) carbon nanomesh [41, 239]. Although some progress has been made to understand graphene growth on SiC as well as other aspects such as the intercalation of atomic species underneath the buffer layer, further efforts are required. Experimental methods which analyse changes in the density of states of the valence band can be of use when wanting to further understand the evolution of graphene growth on SiC or the effect of intercalation of various atomic species such as hydrogen. The work presented in this chapter explores the first study of certain surface reconstructions of 6H-SiC(0001) using MDS supported with measurements performed using XPS, UPS, LEED and LEED I/V as well as *ab initio* calculations using CASTEP. Hydrogen decoration as well as intercalation underneath the buffer layer are explored and some preliminary work investigating intercalation of erbium is presented.

6.1 6H-SiC(0001)

The six-and four-hexagonal polymorphs of silicon carbide, 6H-SiC and 4H-SiC, are crystal structures with the lattice stackings ABCABC and ABCB respectively. As shown in Figure 6.2 (a), the primitive cell of 6H-SiC (as well as 4H-SiC) consists of 12 atoms (or 8 atoms) respectively, with each atomic layer alternating between Si and C atoms.

6.1.1 Background of the $\sqrt{3}$ Surface Reconstruction

It has been previously found that by annealing 6H and 4H-SiC$(0001)/(000\bar{1})$ surfaces to temperatures around 1173 K, the result is the formation of the $(\sqrt{3} \times \sqrt{3})R30°$ surface reconstruction [41, 89, 238]. This surface reconstruction forms on both the silicon (0001) and carbon $(000\bar{1})$ rich faces where the $\sqrt{3}$ periodicity has often been stated to originate from either carbon or silicon adatoms depending on the face [240, 241]. *Ab initio* calculations for both the C-and Si-rich faces were

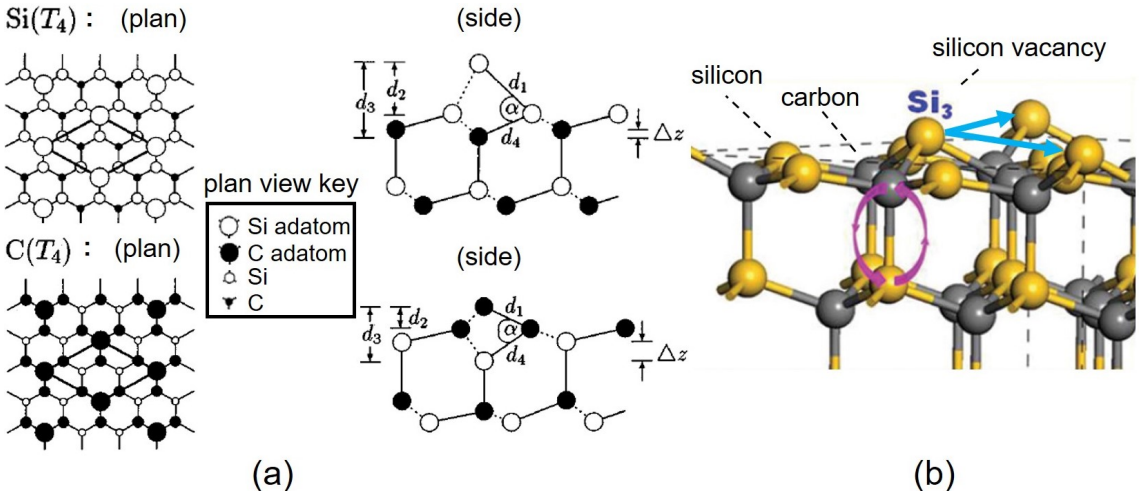

Figure 6.1: (a) Plan and side view schematics of the adatom model used to explain the $(\sqrt{3} \times \sqrt{3})R30°$ periodicity for both the (0001) silicon-rich (Si(T_4)) and (000$\bar{1}$) carbon-rich (C(T_4)) faces of SiC (Si white, C black). Reproduced from Ref. [240]. (b) Silicon vacancy model where silicon vacancies form the $\sqrt{3}$ periodicity as indicated by the blue arrows, and purple arrows indicate the proposed bond flip mechanism (Si orange, C grey reproduced from Ref. [242]).

performed by Sabisch *et al.*, where it was determined that the most energetically favourable location for both silicon and carbon adatoms is on the tetragonal T_4 site [240], as shown schematically in Figure 6.1 (a). The silicon adatom termination is generally a consequence of growth on the (0001) face whilst the (000$\bar{1}$) direction results in a carbon adatom [89, 240]. The most significant difference between the two terminations is the height at which the adatom is situated above the next atomic layer which, correspondingly, affects the bond length as well as the bond angle between this adatom and neighbouring atoms. The carbon termination has a height of 0.73 Å (labelled d_2 of C(T_4) of Figure 6.1 (a)) above the next row of atoms whilst the silicon adatom has a much larger distance of 1.71 Å above the next row of carbon atoms (labelled d_2 of Si(T_4) of Figure 6.1 (a)).

There are also suggestions that the periodicity originates from an ordered array of silicon vacancies instead of adatoms due to a "lack" of silicon at the surface of SiC [89, 242]. Supported through STM and theoretical calculations, Wang *et al.* suggest Si vacancies form the $(\sqrt{3} \times \sqrt{3})R30°$ periodicity as seen in Figure 6.1 (b) where this arrangement of atoms has a lower energy than the (1×1) unit cell. They

propose a "bond flip mechanism" to help explain the origin of the silicon vacancies as well as the graphitisation of SiC, where a carbon atom in the top layer swaps with a silicon atom in the layer below resulting in a silicon vacancy and a "carbon cluster" in the second layer. Both these models show possible reasons for the $\sqrt{3}$ periodicity, however, recent research has tended to favour the adatom model for this surface reconstruction [241].

6.1.2 Background of the $6\sqrt{3}$ Surface Reconstruction

Annealing SiC to temperatures above 1423 K will overcome the energy barrier needed to break Si-C bonds leading to Si desorption at the surface. The carbon left behind then condenses into graphene, with up to three atomic layers of the crystal being involved in the process [89]. This results in a change in surface reconstruction from the $\sqrt{3}$ to the $(6\sqrt{3} \times 6\sqrt{3})R30°$ surface reconstruction for the silicon-rich (0001) face. A variety of different reconstructions such as the (2×2) structure occur for the carbon-rich $(000\bar{1})$ face [89]. The silicon-rich surface is accompanied by a 'buffer layer' [41, 170] which has the same physical structure of graphene and a distinct periodicity of $(6\sqrt{3} \times 6\sqrt{3})R30°$. However, due to the presence of subsurface silicon atoms, 20 - 30 % of this layer is covalently bonded to the substrate [243]. Due to this back-bonding, it does not exhibit linear dispersion at the K-point. It is therefore only subsequent layers that grow on top of this buffer layer as a result of further Si desorption that are considered to be graphene. The distance between the subsurface silicon and the buffer layer as measured by X-ray diffraction (XRD) has been determined to be 1.65 ± 0.05 Å [89, 244]. Different face polarities result in a difference in the predicted bandstructure of the buffer layer. As theoretically predicted by Mattusch *et al.* [245], growth on the (0001) face results in a metallic-like phase with the $(000\bar{1})$ face leading to a semiconducting-like phase.

Growth on the carbon-rich face is not accompanied by this buffer layer so that the carbon layer behaves like an individual layer of graphene, weakly van der Waals bound to the substrate [89]. The lack of a buffer layer makes the carbon-rich face appear more suitable for growth of graphene and therefore device applications, however, due to this face having a lower surface free energy, it is more difficult to control

the rate of Si desorption [89]. Predominantly, for device applications, work has involved growth of graphene on the silicon-rich face with groups such as Maasen *et al.* demonstrating graphene spin valves on the Si polar face [234]. However, the amount of work investigating the enhancement of SOC in graphene on SiC is limited, with only a small number of reports appearing in the literature, such as that by Marchenko *et al.* who observed Rashba-type SOC after the intercalation of gold [93].

6.2 Modelling the Base Cell

To understand the electronic states of the above surface structures that were probed experimentally, the various stages of growth were modelled using the CASTEP code [192]. The first step in modelling any surface reconstruction is to perform a convergence test and determine the ideal k-point grid and cutoff energy to use. This is done to ensure that the final ground state energy remains the same regardless of a geometry optimisation calculation or a bandstructure calculation.

Previous studies used a (6 6 1) mp-grid and a cutoff energy of 650 eV for the $(6\sqrt{3} \times 6\sqrt{3})R30°$ unit cell [245–247]. Using a primitive cell of 6H-SiC (consisting of 12 atoms of Si and C stacked around the c axis with a total height of 15.1248 Å) acquired from Ref. [248], the $(\sqrt{3} \times \sqrt{3})R30°$ reconstruction with no adatom or vacuum gap was constructed from cif2cell [249]. Convergence testing was performed using a series of single-point calculations with the Perdew-Burke-Ernzerhof (PBE) exchange correlation functional (a generalised gradient approach (GGA)). It was found that, similar to the work in Refs. [245, 247, 250, 251], a (6 6 1) mp-grid spacing and a cutoff energy of greater than 650 eV were needed for successful calculations.

To model a surface, the vacuum gap (distance between consecutive cells) also needs to be varied until, once again, the final energy does not significantly change. The vacuum gap must be large enough to ensure that the surface layer does not interact with the bottom of the stack. This can be further prevented by passivating any exposed states at the bottom of the stack with hydrogen. It was found that at any distance greater than 12 to 15 Å the energy did not fluctuate or change when increasing the separation, thus implying that such a gap is sufficient. For the

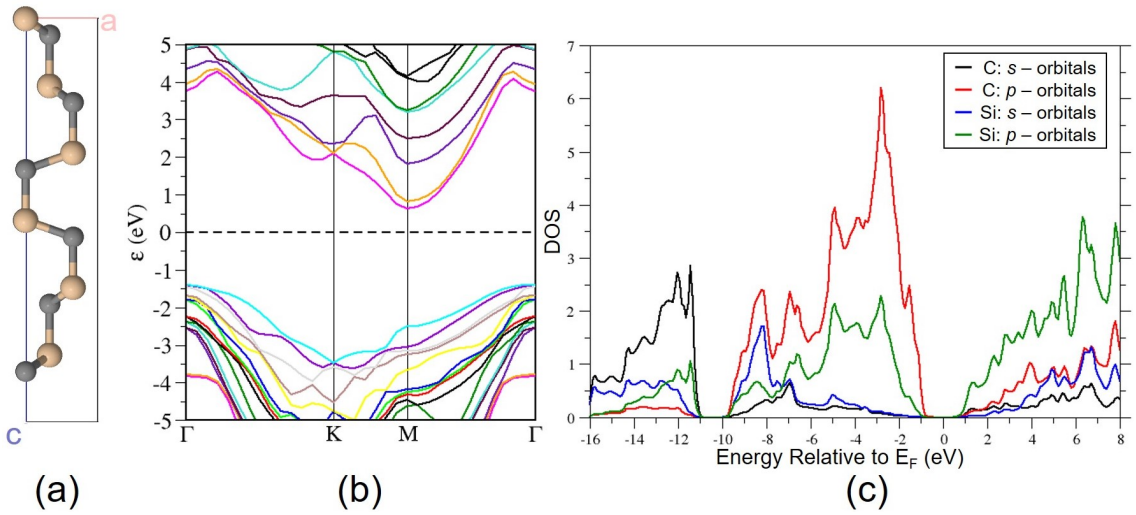

Figure 6.2: (a) The primitive cell of 6H-SiC consisting of 12 atoms stacked along the c axis at different lattice sites C and Si are represented by grey and orange, respectively. (b) A single-point calculation using the PBE GGA of the bandstructure and (c) PDOS show an indirect band gap of around 2 eV which is in close agreement with that reported by Xie *et al.* [246].

remaining calculations, a vacuum gap of 15 Å was therefore maintained.

For the primitive cell, the calculated dispersion relation and partial density of states (PDOS) can be seen in Figure 6.2 (b) and (c). Two aspects of these results are worth highlighting. The first is that the bandstructure and PDOS calculations closely match those by Xie *et al.* [246] which provides support for the validity of our approach. Secondly, as expected, the system is predicted to be an indirect bandgap semiconductor, with the bandgap calculated at around 2 eV. The measured bandgap of undoped 6H-SiC is actually 3.02 eV [246]. Thus, simulations predict this gap to be smaller than in reality which is expected for simulations carried out using DFT which will typically underestimate this value. This arises due to the self-interaction compensated by the exchange correlation energy which shifts the occupied states upwards to lower energies, but not the unoccupied states since they do not contribute to the electron density [192]. Consequently, this reduces the size of the bandgap from its actual value. The peak separation between valence band states in the predicted PDOS will not be influenced by the smaller bandgap calculated using DFT for this system [192]. Since MDS and UPS only probe occupied states, the peak separation in the obtained spectra will be similar to those predicted in the PDOS. Therefore,

despite the smaller bandgap, for its purpose here, the results predicted using DFT are fairly similar to that observed experimentally although shifted closer to the Fermi level. To further improve the results presented here a hybrid functional could have been used but the mixing of functionals would have to be changed between each different surface.

6.3 The $\sqrt{3}$ Surface Reconstruction

6.3.1 Experimental Procedures

For the experiments performed here, wafers of n-type vanadium-and-nitrogen-doped 6H-SiC were purchased from Semiconductor Wafer Inc. These were then mounted onto Omicron direct-current (DC) heating plates with the (0001) silicon-rich face up. Each sample was initially outgassed at around 973 K before being annealed for 30 minutes at 1223 K, 1323 K and 1473 K. Temperature was measured using a Raytek infrared pyrometer (spectral response 8-14 µm) using an emissivity of 0.6. For hydrogen intercalation experiments, molecular hydrogen of 99.999% purity was cracked into atomic hydrogen using a 50 W tungsten filament bulb at close proximity to the sample; a similar approach to that used in Ref. [32]. All measurements were performed at room temperature after allowing the samples to slowly cool. Annealing samples of 6H-SiC(0001) at temperatures around 1273 - 1323 K resulted in a $(\sqrt{3} \times \sqrt{3})R30°$ surface reconstruction as seen by the characteristic LEED pattern shown in Figure 6.3 (b).

6.3.2 Formation of the $\sqrt{3}$ Surface Reconstruction

Relative to the Fermi level, four states are observed in the UPS spectrum at binding energy peak positions of 1.3 eV, 2.3 eV, 4.3 eV and 6.9 eV (Figure 6.3 (a)). The state labelled as (i) at 1.3 eV is associated with the dangling bond of the Si atoms exposed to the vacuum (for the adatom case, this is the dandling bond of the Si(T_4)) [252–254]. The steep slope at 2.3 eV (iii) is the valence band maximum [254] and higher energetic states (iv) at 4.3 eV and (v) at 6.9 eV are most likely a result of back-

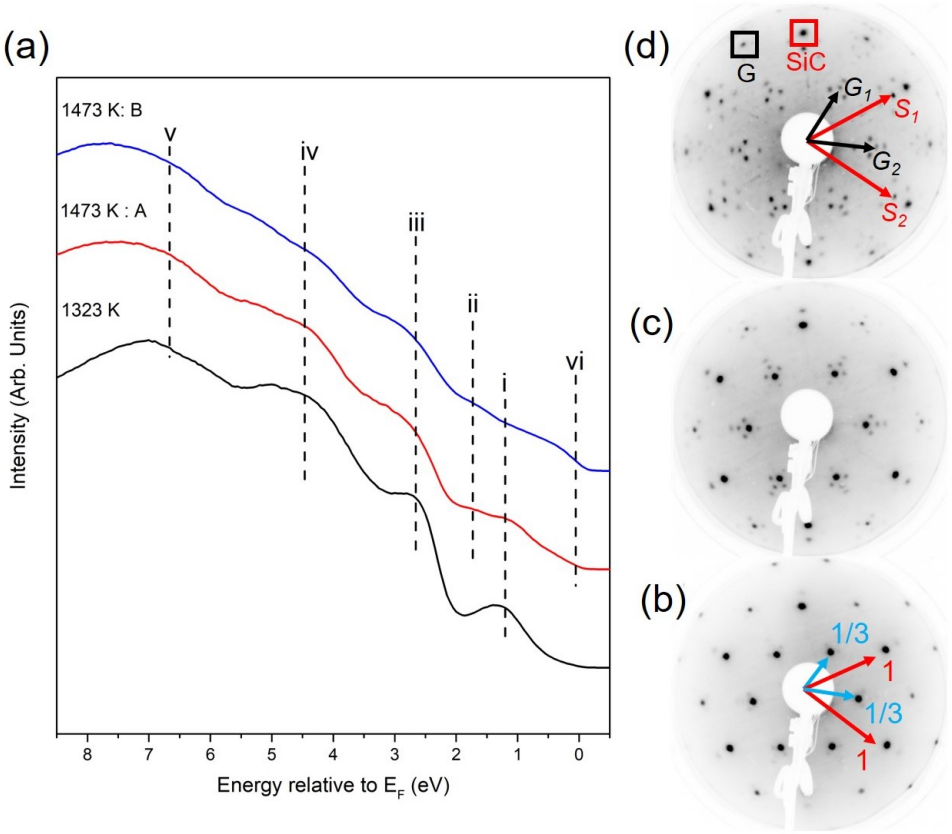

Figure 6.3: (a) Annealing to 1273 - 1323 K results in formation of the $(\sqrt{3}\times\sqrt{3})R30°$ surface reconstruction which is indicated by a well defined surface state in the UPS near the cutoff point (labelled (i)) and $(\sqrt{3}\times\sqrt{3})R30°$ LEED pattern (b). As the sample is brought to higher temperatures of, 1423 - 1473 K, Si starts to desorb and the surface transitions to the $(6\sqrt{3}\times 6\sqrt{3})R30°$ surface reconstruction indicated by a change in LEED, (d), and UPS. LEED images were taken at 80 eV after annealing the sample for 30 minutes at (b) 1323 K, (c) 1423 K and (d) 1473 K.

bonding states between the adatom and bulk as well as between Si and C in the bulk at the T_4 site [240]. This is supported by the PDOS calculations presented below in Figure 6.5 (c) which show a large presence of Si and C p-states within this energy range, as well as previous charge density maps of the Si(T_4) site [240].

Corresponding MDS spectra are shown in Figure 6.4 with three distinct features labelled (i) - (iii) appearing at kinetic energies of 17 eV, 13.9 eV and 11.5 eV, respectively. The state labelled (i) most likely corresponds to the dangling bond state near the Fermi edge. This state and the shoulder at 13.9 eV are broad as a result of the RIAN de-excitation mechanism being dominant for this particular

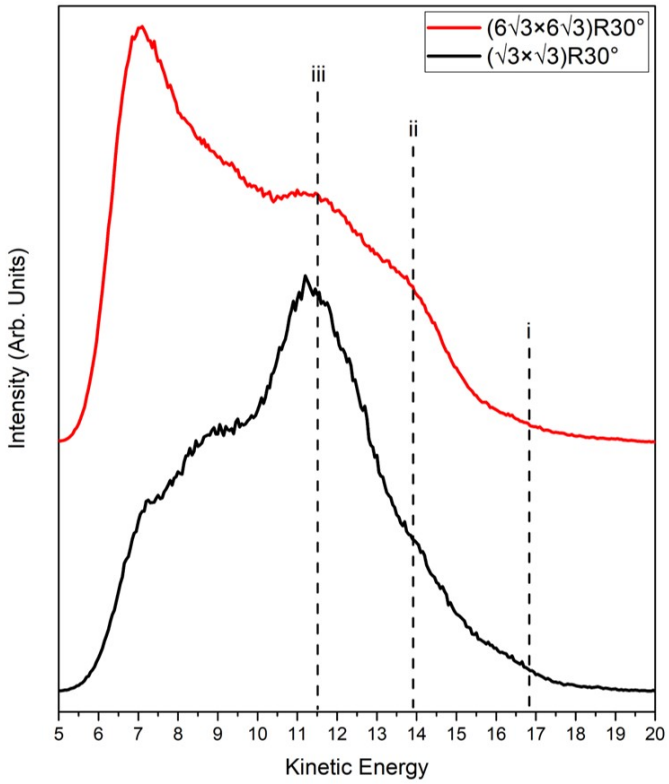

Figure 6.4: The MDS spectra of the $(\sqrt{3} \times \sqrt{3})R30°$ and $(6\sqrt{3} \times 6\sqrt{3})R30°$ surface reconstructions.

surface. Helped by comparison to the features observed in the UPS spectra, it can be deduced that states (ii) and (iii) originate from the back-bonding state between the adatom and the substrate. The peak separation between (ii) and (iii) is around 2.4 eV which is similar to the separation of states (iv) and (v) of the UPS spectrum. Since the state observed at 11.5 eV is a sharp well-defined peak, it is possible that AD is contributing to this state in addition to RIAN. For AD to occur, there needs to be an effective overlap between the ground state of the metastable helium atom and the relevant surface state. It is possible that the back-bonding state between the Si(T_4) and C atoms at the surface is effectively overlapping with the 1s state of the He 2^3S resulting in an intense peak being observed at 11.5 eV. Further observation of a sharp peak can be seen in the PDOS in Figure 6.5 (c), where, at 8 eV from the Fermi level, there is an increase in the DOS due to C and Si p-states.

The only existing study that this MDS spectrum can be compared to is that for a completely different silicon carbide surface structure which is the 3×3 surface reconstruction [255]. In this study, Ikari *et al.* found that states prevalent at kinetic

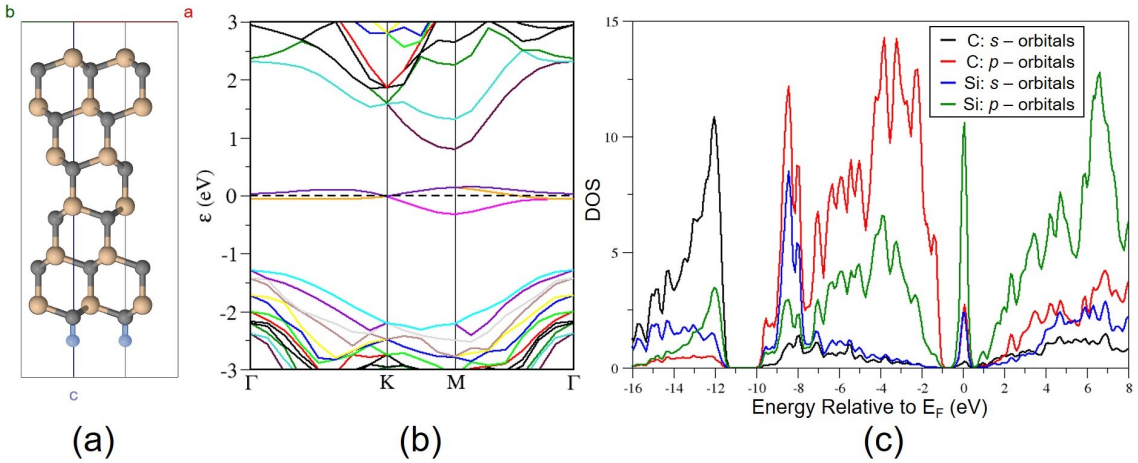

Figure 6.5: (a) The primitive $\sqrt{3}$ cell of 6H-SiC with no adatom (C is grey, Si is orange, H is blue). (b) The dispersion relation and (c) the calculated PDOS. As a result of exposed silicon surface atoms, there is a strong presence of states at the Fermi level.

energies of 10 - 12 eV were associated with Si $3p$ states. It should be highlighted that the 3×3 surface reconstruction is a silicon-rich surface reconstruction when compared to the $\sqrt{3}$ reconstruction, and so the features observed will be different from those observed in Figure 6.4 (b). However, based on PDOS calculations and the peaks observed by Ikari *et al.*, it is very likely that the state at 11.5 eV is a consequence of a Si $3p$ - C $2p$ bonding state.

6.3.3 Modelling the Surface Reconstruction

Prior to modelling the $(6\sqrt{3} \times 6\sqrt{3})R30°$ surface reconstruction, the PDOS of the $(\sqrt{3} \times \sqrt{3})R30°$ unit cell (with no adatom) was explored, with the results shown in Figure 6.5 (c). A strong presence of states at the Fermi level can be seen, particularly due to Si p states which is a consequence of Si states exposed to the vacuum i.e. Si dangling bonds (top of the stack of Figure 6.5 (a)). As seen earlier, this is mirrored experimentally with the UPS showing a strong state near the Fermi level of the Si-terminated $(\sqrt{3}\times\sqrt{3})R30°$ surface reconstruction. However, as discussed, depending on the face termination, this surface reconstruction originates from the presence of Si or C adatoms which form the $\sqrt{3}$ periodicity [240]. The state observed through UPS is due to the dangling bond from the Si adatom. Therefore, to truly model

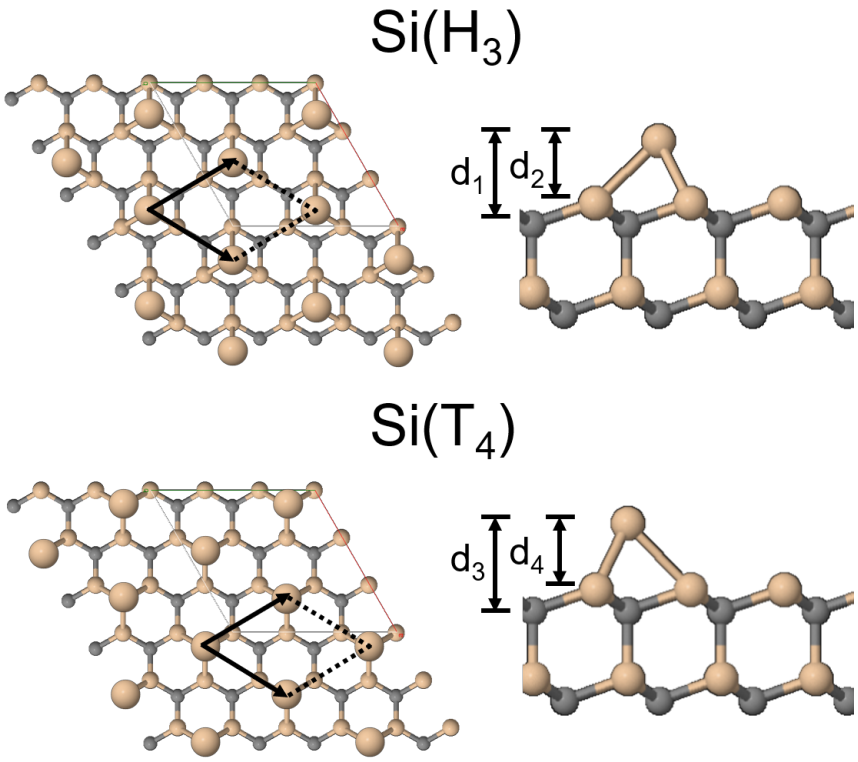

Figure 6.6: The $(\sqrt{3} \times \sqrt{3})R30°$ silicon-rich surface reconstruction has two possible adatom configurations, the T_4 top site (bottom) or the hollow H_3 site (top). The heights of these adatoms were determined from a geometry optimisation calculation using the exchange correlation functional LDA to be $d_1 = 2.41$ Å, $d_2 = 1.77$ Å, $d_3 = 2.56$ Å and $d_4 = 1.75$ Å, which compare closely to the values predicted by Sabisch *et al.* [240]. Plan views shown on the left and side views on the right.

the $(\sqrt{3} \times \sqrt{3})R30°$ surface reconstruction, the adatom case needs to be considered. Previous predictions for this surface reconstruction on the (0001) face ascribe the adatom either to be due to a silicon atom on the T_4 top site or H_3 hollow site, as shown schematically in Figure 6.6, predicting that the silicon-rich face favours the T_4 site [240]. To further confirm that this surface reconstruction is a result of Si(T_4) adatoms, a series of calculations for both sites were run using PBE (van der Waals turned on) and LDA and revised PBE (van der Waals turned off). Table 6.1 shows the final enthalpy values for the entire unit cell from a geometry optimisation for both of these adatom sites. The same parameters were used (k-points and cutoff energy) in all calculations based on a convergence test.

As can be seen in Table 6.1, the difference in total free energy per unit cell calculated

Total Free Energy of Entire Unit Cell (eV)			
System	Si(T_4)	Si(H_3)	ΔE
PBE	-18415.11	-18414.65	0.46
RPBE	-18420.86	-18419.86	1.00
LDA	-18259.20	-18258.34	0.86

Table 6.1: Different final enthalpies calculated using a variety of different functionals. The change in energy marks the difference between the H_3 and T_4 sites.

here using the PBE exchange correlation functional is similar to previously predicted values of 0.54 eV [256] and 0.6 eV [240]. This result reveals that the H_3 hollow site is less energetically favourable with respect to the T_4 top site and this is the case for all exchange correlation functionals used. It is worth noting that the mixing used here was performed in *Kerker* (mixing amplitude 0.3), which helped ensure that the calculation completed. Using *Kerker* mixing will lead to a small difference in the final ground state energy compared to running a geometry optimisation calculation without mixing specified where *Pulay* is used instead. Suggested further work would be to vary this mixing parameter to see the difference in the final ground state energy of the $\sqrt{3}$ reconstructions. Another extension to the work presented here would be to both experimentally and theoretically explore the carbon-rich face and see whether the C(T_4) top site is still the most energetically favourable site.

6.4 Transition to the $6\sqrt{3}$ Surface Reconstruction

Annealing of the SiC sample to temperatures above 1423 K will result in silicon desorption from the surface and a transition to the $(6\sqrt{3} \times 6\sqrt{3})R30°$ surface reconstruction. This is indicated by a characteristic LEED pattern as seen in Figure 6.3 (d), with reciprocal lattice vectors S_1 and S_2 due to the SiC substrate and G_1 and G_2 associated with the carbon layer (graphene) periodicity [180]. The LEED I/V spectra of these spots can be used to differentiate between the number of layers of graphene grown on SiC [41, 171], with distinctly different intensity curves for the $\sqrt{3}$ spot, buffer layer $(6\sqrt{3})$ growth and multilayer growth as seen in Figure 6.7.

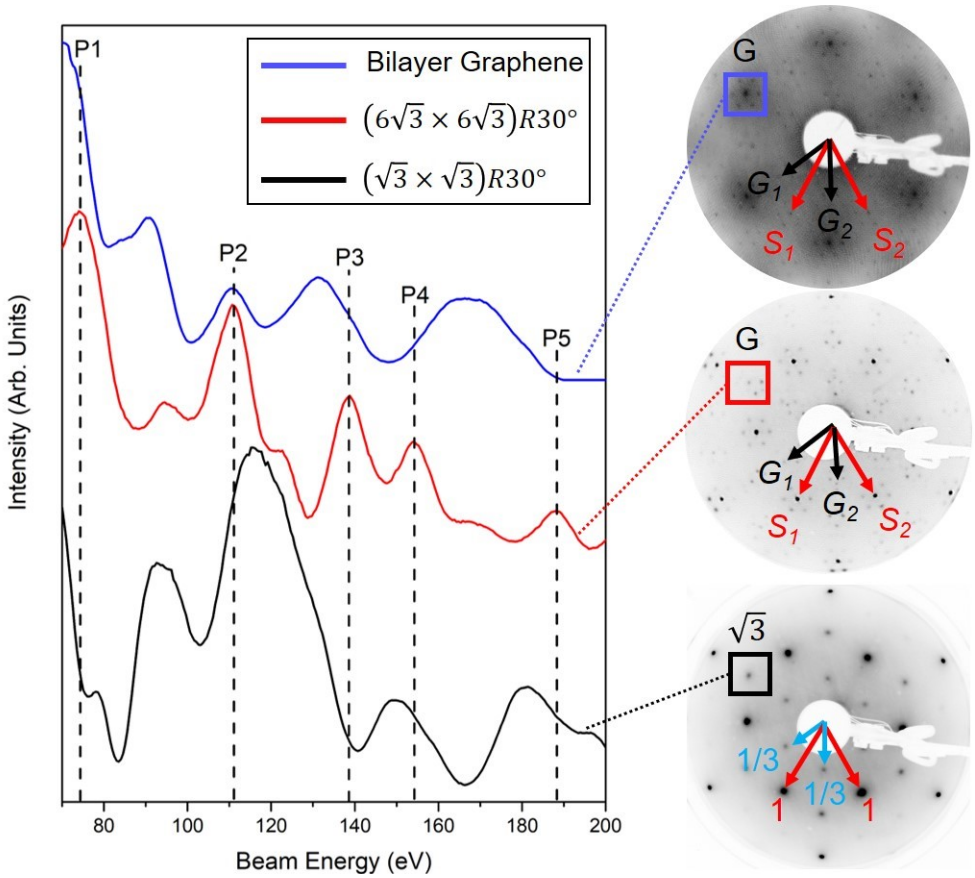

Figure 6.7: LEED I/V curves for the $\sqrt{3}$ spot, the buffer layer $(6\sqrt{3})$ spot and the bilayer graphene spot (left). Respective LEED images taken at 126 eV for the different levels of graphitisation of SiC (right).

Previous work analysing the LEED I/V spectra of different layers of graphene show similar results to those obtained in Figure 6.7 [171]. Peaks at 75 eV (P1), 110 eV (P2), 138 eV (P3), 153 eV (P4) and 188 eV (P5) all have similar positions and separation to those measured by Riedl *et al.* for the $(6\sqrt{3})$ buffer layer [171]. Therefore, it appears that the annealing procedure discussed above results in buffer layer graphene. It was also of interest to explore the LEED I/V of the $\sqrt{3}$ periodicity. As seen in Figure 6.7, the $\sqrt{3}$ periodicity shows some characteristic Bragg peaks with similar peak positions to those observed for the buffer layer. To date, this appears to be the only LEED I/V spectra of this periodicity of the 6H-SiC system. A suggested extension to this work would be to simulate the LEED I/V curves of the adatom and vacancy model to see which one has a better fit with the experimental data presented in Figure 6.7.

To further confirm whether a buffer layer had been achieved following this particular

growth procedure, the workfunction of the surface was measured by offsetting the UPS spectrum by -15 V. A previous measurement of the workfunction of the buffer layer determined it to be 3.89±0.05 eV [178]. Here, the work-function was measured to be $\phi_{6\sqrt{3}} = (3.82 \pm 0.10)$ eV after having annealed the sample at 1473 - 1513 K for 30 minutes, which agrees with the previously measured value (data not shown). In comparison, monolayer and bilayer growth have much higher workfunctions of 4.16 and 4.3 eV respectively [178]. An alternative to determining the extent of graphitisation is by measuring the LEEM reflectivity as can be seen for a bilayer of graphene on SiC (Figure A.1).

As can be seen in Figure 6.3 (a), upon formation of the $6\sqrt{3}$ surface reconstruction, the UPS spectrum transitions from showing a surface state near the cutoff point to one that has a shallow Fermi edge (vi) and a back-bonded state (ii) at 1.7 eV. This transformation is seen quite clearly over two anneals at 1473 K (A and B) where the dangling bond state of the Si adatom (i) becomes a more stable back-bonded state and the valence band maximum is now replaced by a shoulder at around 2.9 eV relative to the Fermi level (iii). This state near 3 eV is a consequence of π-band electrons (sp^2 hybridisation) at the M point in reciprocal space [257]. Since only up to 30% of the carbon atoms are back-bonded to the substrate in the buffer layer [41, 243], the majority of carbon atoms are only bonded to three other atoms and therefore within the buffer layer there is some presence of π-band states. The higher energetic state (v) remains relatively unchanged as a consequence of the transition in the surface reconstruction further indicating that this state is a result of subsurface states in the SiC bulk.

The transition in surface reconstruction results in a significant change to the MDS spectrum as seen in Figure 6.4. The well-defined state at a kinetic energy of 11.5 eV has now been replaced by a broad shoulder at the same energy and an additional broad peak is observed at 13.9 eV. In the MDS spectrum for graphite, a state is observable at 8 - 9 eV from the cutoff point and this is associated with π hybridisation at the Γ point in reciprocal space [122, 258]. A strong peak associated with this state is observed as a consequence of effective overlap between the ground state of the He 2^3S atom and the $2p_z$ orbital associated with the π hybridisation, which results in Auger de-excitation [117]. This $2p_z$ state dominates over in-plane σ-bands resulting

in a sharp feature being observed in the MDS spectrum of graphite [258]. Since the buffer layer is structurally similar to graphite, it is believed that the peak observed at 11.5 eV is a consequence of the π-band. The slope observed at 13.9 eV correlates strongly with σ-band states, with a similar spectrum being observed for graphene on Ni(111) which is also known to back-bond to the substrate [60, 122]. Chambers *et al.* associates this σ-band state to be a result of exposed edges of graphene islands and the back-bonding between it and the substrate. This is therefore most likely an indication that the MDS is possibly observing some regions where the buffer layer has not fully formed across the SiC and the back-bonding state is being observed.

To summarise, using UPS, MDS and LEED, the work presented here shows that annealing the SiC sample to temperatures above 1423 K leads to a change in the surface reconstruction from $\sqrt{3}$ to $6\sqrt{3}$ and the formation of a back-bonding state from a Si surface state. Currently, it appears that this is the only work exploring this transition in surface structure using all three techniques above. By showing this evolution in DOS and SDOS using UPS and MDS respectively in combination with fingerprint of structure using LEED I/V, the work presented here has helped to hopefully provide a greater understanding of the graphitisation of SiC.

6.5 Intercalation/Decoration of the Buffer Layer using Atomic Hydrogen

6.5.1 Background

It is only by intercalation of atomic species such as hydrogen that the back-bond between subsurface silicon atoms and the buffer layer can be broken. The consequence of successful hydrogen intercalation and breaking of the back-bond is the formation of a "quasi-free standing layer of graphene" (QFSG) which displays linear dispersion at the K-point [41, 178]. Currently, the way in which hydrogen intercalates is not fully understood but there have been attempts to find a solution to this. For example, papers such as that by Gerber *et al.* [259] mention that in the case of graphene grown on Ir(111), there is a dissociative chemisorption of hydrogen

molecules on bare Ir(111) patches and subsequent diffusion of the hydrogen atoms under the graphene flakes [259].

Additionally, in order to break the back-bond, it has been found the substrate must be annealed at temperatures above 723 K [170] since the reaction barrier (energy to break the bond) is very large at room temperature [260, 261]. Furthermore, graphene also behaves like an effective impermeable barrier [170], and therefore it is improbable for hydrogen to diffuse through the buffer layer at room temperature.

When the buffer layer is exposed to atomic hydrogen at room temperature, previous studies have shown that the hydrogen will absorb on certain sites on top of the buffer layer implying that it could be used as a system for hydrogen storage [262, 263]. STM work performed by Guisinger *et al.* showed that hydrogen tended to favour carbon atoms which are either on opposite sides of the hexagonal ring or at nearest-neighbour sites [263]. Exposure of atomic hydrogen was varied, with low coverages resulting in dimers occurring preferentially on protruding areas of the buffer-layer SiC surface [264] and higher coverages resulting in the formation of hydrogen clusters [264]. Hydrogen decoration of the buffer layer also results in increased chemical reactivity compared to QFSG [265].

Theoretical studies show that hydrogen preferentially absorbs on top of a threefold C atom in the buffer layer [260] and that hydrogen prefers to absorb on the same lattice sites when diffusing between graphene layers or to the buffer layer [266]. The consequence of hydrogen decoration has been predicted to change the hybridisation of carbon atoms to sp^3 [243, 261, 265] resulting in more Si in the underlayer being freed up due to the induced strain [243, 261]. More recent calculations by Liu *et al.* [261] have suggested such hybridisation leads to buckling of the surface, lowering the reaction barrier of the back-bond and increasing the likelihood of hydrogen atoms diffusing under this layer. They suggest that for a sufficiently high hydrogen exposure, it may be possible to break the back-bond at room temperature, or at least at lower temperatures than have previously been measured [170, 261]. However, at present, there has been no experimental observation of breaking the back-bond at room temperature [267] and all evidence suggests that the buffer layer must be annealed in order for hydrogen to intercalate. Reversibility of this hydrogen

decoration has been reported at low temperatures of around 490 K [268] and results in an overall dimming of the associated LEED pattern.

Graphene with a hydrogen atom attached to each atomic site of the lattice is commonly referred to as graphane. The adsorption of hydrogen changes the hybridisation from sp^2 to sp^3, resulting in the formation of a bandgap at the K-point, changing graphene from a zero-overlap semimetal to an insulator with an associated increase in resistivity by two orders of magnitude [269]. The first evidence of graphane was by Nair *et al.* who created both graphane membranes as well as graphane on SiO_2 [269]. This material has been proposed for a variety of purposes with the most common suggestion for its use being hydrogen storage.

6.5.2 Modelling the Intercalation and Decoration

To model the $6\sqrt{3}$ surface reconstruction, a reduced unit cell was used due to the difficulty of modelling the actual surface reconstruction which consists of 169 graphene unit cells and 108 SiC(0001) unit meshes [180]. The setup used was the same as that reported by Markevich *et al.* [247] with a 2×2 graphene cell placed on a $(\sqrt{3} \times \sqrt{3})R30^\circ$ unit cell of SiC. Here, three atoms in the carbon mesh are back-bound to subsurface Si atoms in the underlayer modifying the electronic properties of the graphene layer. It is worth noting that, whilst a reduced cell is used, its design is almost identical to that of the $6\sqrt{3}$ surface reconstruction such that the calculated PDOS and dispersion relation are in principle very similar. Therefore, this model is an effective way of simulating the buffer layer, helping further support the arguments made for the origin of the states observed in the UPS and MDS spectra.

After placing the carbon layer on top of the silicon-rich (0001) face, the PDOS and dispersion relation shown in Figure 6.8 (a) and (b) were obtained. As a result of the back-bond between the carbon atoms in the buffer layer and the subsurface Si atoms, there is no observation of linear dispersion at the Fermi level at the K-point. Furthermore, this dispersion relation shows the buffer layer to behave like a metal with a relatively strong presence of states at the Fermi level which is consistent with previous work by Mattusch *et al.* who report a similar dispersion relation for 6H-SiC [245].

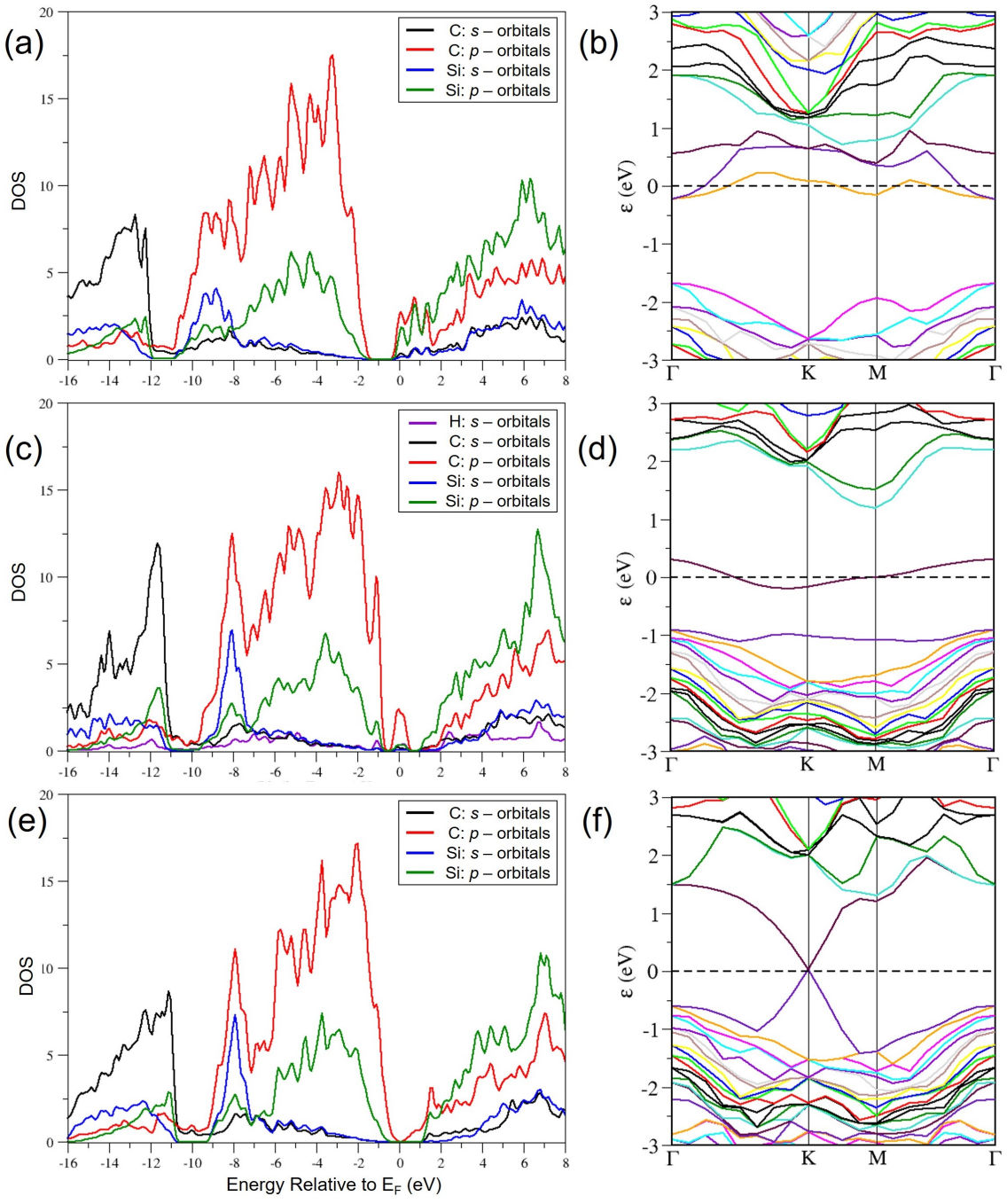

Figure 6.8: The PDOS and dispersion relation of, (a) and (b), the buffer layer, (c) and (d), hydrogen-decorated buffer layer, and, (e) and (f), a quasi-free standing layer of graphene. All calculations were performed using the PBE GGA, a k-point grid spacing (6 6 1) and a cutoff energy of 650 eV.

The observed PDOS, Figure 6.8 (a), shows a strong presence of states at the Fermi level as well as at the edge of the valence band due to silicon and carbon p-states. As discussed earlier, the state labelled (ii) of the UPS spectrum (Figure 6.3 (a)) is believed to be a result of the back-bonding state. Comparing the UPS spectrum for the $6\sqrt{3}$ surface reconstruction to the PDOS shown in Figure 6.8 (a) reveals a significant increase in the density of states at 1.5 - 2.0 eV below the Fermi level due to both C and Si p-states. Since the back-bond is between a Si and C atom, the increase in DOS in the UPS spectrum and the calculated PDOS at ≈ 1.5 eV below E_F appear to provide further evidence therefore that (ii) is a consequence of this back-bonding state.

For the hydrogen-decorated case with a graphane-like buffer layer, hydrogen atoms were placed on adjacent and opposite sites of the carbon ring which were not back-bonded to subsurface silicon atoms, shown in Figure 6.9 (a). The resulting PDOS and bandstructure displayed in Figure 6.8 (c) and (d) show a semiconducting-like system but with a surface state at the Fermi level. At 8 - 9 eV from the Fermi level, both C p-states and Si s-states increase in density as a consequence of hydrogen adsorption on the surface of the buffer layer, which is similar behaviour to the PDOS for QFSG. In both cases the origin of this increase is believed to be a result of the freeing up of silicon atoms in the underlayer due to a buckling effect in the buffer layer [243, 261]. By analysing the atomic positions of atoms in the cell following a geometry optimisation of the graphane-like buffer layer, it was found that carbon atoms bonded to hydrogen moved between 0.2 - 0.3 Å away from the underlayer due to the change in hybridisation. This variation in height shows a buckling-like effect in the buffer layer.

The bandstructure of the buffer layer following intercalation of hydrogen results in the emergence of linear dispersion at the K-point where the dispersion relation seen in Figure 6.8 (f) is consistent with previous DFT calculations presented in Ref. [247]. In this study, Markevich *et al.* remark that the intercalation of atomic hydrogen and the formation of QFSG results in charge-neutral graphene [247]. However, other *ab initio* calculations by Mammadov *et al.* have suggested that the QFSG layer is p-doped on the Si polar face of 6H-SiC and occurs as a consequence of the "spontaneous polarization" of the hexagonal SiC substrate [270]. The results

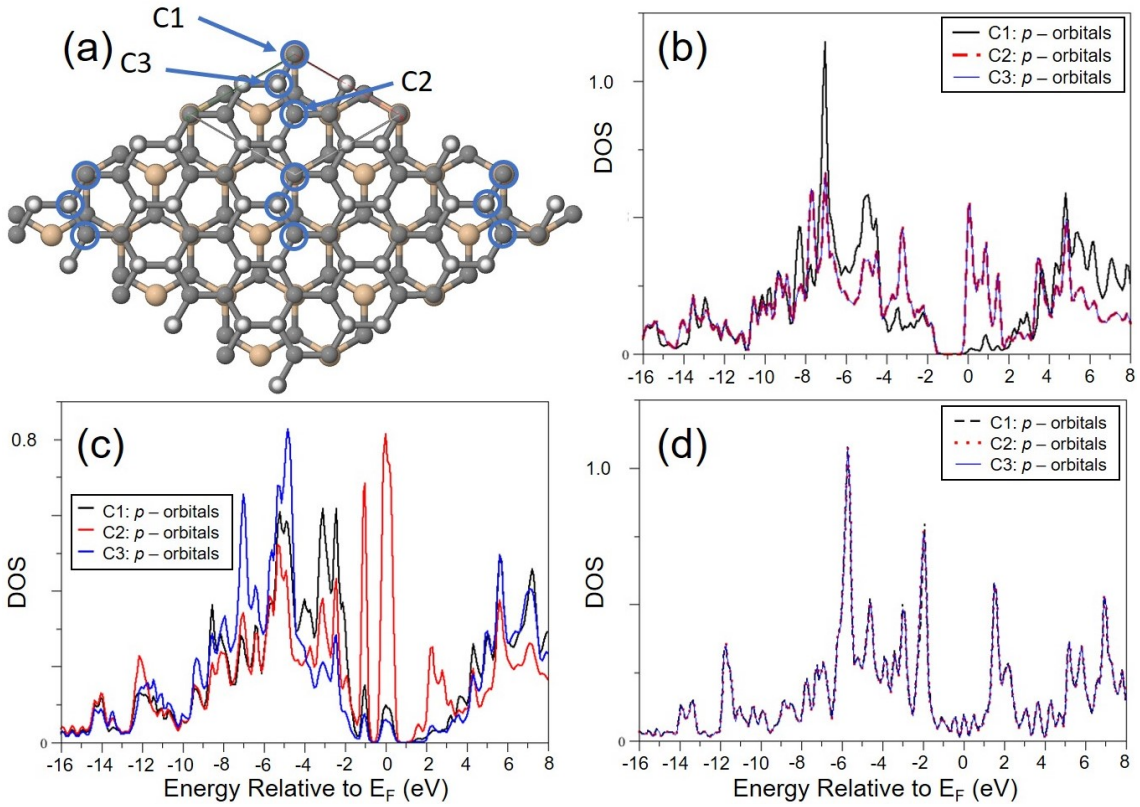

Figure 6.9: (a) For the graphane-like buffer layer, hydrogen atoms (white) were placed on adjacent and opposite sites of the carbon ring (grey; N.B.: silicon in the underlayer is orange). The PDOS of p-states for the carbon atoms shown were calculated where C1 is a back-bonded carbon atom and C2 and C3 are non-back-bonded atoms with C3 also bonded to a single hydrogen atom. (b) - (d) show the PDOS for these carbon atoms for the buffer layer, graphane-like adsorption and QFSG respectively.

presented here show a very small p-doping in the QFSG with the Fermi level sitting 0.035 eV away from the Dirac point within the valence band of the material. Whilst this doping is small, it further supports previous predictions which suggest that the QFSG is slightly p-doped. Furthermore, as a consequence of the intrinsic SOC in graphene, only a small bandgap between the two bands is observed on the µeV scale.

As seen in Figure 6.8 (e), the PDOS of QFSG shows a small DOS at the Fermi level as a result of the slight p-doping. Within the valence band, there are some subtle changes to the overall shape of the PDOS of certain orbitals with the most significant change being the formation of a sharp peak at around 8 eV for both C p-orbitals as well as for Si s and p orbitals. The peak observed in the C p-states is

a mixture of C π and σ bands whilst in the Si s and p states, the peak observed is a consequence of the underlayer (subsurface) silicon now being freed up by the H-Si bond shifting the overall DOS to a higher binding energy.

To more closely understand the origin of any features observed in the MDS spectra presented below, the PDOS of three different carbon atoms were calculated (Figure 6.9 (a)). Only one of these carbon atoms (C1) is a back-bonded atom. For the graphane-like buffer layer, C3 is decorated with atomic hydrogen and for QFSG, the back-bond between C1 and the subsurface Si atom is broken. As can be seen in Figure 6.9 (b), the PDOS of the buffer layer for C1 differs from C2 and C3 due to its back-bond to the subsurface silicon. This differs for the hydrogen-decorated buffer layer, Figure 6.9 (c), where the predicted PDOS for all three carbon atoms are different. The surface state predicted to exist at the Fermi level is primarily a result of the carbon atom, C1, that is only bound to three other carbon atoms. Whilst for the hydrogen-bonded carbon atom, C3, there is a sharp increase in states at deeper binding energies of 6 and 8 eV. This is most likely a result of the sp^3 hybridisation between the carbon atom, the hydrogen and three other carbon atoms. In contrast, the PDOS of all three carbon atoms are the same for QFSG as expected, since it behaves as an independent layer of graphene (Figure 6.9 (d)).

6.5.3 Graphane-like Buffer Layer

To experimentally prepare hydrogen-intercalated graphene on SiC, after growth of the buffer layer, samples were exposed to atomic hydrogen by cracking high purity hydrogen gas (99.999%) in close proximity to the sample using a hot tungsten filament. Exposures were measured using Langmuirs and the sample was at room temperature. As seen in Figure 6.10 (a), exposing the buffer layer at room temperature to 60 L of atomic hydrogen results in only small changes to the buffer layer UPS spectrum. States (ii), (iii) and (vi) of the UPS spectra appear to be similar to those observed prior to exposure but are less intense. Since the back-bonding state (Figure 6.10 (a) (ii)) appears to not have been influenced significantly by 60 L exposure whilst the sample is kept at room temperature, it is unlikely that much, if any, of the atomic hydrogen has intercalated as is expected. Annealing the sample

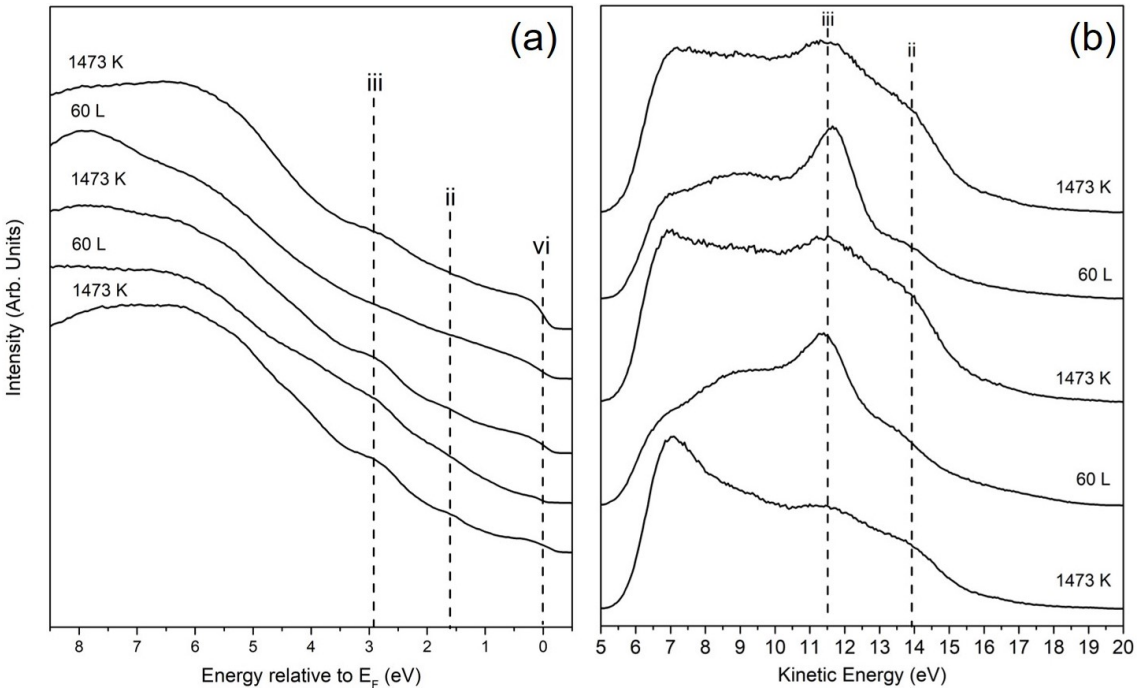

Figure 6.10: (a) UPS and (b) MDS spectra of buffer-layer carbon on SiC followed by subsequent cycles of exposure to atomic hydrogen with the sample at room temperature and annealing at 1473 K. The MDS spectra shows formation of an intense peak at around 11.5 eV due to an effective overlap between the ground state of the metastable helium atom and the sp^3 hybridised C-H state.

at temperatures above 1473 K in order to remove the atomic hydrogen reverses this influence on the spectrum. However, due to this annealing, even for short periods of time, the sample undergoes further graphitisation. After two annealing cycles, there is a stronger presence of states near the Fermi level indicating a transition to a more metallic-like phase at the surface which is consistent with the formation of graphite which is a known semi-metal [117].

Contrary to the UPS spectra, the corresponding MDS spectra show quite significant differences between the clean surface and the hydrogen-decorated surface, as seen by the reversibility of a distinct state at a kinetic energy of 11.5 - 12 eV (Figure 6.10 (b) (iii)), or approximately 8.3 - 7.8 eV from the cutoff point of MDS. This state increases in intensity as a consequence of exposure to atomic hydrogen and then significantly reduces after annealing which suggests that the emergence of this state is most likely due to the adsorption of hydrogen on the surface. Further evidence for hydrogen adsorption is supported by the fact that the pressure in

the chamber increased by a small amount almost immediately upon annealing to temperatures greater than 673 K where hydrogen has been previously reported to desorb from the surface of the buffer layer [268].

The origin of feature (iii) in Figure 6.10 (b) is believed to be the same as for the MDS spectra of graphite and graphene, where there is an effective overlap between the ground state of the He 2^3S atom and out-of-plane orbitals of the surface. However, for the graphane-like (hydrogenated graphene-like) case, instead of $2p_z$ orbitals from π bands, there are bonds which stick out of plane as a result of the sp^3 hybridisation which shield in-plane states within the carbon ring resulting in Auger de-excitation which dominates over RIAN for this surface. Furthermore, since graphane is a semi-insulating system, AD is more likely to be the dominant de-excitation mechanism over RIAN which is consistent with the sharp distinct peak observed in Figure 6.10 (b) (iii). To confirm whether this state is due to the change of hybridisation, the results obtained from MDS were compared to DFT simulations. As highlighted earlier in Figure 6.9 (c), at 6 - 8 eV from the Fermi level, there is an increase in the density of states for the carbon atom bonded to a hydrogen atom as a result of the sp^3 hybridisation for this atom. Therefore, the observed increase in the SDOS measured by MDS at 11.5 eV, Figure 6.10 (b) (iii), is most likely a result of formation of these sp^3 hybridised states across the surface between the carbon and the hydrogen atoms. These effectively overlap with the $1s$ state of the metastable helium atom resulting in AD occurring instead of RIAN for in-plane states. Finally, the origin of this state may also be evidence of some hydrogen intercalating underneath the buffer layer at domain boundaries, breaking the back-bonded state resulting in small regions of QFSG, since a similar peak is expected to appear as a result of the π-band of the QFSG. However, since hydrogen exposure was performed with the sample at room temperature, adsorption of atomic hydrogen on top of the buffer layer is expected to be the dominant contributor to the results obtained.

6.5.4 Quasi-Free Standing Graphene Layer

In order to intercalate hydrogen beneath the buffer layer to form QFSG [41], the sample must be annealed at temperatures above 723 K whilst exposing to atomic

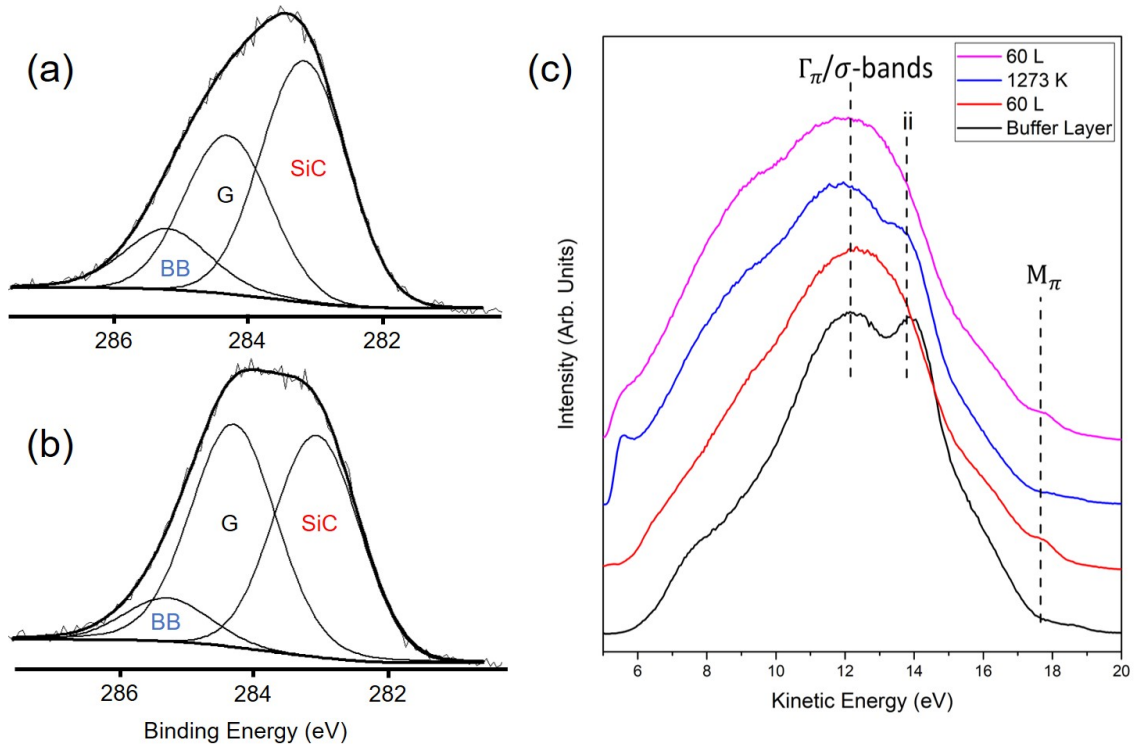

Figure 6.11: XPS of the C 1s core state (a) prior to exposing the buffer layer sample to atomic hydrogen and (b) following a 60 L hydrogen exposure whilst annealing the sample at 743 K. The C 1s peak can be deconvoluted into three peaks each with a FWHM of 1.5, and after subtraction of a Shirley baseline. This yields peak positions 283.1 eV, 284.3 eV and 285.3 eV which are assigned to SiC, graphene-like and back-bond states respectively. (c) Shows the MDS spectra obtained over several cycles of atomic hydrogen exposure and subsequent annealing at 1273 K.

hydrogen [170]. To achieve intercalation of hydrogen and breaking of the back-bond, once the buffer layer had been formed as confirmed via LEED, the sample was first annealed briefly at 1273 K to clean the sample. The temperature was then reduced to around 743 K and exposed to 60 L of hydrogen. The settings of the hydrogen cracker as well as the growth procedure were the same as used for formation of the graphane-like buffer layer.

As seen in the XPS C 1s scans shown in Figure 6.11 (a) and (b), the result of exposing the sample to atomic hydrogen whilst annealing the sample is a change in the C 1s peak as a result of a change in chemical environments [170, 180]. After subtracting a Shirley baseline function, the C 1s peak was deconvoluted into three peaks, one due to the SiC bulk (283.1 eV), one due to carbon-carbon bands (labelled 'G', 284.3 eV)

and one attributed to be primarily a result of the back-bond (labelled 'BB', 285.3 eV) based on previous XPS analysis of hydrogen intercalation by Virojandara *et al.* and Riley *et al.* [170, 180]. Prior to hydrogen exposure, the relative intensity of G is fairly low compared to BB and SiC. Following intercalation of atomic hydrogen, the relative intensity of G has increased significantly in comparison to the SiC peak whilst the BB peak has decreased in intensity, indicating an increase in the carbon-carbon chemical environment. These changes to the relative intensity of these peaks are consistent with the formation of a QFSG layer, since the Si back-bond has now been broken freeing up more carbon atoms at the surface. The changes observed were also seen in previous monochromated XPS measurements [41, 180]. Upon annealing, it was found that this increase in peak G was reversed and this change in the XPS was observed to be reversible over multiple cycles of exposure to atomic hydrogen and annealing.

The reversal of the intercalation of atomic hydrogen is also represented clearly in the MDS spectra as can be seen in Figure 6.11 (c). Before exposure to hydrogen, the buffer layer MDS spectrum shows peaks at kinetic energies around 11.5 eV and 13.9 eV due to π hybridisation at the Γ point and σ-band states respectively. Following exposure to atomic hydrogen whilst annealing the sample, at 17.8 eV there is a broad slope which can be attributed to the flat part of the π-band at the M point. Based on previous MDS analysis of graphene [117], it would be expected that this peak would be nearer to 16.8 eV rather than 17.8 eV, as the peak associated with the M point has been observed and calculated to be 3 eV away from the Fermi level. However, this considers charge-neutral graphene, where the Fermi level is at the centre of the Dirac point. As discussed earlier, QFSG is slightly p-doped as seen in CASTEP simulations (Figure 6.8 (f)) as well as previously measured by ARPES [41]. If the QFSG is doped, then states such as the M_π state will be shifted closer to the cutoff point as is observed in Figure 6.11 (c). Furthermore, as seen in Figure 6.9 (d), there is a sharp increase in the PDOS at a binding energy of 2 eV which is a result of π-band states. Since the feature observed in the MDS spectrum is also approximately 2 eV from the Fermi level and MDS only probes the topmost surface states, i.e. carbon states in the buffer layer, then based on Figure 6.9 (d), the observation of this state in the MDS is further evidence of formation of a QFSG

layer. This feature is broad as a result of RIAN being the dominant de-excitation process as has been previously observed for graphene on other substrates [122].

The other change to the MDS spectrum as a result of hydrogen intercalation is a decrease in relative intensity of (ii) and evolution of a broader feature centred around 12 eV in kinetic energy. This is partially a result of the flat part of the π-band at the Γ point as discussed earlier. However since this feature is broad, it is unlikely that AD is the dominant de-excitation mechanism here and instead RIAN is believed to more likely have occurred. Since RIAN appears to be the dominant de-excitation mechanism here, the feature observed at 12 eV is a contribution from not only the π-band state at the Γ-point but also in-plane σ-band states of QFSG [117]. Since the intercalation of atomic hydrogen only results in a 'quasi-free' layer of graphene, it is still more tightly bound to the substrate than successive layers of graphene and it is believed that this has resulted in the $2p_z$ states not overlapping as effectively with the $1s$ state of the He 2^3S atom as it does for a single layer of graphene. This broad feature seems to have shifted closer to the cutoff point which once again appears to be further evidence of p-doping within the QFSG. Upon annealing at 1273 K, this broad feature and the M_π state are reversed with re-observation of peak (ii) suggesting the hydrogen has desorbed from the surface. Further intercalation of atomic hydrogen was performed as shown by the indigo line labelled 60 L in Figure 6.11 (c), where a similar set of changes to the spectrum were observed thus showing the reversibility of QFSG formation [41].

The effect of hydrogen intercalation on the UPS spectra can be seen in Figure 6.12. Following a 60 L exposure whilst annealing the sample, a decrease in the DOS at 1.3 eV is observed along with a stronger presence of states at around 2 eV and a shift in states labelled (iii) further away from the Fermi level. Comparing this to the UPS spectra presented in Figure 6.10 (a), none of the above changes to the DOS were observed when the sample was at room temperature and exposed to atomic hydrogen. Additionally, as discussed earlier, (ii) is the state associated with the back-bond between the buffer layer and subsurface silicon atoms. A change in the DOS at around this energy is therefore consistent with the idea that this back-bonded state has been influenced by exposure of the buffer layer to atomic hydrogen. Furthermore, as for the MDS spectra, the presence of states at 2 eV from the

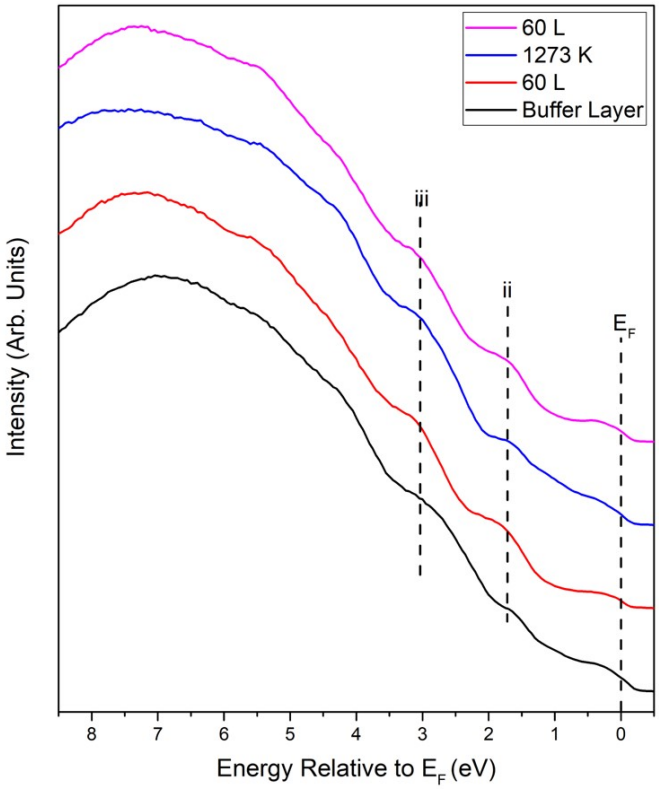

Figure 6.12: UPS spectra of the buffer layer following cycles of exposure to 60 L of atomic hydrogen with the sample at 743 K and annealing at 1273 K.

Fermi level can be associated with the π-band at the M-point as a result of carbon atoms whose back-bond has been broken forming Si-H bonds instead. Therefore, the UPS spectra presented in Figure 6.12 appear to provide further evidence of formation of QSFG when having annealed the SiC sample whilst exposing it to atomic hydrogen. Upon annealing at 1273 K, these changes to the UPS spectrum are reversed as expected and further exposure to atomic hydrogen results in the same changes reappearing therefore further demonstrating the reversibility of QSFG as has been previously reported [41].

In conclusion, the results presented here demonstrate the reversible formation of QSFG. Both the MDS and UPS spectra show the QSFG layer to be p-doped which is believed to originate from the "spontaneous polarization" of the hexagonal SiC substrate. Formation of the M_π state is observed in both the UPS and MDS spectra when exposing the buffer layer to hydrogen and vanishes after annealing the surface to temperatures above 1273 K. These results hopefully shed further light on how the buffer layer can be activated so that it could then be be tailored for spintronic

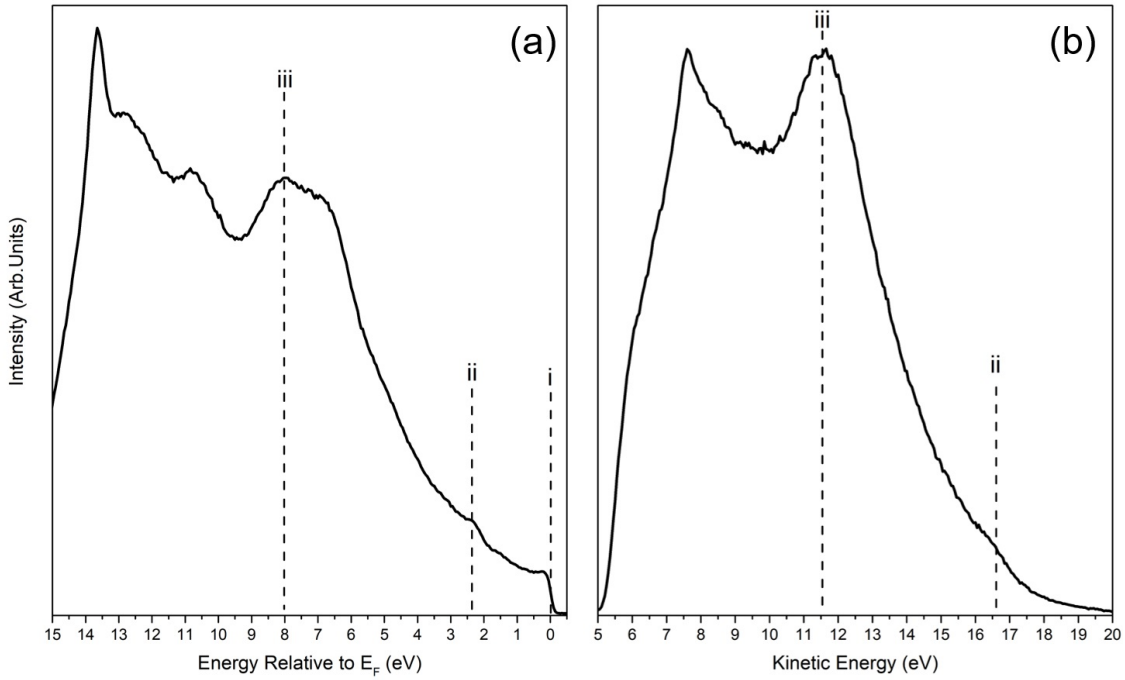

Figure 6.13: (a) UPS and (b) MDS spectra of a SiC sample following extensive annealing at a temperature above 1573 K.

or hydrogen storage applications.

6.6 Graphitisation of SiC

Annealing to temperatures above 1573 K for even a small period of time results in significant graphitisation of the sample due to a higher rate of Si desorption from the surface [41, 238]. After annealing for two minutes at this temperature, the LEED I/V curve is similar to that for a bilayer of graphene on SiC, as seen in Figure 6.7 [171]. Figure 6.13 shows that, after 30 minutes of annealing the SiC sample at 1573 K, the UPS and MDS spectra are consistent with those observed for HOPG [117, 258]. Firstly, the UPS spectrum shows a strong presence of states at the cutoff point, Figure 6.13 (a) (i). A sharper Fermi edge at the cutoff point is associated with an electronic transition at the surface to a more metallic-like phase. Fairly sharp features at 2 - 3 eV (ii) and at 8 eV (iii) are associated with π hybridisation at the M and Γ points in reciprocal space. The observation of these states is consistent with the formation of graphite at the surface of the SiC.

Graphitisation of the sample is also clearly seen in the MDS, Figure 6.13 (b). At around 3 eV from the cutoff point there is a clear shoulder which is associated with the π-band state at the M point in reciprocal space. The broadness of this state is consistent with previous MDS measurements of graphene, further demonstrating resonance ionisation and Auger neutralisation to be the dominant de-excitation channel for this state [117]. At $\approx$ 8 eV from the cutoff point (11.5 eV) there is a sharp peak which, as discussed, before is associated with Auger de-excitation occurring for the flat part of the π band at the Γ point in reciprocal space. Both of these peak positions are similar to those of charge-neutral graphene [258] when compared to QFSG where the states are shifted closer to the Fermi level. Therefore, the results presented in Figure 6.13 (b) are consistent with the formation of multilayer graphene/graphite further demonstrating that significant Si desorption can occur by annealing SiC to temperatures above 1573 K for extended periods of time [238]. The graphitisation of this particular SiC sample was also visible due to a change in the SiC crystal colour from green to black.

6.7 Intercalation of Erbium

To observe possible proximity-effect SOC in graphene grown on SiC, large SOC of around 100 meV can be introduced through the intercalation of elements with a large atomic number [93]. Rare earth metals (REs), with their high Z values, present a possible way of introducing a large SOC within graphene. For this reason, Anderson *et al.* investigated the intercalation of Eu between monolayers of graphene and the buffer layer, observing that it could intercalate [90], as well as the magnetic properties of different REs on graphene/SiC [271]. Two outstanding questions relating to these systems are: which REs can intercalate, and do they induce significant proximity-effect SOC within graphene? In this project, erbium intercalation was explored with the interest of breaking the Si back-bond of the buffer layer and enhancing the SOC within QFSG. Further motivation for using erbium and other REs is that monolayers of the lanthanide group have been grown on silicon to form nanowire Schottky barriers providing applications within electronics for fast-switching-action diodes [272, 273]. Additionally, rare earth metals combined

with semiconducting substrates have been suggested to result in a variety of low-temperature phase transitions such as charge density waves [274]. If erbium can intercalate underneath the buffer layer and break the back-bond, it could result in interesting electronic interactions with the buffer layer as well as possible formation of a quasi-free standing layer of graphene.

6.7.1 LEED and LEED I/V

Following the formation of the buffer layer by annealing the sample at 1473 K for 30 minutes, the sample was then covered with 0.5 ML of erbium at room temperature ($\rho = 8.795$ gcm^{-3}, thickness of an Er monolayer $\tau = 2.36$ Å [275]). Following deposition, none of the LEED spots were visible at any energy as indicated in Figure 6.14 (b) implying formation of an amorphous layer at the surface of the buffer layer and significant electron scattering as a result of the erbium. By annealing for 5 minutes in increasing 100 K steps, the $6\sqrt{3}$ LEED pattern was eventually recovered at 1073 K, with a similar LEED I/V curve to that prior to deposition, Figure 6.14 (e). Partial recovery of the $6\sqrt{3}$ periodicity is consistent with a proportion of the surface now being exposed such that erbium has not changed/influenced the surface structure of the buffer layer. Therefore, this would suggest that annealing an Er/buffer layer sample to 1073 K either results in Er desorbing from the surface, or alternatively, Er clustering at the surface. It is more likely that Er clusters at the surface when annealing the sample to 1073 K since Anderson *et al.* reported Eu to cluster at the buffer layer within a similar temperature range [90].

Annealing above 1073 K results in a significant change to the LEED and LEED I/V as seen in Figure 6.14 (d) and (e), with the subsidiary spots of the $6\sqrt{3}$ periodicity being heavily suppressed over a range of beam energies and at 126 eV, the graphene spot becoming much lower in intensity. This change in intensity of the graphene spot at 126 eV is further reflected in the LEED I/V, where the intensity curve after having annealed at 1273 K is significantly different from the non-deposited and post-1073 K anneal curves. The most notable changes in the intensity curve are the suppression of the Bragg peak at 110 eV and a change in the Bragg peaks observed between 70 - 80 eV. As mentioned earlier, the observation of these characteristic Bragg peaks

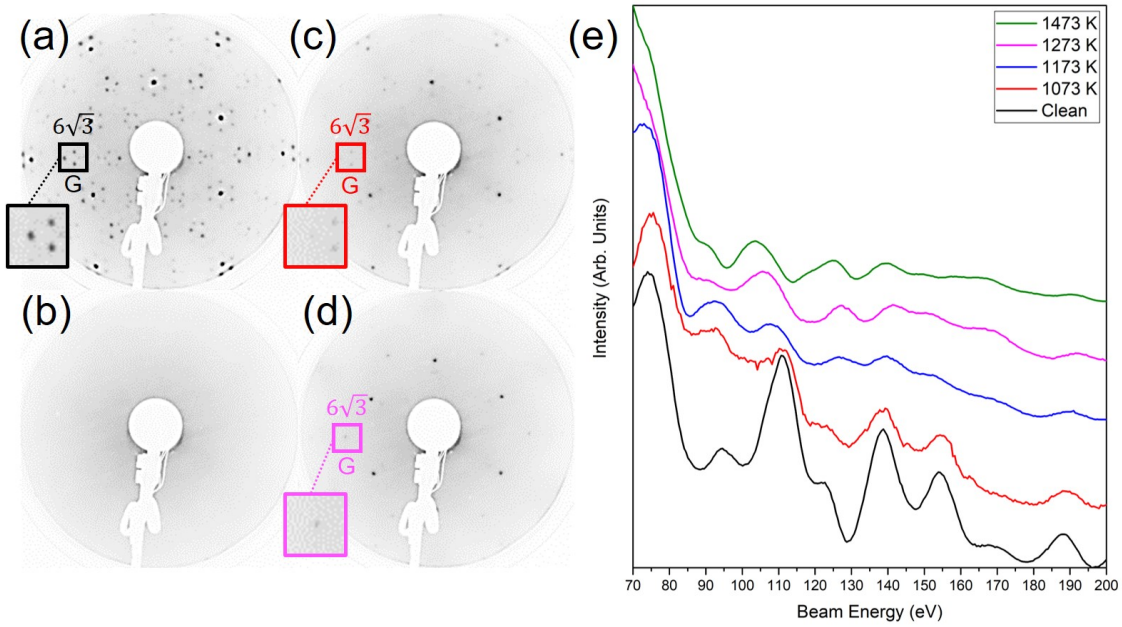

Figure 6.14: LEED images taken at 126 eV of (a) the buffer layer followed by (b) 0.5 monolayer deposition of erbium at room temperature. This 6H-SiC sample was then annealed in increasing 100 K steps. Following an anneal at (c) 1073 K the LEED spots are similar (although fainter) to those prior to deposition, but this then changes at 1173 K where a suppression of the graphene spot and subsidiary spots is observed and at (d) 1273 K there is a significant change to the overall LEED pattern. (e) The change in LEED is reflected by a change in the LEED I/V indicating a structural change at the surface of SiC after annealing above 1173 K.

is an indication of formation of buffer layer graphene. The suppression and change of Bragg peaks around 70 - 110 eV of the LEED I/V spectrum are therefore a strong indication of structural changes close to the surface (within the first few atomic sublayers) based on the information depth of electrons within this energy range (Figure 4.5). Changes to the LEED and LEED I/V appear to suggest that erbium has either desorbed at 1273 K leading to vacancies at the surface, clustered in a manner that is distorting the buffer layer, or has intercalated underneath the buffer layer. Similar to Eu, it is believed that annealing the Er/buffer layer to temperatures above 1273 K results in erbium intercalation and breaking of the Si-C back-bond [90]. However, since the spots associated with the $6\sqrt{3}$ periodicity are still observable following an anneal at 1273 K, this suggests that if erbium has intercalated, then it most likely has formed an amorphous layer underneath

the buffer layer as a uniform layer of erbium is expected to result in considerable electron scattering leading to even more significant changes to the observed LEED pattern and LEED I/V spectra. Annealing the SiC sample to 1473 K for 5 minutes shows a similar LEED I/V curve to that observed at 1273 K. This LEED I/V curve is neither similar to the clean surface nor the bilayer LEED I/V curve (Figure 6.7) and therefore strongly suggests that the erbium has remained after annealing at such temperatures. This is somewhat unexpected since Anderson *et al.* observed europium to "deintercalate" and desorb from the surface at 1473 K. However, they also remark that REs were observed to only desorb after "prolonged annealing" at 1473 K [271]. Annealing SiC at temperatures above 1473 K for longer periods of time leads to further graphitisation of the sample and therefore it is expected that this would also result in any RE or adsorbed atomic species desorbing from the surface. Since this sample was only annealed for a short period of time, it is believed that erbium has still remained.

6.7.2 XPS of 0.5 ML and 2ML deposition

To confirm whether erbium had remained at the surface of buffer layer/6H-SiC following an anneal at 1473 K (as well as possibly having intercalated), the same sample as discussed above, was removed from the LEED I/V UHV system and then placed into the electron spectroscopy UHV system. A survey scan using monochromated XPS revealed a weak presence of states at 450 eV and and a stronger presence of states between 160 - 200 eV corresponding to the Er $4s$ and $4d$ core states respectively, as is seen in Figure 6.15. Whilst there are states present between 160 - 200 eV as a result of the Er $4d$ core state with a shoulder being observable at 168 eV, the relative intensity of this peak is weak and aside from this, it is difficult to distinguish the entire multiplet structure from the SNR. It appears that erbium has still remained at the surface of the sample despite it being taken out of vacuum as well as being annealed at higher temperatures, but the amount of erbium present is small. Additionally, the Er $4d$ core state exists at a similar energy to that of the electron loss peak of the Si $2s$ core state from surface plasmons and therefore it is possible that the observed feature in the XPS is a result of this peak and not a consequence

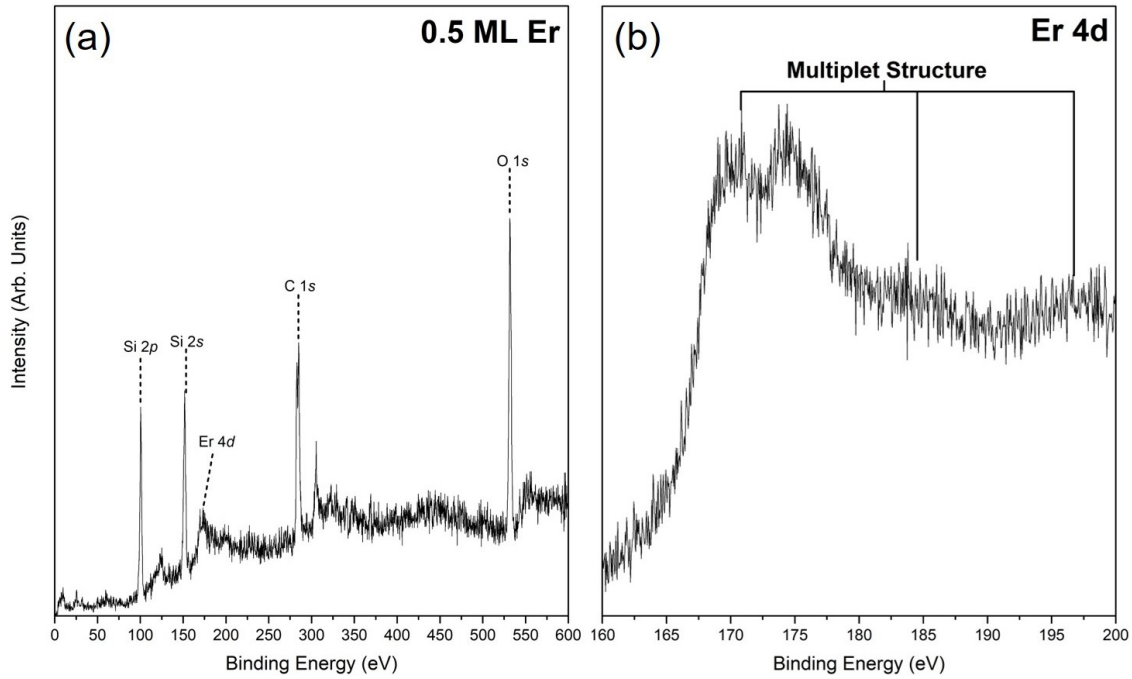

Figure 6.15: (a) A monochromated XPS survey scan of the sample and (b) a detailed scan of the Er 4d region ($E_B = 160 - 200$ eV, 1 s dwell time, 0.05 eV step size) of a SiC sample following deposition of 0.5 ML of Er, multiple annealing cycles and after removal from the LEED I/V UHV system. Both the survey and detailed scan reveal a weak Er presence.

of erbium.

To confirm whether the shoulder observed is a result of erbium, a fresh SiC sample was inserted into the electron spectroscopy system and the buffer layer prepared using the same conditions as before. A bespoke erbium evaporation source attached to the preparation chamber of the electron spectroscopy system was used where a current of ≈ 20 A is passed through a piece of erbium mounted in a tantalum boat. Following an anneal at 1273 K to clean the buffer layer, the sample was allowed to return to room temperature before deposition of 2 ML of erbium. A thicker coverage of Er was chosen in order to provide an XPS reference signal for this material and confirm whether the observed peaks for a 0.5 ML coverage were a consequence of Er.

As can be seen in Figure 6.16 (a), the survey scan following deposition shows the emergence of peaks at 160-200 eV (Er 4d), 325 eV (Er 4p), and 450 eV (Er 4s) as well as peaks at lower binding energies associated with the Er Auger MVV state.

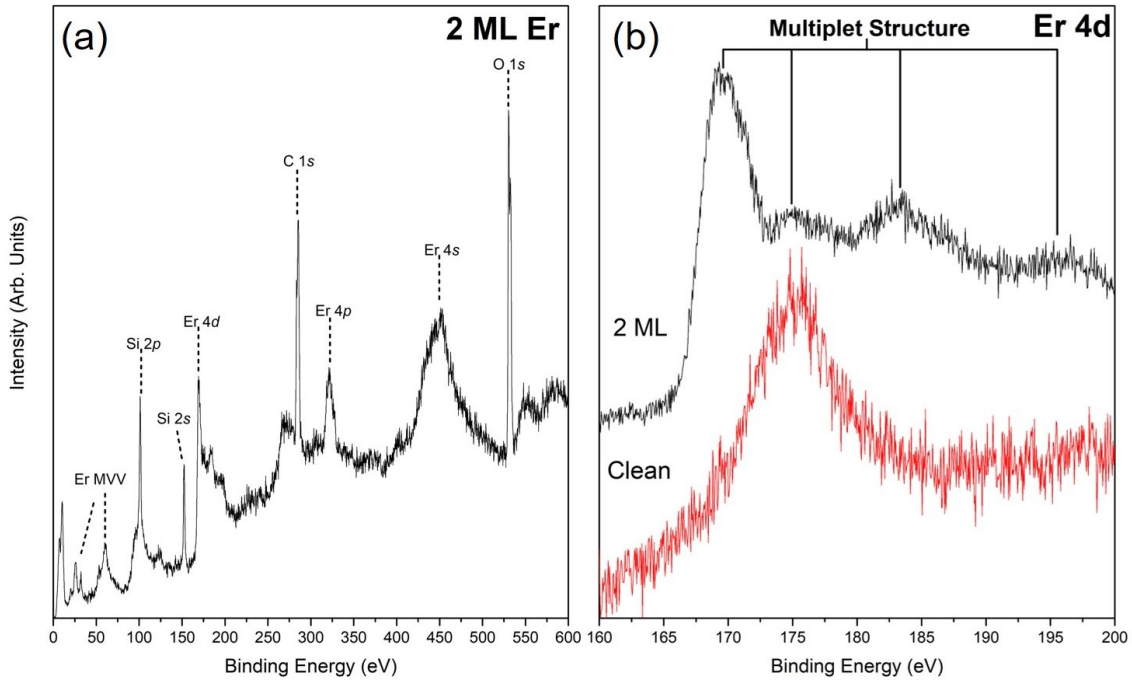

Figure 6.16: In order to distinguish between the Si 2s and Er 4d core states, 2 ML of erbium was deposited onto a clean buffer layer. The *in situ* survey scan (a), and a detailed scan between 160 - 200 eV (b) reveal a strong presence of Er 4d core states as well as the 4s and 4p core states at 450 eV and 325 eV.

Following deposition of 2 ML of Er, not only does the survey scan show a strong presence of states between 160 - 200 eV from the Er 4d multiplet structure, but also states at 450 eV and 325 eV associated with the Er 4s and 4p core states. These states are much more apparent than for the 0.5 ML sample. The difference in the region near the Si 2s core state between the clean surface and following 2 ML of deposition can be clearly seen in Figure 6.16 (b), with a strong shoulder at approximately 168 eV. The thicker film of erbium also reveals clearer observation of the 4d multiplet structure with states existing at 168 eV, 175 eV, 182.5 eV and 197 eV.

Comparing the spectrum in Figure 6.16 (b) to Figure 6.15 (b), the shoulder observed at 168 eV for 0.5 ML is the same shape and energy as for the 2 ML case supporting the idea that Er remained at the surface of the sample following an anneal at 1473 K. Additionally, comparing the 0.5 ML spectrum to the clean spectrum, it can be seen that the second peak in Figure 6.15 at 176 eV is a result of the electron loss peak from the Si 2s core state. The intensity of the two peaks (168 and 176 eV) in Figure 6.15

are similar, which is consistent with the idea that only a small amount of erbium is present near or at the surface of the 0.5 ML sample. By having annealed at 1473 K, it is possible that some of the erbium has desorbed from the surface as a result of further graphitisation of the SiC which can occur at such temperatures. Therefore, the XPS measurements made for the 0.5 ML case strongly suggest that once erbium has been deposited on the sample, that it is extremely difficult to remove it by annealing the sample without further graphitisation of the SiC.

To summarise, LEED, LEED I/V and XPS results appear to show that erbium can intercalate underneath the buffer layer as a result of annealing the sample to 1273 K, where it is then believed to break the back-bond leading to formation of QFSG. Similar to other REs, erbium, once intercalated, is difficult to remove without further graphitisation of the SiC. To further develop on the work presented above, it would be interesting to explore intercalation of Er using MDS and UPS as well as perform SPMDS to see whether possible proximity-effect SOC is induced within the QFSG layer.

6.8 Summary

In this chapter, 6H-SiC has been explored both experimentally and theoretically in order to shed further light on graphene growth on this substrate, the influence of intercalation of different atomic species on the buffer layer, and how it could be tailored for spintronic applications. DFT simulations using CASTEP support previous calculations, showing that the adatom-terminated $(\sqrt{3} \times \sqrt{3})R30^\circ$ surface reconstruction favours the Si(T_4) site over the Si(H_3) site for the silicon-rich face. The surface state from this adatom is clearly seen via UPS through intense emission near the cutoff point. Furthermore, this surface reconstruction has been explored for the first time using MDS showing a clear state at around 8 eV from the Fermi level due to back-bonding between the adatom and the substrate.

Transitioning from the $(\sqrt{3} \times \sqrt{3})R30^\circ$ to the $(6\sqrt{3} \times 6\sqrt{3})R30^\circ$ surface reconstruction results in the surface state changing to a back-bonded state near the cutoff point and development of a stronger Fermi edge in the UPS spectrum. The effects

of decoration and intercalation of atomic hydrogen on the buffer layer were explored using MDS and UPS with supporting calculations using CASTEP. Due to the surface sensitivity of MDS, the decoration of atomic hydrogen resulted in an intense peak being observed at approximately 8 eV from the cutoff point. To explain this, PDOS of specific carbon atoms in the buffer layer were computed, with one back-bonded and one decorated with atomic hydrogen. A similar peak in the PDOS is predicted to exist at 8 eV due to carbon p states for the hydrogen-decorated carbon atom. Comparing this to the literature, the origin of this peak can be explained as an effective overlap between the sp^3 hybridisation of the hydrogen-decorated carbon and the $1s$ state of the He 2^3S atom resulting in AD occurring instead of RIAN. MDS spectra of QFSG show a broad state at 2 eV and a broad shoulder at around 8 eV from the cutoff point as a result of π-band states at the M and Γ points in reciprocal space. The broadness of the feature at 8 eV is most likely a result of RIAN occurring instead of AD suggesting a mixture of the π-band state at the Γ point as well as in-plane σ-band states within the buffer layer. These states are shifted closer to the Fermi level as a consequence of p-doping of QFSG which is believed to originate from the "spontaneous polarization" of the hexagonal SiC substrate. Further demonstration of formation of QFSG is seen by the deconvolution of the C $1s$ core state where the back-bonded state decreases whilst the C-C chemical environment increases as a consequence of exposure to atomic hydrogen.

Annealing to higher temperatures resulted in multilayer graphene, indicated by the same characteristic peaks in the MDS spectra at 3 eV and 8 eV away from the cutoff point as well as a sharp presence of states at the Fermi level of the UPS spectrum. Contrary to QFSG, the observed states in the MDS are at binding energies associated with charge-neutral graphene.

Finally, to try and enhance the SOC within graphene and break the back-bond of the buffer layer, intercalation of Er was explored. Following deposition of 0.5 ML of Er, it was found that no LEED spots were observable until 1073 K where the Bragg peaks observed in the LEED I/V curve are at similar peak positions to those observed prior to deposition. Annealing to temperatures above this resulted in a significant change to the LEED I/V spectra and even after annealing at 1473 K, the LEED I/V curve remained different from that measured prior to deposition. Monochromated XPS

shows that this Er had remained near the surface after multiple annealing cycles which therefore strongly indicates that, similar to Eu, Er can intercalate and break the silicon subsurface back-bond. Furthermore, without further graphitisation of the SiC, removal of Er appears to be extremely difficult.

By using a range of complementary techniques, this chapter has helped provide a greater insight into the evolution of the 6H-SiC(0001) surface, formation of the buffer layer, and how it can be activated. Understanding changes to the DOS of the buffer layer as a result of adsorption or intercalation of hydrogen is crucial when designing SiC devices for a variety of applications whether it be hydrogen storage or spintronics. Additional evidence of the reversibility of the graphane-like buffer layer, the QFSG layer, and the controlled nature of growth of graphene provide further motivation for using SiC in both spintronic and hydrogen storage applications.

Chapter 7

Formation of the LSMO/6T Spinterface

One way of enhancing SOC in graphene through the proximity effect is by placing it on a ferromagnetic or ferrimagnetic substrate. As for magnetite, proximity-effect SOC has been observed in graphene on the ferromagnetic oxide LSMO [58] as a result of the breaking of inversion symmetry in the graphene leading to Rashba-type SOC [276]. LSMO is an attractive material for spintronic applications due to its half-metallicity up to 350 K, colossal magnetoresistance and its easily accessible metal-to-insulator transition making it an ideal material for sensor applications [8, 277]. LSMO has also frequently been used as the bottom electrode in organic spintronic devices, including the first demonstration by Xiong *et al.* of an organic spin valve [278]. This has helped identify the importance of the interface between organic molecules and ferromagnetic substrates in determining device operation and performance. Indeed, 'spinterfaces' are now considered separate spintronic entities that can be activated to show unique phenomena such as interfacial magnetoresistance [279] and magnetic hardening [280]. As for 2D material spintronics, understanding and engineering organic/ferromagnetic interfaces continues to be an essential task in the pursuit of next-generation organic spintronic devices. This chapter outlines an electron spectroscopy study of clean LSMO surfaces and the formation of monolayers of the organic semiconductor, α-sexithiophene (6T).

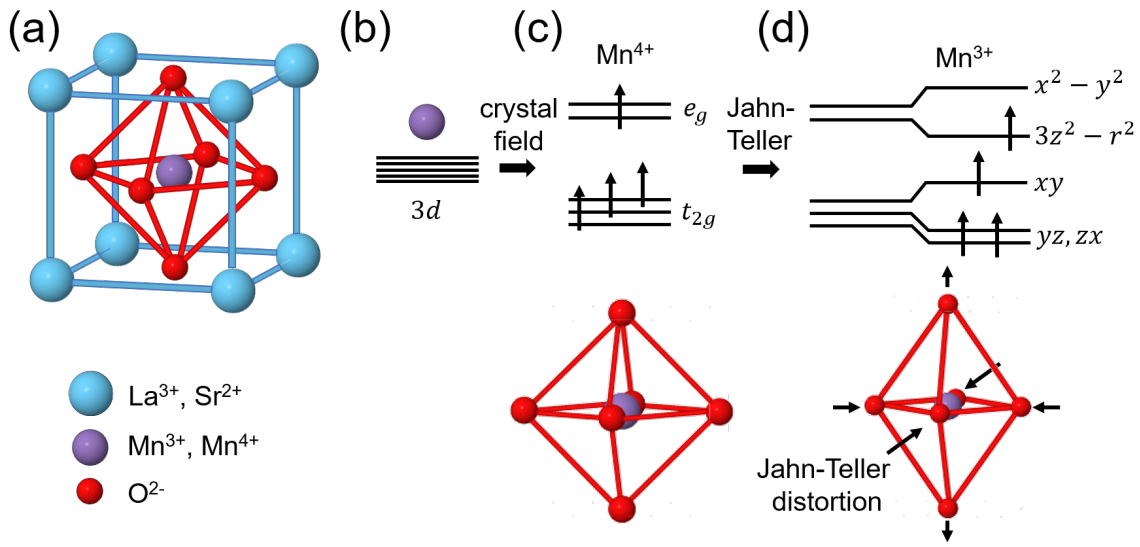

Figure 7.1: (a) LSMO has a perovskite crystal structure with La and Sr cations occupying the vertices, O anions at each face-centre and a Mn cation at the centre of the unit cell. (b) The Mn $3d$ orbitals are (c) split by the crystal field (1.5 eV) into two doubly degenerate e_g bands and three degenerate t_{2g} bands. (d) Due to Jahn-Teller distortion, the degeneracy of these states is further lifted and a single e_g state is occupied for the Mn^{3+} cation.

7.1 $La_{0.66}Sr_{0.33}MnO_3$

$La_{1-x}Sr_xMnO_3$ or LSMO is a hole-doped manganite [281]. The chemical formula for the manganite series is $AMnO_3$, where if A is one of the following elements, then the composition crystallises into a pervoskite structure: La, Ca, Ba, Sr, Pb, Nd, Pr [277]. As can be seen in Figure 7.1 (a), the crystal structure of LSMO is similar to that of a face-centred cubic (FCC) lattice with La and Sr cations occupying the vertices of the FCC lattice and oxygen anions at the face centres. However, additionally for any of the manganites, a Mn cation (both 3^+ and 4^+) occupies the centre of the lattice and so LSMO is considered a manganese perovskite oxide [281]. This perovskite structure results in the formation of a rhombohedral or orthorhombic (the so-called $GdFeO_3$ type) lattice [282]. The type of lattice is governed by the tolerance factor ($t = r_A + r_O/\sqrt{2}(r_B + r_O)$) where r_O, r_A and r_B represent the average ionic size of oxygen, strontium and manganese for LSMO; when $t = 1$, then the manganite is a perfect cubic perovskite structure [282].

In the bulk, the magnetic properties of LSMO originate from the Mn $3d$ orbital (Figure 7.1 (b)). This orbital is split by the crystal field into two degenerate e_g states and three t_{2g} states. Jahn-Teller distortion further lifts the degeneracy of these states and lowers the crystal symmetry where, for the t_{2g} triplet, all three electrons are aligned parallel ($S = 3/2$) whilst in the the e_g doublet, a single electron occupies the $3z^2 - r^2$ level and this occurs only for the Mn^{3+} cation [277, 281]. The Jahn-Teller interaction occurs as a result of the coupling between the manganese cation $3d$ state and the oxygen anion $2p$ states. This leads to a distortion in the crystal lattice, which is partially responsible for the magnetic behaviour of LSMO.

This ratio of La $(1 - x)$ to Sr (x) drastically influences various properties within LSMO. For example, the doping of Sr^{2+} cations within the crystal lattice results in a conversion of manganese cations from Mn^{3+} to Mn^{4+} and a half-filling of electrons in the conduction band. This half-filling results in holes in the valence band and therefore LSMO is regarded as a hole-doped manganite [281]. Varying the doping of divalent alkaline earth ions (Sr) also significantly influences the resistivity of the manganite. Undoped $LaMnO_3$ is an insulator and experiences antiferromagnetic ordering, but when doped ($0.1 \leq x \leq 0.33$), LSMO undergoes a metallic-ferromagnetic phase transition. The origin of this ferromagnetic ordering is currently believed to be a result of the ferromagnetic super-exchange interaction and not the double-exchange interaction which had been previously postulated [282]. Whilst double-exchange provides a qualitative explanation for metallic conduction below the Curie temperature (T_c), it fails to explain certain phenomena such as the high temperature phase [281]. The highest T_c (350 K) occurs when the ratio of Sr to La cations is 1/3 to 2/3. At higher levels of Sr (≤ 0.5) then LSMO will undergo an antiferromagnetic phase ordering.

In hole-doped manganites, the Mn t_{2g} states and the spin-up e_g band are completely separated from the minority bands by a large Hund's energy (≈ 2.5 eV) whilst the oxygen anion $2p$ states are fully occupied in both spin states [281]. Thus, the spin polarisation at the Fermi level is entirely determined by the hybridisation between the oxygen p states and the Mn e_g state. Since there is an insulating band gap between the oxygen $2p$ states and the minority spin states, only the majority spin-state e_g band at the Fermi level is occupied and hence LSMO is a half-metal [281].

As a result of changing chemical composition at the surface, the half-metallicity of LSMO breaks down at room temperature. Multiple measurement techniques including XPS, XRD, atomic force microscopy (AFM) and low-energy ion scattering have shown that at the surface of LSMO there is a strong Mn and Sr rich phase when compared to the bulk [283, 284]. In particular, XPS results indicate that La $3d$ and Mn $2p$ core states remain relatively unchanged whilst O $1s$ and Sr $3d$ core states are significantly influenced by the angle of the X-ray on the LSMO thus indicating a strong presence of Sr at the surface [283]. Annealing at temperatures around 973 K results in further Sr segregation to the surface which consequently drastically influences the electronic properties (such as the metal-to-insulator transition temperature) of the material [284]. The result of this, in addition to oxygen vacancies, is the destruction of the half-metallicity of LSMO, making it more difficult to incorporate in spintronic devices [285]. Furthermore, other dopants aside from Sr such as Pb have also shown segregation to the surface as a result of annealing the manganite and therefore when preparing the surface of LSMO for device applications, the annealing temperature must also be taken into account.

7.2 α -Sexithiophene

α-sexithiophene (6T), shown schematically in Figure 7.2, is an organic molecule with the molecular formula of $C_{24}H_{14}S_6$ and is part of the oligothiophene group. Since the first synthesis of thiophene oligomers in 1945 [287], there has been interest in utilising 6T in electronics, for example, due to its large field-effect mobility at room temperature [288]. Graphene combined with 6T has been used to create a field-effect transistor [288], and in spintronics, due to the antiferromagnetic coupling between 6T and Fe_3O_4, monolayers of 6T sandwiched between two ferromagnetic layers has been used to create a magnetic tunnel junction [289]. To form single crystals of 6T however, it has been found that without annealing the substrate, even after heavy deposition of 6T, only Volmer-Weber (island-by-island) growth is achieved and that it is only by annealing the substrate above 393 K that Stranski–Krastanov (island-by-layer) growth can be realised and a lamellae of 6T formed [290]. In order to fabricate 6T/magnetic layered devices for spintronic applications, further

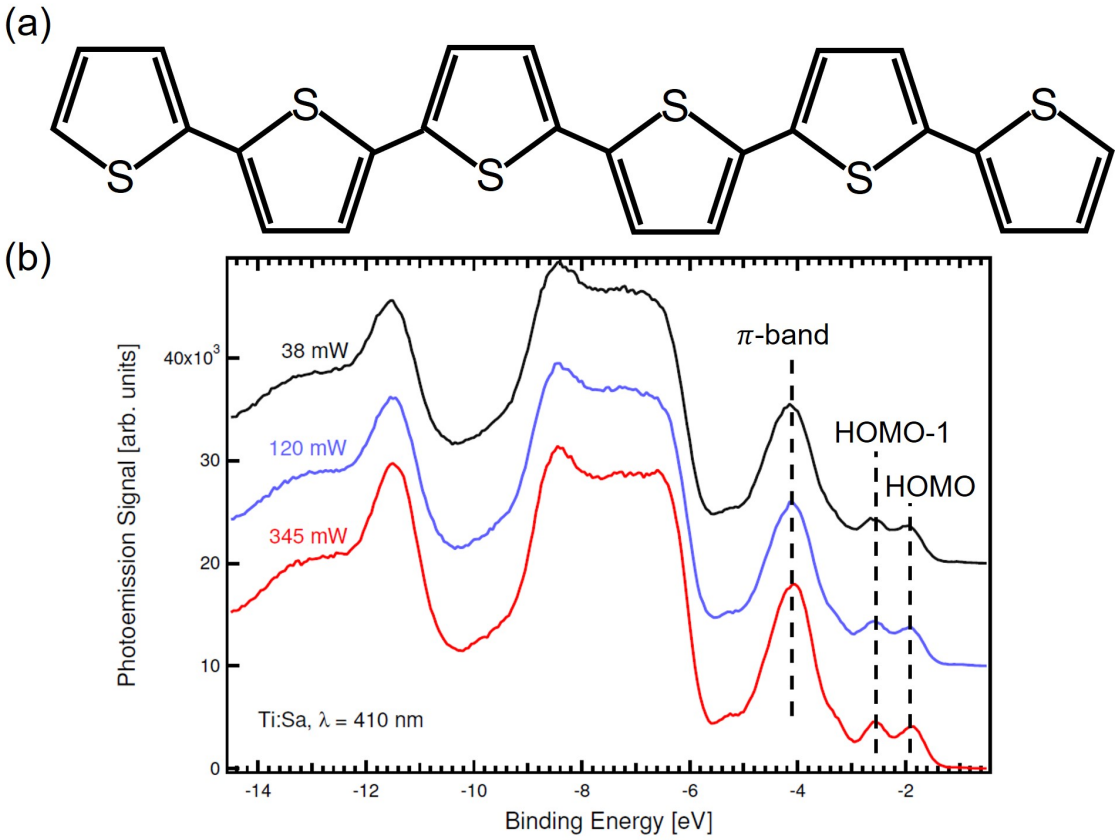

Figure 7.2: (a) α-sexithiophene (6T) is an organic molecule that is part of the oligothiophenes with the chemical formula $C_{24}S_6H_{18}$. (b) The photoemission response of 6T from a 50 eV laser as the power of the laser is adjusted using a series of different filters. (b) reproduced from [286].

understanding of the growth mechanism and electronic interaction it has with a magnetic substrate is required.

7.3 Clean LSMO

Thin films of LSMO ($La_{0.66}Sr_{0.33}MnO_3$) were supplied by Dr. Ilaria Bergenti of the Institute for Nanostructured Materials (ISNM) at CNR-Bologna as a part of a collaborative work on organic spinterfaces. These films were grown on $NdGaO_3(111)$ substrates via channel spark ablation, with an average thickness of 40 nm and surface roughness of around 0.6 nm; for more information on growth using charge spark ablation, the reader is encouraged to look at the work by Graziosi *et al.* [291]. LSMO prepared in such a manner has been used in a variety of devices including

memristors [292] and spin valves [293].

For the experiments described here, the LSMO samples were mounted onto e-beam sample plates and then placed into the electron spectroscopy system with no prior treatment. Monochromated XPS of an as-inserted sample was measured and compared to the spectrum following three cleaning cycles. Cleaning of the sample was performed by a gentle anneal at 503 K for 30 minutes using the pyrolytic boron nitride heater in the analysis chamber. It has been previously reported that annealing LSMO to temperatures as low as $\approx$ 500 K will result in oxygen vacancies at the surface [294] and higher temperatures will result in strontium segregation as well, which consequently modifies the electronic properties of the thin film [283]. LSMO prepared by channel spark ablation has been found by Jong *et al.* to be mostly free of carbon after annealing at 503 K with only a small contribution being measured via XPS due to $SrCO_3$ [294]. Furthermore, higher temperatures were seen not to influence the relative concentration of carbon present [294] and therefore, based on the literature, 503 K appeared to be a suitable temperature to clean the thin films used in this project. Finally, before any measurements were made, the sample was allowed sufficient time to cool to room temperature to prevent the metal-to-insulator transition from influencing the spectroscopic results.

As seen in Figure 7.3, various peaks in the XPS survey scans of the LSMO thin film become clearer following a couple of annealing cycles. The following peaks are observed post anneal: O KVV (976 eV), La multiplet split $3d$ (834 eV), Mn $2s$ (773 eV), Mn multiplet split $2p$ (642 eV), O $1s$ (530 eV), C $1s$ (285 eV), La $4s$ (278 eV), Sr $3p$ (268 eV), Sr $3d$ (133 eV) and La $4d$ (102 eV). Firstly, following annealing of the LSMO thin film, the relative intensity of the C $1s$ peak with respect to all other peaks has decreased. This is consistent with previous XPS analysis of channel spark ablation-grown LSMO thin films, where a small presence of carbon is observed as a result of $SrCO_3$ at the surface. Additionally, it can also be seen that by annealing the LSMO thin film, this has resulted in the emergence of the Mn $2s$ and La $4s$ core states, which prior to annealing are indistinguishable. The reduction in carbon and emergence of these peaks is a good indication of the surface being 'clean' and follows previous cleaning procedures used for preparation of LSMO spintronic devices [293]. It is also worth noting that by annealing to 503 K, this is

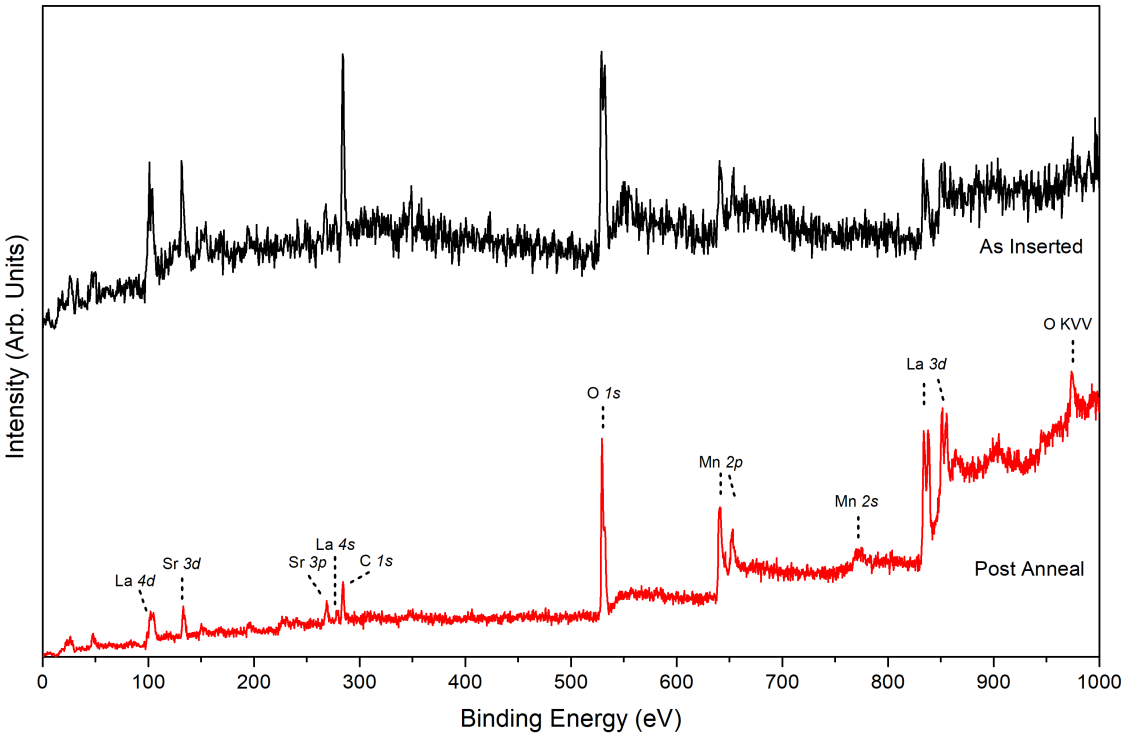

Figure 7.3: Monochromated XPS of a $La_{0.66}Sr_{0.33}MnO_3$ as inserted from air into UHV (black) and after three annealing cycles at 503 K for 30 minutes (red).

expected to have also resulted in oxygen vacancies and a more strontium-rich phase at the surface as has been previously reported [283, 294].

Following a couple of annealing cycles, both UPS and MDS of the clean surface were measured with the results shown in Figure 7.4. In the UPS spectrum, Figure 7.4 (a), up to a binding energy 8 eV relative to the Fermi level, are four distinguishable features. The state at the cutoff point is a result of the Mn e_g band and the shoulder at 2.6 eV is a result of the t_{2g} bands based on previous UPS measurements [285]. The shoulder associated with t_{2g} states is not as well defined as in [285] for a reference LSMO sample implying that there may be some level of defects at the surface influencing the electronic properties of the thin film. As discussed above, previous analysis of $La_{0.66}Sr_{0.33}MnO_3$ thin films found that oxygen vacancies occurred even after annealing at 500 K [294]. The observation of peaks at 5 eV and 6.5 eV relative to the E_F are associated with hybridisation between Mn t_{2g} and O $2p$ states. According to Picozzi *et al.* [285] who used He I α UV radiation to analyse LSMO(0001) thin films, since the peak positions are at 5 and 6.5 eV respectively, these hybridised states have been shifted to higher binding energies as

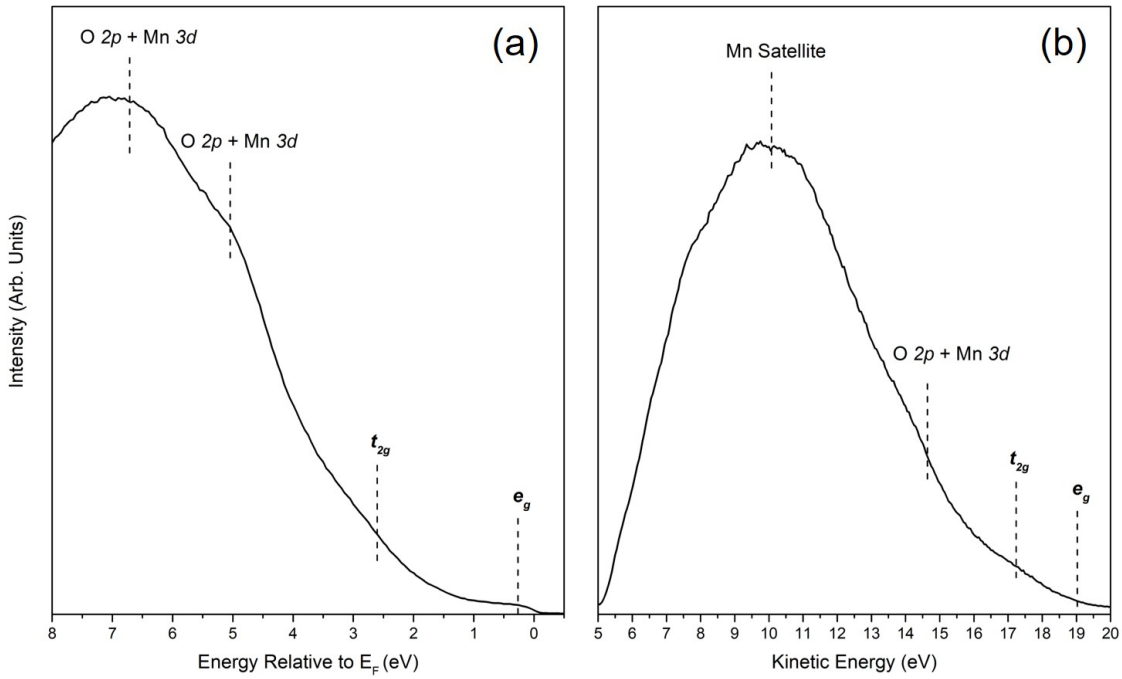

Figure 7.4: The UPS (a) and MDS (b) spectra of LSMO following three cleaning cycles at 503 K, each for 30 minutes.

a result of oxygen vacancies. This is therefore consistent with previous observations which show that annealing LSMO will result in the formation of oxygen vacancies at the surface [285].

The MDS spectrum of the clean surface, Figure 7.4 (b), can be compared to results obtained by Sakai *et al.* when looking at graphene growth on LSMO [295]. They reported that the features observed in the clean LSMO spectrum are a result of the metastable helium atom undergoing Auger de-excitation. Previous reports further support this statement with studies of other perovskite materials having similar spectra to that from He I α UV radiation [117]. With respect to the data presented in Figure 7.4 (b), a series of similar bands can be seen in the MDS compared to the UPS implying that AD is the dominant de-excitation mechanism for this surface. The broad peaks observed near the cutoff point (19.8 eV) at 19 eV and 17.3 eV can be attributed to the Mn e_g and t_{2g} bands. Further away from the cutoff point, a shoulder is observed at around 14.8 eV which, from comparison to the UPS, is a result of the hybridised O $2p$ Mn $3d$ state. According to Harada *et al.*, this will be primarily due to the O $2p$ outer orbitals which effectively overlap with the $1s$ state of the metastable helium atom [117]. Finally, at around 10.5 eV there is a very broad

shoulder which based on its peak position and previous literature, is a result of the Mn 3*d*-derived satellite caused by the final-state effect [295]. The features observed in Figure 7.4 (b) are less well defined than has been previously measured by Sakai *et al.* which is most likely further evidence for oxygen vacancies at the surface of these thin films.

7.4 6T Growth on LSMO

6T growth was calibrated based on AFM and XRD measurements made by Albonetti *et al.* for 6T/SiO_x [290]. Previously, it has been found that a 0.5 ML coverage has a thickness of 13 Å and a 3.2 ML coverage has a thickness of 81 Å. Therefore, 1 ML of 6T forms between 24 Å and 26 Å, with quartz crystal microbalance (QCM) values of $\rho = 1.4\ \mathrm{gcm}^{-3}$ and $Z = 1.0$ (for more information on using a QCM, see Appendix B). During deposition, the substrate was annealed at approximately 393 K. To anneal the LSMO gently, the W/Th e-beam filament in the preparation chamber was used (I=0.8 A) to heat the thin film through thermal radiation. α-sexithiophene molecules were produced using a MBE-Komponenten NTEZ low temperature effusion cell by heating a 6T powder supplied by Sigma-Aldrich. The melting point is 563 K, but the powder was only heated to 493 K which according to Albonetti *et al.* equates to a deposition rate $\approx 0.04\ \mathrm{Ås}^{-1}$, an ideal rate for growth of 6T monolayers [290].

7.4.1 AFM

AFM measurements were performed by Dr. Cristiano Albonetti at ISNM for 6T deposited on LSMO as can be seen in Figure 7.5. It is worth noting that the same samples presented in Figure 7.5 were also prepared by Albonetti, however, preparation/growth of 6T on LSMO as analysed using MDS, UPS and XPS was performed by the author of this thesis instead. Using the same conditions described above, AFM was performed for 0.5 monolayer (ML) and 6 ML deposition to demonstrate the difference between submonolayer and multilayer coverages of 6T. The darker regions in Figure 7.5 (a) are the LSMO substrate and the bright features are a result of islands of 6T. At 0.5 ML, during the nucleation stage of Stranski–Krastanov

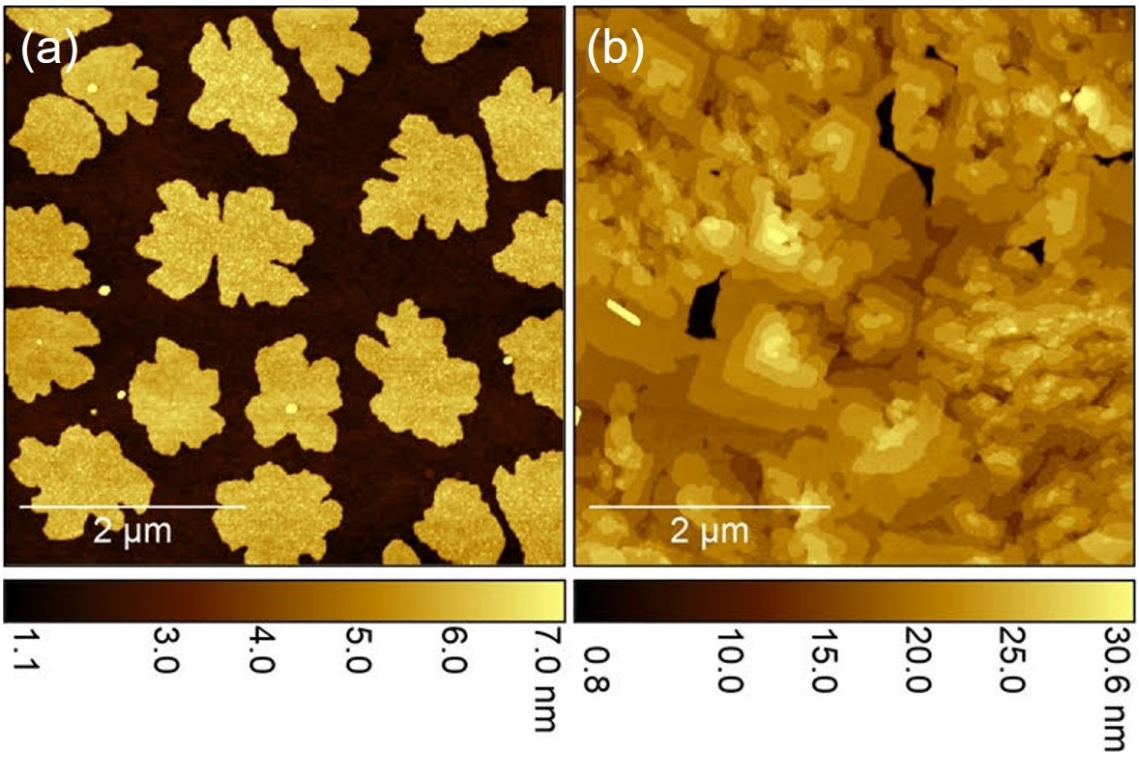

Figure 7.5: AFM of (a) 0.5 ML and (b) 6 ML of 6T on LSMO. Below each image is a colour bar representing the height scale of that image. During deposition, the sample was annealed at 393 K to ensure formation of lamellae of 6T since depositing at lower temperatures results in Volmer-Weber growth.

growth, 6T islands can be seen which, similar to growth on SiO_x, neither coalescence nor undergo Ostwald ripening [290]. Since the surface of the thin film is not patterned, round islands are formed with a random spatial distribution and a height of 40 ± 4 Å. The 6T molecules absorb preferentially along their long axis with respect to the surface, diffusing favourably across regions of lower surface roughness [290].

Transitioning from submonolayer to thicker coverages of 6T whilst annealing the thin film results in formation of µm lamellae across the surface. Small regions of the LSMO substrate are still observed after 6 ML deposition of 6T (Figure 7.5 (b)), which occur as the growth mechanism evolves from molecular diffusion at island edges towards a diffusion limited aggregation scenario (formation of fractal structures) [290]. Similar to submonolayer growth, for thicker coverages of 6T, the molecules stack preferentially along their long axis forming a monoclinic unit cell, with a c-axis height of approximately 44 Å [287]. Without annealing the thin film to temperatures around 393 K whilst depositing 6T, only Volmer-Weber growth will

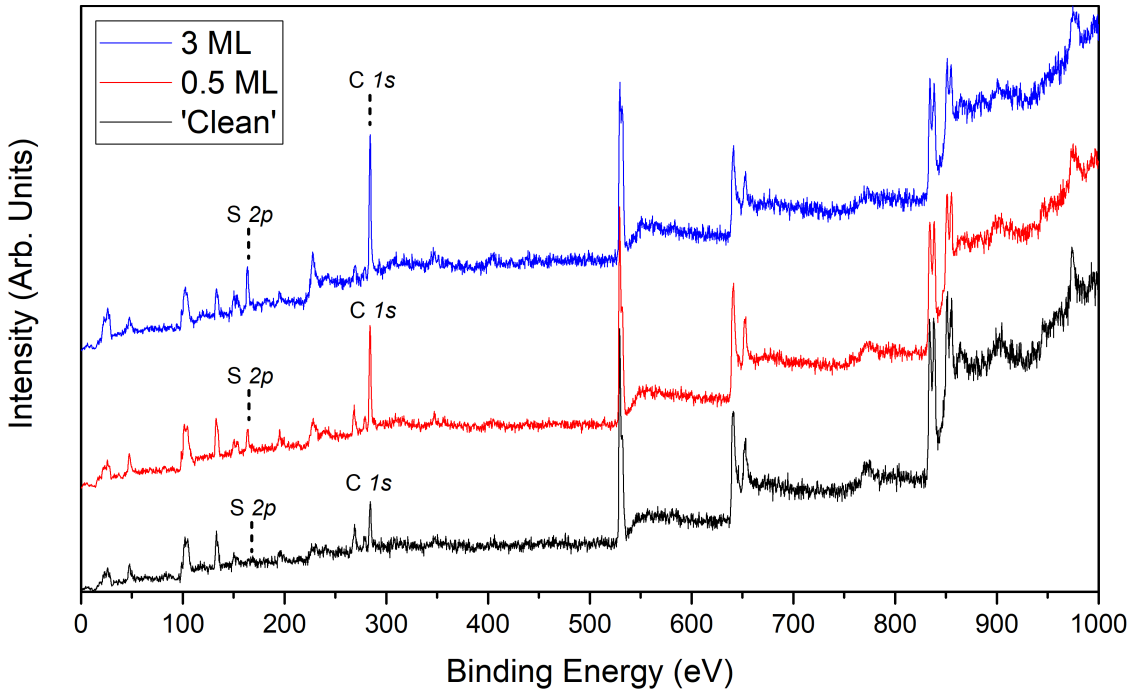

Figure 7.6: Normalised monochromated XPS of a $La_{0.66}Sr_{0.33}MnO_3$ thin film after being 'cleaned' (black), following deposition of 0.5 ML (red) and 3 ML (blue) of 6T whilst annealing the substrate at 393 K. As the coverage of 6T increases, the relative intensities of the C 1*s* and S 2*p* peaks increase.

occur rather than Stranski–Krastanov growth [290]. The latter is important for the fabrication of spintronic devices to ensure a smooth relatively defect free spinterface between the organic molecules and the ferromagnetic substrate. Therefore, it is important that the LSMO thin film undergoes a gentle anneal whilst depositing 6T to ensure formation of lamellae across the surface.

7.4.2 XPS

To further understand the difference between submonolayer and multilayer coverage of 6T on LSMO, a similar approach was performed in the electron spectroscopy system. Following three annealing cycles at 393 K, 0.5 ML and 3 ML of 6T were deposited on the LSMO thin film and XPS survey spectra obtained (Figure 7.6). As expected, increasing coverages of 6T results in the emergence of the S 2*p* core state (164 eV) as well as an increase in the relative intensity of the C 1*s* core state. Additional deposition of 6T was also accompanied by a reduction in the

relative intensity of peaks associated with Mn, La, Sr and O. The reduction in relative intensity of peaks associated with LSMO and increase in intensity of peaks associated with 6T between the 'clean' spectrum and the 3 ML spectrum is consistent with the idea of a thicker coverage of α-sexithiophene at the surface of LSMO. Since Mn, Sr, La and O peaks are observable after 3 ML deposition in the XPS survey spectrum, this is an indication that the coverage is within a few monolayers. For thicker coverages of 6T, the XPS signal would not be able to probe core states associated with the LSMO substrate as is seen similarly for increasing coverages of C_{60} on LSMO [157].

Transitioning between the clean surface and submonolayer deposition is likely to result in a change to the core state spectra observed due to a change in chemical environments present near the surface. Indeed this is the case when looking at the C 1s core state as seen in Figure 7.7 (a), where there is a visible difference between the 'clean' surface and following 0.5 ML deposition of 6T. Following subtraction of a Shirley baseline, the clean spectrum can be seen to be a convolution of three Gaussian-Lorentzian peaks according to Jong *et al.*, with positions 283.7 eV, 284.5 eV and 285.8 eV corresponding to the Sr-C, C-C and C-O/hydrocarbons chemical environments respectively [294]. After 0.5 ML deposition of 6T, the linewidth of the C 1s core state peak decreases and is shifted by approximately 0.2 eV to a lower binding energy. This peak was found to be (not shown in Figure 7.7 (a)) a convolution of two peaks with binding energies 284.9 eV and 283.9 eV corresponding to the C-C and β-C (from C-S) chemical environments respectively [296, 297]. The suppression of the C-O chemical environment and reduction in the linewidth of the C 1s core state is consistent with the observation of 6T formation at the LSMO surface. Increasing the coverage of 6T from submonolayer to multilayer results in no further changes to the C 1s core state suggesting that no additional chemical environments have been introduced. As shown in Figure 7.7 (b), transitioning between submonolayer and multilayer coverages of 6T appears to have not resulted in any visible changes to the S 2p core state spectra. The S 2p core state can be deconvoluted into three peaks at positions 164.7 eV (S_2), 163.8 eV (S_1) and 163.1 eV (B). Peak B is a consequence of the 'base' C-S chemical environment, whilst, according to Ohno *et al.*, the other two peaks (S_1 and S_2) at a higher binding energies

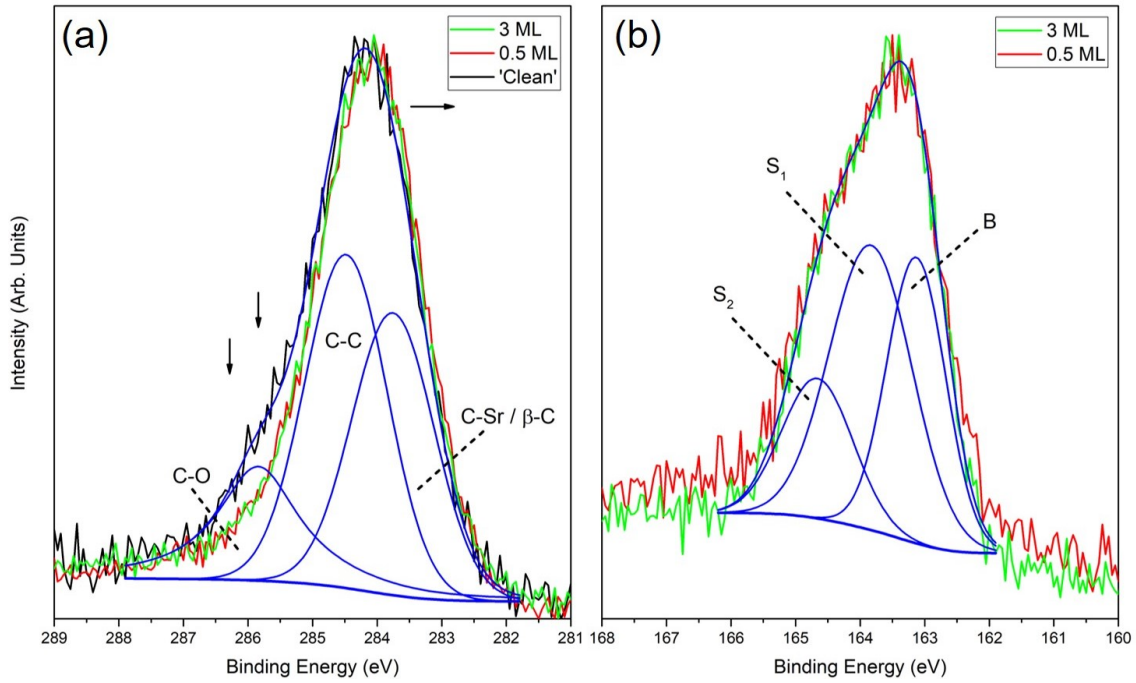

Figure 7.7: Normalised monochromated XPS spectra of the (a) C 1*s* and (b) S 2*p* core states (0.05 eV step size) as a result of different thicknesses of 6T. Black is the 'clean' surface following three annealing cycles, red following 0.5 ML deposition and green after 3 ML deposition. After subtraction of a Shirley baseline, the C 1*s* 'clean' surface and S 2*p* 3 ML deposition were both fitted using a series of Gaussian-Lorentzian peaks (blue) as described in the text. Arrows indicate the shift in the C 1*s* core state transitioning from the 'clean' surface to 0.5 ML deposition of 6T.

are a consequence of charge transfer between the 6T and the LSMO resulting in a 'positively charged' 6T molecule [296].

7.4.3 UPS and MDS

The result of depositing α-sexithiophene on LSMO is the observation of molecular orbitals in both the UPS and MDS spectra as can be seen in Figure 7.8. Photoemission studies of 6T single crystals [286, 298] show a number of distinct peaks relative to the Fermi level: HOMO, HOMO-1, HOMO-3 and π-band. The HOMO state is a result of C 2*p* orbitals within the thiophene whilst the HOMO-1 state is due to the hybridised π bond between the C 2*p* and S 3*p* states [298]. The HOMO-3 and π-band states are due to more tightly bound π bonding states arising from a mixture

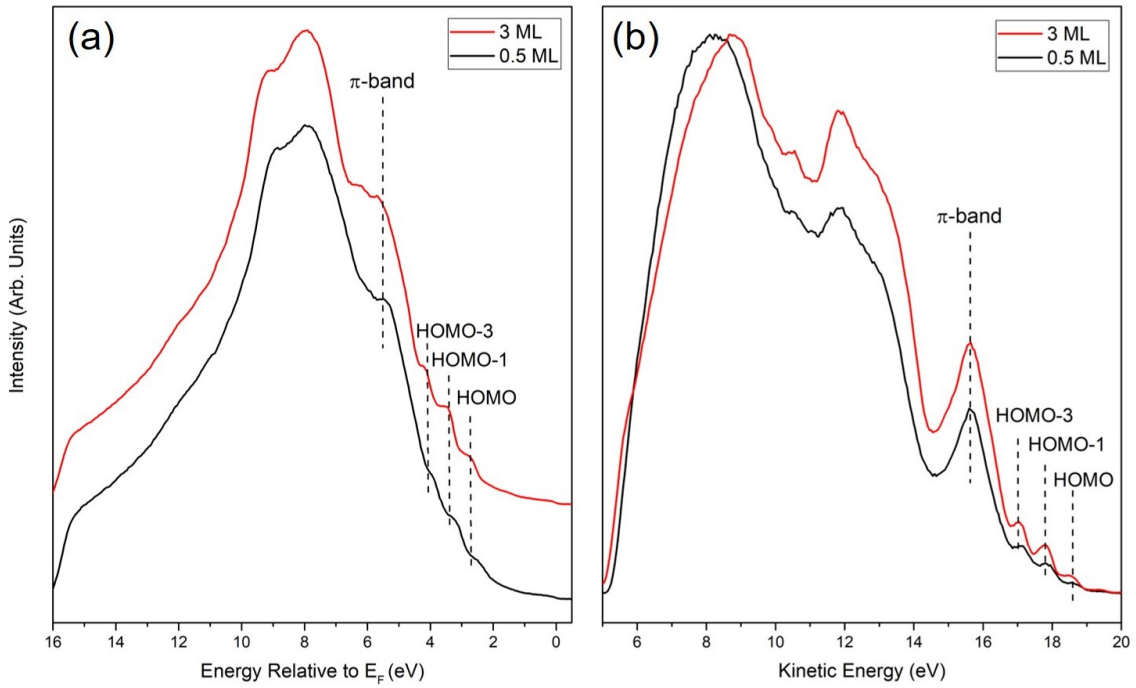

Figure 7.8: Normalised (a) UPS and (b) MDS spectra following deposition of 0.5 ML (black) and 3 ML (red) of 6T whilst annealing the sample at 393 K.

of S 3*s* and S 3*p* as well as C 2*p* states [286]. States at 6 eV and further away from the Fermi level are due to σ bond states within α-sexithiophene.

Relative to the Fermi level, as highlighted in Figure 7.8 (a), HOMO, HOMO-1, HOMO-3 and π-band states are observed at energies of 2.6 eV (HOMO), 3.4 eV (HOMO-1), 4.1 eV (HOMO-3) and 5.4 eV (π-band) in the UPS spectra. In the MDS spectra, the molecular state peak positions relative to the cutoff point are 1.2 eV, 2.0 eV, 2.7 eV and 4.1 eV. By subtracting the clean LSMO signal from the UPS spectrum for submonolayer and multilayer coverages, these molecular orbitals become more apparent as can be seen in Figure 7.9 (a). This technique has been used previously to measure the difference in peak positions between channel spark ablation-grown LSMO on different substrates ($NdGaO_3$ and $SrTiO_3$) [299]. As seen in Figure 7.9, the shape and separation of the observed peaks are similar in both the UPS and MDS spectra which is consistent with AD being the dominant de-excitation mechanism for both islands and lamellae of 6T [117].

Comparing the peak positions of the MDS spectra to previous photoemission spectra as well as DFT and Hartree-Fock calculations, the observed peaks are at similar binding energies with respect to the Fermi level [286, 298]. Transitioning between

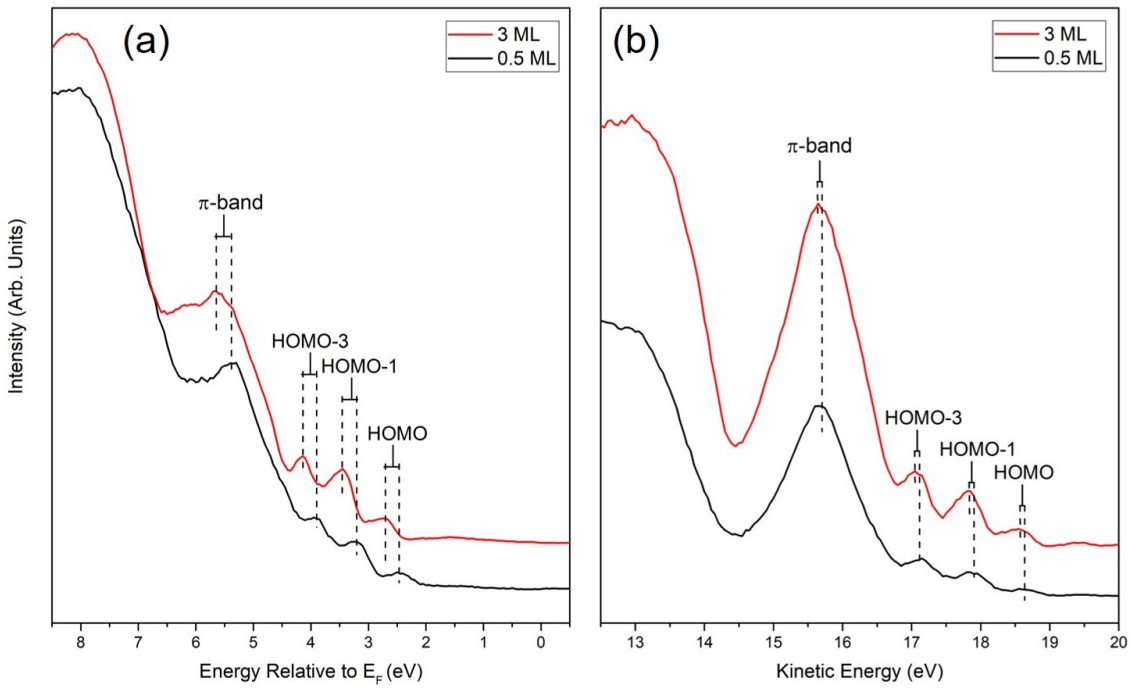

Figure 7.9: Following subtraction of the clean LSMO spectrum from the deposited 6T spectra, the normalised (a) UPS and (b) MDS spectra show more clearly the presence of molecular orbitals due to the 6T. The formation of multilayer 6T shows a shift of 0.2 eV away from the Fermi level in the UPS spectra.

submonolayer and multilayer coverage shows a slight shift in the observed molecular orbitals to higher binding energies (≤ 0.1 eV). As lamellae/single crystals of 6T form, as discussed earlier, the molecules preferentially stack along their long axis, tilted with respect to the surface arranging into a monoclinic unit cell [287]. According to Harada *et al.*, a shift in peak positions to higher binding energies in the MDS spectra for organic monolayers is a result of the molecules tilting as the unit cell forms [117]. This leads to site inhomogeneity of the top-layer molecules which then occupy various nonequivalent positions on the second-layer molecules, resulting in a slight shift in peak positions to higher binding energies [117].

By comparing the UPS spectra for submonolayer and multilayer coverages, it can be seen that a thicker coverage of 6T has resulted in an energetic shift of 0.2 eV away from the Fermi level. There are three possible reasons for this shift: (1) a change in the molecule or structure conformation; (2) chemical bonding between 6T molecules and the substrate; (3) electronic screening of the photoelectron from the hole produced from the photoemission process [286]. Using AFM and XRD, Albonetti *et al.*

report no change in the molecule or structure conformation of 6T when grown on SiO_x, which therefore suggests that the observed shift in the UPS spectra is unlikely to be a consequence of this. A change in chemical bonding seems unlikely as well since as the surface transitions from submonolayer islands to multilayer lamellae of 6T, in principle, no further chemical environments are introduced. The most likely possibility is electronic screening since, as discussed earlier, charge transfer between the 6T and the LSMO is believed to leave the 6T molecules at the LSMO/6T interface slightly positively charged [296]. This screening acts as a possible explanation as to why the peak positions observed in the UPS exist at higher binding energies ($\approx$ 1.4 eV) than observed for MDS. Since metastable helium atoms only probe the top-most states, the observed MDS spectra are unlikely to have been influenced by electronic screening from states at the LSMO/6T interface. In comparison, UPS probes both surface and subsurface states. This screening is also consistent with the deconvoluted XPS core state spectra described earlier. Therefore, the data presented here provide further evidence of charge transfer between 6T molecules and the LSMO surface.

7.5 Summary

The work presented in this chapter further explores the clean surface of thin films of $La_{0.66}Sr_{0.33}MnO_3$ as well as the growth of 6T monolayers on top of this surface using a variety of electron spectroscopy techniques. The MDS, UPS and XPS results shown here further demonstrate that the surface can be cleaned by annealing the LSMO thin film to 503 K. It can be seen that more strongly bound carbon remains at the surface despite multiple annealing cycles and, furthermore, annealing the LSMO thin films leads to formation of oxygen vacancies at the surface. These results show that channel spark ablation-grown LSMO films are good for growth of organic monolayers but are not structurally perfect.

AFM results show that lamellae of 6T can be grown on LSMO thin films by annealing the substrate to 393 K. Consistent with previous measurements made by Albonetti *et al.*, for non-patterned surfaces, submonolayer coverages of 6T result in islands with random spatial distribution. Transitioning to multilayer coverages results in the

formation of µm lamellae across the surface with 6T molecules stacking preferentially along their long axis.

Thicker coverages of 6T show an increase in the relative intensity of the C 1s and S 2p core states as expected. Analysis of the C 1s core state for a clean surface and a submonolayer coverage of 6T reveals a reduction in the relative intensity of the peak associated with C-O bonds and formation of C-C and β-C bonds from the 6T molecule. The S 2p core state appears to be a convolution of three peaks which according to Ohno *et al.* is evidence of positively-charged 6T molecules at the LSMO/6T spinterface.

Submonolayer and multilayer coverages of 6T were explored using both UPS and MDS. A shift in the peak positions to higher binding energies can be seen in both spectra. The shift in the MDS is believed to originate from the slight tilting in the 6T molecules similar to that observed using AFM. In the UPS, the observed shift of 0.2 eV is most likely a result of electronic screening from positively-charged 6T molecules at the LSMO/6T interface.

The work presented in this chapter helps develop a greater understanding of the LSMO/6T spinterface. Using AFM, the growth and formation of 6T single crystals has been characterised and the combination of MDS, UPS and XPS shows that charge transfer occurs at the interface. These results will help in designing LSMO/6T spintronic devices such as spin valves.

Chapter 8

Conclusions and Further Work

8.1 Conclusions

The work presented in this thesis demonstrates the first results from a spin-polarised metastable emission electron microscope, an extensive theoretical and experimental study of graphene on SiC and a brief study of α-sexithiophene molecules on LSMO. Following an introduction, since a large part of this project focused on utilising 2D materials for spintronic applications, Chapter 2 covers in detail how graphene can be tailored for devices by enhancing the SOC through the proximity effect. As both MDS and MEEM are uncommon techniques, Chapter 3 covers the various elements of a He 2^3S beam and how it interacts with a surface. This includes the de-excitation mechanisms of He 2^3S atoms, different methods of producing a metastable helium beam, and how the beam can be spin-polarised. Chapter 4 focuses on the various other experimental techniques which were used in this project.

In Chapter 5, $Fe_3O_4(001)$ was used as test system to see whether SPMEEM could map the surface spin polarisation of magnetic materials and image domain structures. By analysing the clean surface of magnetite, SPMEEM results revealed a significant spin canting effect at the surface of $Fe_3O_4(001)$, where the OP spin asymmetry was measured to be effectively the same as that observed IP. This spin canting effect at the surface is much stronger than previously reported and is believed to originate from uniaxial surface anisotropy. By using micromagnetic simulations and comparing pixel values of spin asymmetry measured IP and OP, the surface

anisotropy constant is estimated to be $1 - 2 \times 10^{-3}$ Jm^{-2}. It was found that a 1 L exposure to naphthalene resulted in a significant increase in the measured spin asymmetry by up to nearly $\approx 25\%$. This is believed to be a consequence of Auger de-excitation and charge transfer between the $Fe_3O_4(001)$ surface and the naphthalene. Furthermore, SPMEEM has also been used to support previous measurements of a spin reorientation phase at the surface of $Fe_3O_4(001)$. The domains observed using SPMEEM were found to change gradually from being small and distinct to broad, large features spanning tens of µm across with a significant change in domain shape and size observed at ≈ 143 K. This is a consequence of the change of the first-order magnetocrystalline anisotropy constant when approaching the Verwey transition temperature. Overall, the work presented in Chapter 5 reveals a new and powerful technique to characterise spin polarisation at the surface of magnetic materials which will hopefully provide a greater understanding of spin dynamics at the surface of such systems.

Based on the techniques described in Chapter 3 and Chapter 4, Chapter 6 explores the growth of graphene on SiC. Both the $(\sqrt{3} \times \sqrt{3})R30°$ and $(6\sqrt{3} \times 6\sqrt{3})R30°$ surface reconstructions of SiC have been explored for the first time using MDS and compared to UPS, showing the transition between the adatom-terminated surface and the buffer layer. By modelling the $\sqrt{3}$ reconstruction, the most stable adatom configuration for the (0001) polar face was found to be Si(T_4) top site, supporting previous *ab initio* calculations. Using MDS, the reversibility of a state due to the formation of a graphane-like buffer layer was observed and supported with DFT calculations. The state observed is a consequence of the formation of the sp^3 hybridisation between the hydrogen and the carbon which effectively overlaps with the ground state of the metastable helium atom. Reversibility of quasi-free standing graphene was also explored, showing the formation of a state around 2 eV from the cutoff point due to the π-band at the M-point in reciprocal space. This state is closer to the Fermi edge as a consequence of p-doping which arises as a result of the spontaneous polarisation of the SiC substrate. Preliminary work studying the intercalation of erbium was carried out using LEED, LEED I/V and XPS. It was found that following deposition of erbium on the buffer layer, annealing SiC samples to temperatures greater than 1073 K resulted in significant changes to the Bragg

peaks observed in LEED I/V, suggesting that erbium intercalates between 1173 - 1473 K. Furthermore, based on XPS and LEED I/V measurements it was found that following intercalation of erbium, removal of it is extremely difficult without further graphitisation of the SiC sample. The results presented in Chapter 6 further demonstrate how the buffer layer can be activated so that it could then be tailored for spintronic or hydrogen storage applications.

In Chapter 7, results from a study of thin films of $La_{0.66}Sr_{0.33}MnO_3$ are presented with both the clean surface and the growth of 6T monolayers investigated as part of a collaboration with Dr. Ilaria Bergenti of ISMN, Bologna. Preparation of the 'clean' surface was characterised using UPS, MDS and XPS. These results showed that channel spark ablation-grown LSMO films are good for growth of organic monolayers but are not structurally perfect due to oxygen vacancies and strontium segregation at the surface. Submonolayer and multilayer coverages of 6T were explored using AFM, UPS, MDS and XPS. AFM results show that lamellae of 6T can be grown on LSMO thin films by annealing the substrate to 393 K and electron spectroscopy measurements suggest charge transfer between 6T molecules and LSMO resulting in positively-charged 6T molecules at the LSMO/6T interface. The work presented in this chapter develops a greater understanding of the LSMO/6T spinterface which will help in designing LSMO/6T spintronic devices such as spin valves.

This thesis explores the surface properties of a number of different systems in order to further highlight how they could be tuned for spintronic applications. Surface sensitivity has been shown to be especially important in characterising 2D materials and organic/magnetic spinterfaces and therefore the development of SPMEEM, a new and extremely surface sensitive technique to map surface spin polarisation is incredibly beneficial in analysing a variety of spintronic systems. Production of high-quality graphene is key for 2D spintronic devices and since SiC presents itself as a route to production of such, Chapter 6 helps to further shed light on the graphitisation of SiC as well as activation of the buffer layer. Finally, considering the interest in utilising organic/magnetic spinterfaces for applications such as spin valves, Chapter 7 helps provide further insight into one such system and its electronic properties at the interface.

8.2 Further Work

Whilst SPMEEM was used to successfully characterise spin asymmetry at the surface of magnetite, it would be of interest to explore a wider range of magnetic surfaces and further compare results to those obtained from UVMCD. To achieve this, magnetic surfaces with a lower workfunction are needed since the UV laser is limited to 4.67 eV. Another interesting observation of the SPMEEM results was spin reorientation at low temperatures. Whilst this was observable via SPMEEM, unfortunately due to image drift and the long acquisition times for UVMCD, it wasn't possible at the time to obtain successful images of the magnetite surface at low temperatures using this technique. To develop on this, one approach would be to take multiple images and correlate this with an image tracking software to remove the influence of drift.

With regards to other ferro/ferrimagnetic systems to explore, a starting point would be to measure the spin asymmetry of the clean surface of nickel and then from there attempt to measure spin asymmetry in a monolayer of graphene on Ni(110). Other magnetic systems such as LSMO thin films could be explored as well, including its interaction with molecules such as 6T. It would be interesting to see whether similar to naphthalene, there is a significant influence to spin asymmetry as a result of formation of a monolayer of 6T. Due to the surface sensitivity of SPMEEM, ultimately it would be ideal to characterise spin asymmetry and possible spin accumulation at the edges of graphene/TMD heterostructures as a result of the intrinsic spin-Hall effect and then compare differences between different TMDs and their influence on graphene.

Graphene grown on SiC has also been used in conjunction with growing TMDs in order to observe charge-density waves (CDWs) [27, 300]. CDW states in TMDs exhibit an intricate interplay with superconductivity [300–302] and tuning TMD systems under extreme conditions can create an electronic instability such as a metal-insulator transition [27, 303]. Considering current interest in TMD/graphene heterostructures for spintronic and optoelectronic applications [25, 83], a suggestion for how to continue the work performed in this project is to look at TMD growth on the activated buffer layer, in particular to see whether there is a transition into

CDWs at low temperatures [27, 300].

Another extension to the work presented in this project is to explore intercalation of metallic species underneath the buffer layer of graphene or monolayer graphene on SiC and measure possible proximity-like SOC within the graphene layer using SPMDS. For this, further testing of the SPMDS system at York is needed which requires setting up both Doppler cooling and optical pumping using resonant laser light. This also requires checking the extent of spin-polarisation of the beam using both the Stern-Gerlach analyser and the Mott polarimeter. Further testing of the Mott polarimeter is also required such that SPMDS can be compared to SPUPS.

Finally, the work presented in this thesis shows some preliminary data of 6T grown on LSMO thin films. The spectroscopic response was measured using MDS, but no attempts were made to measure spin polarisation using SPMDS or SPMEEM. Therefore an extension to the work presented in Chapter 7 would be to look at the SPMDS and SPUPS response in the electron spectroscopy system and furthermore, map the surface spin polarisation using SPMEEM since these 6T monolayers have been seen to remain at the surface after the sample has been removed from vacuum.

Appendix A

PEEM/MEEM/LEEM of SiC

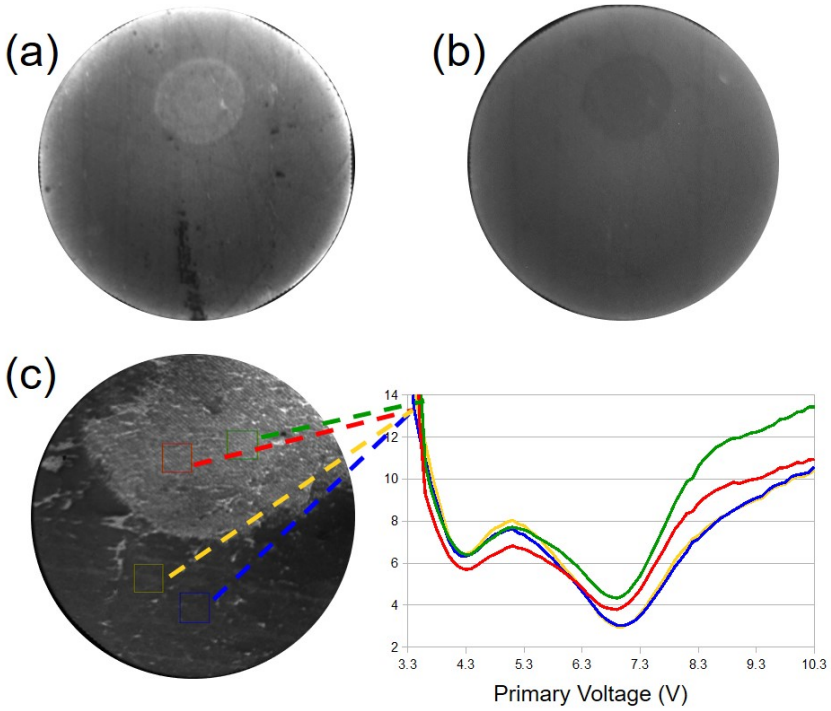

Figure A.1: A 120 µm (a) PEEM and (b) MEEM image of graphene on SiC. A 30 µm (c) (left) LEEM image of the same feature as seen in PEEM and (right) LEEM reflectivity curve of a bilayer of graphene on SiC.

An alternative to determining the thickness of graphene/extent of graphitisation of SiC from thermal decomposition is by measuring the change in reflectivity of LEEM as a function of the energy of the primary beam of electrons. Similar to LEED I/V, the measured reflectivity curve varies depending on the number of layers of graphene. A sample grown in York was analysed using PEEM and MEEM at NIMS

as can be seen in Figure A.1 and then the same region found in a different system equipped with SPLEEM. The difference in intensity of different regions observed using PEEM/MEEM was believed to be a result of different thicknesses of graphene. However the LEEM I/V curve for four different regions, both on and off of the spot, are the same indicating that the thickness of graphene was uniform. This further demonstrates the controlled nature of growing graphene on SiC resulting in high-quality regions of epitaxial graphene.

Appendix B

Quartz Crystal Microbalance and Gas Exposure

A quartz crystal microbalance (QCM) consists of a vibrating piece of quartz at a resonance frequency (f_0) of 6 MHz. Upon arrival of mass from a deposition source, the frequency of the crystal will change. Assuming that a rigid film of the deposited material is formed, then for small frequency changes, where $\Delta f/f_0 < 0.02$, then a linear relationship between change in frequency and mass can be assumed. This linear relationship is known as the Sauerbrey equation:

$$\Delta f = -\frac{2f_0^2}{A\sqrt{\rho_q \mu_q}}\Delta m \tag{B.1}$$

where A is the active area of the crystal (0.25π cm^2), ρ_q is the density of quartz (2.648 gcm^{-3}) and μ_q is the shear modulus of AT-cut quartz (2.947×10^{11} gcm^{-1}s^{-2}). For much thicker films, the assumption that $m_f << m_q$ is not true and this gives rise to a systematic error which increases as the deposition increases. Therefore, the relationship can no longer be assumed to be linear and thus the Sauerbrey equation fails at large depositions. In this circumstance the Z-match equation should be used instead:

$$\frac{\Delta m}{A} = \frac{N_q \rho_q}{\pi Z f_L} \arctan\left[Z \cdot \tan\left(\pi \frac{f_U - f_L}{f_U}\right)\right] \tag{B.2}$$

where f_U and f_L are the unloaded and loaded frequencies, N_q is a frequency constant

for AT-cut quartz crystal (1.668×10^{12} Hz·nm). Z is known as the Z-factor and is expressed as the following:

$$Z = \sqrt{\frac{\rho_q \mu_q}{\rho_f \mu_f}} \tag{B.3}$$

here ρ_f and μ_q are the density and the shear modulus of the film respectively. For non-cooled crystals, the frequency will slightly change over time. This is known as the drift rate and must be taken into account when measuring the deposition rate.

It is worth noting that certain values such as the material density will not be necessarily the same for a thin film as they are for the bulk. This is especially true for organic/aramatic molecules where the arrangement for a thin film is not the same always as it is for bulk.

Finally, the thickness of a monolayer of a single atomic species is dependent on the lattice constant which varies for different crystal structures, for example, face-centred cubic, etc. The crystal structure grown is dependent on the plane in which it is grown and therefore this must be taken into account when determining the deposition rate.

In order to quantify the exposure of gas to a surface when using atomic hydrogen to passivate the Si back-bond of SiC or oxygen atoms at the surface of $Fe_3O_4(001)$, the unit Langmuir was used. This is defined as the exposure of 1×10^{-6} Torr gas to a surface in 1 s. Langmuir as a unit assumes that the sticking coefficient of the gas molecule is 1 and behaves like an ideal gas. Therefore 1 L, can be equated to a monolayer of gas present on the surface. However, the sticking coefficient is rarely 1 since certain molecular groups at the surface of a material may prevent absorption of further atomic species. Therefore, more than 1 L is generally needed to achieve a monolayer of the atom/molecule.

Acronyms

2D two-dimensional.

2DEG 2D electron gas.

6H-SiC six-hexagonal silicon carbide.

6T α-sexithiophene.

AD Auger de-excitation.

AFM atomic force microscopy.

AN Auger neutralisation.

ARPES angle-resolved photoemission spectroscopy.

CASTEP Cambridge serial total energy package.

CEM channel electron multiplier.

CVD chemical vapour deposition.

DBT distorted bulk truncation.

DC direct-current.

DFT density functional theory.

DMI Dzyaloshinskii-Moriya interaction.

DOS density of states.

FCC face-centred cubic.

FEL fast entry lock.

FOV field-of-view.

FWHM full width half maximum.

GGA generalised gradient approximation.

H-BN hexagonal boron nitride.

HOMO highest occupied molecular orbital.

HOPG highly-oriented pyrolytic graphite.

IP in-plane.

ISNM Institute for Nanostructured Materials.

LDA local density approximation.

LEED low energy electron diffraction.

LEEM low energy electron microscopy.

MBE molecular beam epitaxy.

MCD magnetic circular dichroism.

MCP microchannel plate.

MDS metastable de-excitation spectroscopy.

MEEM metastable emission electron microscopy.

NIMS National Institute for Materials Science.

OP out-of-plane.

PBE Perdew-Burke-Ernzerhof.

PDOS partial density of states.

PEEM photoemission electron microscopy.

QCM quartz crystal microbalance.

QFSG quasi-free standing layer of graphene.

QSHE quantum spin-Hall effect.

REs rare earth metals.

RI resonance ionisation.

SCV subsurface cation vacancy.

SDOS surface density of states.

SNR signal-to-noise ratio.

SOC spin-orbit coupling.

SPMDS spin-polarised metastable de-excitation spectroscopy.

SPMEEM spin-polarised metastable emission electron microscopy.

STM scanning tunnelling microscopy.

TMDs transition metal dichalcogenides.

UHV ultra-high vacuum.

UPS ultraviolet photoemission spectroscopy.

UV ultraviolet.

UVMCD ultraviolet magnetic circular dichroism.

XMCD X-ray magnetic circular dichroism.

XPS X-ray photoemission spectroscopy.

XRD X-ray diffraction.

Bibliography

[1] H. J. Richter. Density limits imposed by the microstructure of magnetic recording media. *J. Magn. Magn. Mater.*, 321(6):467 – 476, 2009. Current Perspectives: Perpendicular Recording.

[2] H. J. Richter and S. D. Harkness. Media for Magnetic Recording Beyond 100 Gbit/in.^{2}. *MRS Bull.*, 31(5):384–388, 2006.

[3] S. B. Desai, S. R. Madhvapathy, A. B. Sachid, J. P. Llinas, Q. Wang, G. H. Ahn, G. Pitner, M. J. Kim, J. Bokor, C. Hu, H. S. Philip Wong, and A. Javey. MoS_2 transistors with 1-nanometer gate lengths. *Science*, 354(6308):99–102, 2016.

[4] H. Jang, W. Lee, S. M. Won, S. Y. Ryu, D. Lee, J. B. Koo, S. D. Ahn, C. W. Yang, M. H. Jo, J. H. Cho, J. A. Rogers, and J. H. Ahn. Quantum Confinement Effects in Transferrable Silicon Nanomembranes and Their Applications on Unusual Substrates. *Nano Lett.*, 13(11):5600–5607, 2013. PMID: 24088052.

[5] G. E. Moore. Cramming more components onto integrated circuits, Reprinted from Electronics. *IEEE J. Solid-State Circuits*, 38(8):114, April 1965.

[6] M. Cinchetti, V. A. Dediu, and L. E. Hueso. Activating the molecular spinterface. *Nat Mater.*, 16:507, 2017.

[7] W. Kang, Y. Huang, X. Zhang, Y. Zhou, and W. Zhao. Skyrmion-Electronics: An Overview and Outlook. *Proc. IEEE*, 104(10):2040–2061, Oct 2016.

[8] V. K. Joshi. Spintronics: A contemporary review of emerging electronics devices. *JESTECH*, 19(3):1503 – 1513, 2016.

[9] A. K. Geim and K. S. Novoselov. The rise of graphene. *Nat. Mater.*, 6(3):183 – 191, 2007.

[10] K. S. Novoselov, A. K. Geim, S. V. Morozov, D. Jiang, Y. Zhang, S. V. Dubonos, I.V. Grigorieva, and A. A. Firsov. Electric field effect in atomically thin carbon films. *Science*, 306(5696):666–669, 2004.

[11] H. Aoki and M. S. Dresselhaus. *Physics of Graphene*. Springer, 1 edition, 2014.

[12] D. Kochan, S. Irmer, and J. Fabian. Model spin-orbit coupling hamiltonians for graphene systems. *Phys. Rev. B*, 95:165415, Apr 2017.

[13] J. Balakrishnan, G. K. W. Koon, A. Avsar, Y. Ho, J. H. Lee, M. Jaiswal, S-J. Baeck, J-H. Ahn, A. Ferreira, M. A. Cazalilla, A. H. Castro Neto, and B. Özyilmaz. Giant spin hall effect in graphene grown by chemical vapour deposition. *Nat. commun.*, 5:5:4748, Sep 2014.

[14] M. Offidani, M. Milletarì, R. Raimondi, and A. Ferreira. Optimal Charge-to-Spin Conversion in Graphene on Transition-Metal Dichalcogenides. *Phys. Rev. Lett.*, 119:196801, Nov 2017.

[15] Z. Y. Zhu, Y. C. Cheng, and U. Schwingenschlögl. Giant spin-orbit-induced spin splitting in two-dimensional transition-metal dichalcogenide semiconductors. *Phys. Rev. B*, 84:153402, Oct 2011.

[16] M. R. Rosenberger, C. K. Dass, H. J. Chuang, S. V. Sivaram, K. M. McCreary, J. R. Hendrickson, and B. T. Jonker. Quantum Calligraphy: Writing Single-Photon Emitters in a Two-Dimensional Materials Platform. *ACS Nano*, 13(1):904–912, 2019.

[17] S. Schwarz, A. Kozikov, F. Withers, J. K. Maguire, A. P. Foster, S. Dufferwiel, L. Hague, M. N. Makhonin, L. R. Wilson, A. K. Geim, K. S. Novoselov, and A. I. Tartakovskii. Electrically pumped single-defect light emitters in WSe_2. *2D Mater.*, 3(2):025038, Jun 2016.

[18] F. Xia, H. Wang, D. Xiao, M. Dubey, and A. Ramasubramaniam. Two-dimensional material nanophotonics. *Nat. Photonics.*, 8:899, 2014.

[19] A. A. Sagade, A. I. Aria, S. Edge, P. Melgari, B. Gieseking, B. C. Bayer, J. C. Meyer, D. Bird, P. Brewer, and S. Hofmann. Graphene-based nanolaminates as ultra-high permeation barriers. *npj 2D Materials and Applications*, 1:35, 2017.

[20] M. Gmitra, S. Konschuh, C. Ertler, C. Ambrosch-Draxl, and J. Fabian. Band-structure topologies of graphene: Spin-orbit coupling effects from first principles. *Phys. Rev. B*, 80:235431, Dec 2009.

[21] J. Balakrishnan, G. J. M. Kok Wai Koon, A. H. Castro Neto, and B. Özyilmaz. Colossal enhancement of spin–orbit coupling in weakly hydrogenated graphene. *Nat. Phys.*, 9:284, 2013.

[22] F. Calleja, H. Ochoa, M. Garnica, S. Barja, J. J. Navarro, A. Black, M. M. Otrokov, E. V. Chulkov, A. Arnau, A. L. Vázquez de Parga, F. Guinea, and R. Miranda. Spatial variation of a giant spin-orbit effect induces electron confinement in graphene on Pb islands. *Nat. Phys.*, 11:43, 2014.

[23] K. I. Bolotin, K. J. Sikes, Z. Jiang, M. Klima, G. Fudenberg, J. Hone, P. Kim, and H. L. Stormer. Ultrahigh electron mobility in suspended graphene. *Solid State Commun.*, 146(9):351 – 355, 2008.

[24] E. Pallecchi, F. Lafont, V. Cavaliere, F. Schopfer, D. Mailly, W. Poirier, and A. Ouerghi. High Electron Mobility in Epitaxial Graphene on 4H-SiC(0001) via post-growth annealing under hydrogen. *Sci. Rep.s*, 4:4558, 2014.

[25] Y. K. Luo, J. Xu, T. Zhu, G. Wu, E. J. McCormick, W. Zhan, M. R. Neupane, and R. K. Kawakami. Opto-Valleytronic Spin Injection in Monolayer MoS_2/Few-Layer Graphene Hybrid Spin Valves. *Nano Lett.*, 17(6):3877–3883, 2017. PMID: 28534401.

[26] S. Deng and V. Berry. Wrinkled, rippled and crumpled graphene: an overview of formation mechanism, electronic properties, and applications. *Mater. Today*, 19(4):197 – 212, 2016.

[27] F. Andreatta, H. Rostami, A. G. Čabo, M. Bianchi, C. E. Sanders, D. Biswas, C. Cacho, A. J. H. Jones, R. T. Chapman, E. Springate, P. D. C. King,

J. A. Miwa, A. Balatsky, S. Ulstrup, and P. Hofmann. Transient hot electron dynamics in single-layer TaS_2. *Phys. Rev. B*, 99:165421, Apr 2019.

[28] D. Briggs and M. P. Seah (Editors). *Practical surface analysis by Auger and X-ray photoelectron spectroscopy.*, volume 1. John Wiley and Sons Ltd, 1990.

[29] A. G. Rybkin, A. A. Rybkina, M. M. Otrokov, O. Y. Vilkov, I. I. Klimovskikh, A. E. Petukhov, M. V. Filianina, V. Y. Voroshnin, I. P. Rusinov, A. Ernst, A. Arnau, E. V. Chulkov, and A. M. Shikin. Magneto-spin–orbit graphene: Interplay between exchange and spin–orbit couplings. *Nano Lett.*, 18(3):1564–1574, 2018. PMID: 29365269.

[30] M. Onellion, M. W. Hart, F. B. Dunning, and G. K. Walters. Spin-Polarized Metastable-Atom Deexcitation Spectroscopy: A New Probe of Surface Magnetism. *Phys. Rev. Lett.*, 52:380–383, Jan 1984.

[31] M. W. Hart, M. S. Hammond, F. B. Dunning, and G. K. Walters. Spin-polarized metastable-atom deexcitation spectroscopy: A new probe of the dynamics of metastable-atom–surface interactions. *Phys. Rev. B*, 39:5488–5491, 3 1989.

[32] A. Pratt, M. Kurahashi, X. Sun, D. Gilks, and Y. Yamauchi. Direct observation of a positive spin polarization at the (111) surface of magnetite. *Phys. Rev. B*, 85:180409, May 2012.

[33] S. Entani, M. Kurahashi, X. Sun, and Y. Yamauchi. Spin polarization of single-layer graphene epitaxially grown on Ni(111) thin film. *Carbon*, 61:134 – 139, 2013.

[34] Y. Harada, S. Yamamoto, M. Aoki, S. Masuda, T. Ichinokawa, M. Kato, and Y. Sakai. Surface spectroscopy with high spatial resolution using metastable atoms. *Nature*, 372:657–659, 1994.

[35] Y. S. Dedkov, A. M. Shikin, V. K. Adamchuk, S. L. Molodtsov, C. Laubschat, A. Bauer, and G. Kaindl. Intercalation of copper underneath a monolayer of graphite on Ni(111). *Phys. Rev. B*, 64:035405, Jun 2001.

[36] A. Hirsch and F. Hauke. Post-Graphene 2D Chemistry: The Emerging Field of Molybdenum Disulfide and Black Phosphorus Functionalization. *Angew. Chem. Int. Edit.*, 57(16):4338–4354, 2018.

[37] J. Zhao, H. Liu, Z. Yu, R. Quhe, S. Zhou, Y. Wang, C. C. Liu, H. Zhong, N. Han, J. Lu, Y. Yao, and K. Wu. Rise of silicene: A competitive 2D material. *Prog. Mater. Sci.*, 83:24 – 151, 2016.

[38] H. W. Kroto, J. R. Heath, S. C. O'Brien, R. F. Curl, and R. E. Smalley. C60: Buckminsterfullerene. *Nature*, 318:162 – 163, 1985.

[39] X. Ji, Y. Xu, W. Zhang, L. Cui, and J. Liu. Review of functionalization, structure and properties of graphene/polymer composite fibers. *Compos. Part A Appl. Sci. Manuf.*, 87:29 – 45, 2016.

[40] A. H. Castro Neto, F. Guinea, N. M. R. Peres, K. S. Novoselov, and A. K. Geim. The electronic properties of graphene. *Rev. Mod. Phys.*, 81:109–162, Jan 2009.

[41] C. Riedl, C. Coletti, and U. Starke. Structural and electronic properties of epitaxial graphene on SiC(0001): a review of growth, characterization, transfer doping and hydrogen intercalation. *J. Phys. D Appl. Phys.*, 43(37):374009, 2010.

[42] N. M. R. Peres, F. Guinea, and A. H. Castro Neto. Electronic properties of disordered two-dimensional carbon. *Phys. Rev. B*, 73:125411, Mar 2006.

[43] M. A. Yamoah, W. Yang, E. Pop, and D. Goldhaber-Gordon. High-Velocity Saturation in Graphene Encapsulated by Hexagonal Boron Nitride. *ACS Nano*, 11(10):9914–9919, 2017. PMID: 28880529.

[44] H. Hirai, H. Tsuchiya, Y. Kamakura, N. Mori, and M. Ogawa. Electron mobility calculation for graphene on substrates. *J. Appl. Phys.*, 116(8):083703, 2014.

[45] T. Ohta, A. Bostwick, J. L. McChesney, T. Seyller, K. Horn, and E. Rotenberg. Interlayer interaction and electronic screening in multilayer graphene

investigated with angle-resolved photoemission spectroscopy. *Phys. Rev. Lett.*, 98:206802, May 2007.

[46] G. E. Bacon. A note on the rhombohedral modification of graphite. *Acta Crystallogr.*, 3(4):320, Jul 1950.

[47] H. Gasparoux. Modification des propriétés magnétiques du graphite par création de sequences rhomboédriques. *Carbon*, 5(5):441 – 451, 1967.

[48] H. Gasparoux and B. Lambert. Etude de la cinetique de guerison des defauts crees dans un graphite par broyage. *Carbon*, 8(5):573 – 586, 1970.

[49] P. R. Wallace. The band theory of graphite. *Phys. Rev.*, 71:622–634, May 1947.

[50] S. Y. Zhou, G. H. Gweon, A. V. Fedorov, P. N. First, A. W. de Heer, D. H. Lee, F. Guinea, A. H. Castro Neto, and A. Lanzara. Substrate-induced bandgap opening in epitaxial graphene. *Nat. Mater.*, 6:916, 2007.

[51] T. J. Gay and F. B. Dunning. Mott electron polarimetry. *Rev. Sci. Instrum.*, 63(2):1635–1651, 1992.

[52] S. Majumdar, H.S. Majumdar, R. Österbacka, and E. McCarthy. Organic Spintronics. In *Reference Module in Materials Science and Materials Engineering*. Elsevier, 2016.

[53] C. M. Acosta, M. P. Lima, R. H. Miwa, A. J. R. da Silva, and A. Fazzio. Topological phases in triangular lattices of ru adsorbed on graphene: Ab initio calculations. *Phys. Rev. B*, 89:155438, Apr 2014.

[54] D. Marchenko, A. Varykhalov, M. R. Scholz, G. Bihlmayer, E. I. Rashba, A. Rybkin, A. M. Shikin, and O. Rader. Giant Rashba splitting in graphene due to hybridization with gold. *Nat. commun.*, 3:3:1232, Nov 2012.

[55] P. Zhou and D. W. He. Modulating doping and interface magnetism of epitaxial graphene on SiC(0001). *Chin. Phys. B*, 25(1):017302, 2016.

[56] A. Pachoud, A. Ferreira, B. Özyilmaz, and A. H. Castro Neto. Scattering theory of spin-orbit active adatoms on graphene. *Phys. Rev. B*, 90:035444, Jul 2014.

[57] L. Gao, J. R. Guest, and N. P. Guisinger. Epitaxial Graphene on Cu(111). *Nano Lett.*, 10(9):3512–3516, 2010. PMID: 20677798.

[58] S. Sakai, S. Majumdar, Z. I. Popov, P. V. Avramov, S. Entani, Y. Hasegawa, Y. Yamada, H. Huhtinen, H. Naramoto, P. B. Sorokin, and Y. Yamauchi. Proximity-Induced Spin Polarization of Graphene in Contact with Half-Metallic Manganite. *ACS Nano*, 10(8):7532–7541, 2016. PMID: 27438899.

[59] M. Offidani and A. Ferreira. Anomalous Hall Effect in 2D Dirac Materials. *Phys. Rev. Lett.*, 121:126802, Sep 2018.

[60] A. Dahal and M. Batzill. Graphene-nickel interfaces: a review. *Nanoscale*, 6:2548–2562, 2014.

[61] M. Peralta, L. Colmenarez, A. López, B. Berche, and E. Medina. Ferromagnetic order induced on graphene by Ni/Co proximity effects. *Phys. Rev. B*, 94:235407, Dec 2016.

[62] C. L. Kane and E. J. Mele. Quantum spin hall effect in graphene. *Phys. Rev. Lett.*, 95:226801, Nov 2005.

[63] R. Yu, W. Zhang, H. J. Zhang, S. C. Zhang, X. Dai, and Z. Fang. Quantized anomalous hall effect in magnetic topological insulators. *Science*, 329(5987):61–64, 2010.

[64] T. P. Cysne, A. Ferreira, and T. G. Rappoport. Crystal-field effects in graphene with interface-induced spin-orbit coupling. *Phys. Rev. B*, 98:045407, Jul 2018.

[65] S. Konschuh, M. Gmitra, and J. Fabian. Tight-binding theory of the spin-orbit coupling in graphene. *Phys. Rev. B*, 82:245412, Dec 2010.

[66] E. I. Rashba. Symmetry of energy bands in crystals of wurtzite type: I. symmetry of bands disregarding spin-orbit interaction. *Sov. Phys.-Solid State*, 1:360–80, 1959.

[67] E. I. Rashba and V. I. Sheka. Symmetry of energy bands in crystals of wurtzite type: II. Symmetry of bands including spin-orbit interaction. *Fiz. Tverd. Tela: Collected Papers*, 2:162–76, 1959.

[68] G. Bihlmayer, O. Rader, and R. Winkler. Focus on the Rashba effect. *New J. Phys.*, 17(5):050202, May 2015.

[69] M. Offidani, R. Raimondi, and A. Ferreira. Microscopic Linear Response Theory of Spin Relaxation and Relativistic Transport Phenomena in Graphene. *Condens. Matter*, 3:18, May 2018.

[70] P. Schwab, R. Raimondi, and C. Gorini. Spin-charge locking and tunneling into a helical metal. *EPL*, 93(6):67004, Mar 2011.

[71] D. Hsieh, Y. Xia, D. Qian, L. Wray, J. H. Dil, F. Meier, J. Osterwalder, L. Patthey, J. G. Checkelsky, N. P. Ong, A. V. Fedorov, H. Lin, A. Bansil, D. Grauer, Y. S. Hor, R. J. Cava, and M. Z. Hasan. A tunable topological insulator in the spin helical dirac transport regime. *Nature*, 460:1101, 2009.

[72] V. Brosco, L. Benfatto, E. Cappelluti, and C. Grimaldi. Unconventional dc Transport in Rashba Electron Gases. *Phys. Rev. Lett.*, 116:166602, Apr 2016.

[73] Y. A. Bychkov and E. I. Rashba. Properties of a 2D electron gas with lifted spectral degeneracy. *JEPT Lett.*, 39:78, 1984.

[74] T. G. Rappoport, M. Godoy, B. Uchoa, R. R. dos Santos, and A. H. Castro Neto. Magnetic exchange mechanism for electronic gap opening in graphene. *EPL (Europhysics Letters)*, 96(2):27010, Oct 2011.

[75] Y. Qin, S. Wang, R. Wang, H. Bu, X. Wang, X. Wang, F. Song, B. Wang, and G. Wang. Sizeable Kane–Mele-like spin orbit coupling in graphene decorated with iridium clusters. *Appl. Phys. Lett.*, 108(20):203106, 2016.

[76] X. Sun, S. Entani, Y. Yamauchi, A. Pratt, and M. Kurahashi. Spin polarization study of graphene on the Ni(111) surface by density functional theory calculations with a semiempirical long-range dispersion correction. *J. Appl. Phys.*, 114:143713, 2013.

[77] Y. S. Dedkov M., Fonin, and C. Laubschat. A possible source of spin-polarized electrons: The inert graphene/Ni(111) system. *Appl. Phys. Lett.*, 92(5):052506, 2008.

[78] E. V. Zhizhin, A. Varykhalov, A. G. Rybkin, A. A. Rybkina, D. A. Pudikov, D. Marchenko, J. Sánchez-Barriga, I. I. Klimovskikh, G. G. Vladimirov, O. Rader, and A. M. Shikin. Spin splitting of Dirac fermions in graphene on Ni intercalated with alloy of Bi and Au. *Carbon*, 93:984 – 996, 2015.

[79] F. C. Bocquet, R. Bisson, J. M. Themlin, J. M. Layet, and T. Angot. Deuterium adsorption on (and desorption from) SiC(0001)-(3×3), $(\sqrt{3}\times\sqrt{3})R30°$, $(6\sqrt{3}\times 6\sqrt{3})R30°$ and quasi-free-standing graphene obtained by hydrogen intercalation. *J. Phys. D Appl. Phys.*, 47(9):094014, 2 2014.

[80] D. Xiao, G. B. Liu, W. Feng, X. Xu, and W. Yao. Coupled Spin and Valley Physics in Monolayers of MoS_2 and Other Group-VI Dichalcogenides. *Phys. Rev. Lett.*, 108:196802, May 2012.

[81] D. Xiao, W. Yao, and Q. Niu. Valley-Contrasting Physics in Graphene: Magnetic Moment and Topological Transport. *Phys. Rev. Lett.*, 99:236809, Dec 2007.

[82] R. A. Muniz and J. E. Sipe. All-optical injection of charge, spin, and valley currents in monolayer transition-metal dichalcogenides. *Phys. Rev. B*, 91:085404, Feb 2015.

[83] A. Avsar, D. Unuchek, J. Liu, O. L. Sanchez, K. Watanabe, T. Taniguchi, B. Özyilmaz, and A. Kis. Optospintronics in Graphene via Proximity Coupling. *ACS Nano*, 11(11):11678–11686, 2017. PMID: 29068661.

[84] A. Avsar, J. Y. Tan, T. Taychatanapat, J. Balakrishnan, G. K. W. Koon, Y. Yeo, J. Lahiri, A. Carvalho, A. S. Rodin, E. C. T. O'Farrell, G. Eda, A. H. Castro Neto, and B. Özyilmaz. Spin–orbit proximity effect in graphene. *Nat. Commun.*, 5:4875, 2014.

[85] Z. Wang, D. K. Ki, H. Chen, H. Berger, A. H. MacDonald, and A. F. Morpurgo. Strong interface-induced spin–orbit interaction in graphene on WS_2. *Nat. Commun.*, 6:8339, 2015.

[86] T. Völkl, T. Rockinger, M. Drienovsky, K. Watanabe, T. Taniguchi, D. Weiss, and J. Eroms. Magnetotransport in heterostructures of transition metal dichalcogenides and graphene. *Phys. Rev. B*, 96:125405, Sep 2017.

[87] C. K. Safeer, J. Ingla-Aynés, F. Herling, J. H. Garcia, M. Vila, N. Ontoso, M. R. Calvo, S. Roche, L. E. Hueso, and F. Casanova. Room-Temperature Spin Hall Effect in Graphene/MoS2 van der Waals Heterostructures. *Nano Lett.*, 19(2):1074–1082, 2019.

[88] J. B. Casady and R. W. Johnson. Status of silicon carbide (SiC) as a wide-bandgap semiconductor for high-temperature applications: A review. *Solid-State Electron.*, 39(10):1409 – 1422, 1996.

[89] I. Shtepliuk, V. Khranovskyy, and R. Yakimova. Combining graphene with silicon carbide: synthesis and properties – a review. *Semicond. Sci. Technol.*, 31(11):113004, 2016.

[90] N. A. Anderson, M. Hupalo, D. Keavney, M. C. Tringides, and D. Vaknin. Intercalated europium metal in epitaxial graphene on SiC. *Phys. Rev. Materials*, 1:054005, 10 2017.

[91] C. Xia, A. A. Tal, L. I. Johansson, W. Olovsson, I. A. Abrikosov, and C. Jacobi. Effects of rhenium on graphene grown on SiC(0001). *J. Electron Spectros. Relat. Phenomena*, 222:117 – 121, 2018.

[92] R. Baltic, F. Donati, A. Singha, C. Ẅackerlin, J. Dreiser, B. Delley, M. Pivetta, S. Rusponi, and H. Brune. Magnetic properties of single rare-earth atoms on graphene/Ir(111). *Phys. Rev. B*, 98:024412, Jul 2018.

[93] D. Marchenko, A. Varykhalov, J. Sánchez-Barriga, Th. Seyller, and O. Rader. Rashba splitting of 100 meV in Au-intercalated graphene on SiC. *Appl. Phys. Lett.*, 108(17):172405, 2016.

[94] M. Krivenkov, E. Golias, D. Marchenko, .J Sánchez-Barriga, G. Bihlmayer, O. Rader, and A. Varykhalov. Nanostructural origin of giant Rashba effect in intercalated graphene. *2D Mater.*, 4(3):035010, Jul 2017.

[95] M. Narayanan Nair, M. Cranney, T. Jiang, S. Hajjar-Garreau, D. Aubel, F. Vonau, A. Florentin, E. Denys, M. L. Bocquet, and L. Simon. Noble-metal intercalation process leading to a protected adatom in a graphene hollow site. *Phys. Rev. B*, 94:075427, Aug 2016.

[96] A. Nachawaty, M. Yang, S. Nanot, D. Kazazis, R. Yakimova, W. Escoffier, and B. Jouault. Large nonlocality in macroscopic Hall bars made of epitaxial graphene. *Phys. Rev. B*, 98:045403, Jul 2018.

[97] M. N. Nair, I. Palacio, A. Celis, A. Zobelli, A. Gloter, S. Kubsky, J. P. Turmaud, M. Conrad, C. Berger, W. de Heer, E. H. Conrad, A. Taleb-Ibrahimi, and A. Tejeda. Band Gap Opening Induced by the Structural Periodicity in Epitaxial Graphene Buffer Layer. *Nano Lett.*, 17(4):2681–2689, 2017. PMID: 28345926.

[98] O. D. Restrepo, K. E. Krymowski, J. Goldberger, and W. Windl. A first principles method to simulate electron mobilities in 2d materials. *New J. Phys.*, 16(10):105009, Oct 2014.

[99] Z. Liu, Z. Tu, Y. Li, F. Yang, S. Han, W. Yang, L. Zhang, G. Wang, C. Xu, and J. Gao. Synthesis of three-dimensional graphene from petroleum asphalt by chemical vapor deposition. *Mater. Lett.*, 122:285 – 288, 2014.

[100] A. L. Walter, S. Nie, A. Bostwick, K. S. Kim, L. Moreschini, Y. J. Chang, D. Innocenti, K. Horn, K. F. McCarty, and E. Rotenberg. Electronic structure of graphene on single-crystal copper substrates. *Phys. Rev. B*, 84:195443, Nov 2011.

[101] S. M. Hollen, G. A. Gambrel, S. J. Tjung, N. M. Santagata, E. Johnston-Halperin, and J. A. Gupta. Modification of electronic surface states by graphene islands on Cu(111). *Phys. Rev. B*, 91:195425, May 2015.

[102] J. Li, S. Gottardi, L. Solianyk, J. C. Moreno-López, and M. Stöhr. 1,3,5-Benzenetribenzoic Acid on Cu(111) and Graphene/Cu(111): A Comparative STM Study. *J. Phys. Chem. C*, 120(32):18093–18098, 2016. PMID: 27588158.

[103] S. J. Tjung, S. M. Hollen, G. A. Gambrel, N. M. Santagata, E. Johnston-Halperin, and J. A. Gupta. Crystalline hydrogenation of graphene by scanning tunneling microscope tip-induced field dissociation of H2. *Carbon*, 124:97 – 104, 2017.

[104] H. Kim, C. Mattevi, M. R. Calvo, J. C. Oberg, L. Artiglia, S. Agnoli, C. F. Hirjibehedin, M. Chhowalla, and E. Saiz. Activation Energy Paths for Graphene Nucleation and Growth on Cu. *ACS Nano*, 6(4):3614–3623, 2012. PMID: 22443380.

[105] K. Celebi, M. T. Cole, J. W. Choi, F. Wyczisk, P. Legagneux, N. Rupesinghe, J. Robertson, K. B. K. Teo, and H. G. Park. Evolutionary Kinetics of Graphene Formation on Copper. *Nano Lett.*, 13(3):967–974, 2013. PMID: 23339597.

[106] K. Balasubramanian, T. Biswas, P. Ghosh, S. Suran, A. Mishra, R. Mishra, R. Sachan, M. Jain, M. Varma, R. Pratap, and S. Raghavan. Reversible defect engineering in graphene grain boundaries. *Nat. Commun.*, 1090:1–9, Mar 2019.

[107] M. Khenner. Model for computing kinetics of the graphene edge epitaxial growth on copper. *Phys. Rev. E*, 93:062806, Jun 2016.

[108] A. J. Marsden, M. C. Asensio, J. Avila, P. Dudin, A. Barinov, P. Moras, P. M. Sheverdyaeva, T. W. White, I. Maskery, G. Costantini, N. R. Wilson, and G. R. Bell. Is graphene on copper doped? *Phys. Status Solidi RRL*, 7(9):643–646, 2013.

[109] M. Ghadami Yazdi, P. H. Moud, K. Marks, W. Piskorz, H. Őström, T. Hansson, A. Kotarba, K. Engvall, and M. Göthelid. Naphthalene on Ni(111): Experimental and Theoretical Insights into Adsorption, Dehydrogenation, and Carbon Passivation. *J. Phys. Chem. C*, 121(40):22199–22207, 2017.

[110] Q. Yang, Y. Su, C. Chi, C. T. Cherian, K. Huang, V. G. Kravets, F. C. Wang, J. C. Zhang, A. Pratt, A. N. Grigorenko, F. Guinea, A. K. Geim, and R. R. Nair. Ultrathin graphene-based membrane with precise molecular sieving and ultrafast solvent permeation. *Nat. Mater.*, 4(16):1198, 2017.

[111] K. G. Zhou, K. S. Vasu, C. T. Cherian, M. Neek-Amal, J. C. Zhang, H. Ghorbanfekr-Kalashami, K. Huang O. P. Marshall, V. G. Kravets, J. Abraham, Y. Su, A. N. Grigorenko, A. Pratt, A. K. Geim, F. M. Peeters, K. S. Novoselov, and R. R. Nair. Electrically controlled water permeation through graphene oxide membranes. *Nature*, 559(7713):236 – 240, 2018.

[112] Z. S. Wu, W. Ren, L. Wen, L. Gao, J. Zhao, Z. Chen, G. Zhou, F. Li, and H. M. Cheng. Graphene anchored with co3o4 nanoparticles as anode of lithium ion batteries with enhanced reversible capacity and cyclic performance. *ACS Nano*, 4(6):3187–3194, 2010. PMID: 20455594.

[113] D. Sun, H. Wang, B. Deng, H. Zhang, L. Wang, Q. Wan, X. Yan, and M. Qu. A MnFe based Prussian blue Analogue@Reduced graphene oxide composite as high capacity and superior rate capability anode for lithium-ion batteries. *Carbon*, 143:706 – 713, 2019.

[114] Y. Xu, Q. Wu, Y. Sun, H. Bai, and G. Shi. Three-Dimensional Self-Assembly of Graphene Oxide and DNA into Multifunctional Hydrogels. *ACS Nano*, 4(12):7358–7362, 2010. PMID: 21080682.

[115] W. Yao, D. Xiao, and Q. Niu. Valley-dependent optoelectronics from inversion symmetry breaking. *Phys. Rev. B*, 77:235406, Jun 2008.

[116] S. Cahangirov, M. Topsakal, E. Aktürk, H. Şahin, and S. Ciraci. Two- and One-Dimensional Honeycomb Structures of Silicon and Germanium. *Phys. Rev. Lett.*, 102:236804, Jun 2009.

[117] Y. Harada, S. Masuda, and H. Ozaki. Electron Spectroscopy Using Metastable Atoms as Probes for Solid Surfaces. *Chemical Reviews*, 97(6):1897–1952, 1997. PMID: 11848894.

[118] H. W. Webb. The Metastable State in Mercury Vapor. *Phys. Rev.*, 24:113–128, Aug 1924.

[119] F. M. Penning. Über Ionisation durch metastabile Atome. *Naturwissenschaften*, 15(40):818–818, Oct 1927.

[120] K. Ohno, T. Takami, K. Mitsuke, and T. Ishida. State-resolved collision energy dependence of Penning ionization cross sections for N_2 and CO_2 by He*2^3S. *J. Chem. Phys.*, 94(4):2675–2687, 1991.

[121] A. Pratt. *A Laser-Cooled Helium 2^3S Beam for Surface Analysis*. University of York, 2005.

[122] B. A. Chambers, C. Neumann, A. Turchanin, C. T Gibson, and G. G Andersson. The direct measurement of the electronic density of states of graphene using metastable induced electron spectroscopy. *2D Mater.*, 4(2):025068, 2017.

[123] J. de la Figuera, L. Vergara, A. T. N'Diaye, A. Quesada, and A. K. Schmid. Micromagnetism in (001) magnetite by spin-polarized low-energy electron microscopy. *Ultramicroscopy*, 130:77 – 81, 2013. Eighth International Workshop on LEEM/PEEM.

[124] O. B. Shpenik, A. N. Zavilopulo, A. V. Snegursky, and I. I. Fabrikant. Excitation of metastable levels of noble-gas atoms in crossed electron and gas dynamical atomic beams. *J. Phys. B*, 17(5):887, 1984.

[125] G. Ertl. Electron spectroscopy of surfaces by de-excitation of metastable noble gas atoms. *Philos. Trans. Royal Soc. A*, 318(1541):51–58, 1986.

[126] B. Heinz and H. Morgner. A metastable induced electron spectroscopy study of graphite: The k-vector dependence of the ionization probability. *Surf. Sci.*, 405(1):104 – 111, 1998.

[127] K. Ohno, H. Mutoh, and Y. Harada. Study of electron distributions of molecular orbitals by Penning ionization electron spectroscopy. *J. Am. Chem. Soc.*, 105(14):4555–4561, 1983.

[128] A. Pratt, L. Dunne, X. Sun, M. Kurahashi, and Y. Yamauchi. Energy-level alignment at the $Alq_3/Fe_3O_4(001)$ interface. *J. Appl. Phys.*, 111(7):07C114, 2012.

[129] A. Pratt, A. Roskoss, H. Ménard, and M. Jacka. Improved metastable de-excitation spectrometer using laser-cooling techniques. *Rev. Sci. Instrum.*, 76(5):053102, 2005.

[130] M. Kurahashi, S. Entani, and Y. Yamauchi. Surface magnetization measurement with a spin-polarized metastable He beam under high magnetic fields of 0–5T. *Rev. Sci. Instrum.*, 79(7):073902, 2008.

[131] H. E. Montgomery Jr. and V. I. Pupyshev. Confined helium: Excited singlet and triplet states. *Phys. Lett. A*, 377(40):2880 – 2883, 2013.

[132] C. W. Woffinden. *The surface electronic and magnetic properties of rare earth silicides and iron nanoclusters using metastable de-excitation spectroscopy.* University of York, 2010.

[133] D. A. Wright. Work Function and Energy Levels in Insulators. *Proc. Phys. Soc.*, 60(1):13, 1948.

[134] W. Sesselmann, B. Woratschek, J. Küppers, G. Ertl, and H. Haberland. Interaction of metastable noble-gas atoms with transition-metal surfaces: Resonance ionization and Auger neutralization. *Phys. Rev. B*, 35:1547–1559, Feb 1987.

[135] H. D. Hagstrum. Electron Ejection from Mo by He^+, He^{++}, and He_2^+. *Phys. Rev.*, 89:244–255, Jan 1953.

[136] H. D. Hagstrum, Y. Takeishi, and D. D. Pretzer. Energy Broadening in the Auger-Type Neutralization of Slow Ions at Solid Surfaces. *Phys. Rev.*, 139:A526–A538, Jul 1965.

[137] L. A. Salmi. Theory of spin polarization in the metastable-He–metal interaction. *Phys. Rev. B*, 46:4180–4191, Aug 1992.

[138] W. Sesselmann, B. Woratschek, K. Küppers, G. Ertl, and H. Haberland. Auger neutralization spectroscopy of clean and adsorbate-covered transition-metal surfaces by deexcitation of metastable noble-gas atoms. *Phys. Rev. B*, 35:8348–8359, Jun 1987.

[139] S. Wethekam, D. Valdés, R. C. Monreal, and H. Winter. Face-dependent auger neutralization and ground-state energy shift for He in front of Al surfaces. *Phys. Rev. B*, 78:075423, Aug 2008.

[140] F. B. Dunning, P. Nordlander, and G. K. Walters. Dynamics of metastable-atom deexcitation at metal surfaces. *Phys. Rev. B*, 44:3246–3250, Aug 1991.

[141] R. Souda and K. Yamamoto. Band effect on resonance neutralization. *Nucl. Instrum. Methods. Phys. Res. B*, 125(1):256 – 261, 1997. Inelastic Ion-Surface Collisions.

[142] S. Průša, P. Procházka, P. Bábor, T. Šikola, R. ter Veen, M. Fartmann, T. Grehl, P. Brüner, D. Roth, P. Bauer, and H. H. Brongersma. Highly Sensitive Detection of Surface and Intercalated Impurities in Graphene by LEIS. *Langmuir*, 31(35):9628–9635, 2015. PMID: 26200443.

[143] I. L. Shumay, U. Höfer, Ch. Reuß, U. Thomann, W. Wallauer, and Th. Fauster. Lifetimes of image-potential states on Cu(100) and Ag(100) measured by femtosecond time-resolved two-photon photoemission. *Phys. Rev. B*, 58:13974–13981, Nov 1998.

[144] J. A. Appelbaum and D. R. Hamann. Variational Calculation of the Image Potential near a Metal Surface. *Phys. Rev. B*, 6:1122–1130, Aug 1972.

[145] D. Kędziera, L. Mentel, S. P. Żuchowski, and S. Knoop. Ab initio interaction potentials and scattering lengths for ultracold mixtures of metastable helium and alkali-metal atoms. *Phys. Rev. A*, 91:062711, Jun 2015.

[146] C. Kittel. *Introduction to Solid State Physics*. Wiley, 8th edition, 2004.

[147] M. S. Hammond, F. B. Dunning, G. K. Walters, and G. A. Prinz. Spin dependence in He(2^3S) metastable-atom deexcitation at magnetized Fe(110) and O/Fe(110) surfaces. *Phys. Rev. B*, 45:3674–3679, Feb 1992.

[148] J. C. Lancaster, F. J. Kontur, G. K. Walters, and F. B. Dunning. Dynamics of He^+ ion neutralization at clean metal surfaces: Energy- and spin-resolved studies. *Phys. Rev. B*, 67:115413, Mar 2003.

[149] R. D. Rundel, F. B. Dunning, and R. F. Stebbings. Velocity distributions in metastable atom beams produced by coaxial electron impact. *Rev. Sci. Instrum.*, 45(1):116–119, 1974.

[150] P. D. Johnson and T. A. Delchar. A helium metastable source for surface spectroscopy. *J. Phys. E: Sci. Instrum.*, 10(4):428–431, April 1977.

[151] Y. Yamauchi, M. Kurahashi, and N. Kishimoto. A metastable helium atom source directly pulsed by a nozzle-skimmer discharge. *Meas. Sci. Technol.*, 9(3):531–533, Mar 1998.

[152] J. A. Swansson, K. G. H. Baldwin, M. D. Hoogerland, A. G. Truscott, and S. J. Buckman. A high flux, liquid-helium cooled source of metastable rare gas atoms. *Appl. Phys. B*, 79(4):485–489, Sep 2004.

[153] D. W. Fahey, W. F. Parks, and L. D. Schearer. High flux beam source of thermal rare-gas metastable atoms. *J. Phys. E: Sci. Instrum.*, 13(4):381–383, April 1980.

[154] K. Halbach. Design of permanent multipole magnets with oriented rare earth cobalt material. *Nucl. Instr. Meth.*, 169(1):1 – 10, 1980.

[155] G. Baum, W. Raith, and H. Steidl. Production of a spin-polarized, metastable $He(2^3S)$ beam for studies in atomic and surface physics. *Z. Phys. D Atom. Mol. Cl.*, 10(2):171–178, Jun 1988.

[156] F. Weinert. *Stern-Gerlach Experiment*, pages 746–750. Springer Berlin Heidelberg, Berlin, Heidelberg, 2009.

[157] J. C. Zhang. *An Investigation of C_{60}/Semiconductor and C_{60}/Ferromagnetic Interfaces using a Metastable Helium Beam.* University of York, 2018.

[158] Milton Ohring. Chapter 2 - Vacuum Science and Technology. In M. Ohring, editor, *Materials Science of Thin Films (Second Edition)*, pages 57 – 93. Academic Press, San Diego, second edition, 2002.

[159] P. Adderley and G. Myneni. A road map to extreme high vacuum. *J. Phys. Conf. Ser.*, 114(1):012011, 2008.

[160] K. Siegbahn. Photoelectron Spectroscopy: Retrospects and Prospects. *Philos. Trans. Royal Soc. A*, 318:3–36, 05 1986.

[161] M. Kurahashi, X. Sun, and Y. Yamauchi. Recovery of the half-metallicity of an $Fe_3O_4(100)$ surface by atomic hydrogen adsorption. *Phys. Rev. B*, 81:193402, May 2010.

[162] D. Pingstone. *Characterisation and growth of polar oxide MgO(110) thin films by Molecular Beam Epitaxy.* University of York, 2018.

[163] R. Paschotta. Ultraviolet Lasers, 2019. Last accessed 08th September 2019.

[164] M. Prutton. *Introduction to Surface Physics.* Oxford University Press, 1994.

[165] C. B. Duke. Semiconductor Surface Reconstruction: The Structural Chemistry of Two-Dimensional Surface Compounds. *Chem. Rev.*, 96(4):1237–1260, 1996. PMID: 11848788.

[166] K. Oura, V. G. Lifshits, A. A. Saranin, A. V. Zotov, and M. Katayama. *Surface Science - An Introduction.* Springer-Verlag, 2004.

[167] C. Davisson and L. H. Germer. Diffraction of Electrons by a Crystal of Nickel. *Phys. Rev.*, 30:705–740, Dec 1927.

[168] D. B. Williams and C. B. Carter. *Transmission Electron Microscopy: A Textbook for Materials Science.* Springer US, Boston, MA, 2009.

[169] C. Riedl, C. Coletti, T. Iwasaki, A. A. Zakharov, and U. Starke. Quasi-free-standing epitaxial graphene on SiC obtained by hydrogen intercalation. *Phys. Rev. Lett.*, 103:246804, Dec 2009.

[170] C. Virojanadara, A. A. Zakharov, R. Yakimova, and L.I. Johansson. Buffer layer free large area bi-layer graphene on SiC(0001). *Surf. Sci.*, 604(2):L4 – L7, 2010.

[171] C. Riedl, A. A. Zakharov, and U. Starke. Precise in situ thickness analysis of epitaxial graphene layers on SiC(0001) using low-energy electron diffraction and angle resolved ultraviolet photoelectron spectroscopy. *Appl. Phys. Lett.*, 93(3):033106, 2008.

[172] H. Over, U. Ketterl, W. Moritz, and G. Ertl. Optimization methods and their use in low-energy electron-diffraction calculations. *Phys. Rev. B*, 46:15438–15446, Dec 1992.

[173] H. Hertz. Ueber einen Einfluss des ultravioletten Lichtes auf die electrische Entladung. *Ann. Phys. (Berl.)*, 267(8):983–1000, 1887.

[174] A. Einstein. On a Heuristic Point of View Concerning the Production and Transformation of Light. *Ann. Phys. (Berl.)*, 17:132–148, 1905.

[175] J. Ojeda, C. A. Arrell, J. Grilj, F. Frassetto, L. Mewes, H. Zhang, F. van Mourik, L. Poletto, and M. Chergui. Harmonium: A pulse preserving source of monochromatic extreme ultraviolet (30–110 eV) radiation for ultrafast photoelectron spectroscopy of liquids. *Struct. Dynam.*, 3(2):023602, 2016.

[176] B. Feuerbacher, B. Fitton, and R. F. Willis. *Photoemission and the electronic properties of surfaces.* Wiley London ; New York, 1978.

[177] K. Sakamoto, M. Harada, D. Kondo, A. Kimura, A. Kakizaki, and S. Suto. Bonding state of the C_{60} molecule adsorbed on a $Si(111) - (7 \times 7)$ surface. *Phys. Rev. B*, 58:13951–13956, Nov 1998.

[178] S. Mammadov, J. Ristein, J. Krone, C. Raidel, M. Wanke, V. Wiesmann, F. Speck, and T. Seyller. Work function of graphene multilayers on SiC(0001). *2D Mater.*, 4(1):015043, 2017.

[179] Z. J. Wang, A. Dong, M. Wei, Q. Fu, and X. Bao. Graphene as a surfactant for metal growth on solid surfaces: Fe on graphene/SiC(0001). *Appl. Phys. Lett.*, 104(18):181604, 2014.

[180] J. D. Riley, K. V. Emtsev, F. Speck, Th. Seyller, and L. Ley. Interaction, growth, and ordering of epitaxial graphene on SiC{0001} surfaces: A comparative photoelectron spectroscopy study. *Phys. Rev. B*, 77(155303), 2008.

[181] Dr. Sjuts Optotechnik GmbH. Principles of Operation of a CEM, 2018. Last accessed 6th January 2019.

[182] E. Bauer. LEEM Basics. *Surf. Rev. Lett.*, 05(06):1275–1286, 1998.

[183] J. L. Wiza. Microchannel plate detectors. *Nucl. Instrum. Methods*, 162(1):587 – 601, 1979.

[184] G. A. Rochau, J. E. Bailey, G. A. Chandler, T. J. Nash, D. S. Nielsen, G. S. Dunham, O. F. Garcia, N. R. Joseph, J. W. Keister, M. J. Madlener, D. V. Morgan, K. J. Moy, and M. Wu. Energy dependent sensitivity of microchannel plate detectors. *Rev. Sci. Instrum.*, 77(10):10E323, 2006.

[185] L. Baumgarten, C. M. Schneider, H. Petersen, F. Schäfers, and J. Kirschner. Magnetic x-ray dichroism in core-level photoemission from ferromagnets. *Phys. Rev. Lett.*, 65:492–495, Jul 1990.

[186] W. Kuch, A. Dittschar, K. Meinel, M. Zharnikov, C. M. Schneider, J. Kirschner, J. Henk, and R. Feder. Magnetic-circular-dichroism study of the valence states of perpendicularly magnetized Ni(001) films. *Phys. Rev. B*, 53:11621–11630, May 1996.

[187] C. M. Schneider, Z. Celinski, M. Neuber, C. Wilde, M. Grunze, K. Meinel, and J. Kirschner. Magneto-dichroic effects in energy- and angle-resolved photoemission: contrast mechanisms for the elementally sensitive imaging of magnetic domains. *J. Phys. Condens. Matter*, 6(6):1177–1182, feb 1994.

[188] C. G. Shull, C. T. Chase, and F. E. Myers. Electron Polarization. *Phys. Rev.*, 63:29–37, Jan 1943.

[189] C. M. Schneider and G. Schõnhense. Investigating surface magnetism by means of photoexcitation electron emission microscopy. *Rep. Prog. Phys.*, 65(12):1785–1839, Nov 2002.

[190] G. K. L. Marx, H. J. Elmers, and G. Schönhense. Magneto-optical Linear Dichroism in Threshold Photoemission Electron Microscopy of Polycrystalline Fe Films. *Phys. Rev. Lett.*, 84:5888–5891, Jun 2000.

[191] M. D. Segall, P. J. D. Lindan, M. J. Probert, C. J. Pickard, P. J. Hasnip, S. J. Clark, and M. C. Payne. First-principles simulation: ideas, illustrations and the CASTEP code. *J. Phys. Condens. Matter*, 14(11):2717–2744, mar 2002.

[192] S. J. Clark, M. D. Segall, C. J. Pickard, P. J. Hasnip, M. I. J. Probert, K. Refson, and M. C. Payne. First principles methods using CASTEP. *Z. Kristallogr. Cryst. Mater.*, 220:567, 2009.

[193] K. Ueda and R. Shimizu. Photoelectric Work Function Study on Iron (100) Surface Combined with Auger Electron Spectroscopy. *Japanese Journal of Applied Physics*, 12(12):1869–1873, Dec 1973.

[194] D. J. DiMaria. Dependence on gate work function of oxide charging, defect generation, and hole currents in metal–oxide–semiconductor structures. *J. Appl. Phys.*, 81(7):3220–3226, 1997.

[195] M. W. Davidson. Education in Microscopy and Digital Imaging, 2019. Last accessed 21st July 2019.

[196] G. S. Parkinson. Iron oxide surfaces. *Surf. Sci. Rep.*, 71(1):272 – 365, 2016.

[197] P. J. van der Zaag, P. J. H. Bloemen, J. M. Gaines, R. M. Wolf, P. A. A. van der Heijden, R. J. M. van de Veerdonk, and W. J. M. de Jonge. On the construction of an Fe_3O_4-based all-oxide spin valve. *J. Magn. Magn. Mater.*, 211(1):301 – 308, 2000.

[198] A. V. Ramos, J. B. Moussy, M. J. Guittet, A. M. Bataille, M. Gautier-Soyer, M. Viret, C. Gatel, P. Bayle-Guillemaud, and E. Snoeck. Magnetotransport properties of Fe_3O_4 epitaxial thin films: Thickness effects driven by antiphase boundaries. *J. Appl. Phys*, 100(10):103902, 2006.

[199] R. Bliem, E. McDermott, P. Ferstl, M. Setvin, O. Gamba, J. Pavelec, M. A. Schneider, M. Schmid, U. Diebold, P. Blaha, L. Hammer, and G. S. Parkinson. Subsurface cation vacancy stabilization of the magnetite (001) surface. *Science*, 346(6214):1215–1218, 2014.

[200] R. Bliem, J. Pavelec, O. Gamba, E. McDermott, Z. Wang, S. Gerhold, M. Wagner, J. Osiecki, K. Schulte, M. Schmid, P. Blaha, U. Diebold, and G. S.

Parkinson. Adsorption and incorporation of transition metals at the magnetite $Fe_3O_4(001)$ surface. *Phys. Rev. B*, 92:075440, Aug 2015.

[201] L. Néel. Propriétés magnétiques des ferrites ; ferrimagnétisme et antiferromagnétisme. *Ann. Phys.*, 12:137–198, 1948.

[202] E. Goering, S. Gold, M. Lafkioti, and G. Schütz. Vanishing Fe 3d orbital moments in single-crystalline magnetite. *EPL*, 73(1):97–103, Jan 2006.

[203] K. Jordan, A. Cazacu, G. Manai, S. F. Ceballos, S. Murphy, and I. V. Shvets. Scanning tunneling spectroscopy study of the electronic structure of Fe_3O_4 surfaces. *Phys. Rev. B*, 74:085416, Aug 2006.

[204] E. Goering. Large hidden orbital moments in magnetite. *Phys. Status Solidi B*, 248(10):2345–2351, 2011.

[205] M. Taguchi, A. Chainani, S. Ueda, M. Matsunami, Y. Ishida, R. Eguchi, S. Tsuda, Y. Takata, M. Yabashi, K. Tamasaku, Y. Nishino, T. Ishikawa, H. Daimon, S. Todo, H. Tanaka, M. Oura, Y. Senba, H. Ohashi, and S. Shin. Temperature Dependence of Magnetically Active Charge Excitations in Magnetite across the Verwey Transition. *Phys. Rev. Lett.*, 115:256405, Dec 2015.

[206] Z. Y. Li, M. Jibran, X. Sun, A. Pratt, B. Wang, Y. Yamauchi, and Z. J. Ding. Enhancement of the spin polarization of an $Fe_3O_4(100)$ surface by nitric oxide adsorption. *Phys. Chem. Chem. Phys.*, 20:15871–15875, 2018.

[207] F. Walz. The Verwey transition - a topical review. *J. Phys. Condens. Matter*, 14(12):R285–R340, Mar 2002.

[208] J. de la Figuera and Z. Novotny and M. Setvin and T. Liu and Z. Mao and G. Chen and A. T. N'Diaye and M. Schmid and U. Diebold and A. K. Schmid and G. S. Parkinson. Real-space imaging of the Verwey transition at the (100) surface of magnetite. *Phys. Rev. B*, 88:161410, Oct 2013.

[209] L. Martín-García, A. Mascaraque, B. M. Pabón, R. Bliem, G. S. Parkinson, G. Chen, A. K. Schmid, and J. de la Figuera. Spin reorientation transition of magnetite (001). *Phys. Rev. B*, 93:134419, Apr 2016.

[210] E. J. W. Verwey. Electronic Conduction of Magnetite (Fe_3O_4) and its Transition Point at Low Temperatures. *Nature*, 144:327–328, 1939.

[211] A. R. Muxworthy and E. McClelland. Review of the low-temperature magnetic properties of magnetite from a rock magnetic perspective. *Geophys. J. Int.*, 140(1):101–114, 01 2000.

[212] G. S. Parkinson, Z. Novotný, P. Jacobson, M. Schmid, and U. Diebold. A metastable Fe(A) termination at the $Fe_3O_4(001)$ surface. *Surf. Sci.*, 605(15):L42 – L45, 2011.

[213] L. Martín-García and G. Chen and A. Mascaraque and B. M. Pabón and A. K. Schmid and J. de la Figuera. Memory effect and magnetocrystalline anisotropy impact on the surface magnetic domains of magnetite(001). *Sci. Rep.*, 8:5991, April 2018.

[214] J. de la Figuera and C. Tusche. The Verwey transition observed by spin-resolved photoemission electron microscopy. *Appl. Surf. Sci.*, 391:66 – 69, 2017. European Conference on Surface Science 2015.

[215] J. Park, B. D. Yu, and Y. R. Jang. Ab-initio Study of Physical Properties of $MgO/FeO_x/Fe(001)$ Interfaces. *J. Korean Phys. Soc.*, 73(3):320–324, Aug 2018.

[216] F. Kraushofer, Z. Jakub, M. Bichler, J. Hulva, P. Drmota, M. Weinold, M. Schmid, M. Setvin, U. Diebold, P. Blaha, and G. S. Parkinson. Atomic-Scale Structure of the Hematite α-$Fe_2O_3(1\bar{1}02)$ "R-Cut" Surface. *J. Phys. Chem. C*, 122(3):1657–1669, 2018.

[217] X. Sun, M. Kurahashi, A. Pratt, and Y. Yamauchi. First-principles study of atomic hydrogen adsorption on $Fe_3O_4(100)$. *Surf. Sci.*, 605(11):1067 – 1073, 2011.

[218] H. B. Luo, H. B. Zhang, and J. P. Liu. Strong hopping induced Dzyaloshinskii–Moriya interaction and skyrmions in elemental cobalt. *Npj Comput. Mater.*, 5:50, 2019.

[219] A. Hubert and R. Schäfer. *Magnetic Domains: The Analysis of Magnetic Microstructures*. Springer Berlin Heidelberg, 2008.

[220] R. F. L. Evans, W. J. Fan, P. Chureemart, T. A. Ostler, M. O. A. Ellis, and R. W. Chantrell. Atomistic spin model simulations of magnetic nanomaterials. *J. Phys. Condens. Matter*, 26(10):103202, feb 2014.

[221] E. Lima, A. L. Brandl, A. D. Arelaro, and G. F. Goya. Spin disorder and magnetic anisotropy in Fe_3O_4 nanoparticles. *J. Appl. Phys.*, 99(8):083908, 2006.

[222] P. Janoš, M. Kormunda, O. Životský, and V. Pilařová. Composite Fe3O4/Humic Acid Magnetic Sorbent and its Sorption Ability for Chlorophenols and some other Aromatic Compounds. *Sep. Sci. Technol.*, 48(13):2028–2035, 2013.

[223] M. Mokhtary and M. Torabi. Nano magnetite (Fe_3O_4), an efficient and robust catalyst for the one-pot synthesis of 1-(aryl(piperidin-1-yl)methyl)naphthalene-2-ol and 1-(α-amido alkyl)-2-naphthol under ultrasound irradiation. *J. Saudi Chem. Soc.*, 21:S299 – S304, 2017.

[224] J. Zhang, S. Fan, B. Lu, Q. Cai, J. Zhao, and S. Zang. Photodegradation of naphthalene over Fe_3O_4 under visible light irradiation. *Royal Soc. Open Sci.*, 6(1):181779, 2019.

[225] D. Ambrose, I. J. Lawrenson, and C. H. S. Sprake. The vapour pressure of naphthalene. *J. Chem. Thermodyn.*, 7(12):1173 – 1176, 1975.

[226] F. Brogli, E. Heilbronner, and T. Kobayashi. Photoelectron Spektra of Azabenzenes and Azanaphthalenes: II. A Reinvestigation of Azanaphthalenes by High-Resolution Photoelectron Spectroscopy. *Helv. Chim. Acta*, 55(1):274–288, 1972.

[227] S. Gotovac-Atlagić, T. Hosokai, T. Ohba, Y. Ochiai, H. Kanoh, N. Ueno, and K. Kaneko. Pseudometallization of single wall carbon nanotube bundles with intercalation of naphthalene. *Phys. Rev. B*, 82:075136, Aug 2010.

[228] T. Bally, C. Carra, M. P. Fülscher, and Z. Zhu. Electronic structure of the naphthalene radical cation and some simple alkylated derivatives. *J. Chem. Soc., Perkin Trans. 2*, pages 1759–1766, 1998.

[229] A. Pratt, M. Kurahashi, X. Sun, and Y. Yamauchi. Characterizing ferromagnetic oxide/organic semiconductor interfaces using a spin-polarized metastable helium beam. *J. Magn. Soc. Jpn.*, 38(2-2):71–74, 2014.

[230] R. Aragón. Cubic magnetic anisotropy of nonstoichiometric magnetite. *Phys. Rev. B*, 46:5334–5338, Sep 1992.

[231] J. M. D. Coey, I. Shvets, R. Wiesendanger, and H. J. Guntherodt. Charge freezing and surface anisotropy on magnetite (100). *J. Appl. Phys.*, 73:6742 – 6744, 06 1993.

[232] P. J. Wellmann. Review of SiC crystal growth technology. *Semicond. Sci. Technol.*, 33(10):103001, 9 2018.

[233] V. Cherkez, P. Mallet, T. Le Quang, L. Magaud, and J. Y. Veuillen. Electronic properties of Pb islands on graphene: Consequences of a weak interface coupling from a combined STM and ab initio study. *Phys. Rev. B*, 98:195441, Nov 2018.

[234] T. Maassen, J. J. van den Berg, N. IJbema, F. Fromm, T. Seyller, R. Yakimova, and B. J. van Wees. Long Spin Relaxation Times in Wafer Scale Epitaxial Graphene on SiC(0001). *Nano Lett.*, 12(3):1498–1502, 2012. PMID: 22324998.

[235] I. Cimatti, L. Bondì, G. Serrano, L. Malavolti, B. Cortigiani, E. Velez-Fort, D. Betto, A. Ouerghi, N. B. Brookes, S. Loth, M. Mannini, F. Totti, and R. Sessoli. Vanadyl phthalocyanines on graphene/SiC(0001): toward a hybrid architecture for molecular spin qubits. *Nanoscale Horiz.*, 4:1202–1210, 2019.

[236] S. Xuan, H. Xu, and B. Zhang. Mechanism of silicon vacancies induced ferromagnetism in 6H-SiC. *Nucl. Instrum. Methods Phys. Res. Sec. B*, 453:56 – 60, 2019.

[237] C. Berger, Z. Song, X. Li, X. Wu, N. Brown, C. Naud, D. Mayou, T. Li, J. Hass, A. N. Marchenkov, E. H. Conrad, P. N. First, and W. A. de Heer. Electronic confinement and coherence in patterned epitaxial graphene. *Science*, 312(5777):1191–1196, 2006.

[238] A. J. Van Bommel, J. E. Crombeen, and A. Van Tooren. Leed and auger electron observations of the SiC(0001) surface. *Surf. Sci.*, 48(2):463 – 472, 1975.

[239] W. Chen, H. Xu, L. Liu, X. Gao, D. Qi, G. Peng, S. C. Tan, Y. Feng, K. P. Loh, and A. T. S. Wee. Atomic structure of the 6H-SiC(0001) nanomesh. *Surf. Sci.*, 596(1–3):176 – 186, 2005.

[240] M. Sabisch, P. Krüger, and J. Pollmann. Ab initio calculations of structural and electronic properties of 6H-SiC(0001) surfaces. *Phys. Rev. B*, 55:10561–10570, 4 1997.

[241] T. Wang, Z. Xu, X. Zhang, G. Liu, and G. Qiao. Formation mechanism of multivacancies on H-passivated and Si-reconstructed surfaces of 6H-SiC (0001): a DFT calculation. *Mater. Res. Express*, 5(10):105901, 8 2018.

[242] D. Wang, L. Liu, W. Chen, X. Chen, H. Huang, J. He, Y. P. Feng, A. T. S. Wee, and D. Z. Shen. Optimized growth of graphene on SiC: from the dynamic flip mechanism. *Nanoscale*, 7:4522–4528, 2015.

[243] Y. P. Lin, Y. Ksari, and J. M. Themlin. Hydrogenation of the buffer-layer graphene on 6H-SiC (0001): A possible route for the engineering of graphene-based devices. *Nano Res.*, 8(3):839–850, 3 2015.

[244] F. Varchon, R. Feng, J. Hass, X. Li, B. Ngoc Nguyen, C. Naud, P. Mallet, J. Y. Veuillen, C. Berger, E. H. Conrad, and L. L. Magaud. Electronic structure of epitaxial graphene layers on sic: Effect of the substrate. *Phys. Rev. Lett.*, 99:126805, 9 2007.

[245] A. Mattausch and O. Pankratov. Ab Initio Study of Graphene on SiC. *Phys. Rev. Lett.*, 99:076802, 8 2007.

[246] Changkun Xie, Pengshou Xu, Faqiang Xu, Haibin Pan, and Yonghua Li. First-principles studies of the electronic and optical properties of 6H–SiC. *Physica B Condens. Matter*, 336(3):284 – 289, 2003.

[247] A. Markevich, R. Jones, S. Öberg, M. J. Rayson, J. P. Goss, and P. R. Briddon. First-principles study of hydrogen and fluorine intercalation into graphene-SiC(0001) interface. *Phys. Rev. B*, 86:045453, 7 2012.

[248] G. Capitani, S. Di Pierro, and G. Tempesta. The 6h-SiC structure model: Further refinement from scxrd data from a terrestrial moissanite. *Am. Mineral.*, 92(2-3):403 – 407, 2015.

[249] T. Björkman. CIF2Cell: Generating geometries for electronic structure programs. *Comput. Phys. Commun.*, 182(5):1183 – 1186, 2011.

[250] J. Hass, R. Feng, J. E. Millán-Otoya, X. Li, M. Sprinkle, P. N. First, W. A. de Heer, E. H. Conrad, and C. Berger. Structural properties of the multilayer graphene/$4H-$SiC$(000\overline{1})$ system as determined by surface x-ray diffraction. *Phys. Rev. B*, 75:214109, 6 2007.

[251] F. Varchon, R. Feng, J. Hass, X. Li, B. Ngoc Nguyen, C. Naud, P. Mallet, J. Y. Veuillen, C. Berger, E. H. Conrad, and L. Magaud. Electronic Structure of Epitaxial Graphene Layers on SiC: Effect of the Substrate. *Phys. Rev. Lett.*, 99:126805, 9 2007.

[252] L. I. Johansson and C. Virojanadara. Reactions on the SiC(0001) $\sqrt{3}\times\sqrt{3}$R30° surface after Ti deposition and annealing. *Phys. Status Solidi B*, 248(3):667–673, 2011.

[253] M. L. O'Brien. *Photoemission of SiC surfaces and interfaces*. North Carolina State University, 1999.

[254] D. Stoltz, S. E. Stoltz, and L. S. O. Johansson. Two-dimensional states in the electronic structure of Au/($\sqrt{3}\times\sqrt{3}$)-R30°-4H-SiC(0001). *J. Electron Spectros. Relat. Phenomena*, 163(1):1 – 6, 2008.

[255] T. Ikari, T. Nakamura, K. Hirayama, K. Muraoka, J. Ishii, and M. Naitoh. Oxidation at Cs Pre-Adsorbed Si/6H-SiC(0001)-(3 × 3) Reconstructed Surfaces Studied Using Metastable-Induced Electron Spectroscopy. *e-J. Surf. Sci. Nanotech.*, 14:103–106, 2016.

[256] J. E. Northrup and J. Neugebauer. Theory of the adatom-induced reconstruction of the SiC(0001)$\sqrt{3}\times\sqrt{3}$ surface. *Phys. Rev. B*, 52:R17001–R17004, 12 1995.

[257] A. Siokou, F. Ravani, S. Karakalos, O. Frank, M. Kalbac, and C. Galiotis. Surface refinement and electronic properties of graphene layers grown on copper substrate: An xps, {UPS} and {EELS} study. *Appl. Surf. Sci.*, 257(23):9785 – 9790, 2011.

[258] B. Heinz and H. Morgner. A metastable induced electron spectroscopy study of graphite: The k-vector dependence of the ionization probability. *Surf. Sci.*, 405(1):104 – 111, 1998.

[259] E. Grånäs, T. Gerber, U. A. Schröder, K. Schulte, J. N. Andersen, T. Michely, and J. Knudsen. Hydrogen intercalation under graphene on Ir(111). *Surf. Sci.*, 651:57 – 61, 2016.

[260] B. Lee, S. Han, and Y. S. Kim. First-principles study of preferential sites of hydrogen incorporated in epitaxial graphene on 6H-SiC(0001). *Phys. Rev. B*, 81:075432, 2 2010.

[261] K. Liu, P. Yan, J. Li, C. He, T. Ouyang, C. Zhang, C. Tang, and J. Zhong. Effect of hydrogen passivation on the decoupling of graphene on SiC(0001) substrate: First-principles calculations. *Scientific Reports*, 7:8461, 2017.

[262] K. Sugawara, K. Suzuki, M. Sato, T. Sato, and T. Takahashi. Enhancement of band gap and evolution of in-gap states in hydrogen-adsorbed monolayer graphene on SiC(0001). *Carbon*, 124:584 – 587, 2017.

[263] N. P. Guisinger, G. M. Rutter, J. N. Crain, P. N. First, and J. A. Stroscio. Exposure of Epitaxial Graphene on SiC(0001) to Atomic Hydrogen. *Nano Lett.*, 9(4):1462–1466, 2009. PMID: 19301926.

[264] R. Balog, B. Jørgensen, J. Wells, E. Lægsgaard, P. Hofmann, F. Besenbacher, and L. Hornekær. Atomic Hydrogen Adsorbate Structures on Graphene. *J. Am. Chem. Soc.*, 131(25):8744–8745, 2009. PMID: 19496562.

[265] G. Sclauzero and A. Pasquarello. First-principles study of H adsorption on graphene/SiC(0001). *Phys. Status Solidi B*, 250(12):2523–2528, 2013.

[266] W. X. Wang, Y. W. Wei, S. Y. Li, X. Li, X. Wu, J. Feng, and L. He. Imaging the dynamics of an individual hydrogen atom intercalated between two graphene sheets. *Phys. Rev. B*, 97:085407, 2 2018.

[267] F. C. Bocquet, R. Bisson, J. M. Themlin, J. M. Layet, and T. Angot. Reversible hydrogenation of deuterium-intercalated quasi-free-standing graphene on SiC(0001). *Phys. Rev. B*, 85:201401, 5 2012.

[268] Y. Aoki and H. Hirayama. Hydrogen desorption from 6H-SiC(0001) surfaces during graphitization. *Appl. Phys. Lett.*, 95(9):094103, 2009.

[269] D. C. Elias, R. R. Nair, T. M. G. Mohiuddin, S. V. Morozov, P. Blake, M. P. Halsall, A. C. Ferrari, D. W. Boukhvalov, M. I. Katsnelson, A. K. Geim, and K. S. Novoselov. Control of Graphene's Properties by Reversible Hydrogenation: Evidence for Graphane. *Science*, 323(5914):610–613, 2009.

[270] J. Ristein, S. Mammadov, and Th. Seyller. Origin of Doping in Quasi-Free-Standing Graphene on Silicon Carbide. *Phys. Rev. Lett.*, 108:246104, 6 2012.

[271] N. A. Anderson, M. Hupalo, D. Keavney, M. Tringides, and D. Vaknin. Intercalated rare-earth metals under graphene on SiC. *J. Magn. Magn. Mater*, 474:666 – 670, 2019.

[272] C. Eames, M. Reakes, S. P. Tear, T. C. Q. Noakes, and P. Bailey. Phase selection in the rare earth silicides. *Phys. Rev. B*, 82:174112, 11 2010.

[273] J. Nogami, B. Z. Liu, M. V. Katkov, C. Ohbuchi, and N. O. Birge. Self-assembled rare-earth silicide nanowires on Si(001). *Phys. Rev. B*, 63:233305, 5 2001.

[274] M. Dähne and M. Wanke. Metallic rare-earth silicide nanowires on silicon surfaces. *J. Phys. Condens. Matter*, 25(1):014012, 12 2012.

[275] P. Wetzel, L. Haderbache, C. Pirri, J. C. Peruchetti, D. Bolmont, and G. Gewinner. Electronic structure of epitaxial erbium silicide films on Si(111). *Surf. Sci.*, 251-252:799 – 803, 1991.

[276] P. Avramov, A. A. Kuzubov, A. V. Kuklin, H. Lee, E. A. Kovaleva, S. Sakai, S. Entani, H. Naramoto, and P. B. Sorokin. Theoretical Investigation of the Interfaces and Mechanisms of Induced Spin Polarization of 1D Narrow Zigzag Graphene- and h-BN Nanoribbons on a SrO-Terminated LSMO(001) Surface. *J. Phys. Chem. A*, 121(3):680–689, 2017. PMID: 28075136.

[277] M. B. Salamon and M. Jaime. The physics of manganites: Structure and transport. *Rev. Mod. Phys.*, 73:583–628, Aug 2001.

[278] Z. H. Xiong, D. Wu, Z. Valy Vardeny, and J. Shi. Giant magnetoresistance in organic spin-valves. *Nature*, 427:821, 2004.

[279] S. Merten, O. Shapoval, B. Damaschke, and K. Samwer. Magnetic-Field-Induced Suppression of Jahn-Teller Phonon Bands in $(La_{0.6}Pr_{0.4})_{0.7}Ca_{0.3}MnO_3$: the Mechanism of Colossal Magnetoresistance shown by Raman Spectroscopy. *Sci. Rep.*, 9:238, 2019.

[280] F. A. Ma'Mari, T. Moorsom, G. Teobaldi, W. Deacon, T. Prokscha, H. Luetkens, , S. Lee, G. E. Sterbinsky, D. A. Arena, D. A. MacLaren, M. Flokstra, M. Ali, M. C. Wheeler, G. Burnell, B. J. Hickey, and O. Cespedes. Beating the Stoner criterion using molecular interfaces. *Nature*, 524:69, 2015.

[281] M. Cesaria, A. P. Caricato, G. Maruccio, and M. Martino. LSMO - growing opportunities by PLD and applications in spintronics. *J. Phys. Conf. Ser.*, 292:012003, apr 2011.

[282] Y. Tokura. Critical features of colossal magnetoresistive manganites. *Rep. Prog. Phys.*, 69(3):797–851, feb 2006.

[283] L. Poggini, S. Ninova, P. Graziosi, M. Mannini, V. Lanzilotto, B. Cortigiani, L. Malavolti, F. Borgatti, U. Bardi, F. Totti, I. Bergenti, V. A. Dediu, and

R. Sessoli. A Combined Ion Scattering, Photoemission, and DFT Investigation on the Termination Layer of a $La_{0.7}Sr_{0.3}MnO_3$ Spin Injecting Electrode. *J. Phys. Chem. C*, 118(25):13631–13637, 2014.

[284] H. Xie, H. Huang, N. Cao, C. Zhou, D. Niu, and Y. Gao. Effects of annealing on structure and composition of LSMO thin films. *Physica B*, 477:14 – 19, 2015.

[285] S. Picozzi, C. Ma, Z. Yang, R. Bertacco, M. Cantoni, A. Cattoni, D. Petti, S. Brivio, and F. Ciccacci. Oxygen vacancies and induced changes in the electronic and magnetic structures of $La_{0.66}Sr_{0.33}MnO_3$: A combined ab initio and photoemission study. *Phys. Rev. B*, 75:094418, Mar 2007.

[286] C. Heiner. *Order and Symmetriesof Sexithiophene within Thin Films Studied by Angle-Resolved Photoemission.* Freie Universität Berlin, 2004.

[287] G. Horowitz, B. Bachet, A. Yassar, P. Lang, F. Demanze, J. L. Fave, and F. Garnier. Growth and Characterization of Sexithiophene Single Crystals. *Chem. Mater.*, 7(7):1337–1341, 1995.

[288] T. J. Ha, D. Akinwande, and A. Dodabalapur. Hybrid graphene/organic semiconductor field-effect transistors. *Appl. Phys. Lett.*, 101(3):033309, 2012.

[289] C. Blouzon, F. Ott, L. Tortech, D. Fichou, and J. B. Moussy. Antiferromagnetic coupling in hybrid magnetic tunnel junctions mediated by monomolecular layers of α-sexithiophene. *Appl. Phys. Lett.*, 103(4):042417, 2013.

[290] C. Albonetti, M. Barbalinardo, S. Milita, M. Cavallini, F. Liscio, J. F. Moulin, and F. Biscarini. Selective Growth of α-Sexithiophene by Using Silicon Oxides Patterns. *Int. J. Mol. Sci.*, 12:5719–5735, 2011.

[291] P. Graziosi, M. Prezioso, A. Gambardella, C. Kitts, R .K. Rakshit, A. Riminucci, I. Bergenti, F. Borgatti, C. Pernechele, M. Solzi, D. Pullini, D. Busquets-Mataix, and V. A. Dediu. Conditions for the growth of smooth $La_{0.7}Sr_{0.3}MnO_3$ thin films by pulsed electron ablation. *Thin Solid Films*, 534:83 – 89, 2013.

[292] M. Prezioso, A. Riminucci, P. Graziosi, I. Bergenti, R. Rakshit, R. Cecchini, A. Vianelli, F. Borgatti, N. Haag, M. Willis, A. J. Drew, W. P. Gillin, and V. A. Dediu. A Single-Device Universal Logic Gate Based on a Magnetically Enhanced Memristor. *Adv. Mater.*, 25(4):534–538, 2013.

[293] V. Dediu, L. E. Hueso, I. Bergenti, A. Riminucci, F. Borgatti, P. Graziosi, C. Newby, F. Casoli, M. P. De Jong, C. Taliani, and Y. Zhan. Room-temperature spintronic effects in Alq_3-based hybrid devices. *Phys. Rev. B*, 78:115203, Sep 2008.

[294] M. P. de Jong, V. A. Dediu, C. Taliani, and W. R. Salaneck. Electronic structure of $La_{0.7}Sr_{0.3}MnO_3$ thin films for hybrid organic/inorganic spintronics applications. *J. Appl. Phys*, 94(11):7292–7296, 2003.

[295] S. Sakai, S. Majumdar, Z. I. Popov, P. V. Avramov, S. Entani, Y. Hasegawa, Y. Yamada, H. Huhtinen, H. Naramoto, P. B. Sorokin, and Y. Yamauchi. Proximity-Induced Spin Polarization of Graphene in Contact with Half-Metallic Manganite. *ACS Nano*, 10(8):7532–7541, 2016. PMID: 27438899.

[296] S. Ohno, H. Tanaka, K. Tanaka, K. Takahashi, and M. Tanaka. Electronic structure of α-sexithiophene ultrathin films grown on. *Phys. Chem. Chem. Phys.*, 20:1114–1126, 2018.

[297] L. Sang and J. E. Pemberton. Chemistry at the Interface of α-Sexithiophene and Vapor-Deposited Ag, Al, Mg, and Ca: A Molecular View. *J. Chem. Phys. C*, 123(31):18877–18888, 2019.

[298] W. Feng, S. Rangan, Y. Cao, E. Galoppini, R. A. Bartynski, and E. Garfunkel. Energy level alignment of polythiophene/ZnO hybrid solar cells. *J. Mater. Chem. A*, 2:7034–7044, 2014.

[299] M. P. de Jong, I. Bergenti, V. A. Dediu, M. Fahlman, M. Marsi, and C. Taliani. Evidence for Mn^{2+} ions at surfaces of $La_{0.7}Sr_{0.3}MnO_3$ thin films. *Phys. Rev. B*, 71:014434, Jan 2005.

[300] J. Feng, D. Biswas, A. Rajan, M. D. Watson, F. Mazzola, O. J. Clark, K. Underwood, I. Marković, M. McLaren, A. Hunter, D. M. Burn, L. B.

Duffy, S. Barua, G. Balakrishnan, F. Bertran, P. Le Fèvre, T. K. Kim, G. van der Laan, T. Hesjedal, P. Wahl, and P. D. C. King. Electronic Structure and Enhanced Charge-Density Wave Order of Monolayer VSe_2. *Nano Lett.*, 18(7):4493–4499, 2018. PMID: 29912565.

[301] D. J. Rahn, S. Hellmann, M. Kalläne, C. Sohrt, T. K. Kim, L. Kipp, and K. Rossnagel. Gaps and kinks in the electronic structure of the superconductor $2H$-$NbSe_2$ from angle-resolved photoemission at 1 K. *Phys. Rev. B*, 85:224532, Jun 2012.

[302] E. Morosan, H. W. Zandbergen, B. S. Dennis, J. W. G. Bos, Y. Onose, T. Klimczuk, A. P. Ramirez, N. P. Ong, and R. Cava. Superconductivity in Cu_xTiSe_2. *Nat. Phys.*, 2:544 – 550, 2006.

[303] V. M. Pudalov, M. E. Gershenson, H. Kojima, N. Butch, E. M. Dizhur, G. Brunthaler, A. Prinz, and G. Bauer. Low-Density Spin Susceptibility and Effective Mass of Mobile Electrons in Si Inversion Layers. *Phys. Rev. Lett.*, 88:196404, Apr 2002.